ILMATIETEEN LAITOS
METEOROLOGISKA INSTITUTET
FINNISH METEOROLOGICAL INSTITUTE

132
CONTRIBUTIONS

SIMULATIONS OF SOLAR WIND – MAGNETOSHEATH – MAGNETOPAUSE INTERACTIONS

SANNI HOILIJOKI

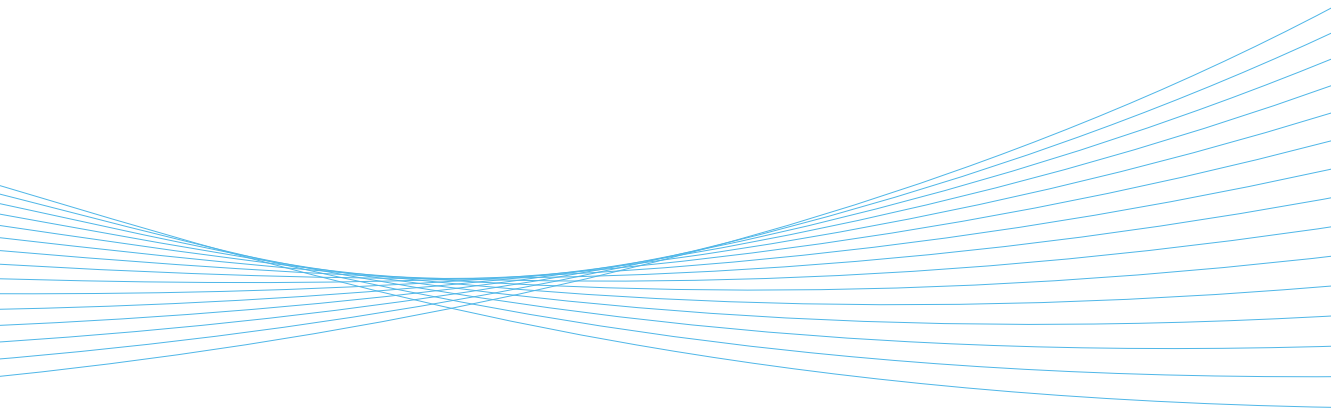

FINNISH METEOROLOGICAL INSTITUTE
CONTRIBUTIONS

No. 132

SIMULATIONS OF SOLAR WIND – MAGNETOSHEATH – MAGNETOPAUSE INTERACTIONS

Sanni Hoilijoki

Department of Physics
Faculty of Science
University of Helsinki
Helsinki, Finland

ACADEMIC DISSERTATION in theoretical physics

To be presented, with the permission of the Faculty of Science of the University of Helsinki, for public criticism in auditorium E204 at noon (12 o'clock) on May 19th, 2017.

Finnish Meteorological Institute
Helsinki, 2017

Supervising professor
Professor Hannu E. J. Koskinen, University of Helsinki, Finland

Thesis supervisor
Professor Minna Palmroth, University of Helsinki, Finland

Pre-examiners
Professor Tuija Pulkkinen, Aalto University, Finland
Professor William Lotko, Dartmouth College, USA

Opponent
Professor Michael W. Liemohn, University of Michigan, USA

ISBN 978-952-336-018-1 (paperback)
ISBN 978-952-336-019-8 (pdf)
ISSN 0782-6117

Erweko
Helsinki, 2017

FINNISH METEOROLOGICAL INSTITUTE

Published by Finnish Meteorological Institute
(Erik Palménin aukio 1) , P.O. Box 503
FIN-00101 Helsinki, Finland

Series title, number and report code of publication
Contributions 132, FMI-CONT-132

Date May 2017

Author

Sanni Hoilijoki

Title

Simulations of solar wind – magnetosheath – magnetopause interactions

Abstract

This thesis investigates interactions between solar wind and the magnetosphere of the Earth using two global magnetospheric simulation models, GUMICS-4 and Vlasiator, which are both developed in Finland. The main topic of the thesis is magnetic reconnection at the dayside magnetopause, its drivers and global effects. Magnetosheath mirror mode waves and their evolution, identification and impacts on the local reconnection rates at the magnetopause are also discussed. This thesis consists of four peer-reviewed papers and an introductory part.

GUMICS-4 is a magnetohydrodynamic model solving plasma as a single magnetized fluid. Vlasiator is the world's first global magnetospheric hybrid-Vlasov simulation model, which solves the motion of ions by describing them as velocity distribution functions, whereas electrons are described as a charge neutralizing fluid. Vlasiator is able to solve ion scale physics in a global scale simulation. However, it is computationally heavy and the global simulations are currently describing Earth's magnetosphere only in two spatial dimensions, whereas the velocity space is three dimensional.

This thesis shows that magnetic reconnection at the dayside magnetopause is controlled by several factors. The impact of dipole tilt angle and sunward component of the interplanetary magnetic field on magnetopause reconnection is investigated with a set of GUMICS-4 simulations. Using Vlasiator simulations, this thesis shows that local reconnection rate is highly variable even during steady solar wind and correlates well with an analytical model for 2D asymmetric reconnection. It is also shown that the local reconnection rate is affected by local variations in the magnetosheath plasma. Fluctuations in the magnetosheath parameters near X-lines are partly generated by mirror mode waves that are observed to grow in the quasi-perpendicular magnetosheath. These results show that that the local reconnection rate at the X-lines is affected not only by the fluctuations in the inflow parameters but also by reconnection at nearby X-lines. Outflow from stronger X-lines pushes against the weaker ones and might ultimately suppress reconnection in the weaker X-lines. Magnetic islands, 2D representations of FTEs, form between X-lines in the Vlasiator simulations. FTEs propagate along the dayside magnetopause driving bow waves in the magnetosheath. The bow waves propagate upstream all the way to the bow shock causing bulges in the shock, from which solar wind particles can reflect back to the solar wind causing local foreshocks.

The overall conclusion of this thesis is that the ion scale kinetic physics is important to accurately model the solar wind – magnetosheath – magnetopause interactions. Vlasiator results show a strong scale-coupling between ion and global scales: global scale phenomena have an impact on the local physics and the local phenomena may have unexpected impacts on the global dynamics of the magnetosphere. Neglecting the global scales in local ion scale simulations and vice versa may therefore lead to incomplete description of the solar wind – magnetosphere interactions.

Publishing unit
Finnish Meteorological Institute

Classification (UDC)
533.9; 52; 52-17;
537.84

Keywords
space plasma physics; numerical simulations;
hybrid-Vlasov; magnetohydrodynamics

ISSN and series title
0782-6117 Finnish Meteorological Institute Contributions

ISBN
978-952-336-018-1 (paperback)
978-952-336-019-8 (pdf)

Language
English

Pages
151

ILMATIETEEN LAITOS

Julkaisija Ilmatieteen laitos
(Erik Palménin aukio 1), PL 503
00101 Helsinki

Julkaisun sarja, numero ja raporttikoodi
Contributions 132, FMI-CONT-132

Julkaisuaika Toukokuu 2017

Tekijä

Sanni Hoilijoki

Nimeke

Simulaatioita aurinkotuulen ja Maan magnetosfäärin vuorovaikutuksista

Tiivistelmä

Aurinkotuuli koostuu plasmasta eli suuresta määrästä sähköisesti varattuja hiukkasia, joita Aurinko jatkuvasti syöksee ympärilleen. Nämä varatut hiukkaset kantavat Auringon magneettikenttää mukanaan planeettojen väliseen avaruuteen. Aurinkotuulen sähkömagneettiset kentät vuorovaikuttavat Maan magneettikentän kanssa muodostaen Maan magnetosfäärin. Vaihtelut aurinkotuulen koostumuksessa, nopeudessa ja magneettikentän suunnassa ja voimakkuudessa aiheuttavat häiriöitä Maan magneetttikentässä. Näitä häiriöitä kutsutaan avaruussääksi. Jotta avaruussään rajuihin muutoksiin voidaan varautua, täytyy aurinkotuulen ja Maan magnetosfäärin vuorovaikutus tuntea. Tärkein vuorovaikutusmekanismi on magneettinen rekonnektio eli magneettisten kenttäviivojen uudelleenkytkeytyminen, jota tapahtuu magnetopausilla eli pinnalla, joka erottaa Maan magnetosfäärin aurinkotuulesta. Rekonnektio avaa Maan kenttäviivoja ja päästää energiaa ja plasmaa virtaamaan sisään ja ulos Maan magnetosfääristä.

Tämä väitöskirja koostuu neljästä vertaisarvioidusta julkaisusta ja johdannosta, joissa tutkitaan aurinkotuulen ja Maan magnetosfäärin vuorovaikutusta käyttäen kahta laskennallista mallia. Toinen malli, GUMICS-4, perustuu magnetohydrodynamiikkaan eli plasman kuvailuun yhtenä magneettisena nesteenä. Toinen malli, Vlasiator, on maailman ainoa koko Maan magnetosfääriä kuvaava malli, jossa käytetään hybridi-Vlasov -menetelmää. Vlasiator mallintaa protonien käyttätymisen ratkaisemalla niiden nopeusjakaumien kehityksen, mutta elektronit se mallintaa nesteenä. Tämä metodi mahdollistaa ioniskaalan fysiikan mallintamisen, mutta on laskennallisesti huomattavasti raskaampi kuin plasman kuvaaminen yhtenä nesteenä, mistä johtuen Vlasiator-simulaatiot kuvaavat tällä hetkellä Maan magnetosfääriä ainoastaan kahdessa tilaulottuvuudessa.

Ensimmäisessä julkaisussa tutkitaan magneettikentän aaltoja, joita kutsutaan peilimoodiksi, alueessa, joka on Maan magnetopausin ja sen keulashokin väliin jäävä pyörteinen välivyöhyke (magnetosheath). Toisessa julkaisussa tutkitaan GUMICS-mallilla, miten Maan dipolikentän kallistuskulma ja aurinkotuulen magneettikentän auringonsuuntainen komponentti vaikuttavat sijaintiin, missä magneettista rekonnektiota tapahtuu. Kolmannessa julkaisussa rekonnektioita tutkitaan käyttäen Vlasiatoria. Vaikka simulaatioissa aurinkotuulen parametrin pidetään vakioina, havaitaan, että magneettisen rekonnektion tahti vaihtelee huomattavasti. Julkaisussa näytetään myös, että mangetosheathin peilimoodeilla on vaikutusta rekonnektioon mangetopausilla. Tämä vaiheteleva rekonnektio johtaa magneettisten saarien muodustumiseen, joiden eteneminen ajaa magnetosheathissa aaltoja, joita tutkitaan tämän väitöskirjan neljännessä julkaisussa. Nämä aallot etenevät ylävirtaan kohti Maan keulashokkia ja aiheuttavat shokissa pullistuman, josta aurinkotuulen hiukkaset voivat kimmota takaisin aurinkotuuleen aiheuttaen paikallisia esishokkeja.

Tämä väitöskirja näyttää, että ioniskaalan fysiikan kuvailu on tärkeää, jotta aurinkotuulen ja Maan magnetosfäärin vuorovaikututsta voidaan mallintaa tarkasti. Nestekuvailulla ei kyetä mallintamaan esimerkiksi esishokin muodostumista eikä magnetosheathin peiliaaltoja, jotka vaikuttavat rekonnektioon. Vlasiator-mallin tulokset osoittavat, että suuren mittakaavan ilmiöllä on vaikutusta paikallisiin pienen ioniskaalan ilmiöihin ja vastaavasti paikallisilla ilmiöllä voi olla odottamattomia vaikutuksia globaaliin dynamiikkaan. Satelliitit pystyvät tuottamaan havaintoja vain hyvin rajatulta alueelta ja tämän vuoksi magnetosfäärin mallintaminen ja mallien kehittäminen on erityisen tärkeää.

Julkaisijayksikkö
Uudet havaintomenetelmät

Luokitus (UDK)
533.9; 52; 52-17;
537.84

Asiasanat
avaruusplasmafysiikka; numeeriset simulaatiot;
magnetohydrodynamiikka; hybrid-Vlasov -malli

ISSN ja avainnimike
0782-6117 Finnish Meteorological Institute Contributions

ISBN
978-952-336-018-1 (nidottu)
978-952-336-019-8 (pdf)

Kieli
Englanti

Sivumäärä
151

Contents

Preface

First and foremost I am grateful to my supervisor Prof. Minna Palmroth for accepting me to be a part of the Vlasiator team. Thank you for giving me this awesome opportunity and for being an inspiring role model for a young researcher. I also want to thank Prof. Hannu Koskinen who pointed me to the direction of the Vlasiator team and magnetospheric physics. My special thanks go to Dr. Yann Pfau-Kempf for all these years of being a PhD student together. Thank you for always being willing to help me with all my coding and plasma physics problems. I am also grateful to all the rest of the current and past members of the Vlasiator team, especially Dr. Urs Ganse for the help with python and computer issues and Dr. Sebastian von Alfthan for all the work he has done to make Vlasiator even better. I also want to thank all my co-authors, especially Dr. Heli Hietala, Prof. Rami Vainio, Dr. Brian Walsh and Prof. Paul Cassak, for the fruitful discussions, guidance and inspiration. I am also grateful to Prof. Tuija Pulkkinen and Prof. William Lotko for pre-examining this thesis and giving comments, which improved the final result.

Ten years have passed since I came to the Kumpula Campus for the first time. It have been a pleasure to know you and experience all these years with you, Harriet, Sofia, Iida, Terhi and Maija. Last but not least, I want to thank my family for always supporting me.

The work lead to this thesis was mainly conducted at the Finnish Meteorological Institute. My work at FMI and at the University of Helsinki have been funded by Minna Palmroth's European Research Council starting and consolidator grants QuESpace and PRESTISSIMO and grants from the Academy of Finland. My conference trips, summer schools and international networking have been made possible by travel grants from the Emil Aaltonen Foundation, Magnus Ehrnrooth Foundation, Oscar Öflund's Foundation, Finnish Concord Fund, the University of Helsinki Chancellor's grant, Geospace Environment Modeling Workshop student support, the Finnish National Doctoral Programme in Astronomy and Space Physics, and the University of Helsinki Doctoral program in Particle Physics and Universe Sciences. I also acknowledge computing grants from CSC and PRACE, which were used to run the simulations used in this thesis.

Sanni Hoilijoki
Helsinki, 2017

Research articles and the author's contributions

This thesis consists of an introduction and four articles that are published in peer-reviewed journals. Papers are referred to as **Paper I**, **II**, **III** and **IV** in the text. Three first papers have not been included in prior theses but Paper IV was part of the thesis by Pfau-Kempf [2016].

Paper I:

Hoilijoki, S., Palmroth, M, Walsh, B. M., Pfau-Kempf, Y., von Alfthan, S., Ganse, U., Hannuksela, O., and Vainio, R. (2016), Mirror modes in the Earth's magnetosheath: Results from a global hybrid-Vlasov simulation, *Journal of Geophysical Research: Space Physics*, volume 121, pages 4191–4204, 2016.
doi:10.1002/2015JA022026

The author planned and carried out the analysis of the magnetosheath mirror modes in the simulation with help from the other authors. The author created most of the tools used in the analysis of the simulation data and wrote the paper with guidance from other authors.

Paper II:

Hoilijoki, S., Souza, V. M., Walsh, B. M., Janhunen, P., and Palmroth, M., Magnetopause reconnection and energy conversion as influenced by the dipole tilt and the IMF B_x, *Journal of Geophysical Research: Space Physics*, volume 119, pages 4484–4494, 2014.
doi:10.1002/2013JA019693

The author carried out the GUMICS-4 simulation runs used in this paper and performed the analysis using existing tools. The author wrote the paper except Section 3 with help from other authors.

Paper III:

Hoilijoki, S., Ganse, U., Pfau-Kempf, Y., Cassak, P. A., Walsh, B.M., Hietala, H., von Alfthan, S., and Palmroth, M., Reconnection rates and X line motion at the magnetopause: Global 2D-3V hybrid-Vlasov simulation results, *Journal of Geophysical Research: Space Physics*, volume 122, 2017.
doi:10.1002/2016JA023709

The author planned and carried out the analysis of the dayside reconnection described in this paper with guidance from other authors. The tools used in the analysis and plotting of the simulation data were created by the author with help from the other authors. The paper was written by the author with assistance from the co-authors.

Paper IV:

Pfau-Kempf, Y., Hietala, H., Milan, S. E., Juusola, L., **Hoilijoki, S.**, Ganse, U., von Alfthan, S., Palmroth, M. Evidence for transient, local ion foreshocks caused by dayside magnetopause reconnection, *Annales Geophysicae*, volume 34, pages 943-959, 2016.
doi:10.5194/angeo-34-943-2016

This paper was also included in the thesis of Pfau-Kempf [2016]. The author contributed to the model used to produce the simulation. The author participated in the analysis of the dayside magnetopause reconnection and FTEs and took part in the discussion that led to the final results.

The author has also contributed to two peer-reviewed research articles that are relevant to the topic of this thesis, *Vlasiator: First global hybrid-Vlasov simulations of Earth's foreshock and magnetosheath* by von Alfthan et al. [2014] and *ULF foreshock under radial IMF: THEMIS observations and global kinetic simulation Vlasiator results compared* by Palmroth et al. [2015].

The author have participated to the development of Vlasiator model. The largest contribution to the code is the 2D line dipole used in the polar plane simulations. The author has significantly contributed to creating tools for analyzing and plotting of data from Vlasiator simulations.

Terminology

1D, 2D, ...	One, two, ... -dimensional or one, two, ... dimensions
IMF	interplanetary magnetic field
MHD	magnetohydrodynamic(s)
PIC	particle-in-cell
FTE	flux transfer event
CFL	Courant–Friedrichs–Lewy condition for calculating time step in simulation

Variables

$\mathbf{r} = (x, y, z)$	position vector
$\mathbf{v} = (v_x, v_y, v_z)$	velocity vector
$\mathbf{a} = (a_x, a_y, a_z)$	acceleration vector
t	time
ω	angular frequency
$\mathbf{B}$, B	magnetic field and its magnitude
$\mathbf{E}$, E	electric field and its magnitude
$\mathbf{V}$, V	bulk velocity of plasma and its magnitude
$\mathbf{J}$, J	current density and its magnitude
$\mathbf{k}$, k	wave vector and wave number
$\bar{\bar{P}}$, P	pressure tensor, scalar pressure
T	temperature
ρ, n	mass density and particle number density
m_i, q_i	mass and electric charge of particle species i
$\omega_{pi} = n_i q_1^2 / \epsilon_0 m_i$	plasma frequency of species i
$\Omega_{c,i} = q_i B / m_i$	gyrofrequency of particle species i
$r_c = m_i v_\perp / q_i B$	qyroradius of particle species i
$d_i = c/\omega_p i$	ion inertial length
$v_\parallel$, $v_\perp$	velocity vector components parallel and perpendicular to $\mathbf{B}$

Constants

e	elementary charge ($1.602 \cdot 10^{-19}$ C)
μ_0	vacuum permeability ($4\pi \cdot 10^{-7}$ A^{-2} kg m s^{-2})
ε_0	vacuum permittivity ($= (\mu_0 c^2)^{-1} \approx 8.854 \cdot 10^{-12}$ A^2 kg^{-1} m^{-3} s^4)
c	Speed of light in vacuum ($= 299\,792\,453$ m/s)
k_B	Boltzmann constant ($\approx 1.381 \cdot 10^{-23}$ m^2 kg s^{-2} K^{-1})
R_E	Earth radius (≈ 6372 km)

Chapter 1

Introduction

Life on Earth is maintained by the Sun. The Sun, as well as over 99% of the visible matter in our Universe consists of plasma. Plasma is the fourth sate of matter besides solid, fluid and gas. Solar wind, a stream of plasma from the Sun, carries the magnetic field of the Sun into the interplanetary space filling up the whole heliosphere.

Solar eruptions, such as coronal mass ejections, are enormous bursts of plasma from the Sun. They usually propagate faster and have much higher magnetic field and density than is typical for solar wind. Electromagnetic fields and plasma that propagate in the interplanetary space affect obstacles on their way, planets but also man-made satellites. One of these obstacles is the Earth and its dipolar magnetic field. The magnetic field shields Earth from the solar wind by forming a cavity, known as the magnetosphere, in the solar wind flow.

Solar eruptions and other large variations in the solar wind can disturb the Earth's magnetosphere causing variations in the physical state of the near-Earth space. This is known as space weather. Severe space weather events can be harmful, for example, for the electronics of satellites, airplanes flying over polar regions, and even for power grids on ground. If society is not properly prepared for these events, the consequences could be disastrous and costly, for instance, as space weather may cause large-scale power outages and destroy satellite components. Being prepared can help us to prevent the damage if the arrival times of solar eruptions and severeness of the space weather can be predicted. In order to predict space weather accurately with a long lead time, the whole Sun–solar wind–magnetosphere–ionosphere chain needs to be understood.

Improving space weather prediction is not the only reason for space plasma research. Understanding fundamental plasma physics helps us to improve understanding how the visible universe works; fundamental plasma phenomena define the behavior of the Sun and other stars. Near-Earth space plasma provides a laboratory that can be studied *in situ* using spacecraft measurements. However, spacecraft can provide data only from one point at a time with limited

temporal cadence thus leaving most of the space unobserved.

Numerical simulations can be used to complement the spacecraft observations and fill in the gaps. Plasma is a complicated system with multiple length and time scales. Thus, accurate numerical modeling of plasma is computationally very challenging requiring supercomputers.

This thesis concentrates on improving understanding of the near-Earth part of the Sun–solar wind–magnetosphere chain. The main theme of this thesis is that the global scale phenomena have an impact on the local phenomena and the local phenomena affect the global system. The focus of this thesis lies on the dayside magnetopause reconnection during southward IMF, which opens the magnetospheric field lines, letting plasma and energy flow into the magnetosphere. The evolution and identification of magnetosheath mirror mode waves and their impact on the on the local reconnection rates at the magnetopause are also discussed. It is also shown that the dayside magnetopause reconnection can have an impact upstream all the way to the solar wind. Two numerical magnetospheric simulations models are used in this thesis, magnetohydrodynamic model GUMICS-4 and hybrid-Vlasov model Vlasiator. The majority of the results in this thesis are obtained with Vlasiator, which is the world's first global magnetospheric hybrid-Vlasov simulation. This thesis shows that the Vlasiator results are consistent with analytical theories as well as spacecraft observations and previous studies with simulations. The difference between different modeling approaches, especially GUMICS-4 and Vlasiator, and the importance of global kinetic models are also discussed.

This thesis is organized as follows: Chapter 2 describes shortly basics of space plasma physics and the structure and dynamics of the Earth's magnetosphere that are relevant for this thesis. Chapter 3 introduces the methods of global magnetospheric simulations and the two global magnetospheric models applied in this thesis: GUMICS-4 and Vlasiator. The Earth's magnetosheath and mirror mode waves are discussed in Chapter 4 by shortly describing the methods and results as well as the context of the results obtained. Chapter 5 summarizes the results obtained in this thesis about dayside magnetopause reconnection and shortly presents the relevant background. Chapter 6 concludes the thesis with discussion.

Chapter 2

Space physics background

2.1 Plasma

This section describes the basic plasma concepts that are important for this thesis. Derivations of the equations are omitted and for a more complete description, books such as those by Koskinen [2011] and Kivelson and Russell [1995] are suggested to the interested reader.

2.1.1 Plasma description

Plasma is ionized gas that contains unbound electrons and ions. Therefore, the electromagnetic interactions are important for the collective behavior of the particles. Plasma is quasi-neutral, which means that there are as many positively charged particles as there are negative. In order for gas to become and behave like plasma as electromagnetic forces become dominant, 1% ionization can be enough [e.g. Koskinen, 2011]. In dense plasmas, the collisions between charged particles and with neutral particles are important. However, dilute and/or hot plasmas can often be regarded as collisionless because the mean free paths or the collision time scales of the charged particles become larger than the considered length and time scales. This is the case for the plasma in the near Earth space above the collisional ionosphere and in the solar wind.

Electromagnetic interactions are essential in the plasma behavior. The physics of electromagnetic fields is defined by the Maxwell equations:
1. Coulomb's law: The source of electric field $\mathbf{E}$ is the charge density ρ_c:

$$\nabla \cdot \mathbf{E} = \rho_c/\varepsilon_0. \tag{2.1}$$

2. Sourceless magnetic field $\mathbf{B}$:

$$\nabla \cdot \mathbf{B} = 0 \tag{2.2}$$

3. Faraday's law:

$$\nabla \times \mathbf{E} = -\frac{\partial \mathbf{B}}{\partial t}. \tag{2.3}$$

4. Ampère's law for current density **J**:

$$\nabla \times \mathbf{B} = \mu_0 \mathbf{J} + \frac{1}{c^2}\frac{\partial \mathbf{E}}{\partial t}. \tag{2.4}$$

Above t is time, ε_0 is the vacuum permittivity, μ_0 is the vacuum permeability, and c is the speed of light.

Electric field in plasma is determined by Ohm's law, whose general form is:

$$\mathbf{E} + \mathbf{V} \times \mathbf{B} = \eta \mathbf{J} + \frac{1}{ne}(\mathbf{J} \times \mathbf{B}) - \frac{1}{ne}\nabla \cdot \bar{\bar{P}}_e + \frac{m_e}{ne^2}\frac{\partial \mathbf{J}}{\partial t}. \tag{2.5}$$

The terms on the right hand side are the resistive term, the Hall term, the electron pressure term, and the electron inertial term, respectively. The ideal Ohm's law assumes that the entire right hand side is zero.

The ratio between the plasma pressure $P = nk_BT$ and the magnetic pressure $P_m = B^2/2\mu_0$ is called plasma beta: $\beta = \frac{2\mu_0 nk_BT}{B^2}$. In low beta plasma ($\beta < 1$), the magnetic field dominates the plasma motion and behavior. In a high beta plasma, $\beta \gtrsim 1$, the plasma pressure dominates over the magnetic pressure, and defines the behavior of plasma.

Plasma itself can be described at different levels that are illustrated in Figure 2.1. Plasma consists of free charges so the motion of individual particles defined by the electromagnetic fields (Eq's 2.1–2.4) and interaction with other particles and waves can be important (Fig. 2.1a). When studying plasma as a collection of multiple particles, the collective phenomena become important and one may choose not to solve the motion of each particle separately. The motion of a large amount of particles can be described using velocity distribution functions (Fig. 2.1b). At larger scales one may choose to treat the plasma as a fluid. In the fluid treatment plasma has a single temperature. Velocity distributions are assumed to be Maxwellian (Fig. 2.1c). Below, these three different descriptions are presented briefly.

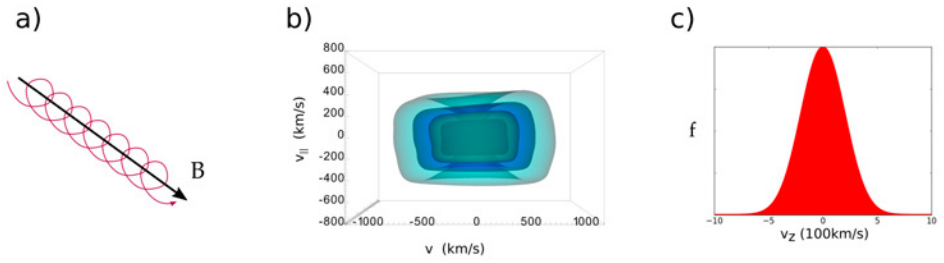

Figure 2.1: Illustrations of different plasma descriptions: a) single particle, b) kinetic description with a distribution function, c) Maxwellian plasma distribution.

Single particle motion

Charged particles move under the influence of the Lorentz force:

$$\mathbf{F} = q_i(\mathbf{E} + \mathbf{V} \times \mathbf{B}). \tag{2.6}$$

If the electric field is zero and the magnetic field is uniform the particles gyrate on a plane perpendicular to $\mathbf{B}$. The angular frequency of the spiral motion is known as cyclotron frequency or gyrofrequency, $\Omega_{c,i} = q_i B/m_i$, and the radius of the circle is the gyroradius $r_c = m_i v_\perp / q_i B$. Since the electron mass is much smaller than the proton mass (by a factor of 1836), electrons gyrate with a much smaller radius. They also gyrate in the opposite direction due to the different sign of the electric charge. The orbit of the particle is distorted from a circle in the case of non-zero electric field and/or non-uniform magnetic field.

Charged particles are said to be magnetized when the magnetic field is strong enough to dominate the particle motion. The motion of a magnetized charged particle can be divided into the gyrating motion and motion of the center of the gyration, called the guiding center. The particle velocity can be given as a sum of components parallel to the magnetic field $v_\parallel$ and perpendicular to the magnetic field $v_\perp$. The pitch angle between the velocity vector and the magnetic field is defined as $\tan\alpha = v_\perp / v_\parallel$.

An electric field component parallel to the magnetic field accelerates particles along the magnetic field but a perpendicular electric field causes particles to drift perpendicularly to both $\mathbf{B}$ and $\mathbf{E}$ with a velocity $\mathbf{v}_{E\times B} = \mathbf{E} \times \mathbf{B}/B^2$. Similarly, due to the gradient in the magnetic field, particles drift in a direction that is perpendicular both to the gradient and $\mathbf{B}$. Curvature in the magnetic field also drives a drift current. These drift velocities can be generalized to any force that can accelerate the particles: $\mathbf{v}_F = \mathbf{F} \times \mathbf{B}/qB^2$ [e.g. Koskinen, 2011].

The magnetic moment $\mu = W_\perp/B = mv_\perp^2/2B = (mv^2/2B)\sin^2\alpha$ of a particle is conserved if the magnetic field changes sufficiently slowly [e.g. Koskinen, 2011]. This is called the first adiabatic invariant. This means that if the magnetic field increases, so does the velocity of the charged particle perpendicular to the magnetic field. Because the total kinetic energy of the particle, $W = 1/2mv^2 = 1/2m(v_\perp + v_\parallel)$, is also conserved, $v_\perp$ increases until $v_\parallel$ becomes zero. The motion of the guiding center of the particle slows down and α increases until the motion along the magnetic field stops and the pitch angle reaches $\alpha = 90^\circ$ as illustrated in Figure 2.2. Because of the gradient of the magnetic field (parallel to the field) there is a force $\mathbf{F} = -\mu\nabla_\parallel B$. This mirror force slows down the particle until it reverses its motion back toward the weaker magnetic field. The point where the particle stops and turns back is called a magnetic mirror point. A particle that initially has pitch angle α_0 in a magnetic field B_0, has pitch angle $\alpha_m = 90^\circ$ at the mirror point where the magnetic field strength is B_m. The relation between the initial pitch angle and magnetic field and the magnetic field at the mirror point is

$\sin^2\alpha_0/\sin^2\alpha_m = \sin^2\alpha_0 = B_0/B_m$. Figure 2.2 shows a magnetic bottle that is formed by two magnetic mirrors facing each other. Charged particles can get trapped inside a magnetic bottle bouncing between the mirror points. The bouncing motion is nearly periodical if magnetic field does not change much during one bounce period [e.g. Koskinen, 2011]. Motion of a particle in a magnetic bottle is related to the second adiabatic invariant known as the longitudinal invariant: $j = \oint m_i v_\parallel \mathrm{d}s$, where s is the distance along the guiding center orbit. When the mirror points move closer to each other, the distance $\oint \mathrm{d}s$ decreases. In order to conserve j, $v_\parallel$ must increase. Similarly, $v_\parallel$ decreases if the distance between the mirror point increases.

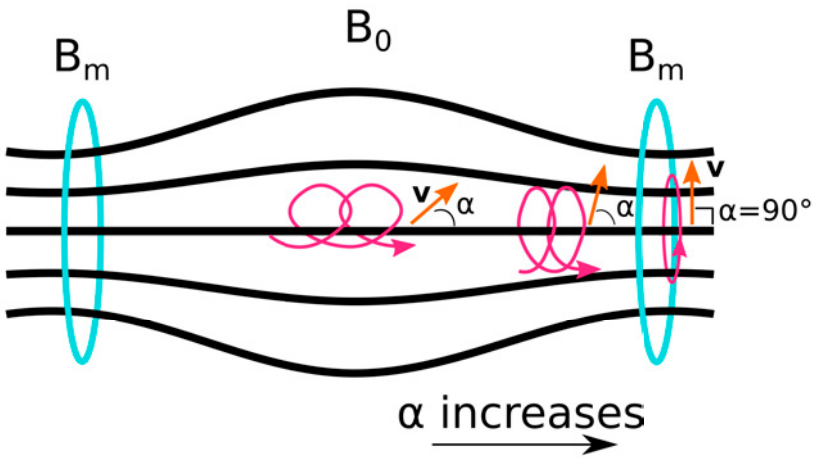

Figure 2.2: Illustration of a magnetic bottle. Pink spirals show the particle trajectories, orange arrows show the velocity vector of the particle, and α is the pitch angle. Blue rings mark the location of the magnetic mirror points.

Kinetic description

When looking at plasma in a larger scale it is not possible to solve the propagation of each particle separately. For most purposes, it suffices to know where the collective ensemble of particles is going and at which velocity. This can be done by describing plasma particles as a velocity distribution function $f(\mathbf{r}, \mathbf{v}, t)$. It expresses the number of particles in a 6-dimensional phase space element $\mathrm{d}x\mathrm{d}y\mathrm{d}z\mathrm{d}v_x\mathrm{d}v_y\mathrm{d}v_z$. In other words, it represents how many particles at a certain location $\mathbf{r}(t)$ are going at certain velocity $\mathbf{v}(t)$. Since dilute plasmas are collisionless there can be multiple different plasma populations at the same location moving in different directions. Each species (denoted by subscript s) is described by a different $f_s(\mathbf{r}, \mathbf{v}, t)$.

The evolution of the distribution function in time and space can be determined by solving the Vlasov equation:

$$\frac{\partial f}{\partial t} + \mathbf{v} \cdot \nabla_r f + \mathbf{a} \cdot \nabla_v f = 0, \tag{2.7}$$

which is the Boltzmann equation without a collision term (as mentioned earlier, collisions are often negligible in space plasma) [e.g. Koskinen, 2011]. Macroscopic parameters such as particle flux, number density, pressure and temperature can be calculated as velocity moments. The number density of plasma as a function of location can be obtained by integrating over the whole velocity space $n(\mathrm{r}, t) = \int f(\mathrm{r}, \mathrm{v}, t)\mathrm{d}^3 v$ and the bulk velocity is the particle flux, which is the first velocity moment, divided by the number density: $V(\mathbf{r}, t) = \int \mathbf{v} f \mathrm{d}^3 v / \int f \mathrm{d}^3 v$.

Magnetohydrodynamic description

At larger scales, plasma behaves like a continuous medium. Therefore, plasma can be described as a fluid. The description of plasma as a magnetized fluid with electromagnetic interactions is called magnetohydrodynamics (MHD). The collective state of plasma is described with macroscopic parameters: bulk velocity $\mathbf{V}$, temperature T and number density n. In multi-fluid MHD, different plasma populations can be described as separate fluids, each population having their own macroscopic parameters. This allows description of interactions between different particle species that have large differences in the macroscopic plasma parameters.

The most simple approach is the ideal MHD that assumes infinite conductivity. The Ohm's law (2.5) in ideal MHD reduces to $\mathbf{E} = -\mathbf{V} \times \mathbf{B}$. Set of ideal MHD equations (including conservation of mass, momentum and energy) is closed with the equation of state usually assuming adiabatic plasma. Plasma pressure is also often assumed to be isotropic.

A basic wave mode in a non-magnetized medium is a sound wave, which is driven by pressure perturbations. The speed of the sound wave in a fluid is $v_s = \sqrt{\gamma k_B T / m}$, where γ is the polytropic index, which is usually 5/3 for plasma. In MHD plasma, there are three basic wave modes that carry information: Alfvén wave, magnetosonic wave and fast/slow mode wave. Basic Alfvén wave is a transverse wave that propagates along the magnetic field lines with speed $v_A = \sqrt{(B^2/\mu_0 \rho_m)}$, also called Alfvén speed [e.g. Koskinen, 2011]. The fastest waves are the magnetosonic waves that are longitudinal waves propagating perpendicular to the magnetic field. The magnetosonic velocity is a combination of the speed of sound and the Alfvén speed: $v_{ms} = \sqrt{v_s^2 + v_A^2}$. Phase velocities of the fast and slow MHD waves are combinations of the sound speed and the Alfvén speed and can be written in the form: $v_{f/s}^2 = \frac{1}{2}(v_s^2 + v_A^2) \pm \frac{1}{2}\sqrt{(v_s^2 + v_A^2)^2 - 4 v_s^2 v_A^2 \cos^2\theta}$, where the plus sign is

for the fast mode wave (v_f) and the minus sign for the slow mode wave (v_s), respectively, and θ is the angle between the wave vector and magnetic field.

2.1.2 Shocks and sheath regions

In a fluid medium, motion of an object causes pressure enhancement, which propagates with the speed of sound in front of the object. If the medium is magnetized, the perturbations propagate with the Alfvén or magnetosonic speed. A shock wave is formed if the relative motion of the object is faster than the propagation speed of the fastest wave mode. In the solar wind, the object can be a planet or slower solar wind flow in front of a fast propagating solar eruption or otherwise fast solar wind.

The shock is a discontinuity in plasma parameters. A discontinuity must be compressional and have flow across it in order to be a shock. In MHD plasma, two actual shock types, slow and fast shock, can be defined according to how the plasma parameters change in the shock crossing. They both conserve the normal component of the magnetic field and the sign of the tangential component. The parallel velocity decreases in the shock crossing. The magnitude of the magnetic field decreases in the slow shock crossing and increases in the fast shock crossing. The third type is the Alfvén "shock" that is discontinuity rather than a shock because the density is conserved in the crossing and, therefore, there is no compression. It is a rotational discontinuity because it preserves the magnitude of tangential component (perpendicular to the shock normal) of the magnetic field across the shock, but may rotate it.

An important parameter in the shock crossing is the angle between the shock normal and the upstream magnetic field, θ_{Bn} [e.g. Stone and Tsurutani, 1985]. The shock structure and dynamics depend drastically on θ_{Bn}. This is illustrated in the Figure 2.3. If θ_{Bn} is small the shock is called quasi-parallel (Fig. 2.3a). The particles that are reflected from the shock back to the upstream direction are able to escape the shock and propagate upstream and interact with the ambient plasma forming a foreshock. The particles reflected from a quasi-perpendicular shock that have large θ_{Bn} gyrate back to the shock and are not able to escape upstream (Fig. 2.3b).

A sheath region forms between the obstacle and the shock. In the sheath the plasma parameters are different from the upstream parameters depending on the shock type. Change in the plasma parameters across an MHD shock can be described using so called Rankine-Hugoniot relations [see e.g. Koskinen, 2011]. The magnetosheath forms as the solar wind flows around the Earth's magnetic field. Sheaths have been also observed downstream of interplanetary shocks, for example, driven by magnetic clouds created by solar eruption [e.g. Gosling and McComas, 1987, Tsurutani et al., 1988].

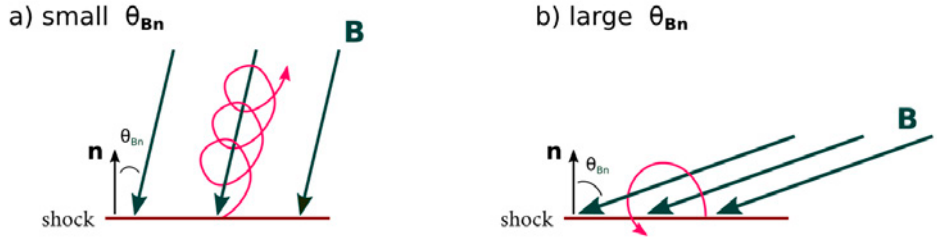

Figure 2.3: Difference between a) the quasi-parallel and b) quasi-perpendicular shock.

2.1.3 Magnetic reconnection

Alfvén [1943] suggested the concept of frozen-in magnetic field. If in an ideal collisionless plasma the fluid parcel is located on one magnetic field line at one time it will remain on the same line at all times. This means that two magnetically separate regions will remain separate at all times. Magnetic reconnection was suggested to break the frozen-in condition. Reconnection is a plasma process that leads to a large scale magnetic topology change due to local breaking of the frozen-in condition. In magnetic reconnection the magnetic energy is converted to kinetic and thermal energy of the charged particles.

The induction equation,

$$\partial \mathbf{B}/\partial t = \nabla \times (\mathbf{V} \times \mathbf{B}) + \eta \nabla^2 \mathbf{B}, \tag{2.8}$$

where $\mathbf{V}$ is the plasma velocity, $\eta = 1/\mu_0 \sigma$ is the resistivity and σ is the conductivity, describes the temporal evolution of the magnetic field. The first term on the right hand side is the convection term and the second term is the diffusion term that is required to be non-zero to break the frozen-in condition. The basic concept of 2D magnetic reconnection can be explained using a simple cartoon in Figure 2.4 and the induction equation. Panel 2.4a shows two regions of magnetized plasma with oppositely oriented magnetic fields convecting towards each other. In these regions the convection term dominates and the diffusion term is negligible. A current sheet forms in between these two regions according to the Ampère's law (Eq. 2.4). In the current sheet the diffusion term becomes significant and may lead to formation of a neutral X-line (panels b and c in Fig. 2.4). At the X-line the field lines are broken and reconnected as shown in Figure 2.4c.

One of the first models of 2D steady MHD reconnection was derived by Sweet [1958] and Parker [1957]. In their model the thickness of the diffusion region is 2δ and the length $2L$ (see Fig. 2.4c) with $L \gg \delta$. The Sweet-Parker reconnection model predicts slow inflow velocity, v_{in}, and consequently slow reconnection rate, the amount of magnetic flux per unit time that is reconnected

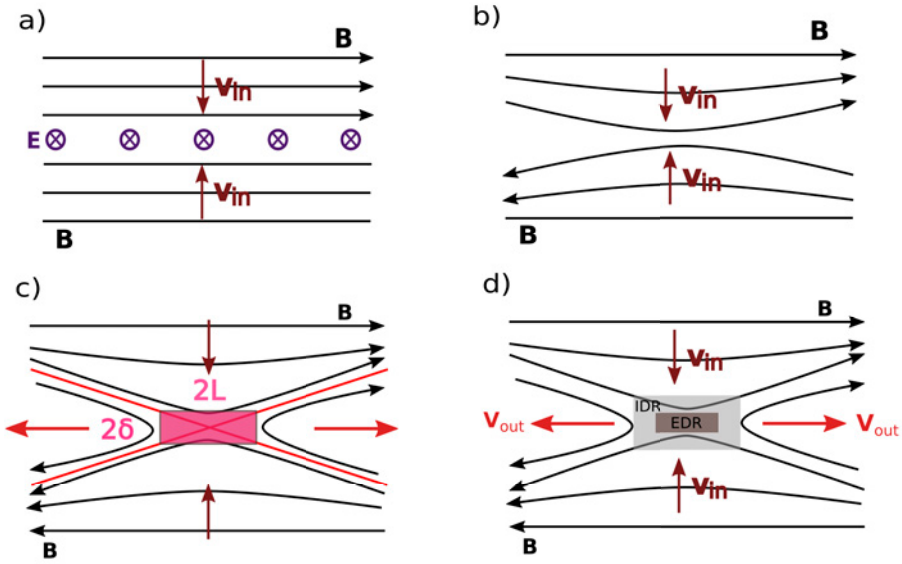

Figure 2.4: Formation of a reconnection X-line. a) Formation of a current sheet. b) Formation of an X-line. c) X-line and diffusion region (square box). Red lines are the separatrices between the inflow magnetic field and reconnected magnetic field. d) X-line illustrating the separation between the ion diffusion region (IDR, light gray rectangular box) and the electron diffusion region (EDR, dark gray rectangular box).

at the X-line. Therefore, the Sweet-Parked model is not able to describe the fast reconnection that has been observed to occur, for example, in the solar eruptions or in the magnetospheric boundaries and in the magnetotail.

Petschek [1964] offered a solution to the slow reconnection by suggesting a model where all plasma accelerated in the reconnection process does not need to flow through the diffusion region. Plasma is accelerated at standing slow MHD shock waves that are connected to the diffusion region. Location of the shocks are shown with red lines in Figure 2.4c. Now the diffusion region can be very small. However, it is required to exist since the magnetic field lines need to be reconnected at the X-line. The Petschek model estimates a higher inflow velocity, up to 10% of the inflow v_A, giving faster estimates to the reconnection rate compared to the Sweet-Parker model.

Diffusion regions

Because of their different mass and hence gyroradius, ions and electrons decouple from the magnetic field at different distance from the center of the X-line. Ions decouple first at larger distances but electrons still remain magnetized as they approach the X-line. The area where the ions decouple is called the ion dif-

fusion region (IDR, larger box in Fig. 2.4c). The size of the IDR is comparable to the ion inertial length, which is defined as the gyroradius of a particle with the local Alfvén speed: $d_i = v_A/\Omega_{ci} = c/\omega_{pi}$, where ω_{pi} is the local ion plasma frequency. At much smaller scales, comparable to electron inertial scales the electrons demagnetize as well. This is called the electron diffusion region (EDR, smaller dark gray box in Fig. 2.4c). The separation of electron and ion motion is produced by the Hall term, $\frac{1}{ne}(\mathbf{J} \times \mathbf{B})$, included in the generalized Ohm's law (Eq. 2.5).

Reconnection triggering

The current sheet that is formed between the two oppositely oriented magnetic field regions can start to reconnect spontaneously or the initiation of reconnection may be driven. Driven reconnection means that reconnection is forced by the system's boundary conditions. Spontaneous reconnection is initiated by an instability of the current sheet. The most studied instability that can initiate reconnection is the resistive tearing mode instability [e.g. Coppi et al., 1966, Furth et al., 1963]. The tearing mode is a long wave instability compared to the current sheet thickness. It causes the current sheet to break into adjacent parallel pinches [Furth et al., 1963]. Therefore the tearing can lead to macroscopic scale changes in the current sheet. At the location where the current sheet breaks, X-lines form and reconnection starts. Between the X-lines the tearing instability leads to the formation of magnetic islands (O-type neutral points) as is illustrated in Figure 2.5.

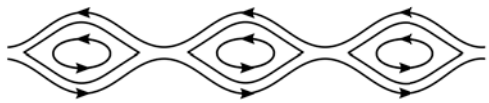

Figure 2.5: Formation of magnetic islands and X-lines due to reconnection triggered by the ion tearing mode instability in the current sheet.

Asymmetric reconnection

Sweet-Parker and Petschek reconnection models assume that that the plasma parameters in the two inflow regions are identical. This is not the case, for example, with the reconnection between the solar wind and the Earth's magnetosphere. Cassak and Shay [2007] derived an analytical Sweet-Parker-type model for asymmetric antiparallel reconnection described below. The inflow parameters, B, ρ, and v are different on the different inflow sides of the X-line and the subscript 1 and 2 refer to both inflow sides. The relation between the inflowing and outflowing mass flux in asymmetric reconnection yields:

$$L(\rho_1 v_1 + \rho_2 v_2) \sim 2\delta\rho_{out} v_{out}, \tag{2.9}$$

where L is the length of the reconnection diffusion region and δ is the width. Their ratio δ/L is the aspect ratio of the diffusion region. The outflow velocity can be written as:

$$V_{AH}^2 \sim \frac{B_1 B_2}{\mu_0} \frac{B_1 + B_2}{\rho_1 B_2 + \rho_2 B_1}, \tag{2.10}$$

if energy and magnetic field are assumed to be conserved in reconnection. V_{AH} is also known as the hybrid Alvén velocity of the inflow plasmas. The reconnection rate in the asymmetric reconnection is

$$E \sim \left(\frac{\rho_{out} v_{out} B_1 B_2}{\rho_1 B_2 + \rho_2 B_1} \right) \frac{2\delta}{L} = v_{out} \left(\frac{B_1 B_2}{B_2 + B_1} \right) \frac{2\delta}{L}, \tag{2.11}$$

where $\rho_{out} \sim (\rho_1 B_2 + \rho_2 B_1)/(B_1 + B_2)$ is the density of the outflowing plasma.

Doss et al. [2015] added a velocity shear in tangential direction between the inflow regions in the model by Cassak and Shay [2007]. Earlier, it had been found that the velocity shear decreases the reconnection rate finally suppressing it [e.g. Chen et al., 1997, Cowley and Owen, 1989, Gosling et al., 1991]. Doss et al. [2015] showed that due to the velocity shear the isolated X-lines start to drift with a velocity:

$$v_{drift} \sim \frac{\rho_1 B_2 v_{L,1} + \rho_2 B_1 v_{L,2}}{\rho_1 B_2 + \rho_2 B_1}, \tag{2.12}$$

where v_L refers to the upstream velocity in the direction of reconnecting magnetic field. The shear also introduces a correction factor to the reconnection rate so that the new rate is

$$E_{shear} \sim E_0 \left(1 - \frac{v_{shear}^2}{V_{AH}^2} \frac{4\rho_1 \rho_2 B_1 B_2}{(\rho_1 B_2 + \rho_2 B_1)^2} \right), \tag{2.13}$$

where E_0 is the rate without the shear given by Eq. 2.11.

2.2 Earth's Magnetosphere

2.2.1 Structure

Outer regions

The magnetic field of the Earth, which at the surface of the Earth is roughly dipolar, has the dipole axis slightly tilted from the rotational axis. The Earth's magnetic field is distorted from the dipolar morphology by solar wind – magnetosphere interactions as it diverts the solar wind flow around the Earth. On the dayside the solar wind flow pushes the field lines towards the Earth and on the nightside drags them into a long structure called the magnetotail, reaching distances of hundreds of Earth radii (R_E).

The structure of the magnetosphere is illustrated in Figure 2.6. Since the solar wind flow at 1 AU is super-sonic and super-Alfvénic a bow shock forms upstream of the Earth. The bow shock is a dynamic structure located around 14 R_E upstream from the center of the Earth [Kivelson and Russell, 1995]. As the plasma crosses the bow shock the speed of the plasma (V) drops to sub-magnetosonic and the density (ρ) and magnetic field strength (B) increase. These changes in plasma parameters indicate that the bow shock is a fast-mode shock. Depending on the IMF direction a foreshock can form upstream of the bow shock. The foreshock of the Earth is known to be populated by 30-second waves that are created by the particles reflected at the bow shock [e.g. Eastwood et al., 2005]. The shocked solar wind region between the bow shock and the Earth's magnetic domain is called the magnetosheath. The magnetosheath plasma is unstable to the growth of low frequency waves (0.1 Hz), such as mirror mode waves [Denton, 2000]. The magnetosheath and the mirror mode waves will be discussed further in Chapter 4.

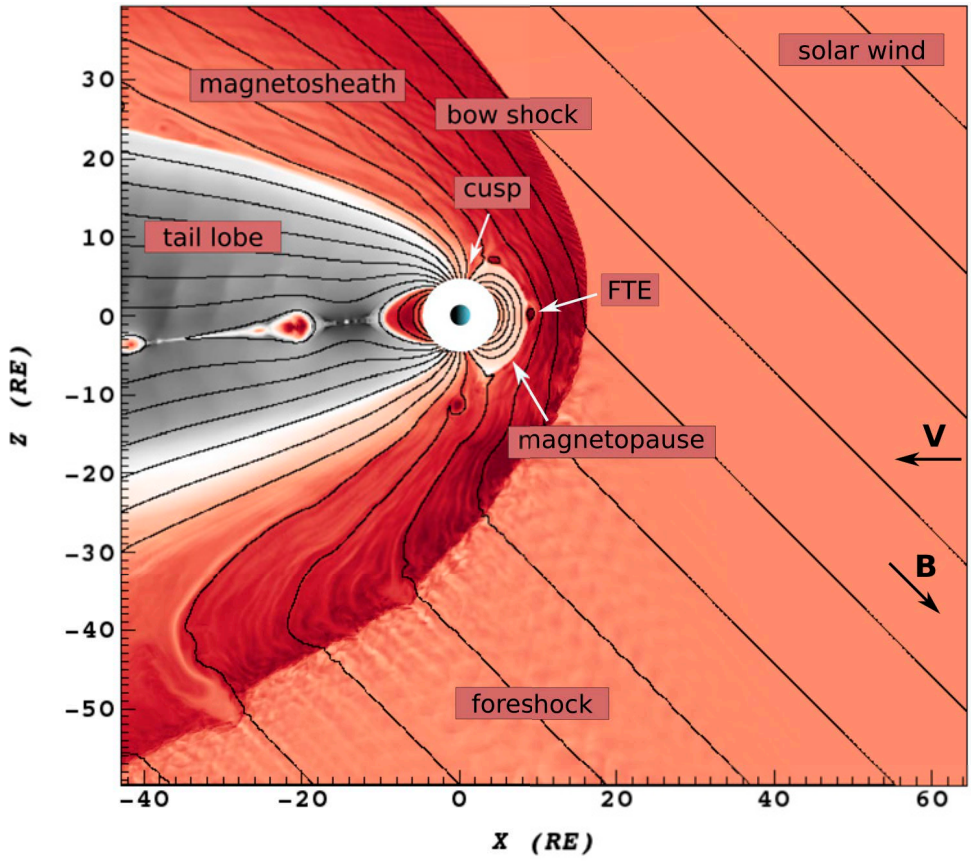

Figure 2.6: Structure of the outer regions of the Earth's magnetosphere in a polar plane cut.

The magnetopause is the boundary encompassing the Earth's magnetosphere separating it from the magnetosheath. The boundary between the solar wind and the Earth's magnetic field was first discussed by Chapman and Ferraro [1931a,b], who suggested that there is a diamagnetic current shielding the magnetosphere from the solar wind, known as the Chapman-Ferraro current. The location of the dayside magnetopause can be defined by hydrostatic equilibrium between the dynamic pressure of the solar wind and magnetic pressure of the Eart's magnetic field: $\rho_{SW} V_{SW}^2 = B_{MS}^2 / 2\mu_0$, where ρ_{SW} and V_{SW} are the mass density and bulk velocity of the solar wind, respectively, and B_{MS} is the magnetic field magnitude of the magnetosphere. At the dayside the magnetopause resides around 10 R_E distance from the center of the Earth [e.g. Pulkkinen, 2007].

The magnetotail consists of two lobes, that have oppositely oriented magnetic field lines. The field lines are connected to Earth from the one end and to solar wind from the other. The northern lobe field lines point towards the Earth and southern field lines away from the Earth. Plasma in the tail lobes is much more dilute than, for example, in the dayside magnetosphere, where the field lines are closed. Between the two lobes is a hot and dense plasma sheet where the cross tail current J_{CT} flows from dawn towards dusk, and closes with magnetopause currents that flow around the tail lobes. Magnetic field lines in the tail lobe map to the polar cap inside the auroral oval [e.g. Pulkkinen, 2007]. Therefore, the magnetic flux inside the polar cap is the same as in the tail lobe of the same hemisphere.

In the northern and southern hemisphere between the closed dayside magnetic field lines and field lines of the tail lobes are the polar cusps. They are connected directly to the magnetosheath and along those field lines solar wind plasma can flow into the magnetosphere and ionospheric plasma can escape from the magnetosphere.

Inner regions

The innermost part of the magnetosphere is the plasmasphere that resides in the near-Earth region from about 1000 km to a few R_E. It is populated by cold and dense plasma that originates from the ionosphere. The ionosphere is the uppermost part of the Earth's atmosphere from around 80 km altitude, and it is ionized by the solar extreme ultraviolet (EUV) radiation and particle precipitation. The plasmasphere is partially overlapping with the high energy radiation belts. Radiation belt particles are trapped within the dipole field as they bounce between the northern and southern mirror points. Particles trapped in the Earth's magnetic field drift around the Earth due to the gradient and curvature drifts forming a ring current between 4 to 6 R_E on the equatorial plane [e.g. Pulkkinen, 2007].

2.2.2 Dynamics

The dynamics of the Earth's magnetosphere during southward interplanetary magnetic field (IMF) was explained by Dungey [1961]. In the so called Dungey cycle, illustrated in Figure 2.7, the closed magnetic field lines of the Earth's magnetosphere that are pointing northward reconnect with the southward IMF (1). Magnetic reconnection forms new "open" field lines that are connected to the Earth from one end and to the solar wind with the other end (2). These field lines are straightened by the $\mathbf{J} \times \mathbf{B}$ force and advected tailward with the solar wind flow (2,3). New magnetic flux coming from the dayside pushes the field lines towards the center of the tail (4). Oppositely oriented field lines that are connected to the northern and southern polar caps reconnect in the tail again (5,6) and then return back to the dayside through dusk or dawn of the magnetosphere (7).

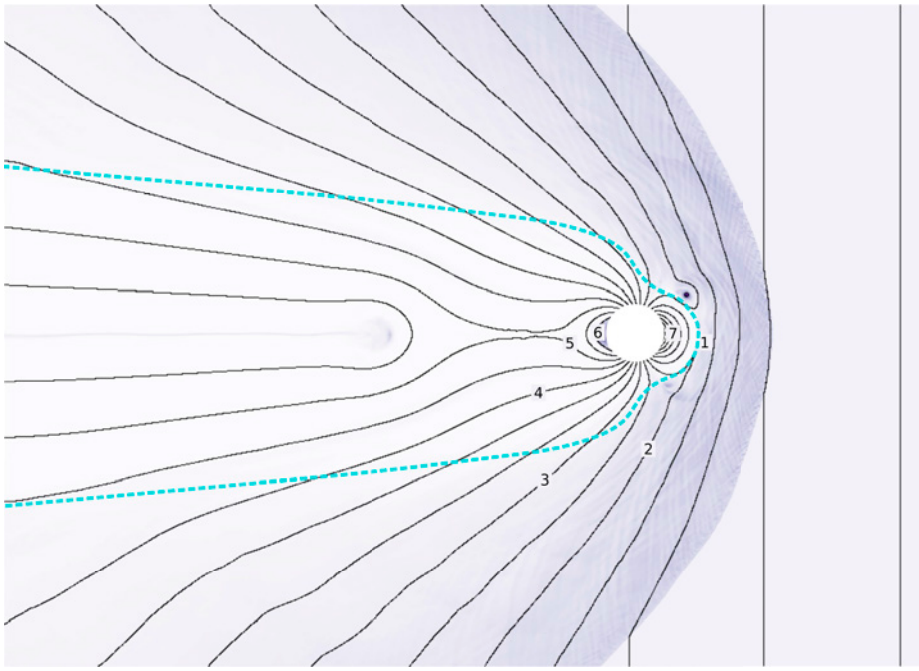

Figure 2.7: Dungey cycle: Reconnection of magnetic field lines at the dayside magnetopause (1), field line convection towards the tails (2,3), field line piling up in the tail lobes (4), tail reconnection (5,6), field lines return back to the dayside (7). Cyan dotted line depicts the approximate location of the magnetopause.

The Dungey cycle describes the magnetospheric dynamics during southward IMF but reconnection between the solar wind and magnetospheric field lines occurs also with other IMF directions. The orientation of the X-line is strongly dependent on the IMF clock angle, which is the angle between IMF direction

and z axis in global ($\arctan(B_y/B_z)$) [e.g. Laitinen et al., 2007, Trattner et al., 2007]. When IMF is northward, reconnection takes place tailward of the cusps where the magnetic field of the solar wind is nearly antiparallel with the lobe field lines. Even though reconnection occurs essentially with all IMF directions, the global convection is strongest during southward IMF. Then the reconnecting field lines are nearly antiparallel and the energy transfer from solar wind to the magnetosphere is the most efficient [e.g. Akasofu, 1981].

2.3 Current spacecraft missions

This thesis focuses on interactions between solar wind, magnetosheath and magnetopause using global magnetospheric simulations, which are presented in the next Chapter. These regions in the near-Earth space are continuously probed by multiple spacecraft missions. Below the most important missions for the scope of this thesis are introduced shortly.

Both Wind [Acuña et al., 1995] and *Advanced Composition Explorer* (ACE) [Stone et al., 1998] spacecraft are currently located in the L1 Lagrangian point of the Sun-Earth system and provide information on the solar wind plasma and IMF. The European Space Agency's (ESA) *Cluster* mission [Escoubet et al., 1997] with four spacecraft orbit the Earth in a tetrahedron formation on a polar orbit to gain 3D information on the solar wind interaction with the magnetosphere. The formation and separation between the spacecraft allows Cluster mission to resolve ion scale details of magnetic reconnection [e.g. Vaivads et al., 2004]. NASA's *Time History of Events and Macroscale Interactions during Substorms* (THEMIS) [Angelopoulos, 2008] originally with five spacecraft, now with three, orbits Earth closer to the equatorial plane aiming to measure effects of tail reconnection simultaneously at different distances. Two of the original THEMIS mission spacecraft were send to orbit the Moon in a mission called *Acceleration, Reconnection, Turbulence, and Electrodynamics of the Moon's Interaction with the Sun* (ARTEMIS) [Angelopoulos, 2011]. *Geotail* that was launched already in 1992 to study the magnetotail dynamics is still operating. *Double Star* spacecraft mission consisted of two spacecraft [Liu et al., 2005]. The first one, TC-1, was launched to an elliptical orbit in 2003 and the second one, TC-2, was launched to polar orbit in 2004. In 2007 TC-1 entered the Earth's atmosphere but TC-2 remains functional.

For a long time the electron diffusion region in the dayside magnetopause could be studied only using theoretical calculations and high resolution kinetic simulations. The high temporal and spatial scales could not be resolved by the previous spacecraft missions. NASA's *Magnetospheric Multiscale Mission* (MMS) [Burch et al., 2016], launched in 2015, was built for solving the smallest electron scales of the magnetic reconnection. MMS has managed to fly through the dayside X-lines and the first results of the electron diffusion region have been published [e.g. Burch et al., 2016]

Chapter 3

Global magnetospheric simulations

Even though multiple spacecraft missions are measuring the plasma simultaneously in the near-Earth space, each satellite covers only its 1D track in time and space, leaving most of the space unobserved as was already mentioned in Chapter 2. With good luck the spacecraft can disperse and sample a broader region of the near-Earth space so that they can observe the responses to a particular event at different locations of the magnetosphere. To fill the gaps and to complement the observations, global magnetospheric simulations are needed.

There are different approaches that numerical models can take to solve the plasma phenomena in the magnetosphere. In this thesis the global models are discussed in two main categories: MHD and hybrid-kinetic simulations. The main focus of this chapter lies on the two simulation models applied in this thesis: the MHD model GUMICS-4 and the hybrid-Vlasov model Vlasiator.

3.1 MHD

The most widely used method to simulate large-scale properties of the Earth's magnetosphere is to use global MHD models. MHD models assume plasma to be a magnetized fluid. MHD is a good approximation of the plasma behavior in large scale systems where the temporal and spatial scales of the plasma phenomena are much larger than the ion scales. This is a good approximation in the magnetosheath and the outer magnetosphere of the Earth. MHD models are widely used also to simulate other solar system plasma environments: the dynamo of the Sun [e.g. Käpylä, 2011], initiation of coronal mass ejection and related waves [e.g. Hoilijoki et al., 2013, Pomoell et al., 2008], solar wind and coronal mass ejection propagation in the interplanetary space [e.g. Gressl et al., 2014, Temmer et al., 2011] and even the structure of the whole heliosphere [e.g. Opher et al., 2009]. The inner magnetosphere and the boundaries of the

magnetosphere include physical processes that require more detailed models.

Results of the first global magnetospheric MHD simulations were published in the late 1970s and early 1980s [e.g. Brecht et al., 1981, 1982, Leboeuf et al., 1978, Lyon et al., 1981]. Leboeuf et al. [1978] were the first ones to verify the magnetospheric topology and dynamics proposed by Dungey [1961] using a global 2D MHD simulation. Their simulation produced reconnection in the magnetotail and a substorm-like process. Lyon et al. [1981] also presented results of a substorm process in a 2D global MHD model. Using a 3D MHD simulation Brecht et al. [1982] studied the tail reconnection during southward IMF and reported formation of multiple X-lines. Since the early times the models as well as computers have become more efficient allowing more detailed studies of the magnetosphere. Various global magnetospheric MHD models have been developed and are used in space physics research.

3.1.1 GUMICS-4

GUMICS-4, the Grand Unified Magnetosphere Ionosphere Coupling Simulation, is a global MHD magnetosphere-ionosphere simulation model developed at the Finnish Meteorological Institute [Janhunen, 1996, Janhunen et al., 2012]. Technical details of GUMICS-4 are described in the paper Janhunen et al. [2012]. Here the main points of the numerical scheme are summarized.

GUMICS-4 couples a 3D global ideal MHD magnetosphere to an electrostatic ionosphere model. The magnetospheric part solves the fully conservative ideal MHD equations that are written using the conserved variables density ρ, momentum density $\mathbf{p} = \rho\mathbf{v}$, total energy density U, and magnetic field that separates the dipole field from the varying field $\mathbf{B} = \mathbf{B}_0 + \mathbf{B}_1$ [Janhunen et al., 2012]:

$$\frac{\partial \rho}{\partial t} = -\nabla \cdot (\rho \mathbf{v}), \tag{3.1}$$

$$\frac{\partial \mathbf{p}}{\partial t} = -\nabla \cdot \left[\frac{\mathbf{pp}}{\rho} + \left(P + \frac{B^2}{2\mu_0} - \frac{\mathbf{BB}}{\mu_0} \right) \mathbb{1} - \frac{1}{\mu_0}(\mathbf{BB} - \mathbf{B}_0\mathbf{B}_0) \right], \tag{3.2}$$

$$\frac{\partial U_1}{\partial t} = -\nabla \cdot \left[\left(U_1 + P - \frac{B_1^2}{2\mu_0} \right) \frac{\mathbf{p}}{\rho} - \frac{\mathbf{B}_1(\mathbf{p} \cdot \mathbf{B}_0)}{\mu_0 \rho} + \frac{\mathbf{B}_1 \times (\mathbf{p} \times \mathbf{B})}{\mu_0 \rho} \right], \tag{3.3}$$

$$\frac{\partial \mathbf{B}_1}{\partial t} = \nabla \times \left(\frac{\mathbf{p} \times \mathbf{B}}{\rho} \right), \tag{3.4}$$

where $\mathbb{1}$ is a unit dyad, and U_1 is the total energy density after subtracting the effect of dipole, $U_1 = U - (\mathbf{B}_1 \cdot \mathbf{B}_0)/\mu_0 - B_0^2/(2\mu_0)$. Total energy density is $U = P/(\gamma - 1) + \rho\mathbf{v}^2/2 + B^2/2\mu_0$.

The simulation domain of the magnetosphere, which is shown in a polar plane cut in Figure 3.1, extends from $+32\ R_E$ to $-224\ R_E$ in x-direction and $\pm 64\ R_E$ in y- and z-directions in GSE (Geocentric Solar Ecliptic) coordinates. Each boundary has a layer of ghost cells where the boundary conditions are

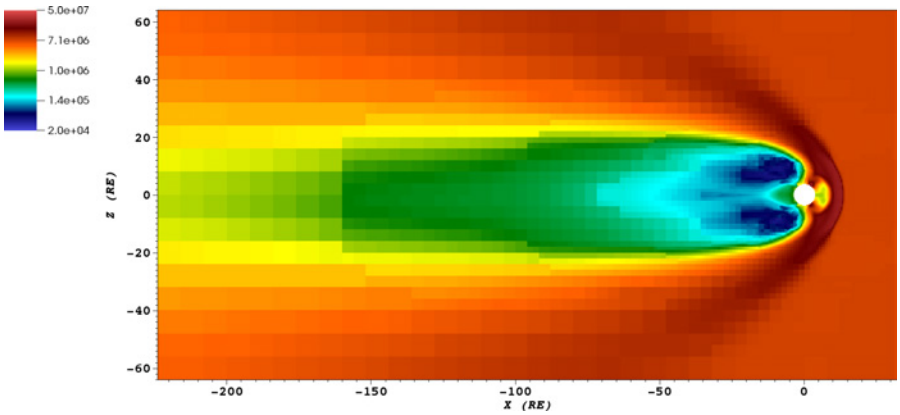

Figure 3.1: Cut of a 3D GUMICS-4 simulation in a polar plane. Color coding shows the number density (m^{-3}) in logarithmic scale.

applied to allow a smooth physical inflow or outflow of plasma at the simulation boundary. The solar wind inflow boundary applies Dirichlet boundary condition: all values in the ghost cells are set to the solar wind input values. Solar wind parameters that are used as input are the plasma density (ρ), velocity ($\mathbf{v}$), temperature (T), and magnetic field ($\mathbf{B}$). The other outer boundaries apply Neumann boundary conditions; every time step each parameter is copied from the simulation cell to the neighboring ghost cell. The inner boundary is at 3.7 R_E distance from the center of the Earth. From the inner boundary, field aligned currents and electron precipitation are mapped to the ionospheric domain along the dipole field lines. The electric potential is calculated in the ionosphere and it is mapped back to the inner boundary of the magnetospheric domain where it is used as a boundary condition.

Initially the simulation domain includes the dipole magnetic field in an empty space and the solar wind parameters at the sunward wall. It takes about 1 hour simulated time from the beginning of the simulation to reach properly formed magnetosphere. GUMICS-4 uses two different numerical solvers; the primary solver is Roe's approximate Riemann solver [Roe, 1981] and the secondary one is the Harten-Lax-van Leer (HLL) solver. Roe's solver has small numerical diffusion but can sometimes produce unphysical negative pressures or densities. If this happens the solution is recalculated using the HLL solver that produces physical results but is more diffusive. Divergence of $\mathbf{B}$ accumulates over time in the simulation due to the truncation error of the solver. The divergence is removed every 20 s of simulation time using a projection method [Brackbill and Barnes, 1980]. The discretization to grid cells is done using finite volume method (FVM). In FVM the volume averages of the variables are calculated in every cell and the sum of the fluxes through the cell faces are subtracted from the average.

GUMICS-4 applies adaptive mesh refinement with a basic grid size of 8 R_E. The grid is refined automatically in regions of large gradients. The refinement is also set to depend on location; the grid is preferably refined close to the Earth. Each cubic grid can be independently divided into eight smaller cells. The refinement of the cells can be repeated until maximum adaptation level, usually set to 5, is reached. This results in a refined grid with maximum resolution of 0.25 R_E. The time step can also be changed using subcycling. The basic initial time step is 1 s. In each cell the local time step is calculated by dividing the base time step by two until it satisfies the local Courant–Friedrichs–Lewy (CFL) condition [Courant et al., 1928]. The CFL condition ensures that the time step is smaller than the time it takes for the fastest wave mode to travel a distance that corresponds to the cell size. For ideal MHD the fastest wave mode is the magnetosonic wave.

Because GUMICS-4 solves the ideal MHD equations the conductivity is assumed to be infinite and thus the resistivity is zero. If there is no resistivity there is no physical diffusion. However, as discussed in Section 2.1.3 diffusion is required to break the frozen-in condition to allow reconnection. In order to describe the magnetospheric dynamics and its interaction with the solar wind properly, reconnection has to take place. Numerical diffusion caused by the discretization mimics the physical diffusion allowing magnetic field lines to reconnect in current sheets. Even though ideal MHD simulations cannot produce as fast reconnection rates as the Hall-MHD or (hybrid-)kinetic models [Birn et al., 2001] GUMICS simulations as well as other global ideal MHD models have been widely used to study the global dynamics that are driven by magnetic reconnection. Reconnection related parameters such as energy transfer through the magnetopause have been found to scale with observations [Palmroth et al., 2003, Palmroth et al., 2012].

Figure 3.1 shows an example of a GUMICS simulation in the polar plane. The color coding depicts the number density. The bow shock, magnetosheath and magnetopause can be easily seen on the dayside as well as the tenuous tail lobes.

3.1.2 Other global MHD models

Other well-known and widely used global magnetospheric MHD models are the Lyon-Fedder-Mobarry (LFM) code [Lyon et al., 2004], Open Geospace General Circulation Model (OpenGGCM) [Raeder et al., 1998, Raeder, 2003, Raeder et al., 2008], and the Block-Adaptive-Tree-Solarwind-Roe-Upwind-Scheme (BATS-R-US) [Powell et al., 1999] and the MHD model by Tanaka [2000] applying a finite volume total variation diminishing scheme. Both LFM and OpenGGCM are single fluid global MHD models that solve the ideal MHD equations semiconservatively, conserving mass, momentum, and plasma energy but not requiring a strict conservation of the total energy. A multi-fluid version

of LFM (MFLFM) have also been developed and used to study, for example, ionospheric outflow of oxygen ions [Brambles et al., 2010, Garcia et al., 2010, Wiltberger et al., 2010].

BATS-R-US is developed as a part of the Space Weather Modeling Framework and it includes more physics than basic ideal MHD models. One of the extensions is a multifluid version that can be used to model behavior of multiple ion species [Glocer et al., 2009]. It can also be run with Hall MHD equations, meaning that also the Hall term, resistive term and the electron pressure term can be included in the Ohm's law (Eq. 2.5). The ion population in BATS-R-US could also be described with an anisotropic pressure tensor instead of only Maxwellian populations [Tóth et al., 2012]. BATS-R-US has also been coupled to the local PIC simulation model iPIC3D [Markidis et al., 2010] and together they are called the MHD-EPIC (embedded particle-in-cell) [Daldorff et al., 2014, Tóth et al., 2016]. This coupling of MHD to local kinetic models allows to model only the region of most interest with kinetic scale physics, but it does not allow investigation how the kinetic physics couples to the overall simulation box.

3.2 Hybrid models

MHD is not sufficient if the aim is to model phenomena that have time and spatial scales comparable to ion scales: Time scales close to the ion gyroperiod ($2\pi/\Omega_{ci}$) and spatial scales close to the ion gyroradius or the ion inertial length. These scales can be reached using hybrid-kinetic models that treat ions and electrons separately; a kinetic model is used to describe ion motion whereas the electrons are treated as fluid. Hybrid-PIC models describes ions as particles whereas hybrid-Vlasov models treats ions as distribution functions.

3.2.1 Hybrid-PIC

As suggested by the name of the method, hybrid-PIC treats ions as particles and electrons usually as charge-neutralizing massless fluid. If the initial location and velocity of a particle is known, its motion can be determined using the Lorentz force (Eq. 2.6) and the fields with Maxwell's equations (Eq. 2.1-2.4) and Ohm's law (Eq. 2.5) with desired approximations. However, it is numerically not feasible to model all ions in a plasma. Therefore, the number of particles in simulations can be reduced by grouping many particles to larger elements, so called macroparticles, that preserve the ratio q_i/m_i of the original particles. In this way the motion under the Lorentz force is the same for the original particles and macroparticles.

The computational requirements of PIC simulations can be controlled with the number of macroparticles used in the simulations. The downside of PIC models is the statistical noise in the velocity distribution function that is caused

by the limited number of macroparticles per cell. This noise is also transferred to the physical quantities that are calculated from the velocity distributions, such as density, temperature, and bulk velocity. The amount of noise can be, however, controlled by increasing the number of particles launched in each cell. This also increases computational requirements. In order to make the global simulations more feasible, hybrid-PIC simulations also often apply a downscaled dipole strength [e.g. Omidi and Sibeck, 2007, Omidi et al., 2004] or, for example, use upscaled solar wind ion inertial lengths [Lin et al., 2014, Lu et al., 2015], so the length-scale of the simulation cannot be readily compared to the magnetosphere.

The history of the 1D hybrid-PIC simulations started already in the 70s [e.g. Chodura, 1975, Sgro and Nielson, 1976] and the 2D version followed shortly thereafter [e.g. Hewett, 1980]. Use of local hybrid-PIC simulations and also full-PIC simulations, which describe electrons also as particles, have increased rapidly and since the early times they have been widely used to study, for example, the ion foreshock, bow shock structures, magnetic reconnection, and low frequency waves in the magnetosheath [e.g. Ganse et al., 2012, Lapenta et al., 2017, Pritchett, 2003, Winske et al., 2003].

First semi-global Earth-like magnetospheric hybrid-PIC simulations with a downscaled dipole concentrated on the dayside magnetopause structure [Omidi et al., 1998, Swift, 1995] and soon after that the first global simulations including the magnetotail were reported [Omidi et al., 2001]. Recently global hybrid-PIC simulations have been used to study filamentary structures in the quasi-parallel magnetosheath [Omidi et al., 2014a] and hot flow anomalies [Omidi et al., 2014b, 2016], magnetopause reconnection and formation of flux transfer events (FTE) both in 2D [Sibeck and Omidi, 2012], and in 3D global simulations [Tan et al., 2011]. Magnetic reconnection has also been studied in the quasi-parallel magnetosheath using 2D simulations [Karimabadi et al., 2014], and in the Earth's magnetotail especially within multiple X-lines associated with forming flux ropes using a 3D global simulation [Lu et al., 2015].

3.2.2 Hybrid-Vlasov: Vlasiator

Instead of modeling ions as particles they can be described as six dimensional velocity distribution functions $f(\mathbf{r}, \mathbf{v}, t)$, having three dimensions in the real space ($\mathbf{r}$) and three in the velocity space ($\mathbf{v}$). This is known as the hybrid-Vlasov approach. Vlasiator is currently the only existing global hybrid-Vlasov simulation code but in local simulations this method has been applied before [e.g. Eliasson and Shukla, 2007, Valentini et al., 2007]. The hybrid-Vlasov method is computationally very heavy and requires a lot of memory. However, the advantage of the hybrid-Vlasov simulations is that they do not have the numerical noise that is present in PIC simulations.

The technical details of Vlasiator were first published by von Alfthan et al.

[2014]. As the development of the code is ongoing, some of the details described in von Alfthan et al. [2014] have been already changed and more changes will come in the future. Pfau-Kempf [2016] describes the technical details of the current status of the code. Below the main technical points of Vlasiator are shortly reviewed.

Ions in Vlasiator are described as velocity distribution function $f(\mathbf{r}, \mathbf{v}, t)$ whose development is calculated by solving the Vlasov equation given by Eq. 2.7. Acceleration in the Vlasov equation comes from the Lorentz force (Eq. 2.6), the magnetic field is calculated using Faraday's law (Eq. 2.3) and the electric field is obtained from Ohm's law (Eq. 2.5) that includes the Hall term but not the resistivity or electron pressure terms:

$$\mathbf{E} = -\mathbf{V} \times \mathbf{B} + \frac{\mathbf{J} \times \mathbf{B}}{ne}. \tag{3.5}$$

The total current density $\mathbf{J}$ is calculated using Ampère-Maxwell's law (2.4) by neglecting the displacement current: $\nabla \times \mathbf{B} = \mu_0 \mathbf{J}$. The number density n and ion current density $\mathbf{J}_i$ can be calculated as velocity moments of the distribution function.

The distributions are propagated using a less diffusive 5th order accurate semi-Lagrangian method [White and Adcroft, 2008, Zerroukat and Allen, 2012] that has replaced the finite volume method described by von Alfthan et al. [2014] [for more details see Pfau-Kempf, 2016]. The six dimensional phase space is divided into a 3D Cartesian real space mesh and each of the real space cells contains a 3D Cartesian velocity mesh. Currently the resolution of both the real space mesh and the velocity space mesh are uniform and kept constant during the simulation. The time step can vary and it is adapted according to the CFL condition.

Even though Vlasiator is inherently 3D, in global simulations the real space is for the time being set to be 2D in order for the runs to be computationally feasible. Another way to save computational resources and memory is to apply a sparse velocity grid. The distribution functions are usually very localized and in order to save resources, only the parts having content are saved and propagated. The velocity space is divided into blocks each of which contains $4 \times 4 \times 4$ cells. A block is defined to have content if any of its cells has content more than the threshold value specified by the user. In the papers of this thesis the threshold has been set to 10^{-15} m^{-6} s^{-3}. A block exists if it has content or if any of its neighbors in six dimensions (both in real and velocity space) have content. Either the whole block exists with all of its cells or it does not exist at all.

Initially the simulation domain includes a dipole field, and plasma density and velocity are constant throughout the whole simulation box. The solar wind flows into the simulation domain through the sunward boundary. At each of the boundary cells the velocity distribution function is Maxwellian. Solar wind

T, n, $\mathbf{v}$ and $\mathbf{B}$ are given as input parameters. To allow the plasma to flow out through the other three boundaries, a copy condition is applied. This condition allows copying of plasma parameters and the distribution function from a cell next to the boundary to the nearest ghost cell. Periodic boundary conditions are used in the direction out of the simulation plane. The inner boundary is at a user defined distance, usually $5\,R_E$, from the center of the Earth. The inner boundary condition is a perfectly conducting sphere.

When solar wind flows into the simulations domain the magnetosphere forms self-consistently. The equatorial plane simulation used in **Paper I** is considered to be initialized after the inflowing solar wind have crossed the entire simulation domain. The dayside of the polar plane simulations used in **Paper III** and **IV** is considered to be initialized when the inflowing solar wind magnetic field have passed the magnetosheath and reached the dayside magnetopause.

The magnetic field propagation method [Londrillo and Del Zanna, 2004] does not produce divergence if there is no divergence in the initial state and boundary conditions. Vlasiator does not have divergence removal so currently the user needs to make sure that the solar wind inflow conditions are divergence free.

The equatorial plane simulation used in **Paper I** has a 3D dipole field with a strength of the Earth dipole. In the polar plane runs used in **Papers III** and **IV** a 2D line dipole is applied instead, because the out-of-plane component of the field in the polar plane run provides a source of divergence. The line dipole is similar to the one described in Daldorff et al. [2014]:

$$\begin{aligned} B_x &= D\frac{2xz}{r^4} \\ B_z &= D\frac{z^2 - x^2}{r^4}. \end{aligned} \tag{3.6}$$

The strength of the line dipole D is chosen so that the stand off distance of the magnetopause corresponds to the stand-off distance of Earth's magnetopause. A mirror dipole is set on the other side of the sunward boundary to have only the solar wind magnetic field flowing in.

In order to run Vlasiator at large scale it has been parallelized at two levels. The first level is the Message-Passing-Interface (MPI) that is used to parallelize the three dimensional real space grid. The second level applies OpenMP (Open Multi Processing) by threading the computation on each MPI process.

Vlasiator results have shown that the code is able to model the solar wind-magnetosphere interaction and it can be used to study physics of the near-Earth space. It is able to reproduce the foreshock, its 30 s waves and the velocity distribution functions that correspond to spacecraft observations [Kempf et al., 2015, Palmroth et al., 2015]. **Paper I** demonstrates that the code produces magnetosheath waves and their distribution in the sheath corresponds to obser-

vations. In addition, **Paper III** shows that the reconnection rate at the dayside magnetopause correlates very well to the analytical model of 2D reconnection rate derived by Cassak and Shay [2007].

3.3 Comparison of modeling approaches

The global MHD models are not able to model the ion scale physics of plasma as the hybrid-kinetic models can. On the other hand their computational requirements are not as demanding. For example, GUMICS-4 is a serial code and a global-scale simulation of a space weather event can be run on a laptop computer. Parallelized global MHD models are advancing to the real time limit providing nowcasting of space weather.

Hybrid models run on multiple computational units but near-real time simulations can only be dreamed of. However, the hybrid approach is required to model the ion scale physics. The accuracy and the computational resources of hybrid models vary significantly depending on the set up of a simulation. Increasing resolution of the simulation domain requires more resources but improves the accuracy. In hybrid-PIC simulations the level of noise can be decreased and the accuracy of the ion velocity distribution functions can be increased by increasing the number of particles in the simulation. Similarly, the accuracy in Vlasiator simulations can be controlled by varying the resolution of the velocity space grid. The hybrid-PIC simulations can be computationally less demanding than Vlasiator. However, the velocity distribution functions in Vlasiator do not have numerical noise even when the resolution of the velocity space is decreased unlike in hybrid-PIC. Also, increasing the number of macroparticles in PIC simulations in order to make the velocity distribution functions smoother increases the computational requirements of the hybrid-PIC simulations. The large number of particles would make them almost as computationally demanding as the Vlasiator simulations.

Global MHD simulations are able to model the coupling between the magnetospheric MHD domain and the ionosphere, unlike 2D hybrid models. Another advantage of global MHD models is that they can be 3D whereas the hybrid-kinetic simulations in the scales corresponding to the Earth's magnetosphere are still only feasible in 2D. Global simulations in 2D might not reach steady state solution at all as the stand-off distance of bow shock and magnetopause keep changing [Winske et al., 2003]. Limitation to a 2D plane cloud also cause other effects that would not exist in 3D. Plasma can flow around the Earth only on the simulation plane causing pile-up at the nose of the magnetopause, making the magnetosheath thicker than in reality. The complete Dungey cycle cannot be simulated either because the field lines reconnected in the tail cannot convect back to the dayside in 2D polar plane simulations.

In summary, the different global modeling approaches have their respective advantages and disadvantages. MHD models are not able to simulate

features that are arise from ion kinetic physics, such as the foreshock. Therefore, foreshock-related studies need to be investigated using global models with kinetic physics. Nevertheless, a global MHD model can be the only feasible solution to carry out a 3D systematic study consisting of a set of simulations with different parameters. Therefore, all models should be regarded as complementary methods of simulating the near-Earth space plasma.

Chapter 4

Magnetosheath mirror mode waves

4.1 Magnetosheath structure

The magnetosheath is the region of shocked solar wind plasma between the bow shock and the magnetopause. The magnetosheath structure depends on θ_{Bn}, the angle between the bow shock normal and the IMF as can be seen in Figure 4.1. This figure shows the equatorial plane simulation with a 30° cone angle (angle between IMF and Sun-Earth line). In the quasi-parallel bow shock backstreaming particles cause the solar wind to become unstable to various wave instabilities [e.g. Hoppe et al., 1981, Russell et al., 1987a]. Due to the backstreaming particles and foreshock waves the quasi-parallel bow shock is perturbed and the downstream magnetosheath becomes turbulent. Waves that are observed in the quasi-parallel magnetosheath are usually broadband turbulent waves and they are thought to be at least partly generated by the ion foreshock waves [Engebretson et al., 1991, Engebretson et al., 1994, Krauss-Varban, 1994].

The quasi-perpendicular magnetosheath is more regularly structured (Fig. 4.1). At the crossing of the quasi-perpendicular bow shock, the plasma temperature becomes anisotropic; temperature perpendicular to the magnetic field increases. Temperature anisotropy forms as the plasma is compressed and heated adiabatically in the perpendicular direction [e.g. Koskinen, 2011]. Figure 4.2a shows temperature anisotropy $T_\perp/T_\parallel$ in the magnetosheath in the equatorial plane run from **Paper I**. The temperature anisotropy is largest right behind the quasi-perpendicular bow shock and close to the dayside magnetopause. The anisotropy decreases in the sheath as the distance to the bow shock increases. The increase in front of the magnetopause is due to plasma piling up and draping around the magnetopause. Similar behavior of the temperature anisotropy has been seen also in a statistical study of THEMIS spacecraft observations

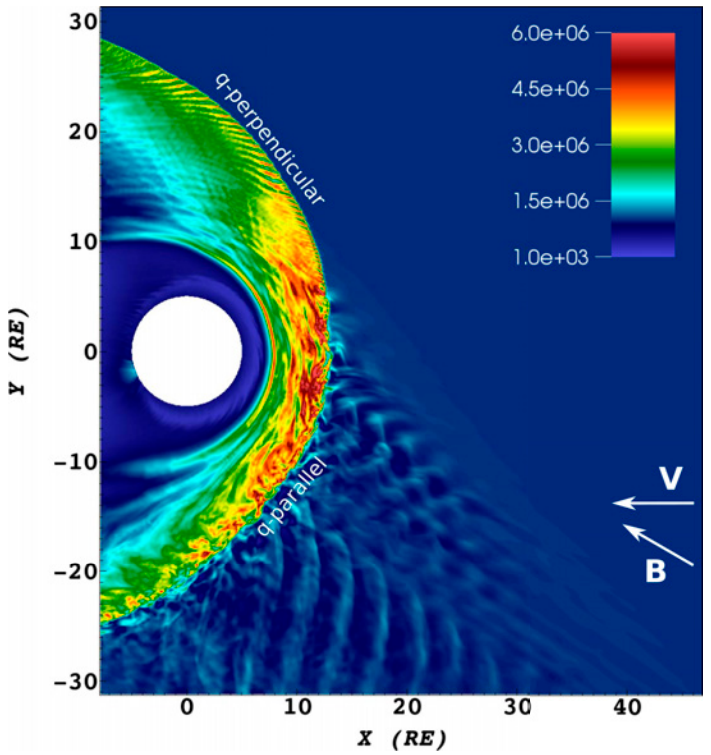

Figure 4.1: Vlasiator simulation in the equatorial plane showing the foreshock structure and magnetosheath asymmetry during IMF with 30° cone angle. Color coding shows the number density (m^{-3}).

[Dimmock et al., 2015].

A dawn-dusk asymmetry has been observed also in other plasma parameters besides the temperature anisotropy [e.g. Dimmock and Nykyri, 2013, Longmore et al., 2005, Němeček et al., 2002, Paularena et al., 2001, Walsh et al., 2012]. In a statistical study using THEMIS spacecraft observations Walsh et al. [2012] found that the density and temperature are higher on the dawn side whereas the magnetic field strength and the bulk velocity are higher on the dusk side. When the IMF is close to the Parker spiral, which is the most common IMF direction at 1 AU with $\sim 45°$ cone angle, the dusk side is quasi-perpendicular and the dawn is the quasi-parallel side. They demonstrated using BATS-R-US simulations that the observed dawn-dusk asymmetry is associated with the the commonly occurring Parker spiral IMF direction [Walsh et al., 2012].

4.2 Mirror mode waves

A temperature anisotropy, $T_\perp/T_\parallel > 1$, can make the plasma unstable to both mirror and ion cyclotron wave modes [e.g. Gary et al., 1976]. Therefore, the

quasi-perpendicular magnetosheath plasma is favorable for ultra low frequency (ULF) wave formation. In addition to these two modes, two other ULF wave modes can be observed in the magnetosheath: slow (/ion-acoustic/sound) mode waves and fast (/magnetosonic) mode waves [Denton, 2000]. The frequency of the ULF waves is smaller than the ion cyclotron frequency. Various methods, including transport ratios, wave polarization and phase difference between different parameters, have been used to distinguish different wave modes from each other (see e.g. review by Schwartz et al. [1996]).

The growth of proton mirror modes competes with the proton cyclotron waves in the plasma with $T_\perp/T_\parallel > 1$. The dominant wave mode is determined by the values of $\beta_\parallel = \frac{2\mu_0 n k_B T_\parallel}{B^2}$, the plasma β in the parallel direction, and $T_\perp/T_\parallel$. Mirror modes dominate for lower $T_\perp/T_\parallel$ and higher $\beta_\parallel$ whereas the ion cyclotron mode dominates with higher $T_\perp/T_\parallel$ and low $\beta_\parallel$ [e.g. Gary, 1992, Lacombe and Belmont, 1995].

Mirror mode waves are commonly observed in the Earth's magnetosheath but they have also been observed in other sheath regions in the solar system. For example, Pioneer 11 observed mirror mode type fluctuations at both Jupiter and Saturn [Tsurutani et al., 1982], they have been seen in the magnetosheath of Uranus by Voyager 2 [Russell et al., 1989], and even in the wake of comet Halley by Vega 1 [Russell et al., 1987b].

Many observational studies report dominance of mirror modes over ion cyclotron waves even though $\beta_\parallel$ suggests that ion cyclotron instability should dominate [e.g. Génot et al., 2009, Soucek et al., 2008]. Heavier ion species, such as helium ions, have been found to suppress the growth of the ion cyclotron instability leaving the growth rate of mirror mode waves mostly unaffected so that the mirror mode waves can dominate even when $\beta_\parallel \gtrsim 1$ [e.g. Gary et al., 1993, Price et al., 1986]. Nonzero electron temperature and electron temperature anisotropy ($T_{\perp,e}/T_{\parallel,e} \gtrsim 1.2$) is also shown to increase the growth rate of the proton mirror instability [Pokhotelov et al., 2000, Remya et al., 2013]. However, Ahmadi et al. [2016] showed using local PIC simulations that the electron whistler waves consume the free energy of the electrons so fast that the electron temperature anisotropy does not have time to influence the growth of the mirror mode waves. As the electron temperature anisotropy is not necessary for accurate modeling of the mirror mode growth, the hybrid-kinetic models are well suited for the task.

4.2.1 Properties

Mirror mode waves form in the region where plasma fulfills the mirror instability condition that for bi-Maxwellian plasma can be written in the form [Hasegawa, 1969]:

$$T_\perp/T_\parallel > 1 + \frac{1}{\beta_\perp}. \tag{4.1}$$

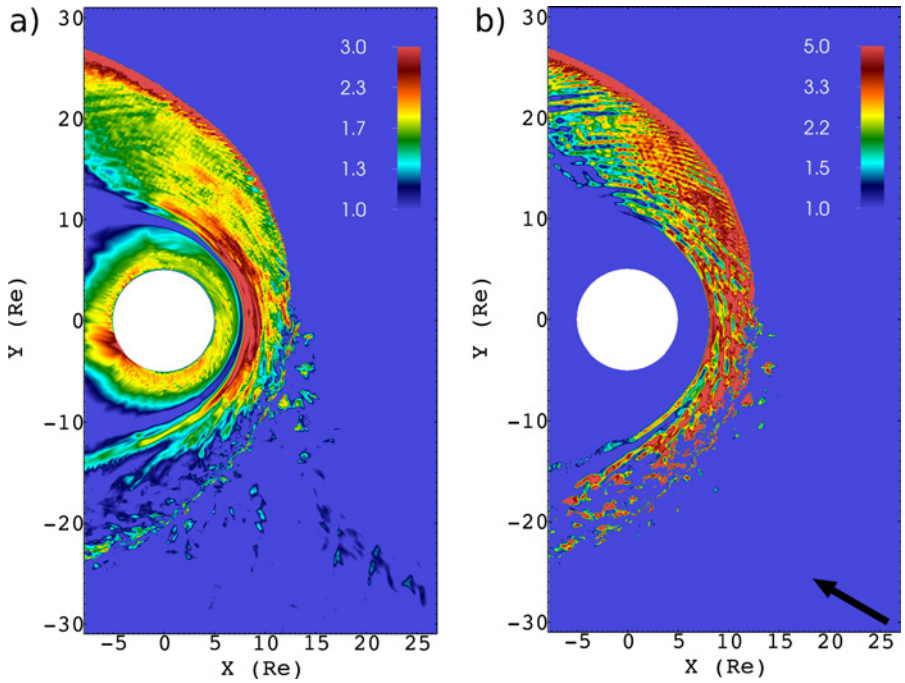

Figure 4.2: a) Temperature anisotropy $T_\perp/T_\parallel$. b) Mirror mode instability condition $R = \beta_\perp(T_\perp/T_\parallel - 1)$. Adapted from **Paper I**.

Color coding of Figure 4.1b shows the $R = \beta_\perp(T_\perp/T_\parallel - 1)$ in the simulation used in **Paper I**. In the regions where R is larger than 1, the mirror instability condition holds. In this simulation the instability condition is fulfilled almost in the entire quasi-perpendicular dayside magnetosheath. Even if the mirror instability condition is required for the mode to grow, they can propagate also to mirror stable plasma regions [Soucek et al., 2008].

Mirror mode waves are compressive fluctuations with anticorrelation between the magnetic field strength and density [e.g. Hasegawa, 1969, Tajiri, 1967]. This feature is formed as the plasma gets trapped inside the magnetic bottles that have been formed in the magnetic field fluctuations. An observer flying through the mirror mode waves observes anticorrelation in these two parameters as is demonstrated in Figure 4.3.

In homogeneous plasma mirror mode waves are linearly polarized and they do not propagate in the plasma frame i.e. their frequency in the plasma frame is $\omega \approx 0$. However, the magnetosheath plasma is not homogeneous because the plasma piles up in front of the magnetopause, creating gradients in the magnetic field strength and density. In the inhomogeneous plasma, due to the large gradients, mirror mode waves can start to drift with respect to the plasma frame [e.g. Johnson and Cheng, 1997, Omidi and Winske, 1995]. Drifting can also change the polarization of the waves. Génot et al. [2001] found that in

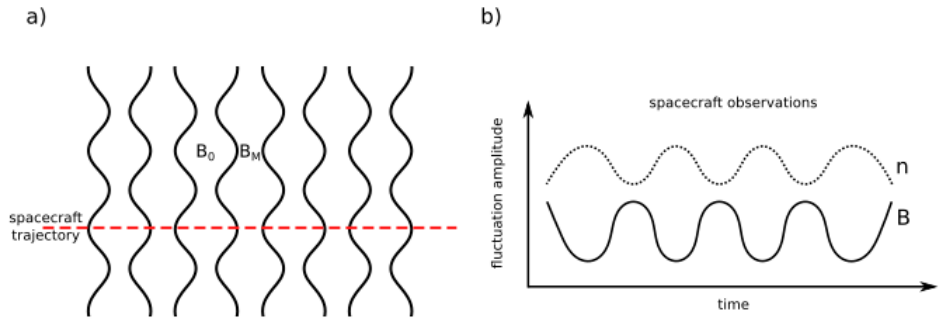

Figure 4.3: Illustration explaining the anticorrelation of magnetic field magnitude and plasma density in mirror mode observations. Figure after Koskinen [2011].

8 out of 13 events observed with the Active Magnetospheric Particle Tracer Explorers (AMPTE) mission the mirror mode waves were elliptically polarized.

The polarization of a wave can be studied using minimum variance analysis [e.g. Sonnerup and Scheible, 1998]. For linearly polarized waves the ratio of the minimum and intermediate eigenvalues of the variance matrix ($\lambda_{min}/\lambda_{int}$) should be close to 1, while the ratio of the maximum and intermediate eigenvalues should be much larger than one $\lambda_{max}/\lambda_{int} \gg 1$. Linear polarization of the mirror mode waves is aligned with the background magnetic field, therefore to support linear polarization the angle between the maximum variance direction and the background magnetic field, θ_{BM}, needs to be relatively small [e.g. Génot et al., 2009, Génot et al., 2011, Soucek et al., 2008].

In spacecraft observations mirror modes are often seen as quasi-periodic large amplitude structures. They can be observed as a train of either peaks or dips in the magnetic field strength rather than sinusoidal oscillations [Soucek et al., 2008]. In mirror unstable plasma mirror modes waves develop into peaks. As the mirror mode waves propagate to a mirror stable region the peaks develop into dips [e.g. Soucek et al., 2008].

4.2.2 Identification from the simulation

Mirror mode waves are identified from spacecraft observations and global simulations using criteria based on the wave properties described above. The first criterion in the mirror mode identification is the anticorrelation of density and magnetic field strength fluctuations. Other criteria applied in the identification vary in different studies.

One of the aims of **Paper I** was to compare how much identification of the mirror mode waves depends on the chosen criteria. Three different sets of criteria based on wave polarization were chosen. In addition to requiring the

correlation coefficient between density and magnetic field strength to be smaller than -0.5 and the amplitude of magnetic field fluctuations larger than 5% of the background magnetic field, we used three different sets of values to limit the results of the minimum variance analysis:

1. $\lambda_{max}/\lambda_{int} > 1.5$, $\lambda_{min}/\lambda_{int} > 0.3$, $\theta_{BM} < 30°$ [Soucek et al., 2008]
2. $\theta_{BM} < 20°$ [Génot et al., 2009, Génot et al., 2011]
3. $\lambda_{max}/\lambda_{int} > 5$, and $\theta_{BM} < 20°$ [Tátrallyay et al., 2010].

The whole dayside magnetosheath was tested against these criteria every 0.5 R_E excluding the points that the bow shock crosses as it expands during the simulation. Figure 4.4 shows that the extent of the observed mirror mode activity (black dots) depends highly on the criteria. Panel a) shows the mirror mode waves that were identified using the criterion 1 and panel b) shows the locations identified using criterion 2, which are significantly fewer than found using criterion 1. Criterion 3 did not yield any mirror mode activity.

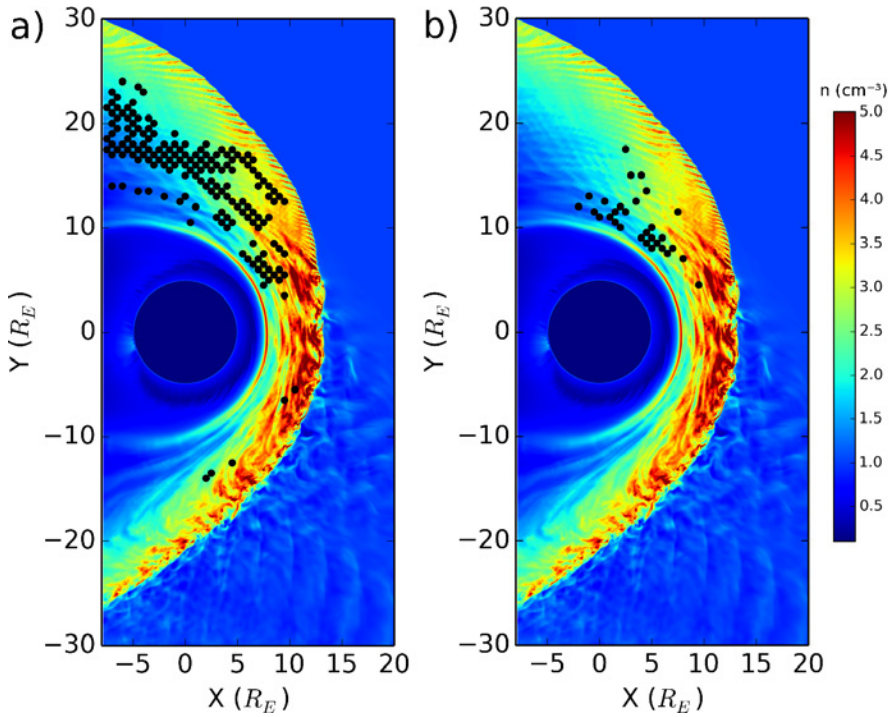

Figure 4.4: Extent of the located mirror modes a) using the criterion 1 and b) using criterion 2. Black dots show the points where the mirror mode conditions are fulfilled. The background is color coded with the number density. Figure from **Paper I**.

In global 3D hybrid-PIC simulations of the Hermean magnetosphere, Herčík et al. [2013] checked if the anticorrelated waves are mirror mode waves by testing that the plasma fulfills the mirror instability condition and β is favorable for

mirror mode growth. They used spatial Fourier transform to confirm that the angle between the background magnetic field and the wave vector is in the range that has been observed for mirror mode waves ($60° < \theta < 90°$ by Trávníček et al. [2007]).

4.2.3 Occurrence and dynamics

Mirror mode waves are commonly observed in the terrestrial magnetosheath. Tátrallyay and Erdős [2002] reported that mirror mode waves were observed in different regions of the magnetosheath in 20% of the first 30 orbits that the ISEE-1/2 spacecraft moved through the magnetosheath. Lucek et al. [1999] observed mirror mode waves in 30% of the studied magnetosheath passes of Equator-S spacecraft observations.

Mirror mode waves have often been found in the inner magnetosheath near the magnetopause [e.g. Hubert et al., 1998, Lucek et al., 1999, Tátrallyay and Erdős, 2005, Tsurutani et al., 1982]. In the Vlasiator simulation in **Paper I** the mirror mode activity is found mainly in the quasi-perpendicular magnetosheath as shown in Figure 4.4. This is consistent with statistical spacecraft studies [Soucek et al., 2008, 2015, Tátrallyay et al., 2008] and global hybrid-PIC simulations of the Hermean magnetosheath [Herčík et al., 2013]. However, the results show very little to no mirror mode activity in the quasi-parallel magnetosheath even though some observational studies have reported the mirror modes there [e.g. Dimmock et al., 2015, Tátrallyay and Erdős, 2005].

Most of the mirror mode activity in **Paper I** is located near or along the velocity streamlines that enter the magnetosheath close to the foreshock ULF wave boundary. Dawnward (towards negative y) from the ULF wave boundary the bow shock becomes more quasi-parallel and the magnetosheath is too turbulent for mirror mode waves to grow. The streamlines that enter the bow shock further in the quasi-perpendicular flank have higher velocities and smaller initial perturbations. This may explain why there is less mirror mode activity closer to the bow shock. It takes a while for the waves to grow enough to fulfill the mirror mode criteria. The plasma entering the magnetosheath near the ULF foreshock edge spends the longest time in the dayside magnetosheath and the initial perturbations are favorable for the mirror mode formation.

Figure 4.5 shows an example of two proton velocity distribution functions from the Vlasiator simulation from **Paper I**. The first one is taken near the mirror point, i.e., from the crest of the wave and the second is taken from the middle of the bottle, i.e., the trough of the wave (shown in Fig. 4.5c). At the crest of the wave most of the particles are close to 90° pitch angle. This is caused by conservation of the magnetic moment: as the particles come closer to the mirror point their parallel velocity decreases and perpendicular velocity increases. In the trough of the wave there are more particles at both perpendicular and intermediate pitch angles. These are the particles that are

trapped inside the magnetic bottles. The particles with larger parallel velocities that do not get trapped into the magnetic bottles are in the loss cone. The behavior of the simulated velocity distribution function is similar to those in the Cluster spacecraft observations by Soucek and Escoubet [2011].

Ion kinetic scale effects have been known to be important for the evolution of mirror instability since the early theoretical studies [e.g. Tajiri, 1967]. Ions at small parallel velocities that get trapped in the mirror mode waves have been shown to be important for the evolution of the instability [e.g. Hellinger et al., 2009, Pokhotelov et al., 2008, Southwood and Kivelson, 1993]. They have been found, for example, to lead to saturation of the non-linear growth of the large amplitude mirror mode waves [e.g. Califano et al., 2008, Kivelson and Southwood, 1996].

In **Paper I** the growth rate of the mirror mode waves estimated by comparing amplitudes and propagation times of a wave at different locations along a velocity stream line ($\gamma_m \approx \ln(\delta B_2/\delta B_1)/(t_2 - t_1)$ by Tátrallyay et al. [2010]) is found to be one to two orders of magnitude smaller than that given by the theoretical growth rate derived by Liu et al. [2006]. Similarly, Tátrallyay et al. [2008] reported that the estimated growth rate using an event observed by Cluster is an order of magnitude smaller than the theoretical growth rate. They discuss the possibility that the waves become saturated as they respond to local changes in the plasma parameters. The ion temperature anisotropy decreases as the waves interact with the ions, which reduces the local growth rate. This mechanism could also take place in Vlasiator simulations. In simulations the growth rate is also affected by the resolution of both real and velocity space. The dynamics of particles at small parallel velocities that have been shown to affect the growth rates cannot be resolved with high accuracy. Nevertheless, in a study of mirror mode waves in the magnetosphere of Venus, Volwerk et al. [2016] showed that their estimated range of growth rate is similar to ones reported in **Paper I** and by Tátrallyay et al. [2008].

Summary

In the Vlasiator simulation in **Paper I** the mirror modes are mainly observed in the quasi-perpendicular magnetosheath, which is consistent with previous statistical spacecraft studies and simulations [e.g. Herčík et al., 2013, Soucek et al., 2015]. In the simulation the most ideal region for the mirror mode growth seems to be along the velocity streamlines that enter the magnetosheath at the vicinity of the foreshock ULF wave boundary. It is also shown that the extent of the detected mirror mode activity is highly dependent on the criteria that is used to identify the waves. In the simulation the mirror mode structures do not evolve to form large peaks or dips as has been often observed by spacecraft [e.g. Soucek et al., 2008]. In addition, the amplitudes of the magnetic fluctuations remain relatively small ($\sim 5\%$) compared to what is usually observed. This may

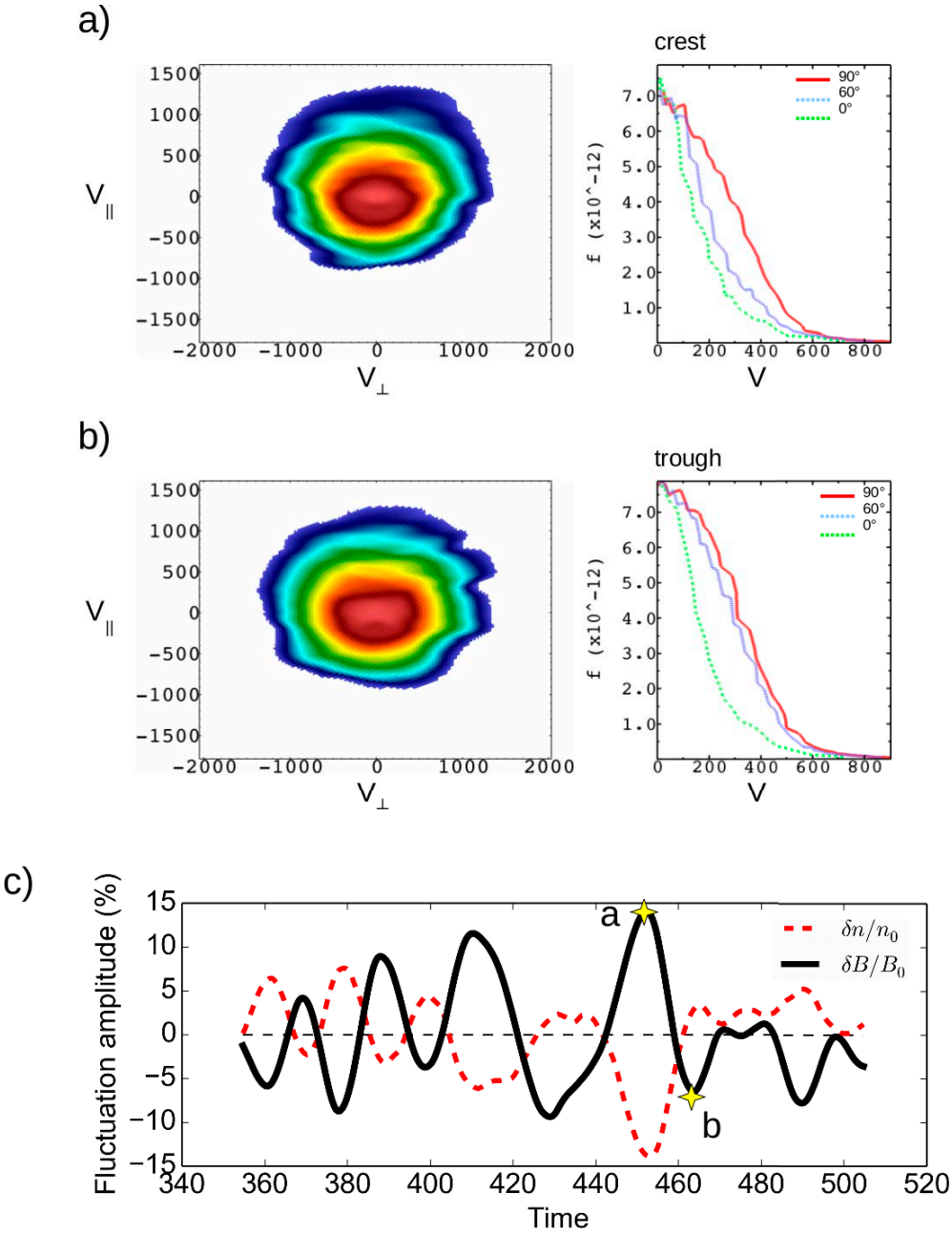

Figure 4.5: Proton velocity distribution functions measured from different phases of the mirror mode wave. Figure adapted from **Paper I**.

be caused by the limitation to a 2D spatial plane or by resolution of either the spatial or velocity grid. Nevertheless, the behavior of the velocity distribution functions in mirror structures is similar to that observed by Cluster spacecraft [Soucek and Escoubet, 2011].

Chapter 5

Dayside magnetopause reconnection

Magnetic reconnection at the dayside magnetopause during southward IMF conditions is one of the main drivers of the severe space weather phenomena. Reconnection accelerates charged particles to high energies and allows plasma to flow into the magnetosphere. The investigation of the dayside reconnection is currently of great interest in the space science community as the recently launched MMS spacecraft have been measuring the electron scale details of the reconnection diffusion region [e.g. Burch and Phan, 2016, Burch et al., 2016].

This Chapter summarizes the results obtained with both GUMICS-4 and Vlasiator simulations about the dayside magnetopause reconnection during southward IMF and the relevant background of the current knowledge. In order to investigate how the the magnetosheath interacts with the magnetosphere and, for example, how efficient magnetic reconnection is between the terrestrial and magnetosheath field lines, the magnetopause and the region where the reconnection occurs need to be located.

5.1 Magnetopause location

In spacecraft studies magnetopause can be located from measured parameters as the spacecraft crosses the magnetopause from the magnetosheath to the magnetosphere or vice versa. Observed crossings can be used to create empirical models to obtain approximated location for the whole magnetopause. Most of the empirical models predict the location of the magnetopause based on the solar wind dynamic pressure, $p_{d,sw} = \rho_{sw} v_{sw}^2$, and the IMF B_z component [e.g. Chao et al., 2002, Petrinec and Russell, 1996, Shue et al., 1997, 1998]. The most used model is the Shue et al. [1998] model. Boardsen et al. [2000] presented an empirical model that included also the effect of the dipole tilt, because they found that at the high latitudes the magnetopause location is as

dependent on the dipole tilt angle as it is on the solar wind pressure. Lin et al. [2010] expanded the model by Shue et al. [1997] by including the effect of the dipole tilt. Case and Wild [2013] compared the location of the magnetopause in Cluster observations to different empirical magnetopause models. They showed, for instance, that on average Shue et al. [1998] model overestimated the radial distance to the magnetopause by 1 R_E and the model by Lin et al. [2010] underestimated the distance by 0.25 R_E.

In a global 2D simulation with southward IMF the location of the dayside magnetopause can be found as a reversal of the B_z from magnetospheric northward component to the southward component in the magnetosheath. This method was applied in **Paper III** but it is not applicable for locating the magnetopause in the magnetotail or during other IMF orientations.

A more general method was applied for the 3D MHD simulations in **Paper II**, where the magnetopause was located by using a method developed by Palmroth et al. [2003]. It is based on tracing velocity streamlines from upstream ($X_{GSE} = +15R_E$) to the tail. The streamlines flow around the magnetosphere forming a cavity and the boundary of this cavity is considered the magnetopause. This method for GUMICS-4 simulations yields a magnetopause that has been found to correspond to the Shue et al. [1998] model [Palmroth et al., 2003]. Another possible method for locating the magnetopause from a global 3D simulation is to use the location of the local maximum of the current density and local maxima of the density and velocity gradients [Komar et al., 2015, Němeček et al., 2011].

5.2 Reconnection location

There are multiple theories for predicting the location of dayside magnetopause reconnection. One of the oldest debates in this field has been between the antiparallel [Crooker, 1979] and component [Gonzalez and Mozer, 1974, Sonnerup, 1970] reconnection hypotheses. The antiparallel hypothesis states that reconnection occurs at the location where the magnetic field lines on both sides of the magnetopause are almost antiparallel. During purely southward IMF this occurs along a continuous line at the subsolar point but non-zero B_y makes the X-line to split into two parts at the northern and southern hemispheres [Crooker, 1979, Luhmann et al., 1984]. According to the component hypothesis the most optimal place for reconnection is the subsolar region where the solar wind flow first makes contact with the magnetopause. From this point the X-line extends as a continuous line across the dayside magnetopause. The ratio between the IMF B_z and B_y defines how much the X-line is tilted compared to the equatorial plane.

GUMICS simulations support the component hypothesis as the X-line remains continuous even in simulations with northward IMF [Laitinen et al., 2007]. The spacecraft observations have been found to support both the an-

tiparallel and the component hypothesis depending on the IMF conditions [e.g. Fuselier et al., 2011, Paschmann, 2008, Trattner et al., 2007, 2012]. Trattner et al. [2007, 2012] showed that when the IMF was B_y dominated the X-line was found to be continuous along the dayside magnetopause supporting the component hypothesis but during IMF with strong B_x component the X-line was split into two lines on the two hemispheres. Connor et al. [2015] also showed that in global MHD simulations both component and antiparallel reconnection can occur depending on the IMF clock angle.

Because neither antiparallel nor component hypothesis were able to explain the behavior of the X-line in all IMF cases, other models have been developed to predict the X-line location. Many of them are based on maximization of some reconnection related parameter. Trattner et al. [2007] continued the idea of the antiparallel hypothesis and proposed that the reconnection location is defined by the location of the maximum magnetic shear between the reconnecting field lines. This model has been found to correspond to spacecraft observations [Dunlop et al., 2011, Trattner et al., 2007, 2012]. Other models suggest, for example, maximization of the reconnection outflow velocity [Swisdak and Drake, 2007] or the reconnection rate [Borovsky, 2013].

Komar et al. [2015] used BATS-R-US simulations to test the X-line models mentioned above.. They found that when the IMF had a southward component most of the models predicted the location of the X-line well but the models based on maximization of the outflow speed or reconnection rate worked the best. In simulations with northward IMF none of the models were able to predict the location of the whole X-line but in the cusp regions the maximum magnetic shear model gave the best result.

5.2.1 Methods for locating the X-line in simulations

In 2D simulations, where the derivative in the out-of-plane direction is zero, the X-lines can be located using the magnetic flux function Ψ that is defined as $\mathbf{B} = \hat{\mathbf{y}} \times \nabla\Psi$ [e.g. Yeates and Hornig, 2011]. The X-lines are the local saddle points of Ψ, whereas the local maxima of Ψ yield the location of the magnetic O-type neutral points. This method is applicable to both local and global 2D simulations and it was applied in **Paper III**.

In 3D the X-line can extend along the whole dayside magnetopause and is more complicated to locate. The X-line, which in 3D is usually called the separator, is located at the intersect of four topologically distinct domains. Many methods for finding the approximate location of the X-line are based on tracing field lines and finding a region where all four topologies are close to each other. In **Paper II** a four-field junction method introduced by Laitinen et al. [2006] was used to find the X-line. This method traces the field lines starting from grid cells that are placed in the expected location of the separator. Field lines are labeled as free (not connected to Earth at all), closed (both ends of the

field lines connected to Earth), away (connected to the southern hemisphere, other end in solar wind) or toward (connected to the northern hemisphere, other end in solar wind). The grid is then checked again and if there are all four of the field line types within a distance of three cells from each other, the point is regarded as a separator point.

The separator line often connects two magnetic null points and they can be used to find the separator. First the null points are located and then, starting from one null the separator points can be located by either tracing along the magnetic field line [Haynes and Parnell, 2010] or by tracing the points that separate the four topologies [Komar et al., 2013] until the other null is reached. The separator in 3D simulations can also be found by slicing the simulation in 2D slices and locating the separator point independently on each slice [Glocer et al., 2016]. Another method is to first locate the open-closed field line boundary and then the solar wind-open field line boundary. The separator is the line where these two boundaries intersect. Glocer et al. [2016] found that this method, the null method and the 2D slicing method give the same result for the separator. Ouellette et al. [2010] used a method that was based on first locating the boundary between the solar wind and open field lines. Then the separator line was defined to be the line along this boundary separating the open field lines that are connected to different hemispheres.

5.2.2 Effect of the IMF B_x and dipole tilt angle

Previous studies have shown that the IMF B_x component can have an impact on the location of the X-line on the dayside magnetopause as well as on the reconnection rate [e.g. Peng et al., 2010, Trattner et al., 2007]. Using Polar spacecraft observations Trattner et al. [2007] noted that when the IMF had a large B_x component ($B_x/B > 0.7$), reconnection did not occur as a continuous line along the dayside magnetopause but along two lines at high latitudes, consistent with the antiparallel reconnection hypothesis. Peng et al. [2010] reported that when B_x is positive the magnetopause expands southward and the X-line moves northward in a global MHD simulation during low Alfvén Mach number ($M_A < 3$) solar wind. With negative B_x, the shifts were in the opposite direction. The amount of the shift of the X-line was found to be dependent on the magnitude of the B_x component. However, during higher Alfvén Mach number, the magnetopause shape was not affected by the changes in B_x. The results of **Paper II** were in line with Peng et al. [2010]: positive (negative) B_x shifts the X-line northward (southward).

MHD simulations by Park et al. [2006] suggested that during the northern summer, when the dipole tilt is positive, the X-line shifts southward and similarly, it shifts northward during northern winter. Polar observations by Trattner et al. [2007] show similar behavior of the location of the maximum magnetic shear as well as the observed reconnection location during large dipole tilt an-

gle. GUMICS simulations in **Paper II** are also consistent with the direction of the X-line shift during large positive and negative dipole tilt angle. Recent observations have shown that the dipole tilt angle does have a significant effect on the X-line location [Zhu et al., 2015]. MMS and Geotail spacecraft observations by Kitamura et al. [2016] endorse the earlier finding of the shift of the X-line towards the winter hemisphere.

Previously, the effect of the IMF B_x and dipole tilt angle on the X-line location have been investigated in separate studies. Both B_x and dipole tilt have been found to affect the location of the X-line on the dayside magnetopause, therefore, in **Paper II** the effect on the X-line of the combination of these two parameters is tested. **Paper II** presents results of simulations with 0° and ±20° dipole tilt angle with a purely southward IMF component as well as with different combinations of $B_x = \pm 5$ nT or 0 nT and $B_y = \pm 5$ nT or 0 nT. A selection of these simulation results is presented in Figure 5.1. If a positive tilt angle, which is able to shift the X-line southward, is added to the simulation with positive B_x they produce counteracting effects on the X-line shift (compare panels b and d in Fig. 5.1). This makes the shift less significant than it would be without the tilt angle. When the tilt angle is negative, which also shifts X-line northward, the combined effect is not as noticeable. The behavior is similar but opposite for opposite signs of B_x and the dipole tilt angle.

5.2.3 X-line motion

Cowley and Owen [1989] and Gosling et al. [1991] studied the X-line motion caused by the velocity flow shear between the magnetosphere and the magnetosheath tailward of the cusps during northward IMF. They concluded that the X-lines start drifting when the magnetosheath flow becomes super-Alfvénic but remain steady with sub-Alfvénic velocity. They found that magnetosheath speed that is more than twice the magnetosheath Alfvén speed suppresses reconnection. An analytical result of the X-line drift motion due to the shear flow in asymmetric reconnection was presented by Doss et al. [2015]. Contrary to the result of Cowley and Owen [1989], Doss et al. [2015] found that the X-lines may drift also during sub-Alfvénic flow shears.

X-lines have been found to move along the dayside magnetopause also during steady solar wind conditions. Swisdak et al. [2003] suggested that the diamagnetic drift driven by a large guide field causes the X-lines to move along the dayside magnetopause in the direction of electron drift. The northward or southward direction of the X-line motion in Double Star TC-1 observations by Trenchi et al. [2015] was consistent with the diamagnetic drift direction.

Paper III shows that the X-lines are able to move over significant distances along the dayside magnetopause with steady southward IMF. Figure 5.2 plots the motion of the X-lines (color coded points) and the O-points (black points), which represent the centers of the magnetic islands, along the magnetopause

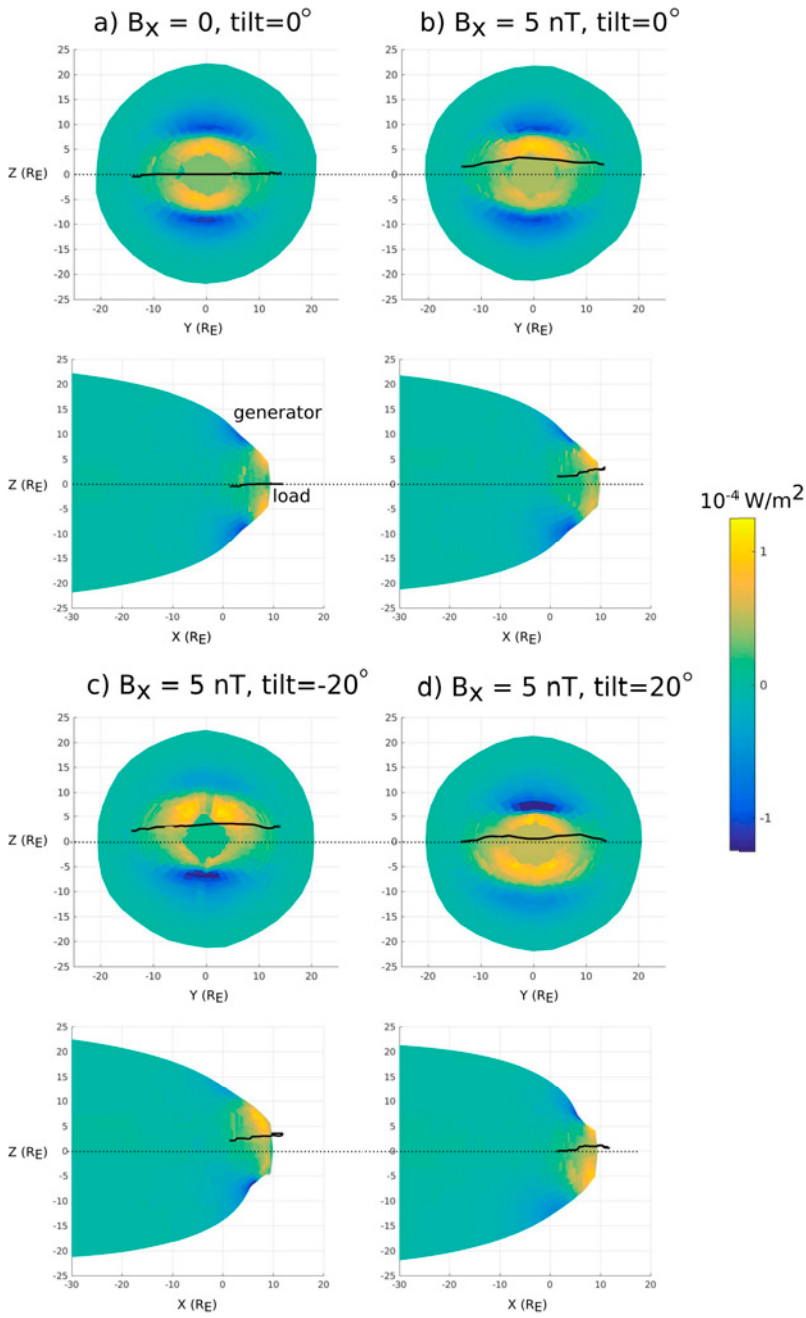

Figure 5.1: X-line location (black lines) on the magnetopause and energy conversion, discussed in Section 5.4, through the magnetopause during $B_x = 0$ and $B_x = 5$ nT and different tilt angle.

as a function of Z_{GSE}. **Paper III** shows that at the dayside magnetopause in the Vlasiator simulation close to the subsolar region, the shear has little to no impact on the X-line motion. Sometimes X-lines even move to the opposite direction than they should based on the direction of the shear flow. A similar conclusion was reached by Trenchi et al. [2015] who tested the X-line motion measured by Double Star TC-1 against the ambient magnetosheath velocity and found that in five out of ten events the X-line was moving in the opposite direction at the dayside magnetopause. In the simulation of **Paper III** the guide field is also negligible; the IMF $B_y = 0$ and the magnetosheath causes only small fluctuations in B_y. Therefore the diamagnetic drift proposed by Swisdak et al. [2003] cannot cause the motion of the X-lines.

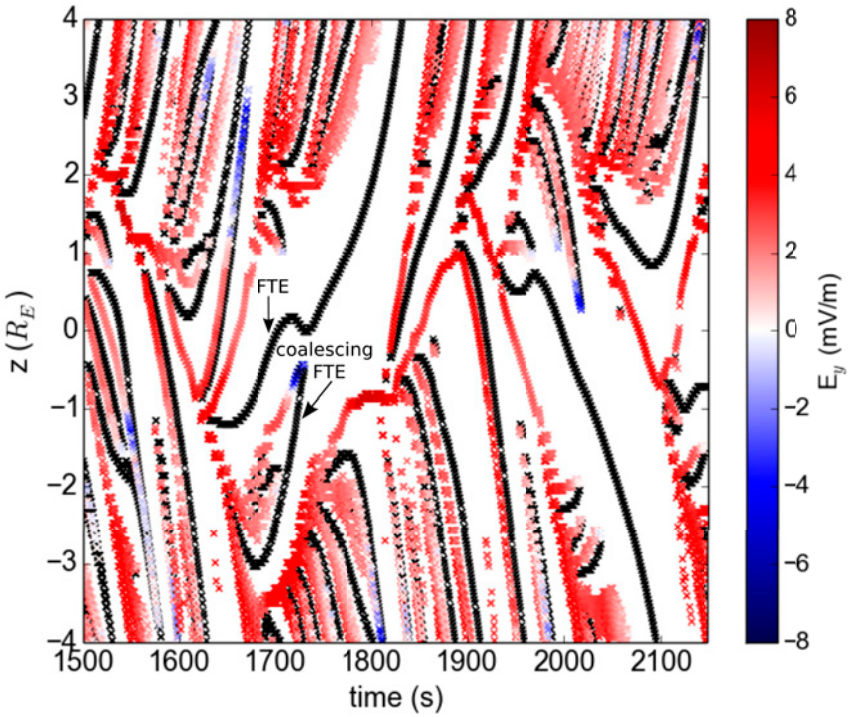

Figure 5.2: Motion of X-lines (color coded points) and O-points (black points) on the dayside magnetopause. Color coding shows the reconnection rate measured as E_y at the X-line locations. Figure adapted from **Paper III**.

Oka et al. [2008] using a local 2D PIC simulation demonstrated that the X-line starts to move if there is a rigid wall on one reconnection outflow side but the other outflow can flow more freely. The X-line starts to move towards the unblocked outflow region after the piled-up magnetic field in the blocked side reaches the diffusion region. A magnetic island can work as such wall next to an X-line [Nakamura et al., 2010]. This is the most probable cause of the

X-line motion at the dayside magnetopause in Vlasiator simulation in **Paper III**. Figure 5.2 shows that there are multiple X-lines concurrently and O-points i.e. magnetic islands grow in between the X-lines. The outflow velocities measured in the two outflow regions at the Vlasiator magnetopause are commonly asymmetric in agreement with the X-line next to an obstacle reported by Oka et al. [2008]. The reconnection rate, though, remained unaffected by this X-line motion caused by the blocked outflow [Oka et al., 2008]. The reconnection rate seems to be unaffected by the motion of X-lines also in Vlasiator simulations as long as reconnection is not suppressed by two magnetic islands blocking both of the outflow regions.

5.3 Local reconnection rate

The dayside reconnection rate has been found to be affected not only by variations in the solar wind and in magnetosheath but also by mass loading from the magnetosphere. The mass loading from the magnetosphere can be caused by so called plasmaspheric plumes [e.g. Borovsky, 2013, Ouellette et al., 2016, Walsh et al., 2013, Walsh et al., 2014]. Spacecraft observations have indicated that the mass loading from the plasmaspheric plumes slows down the local reconnection rate [Walsh et al., 2013]. Global MHD simulations imply that the plumes have an impact on both local and total reconnection rates [Borovsky, 2013, Ouellette et al., 2016].

There are two different theories for the control of the integrated reconnection rate i.e., the reconnection potential, at the dayside magnetopause: a local control theory and a global control theory [Zhang et al., 2016]. The local theory by Borovsky et al. [2008] and Borovsky et al. [2013] states that reconnection is a local process and that local variations in the plasma parameters in the magnetosheath and in the magnetosphere control the reconnection rate. Local changes to the reconnection rate at some point along the X-line contribute to changes in the total reconnection rate. According to the global theory by Lopez et al. [2010], the integrated reconnection rate is controlled by the solar wind electric field and forces that act on the magnetosheath flow and the ionospheric conductivity. The global theory also states that if the reconnection rate at some point of the X-line is increased due to local changes, e.g. mass loading, it must decrease at other points along the X-line because the total integrated rate should remain constant. Comparison of these two models cannot be done using spacecraft observations because they provide only local measurements. A recent study by Zhang et al. [2016] compared these two theories in global MHD simulations and suggested a mixed control theory. They pointed out that a small amount of mass loading only changed the local reconnection rate but did not affect the global rates whereas a large amount of mass loading affected both local and global rates.

The local reconnection rate at the dayside magnetopause is often tested

against the analytical rate for 2D asymmetric reconnection [Cassak and Shay, 2007] given by Eq. 2.11, henceforth referred to as E_{pred}. Using BATS-R-US MHD simulations Komar and Cassak [2016] found a good agreement between the reconnection rate in simulation and E_{pred} with due southward IMF. They also found that as the clock angle turns northward, the scaling holds between the measurement and prediction, but the scaling factor increases. Borovsky et al. [2008] also found a good correlation between the measured and predicted reconnection rate in a global simulation with southward IMF. Ouellette et al. [2014] found that the reconnection rate at the subsolar point in MHD simulation correlates with E_{pred}, but noted that the Cassak and Shay [2007] model overestimates the outflowing mass and energy flux. Wang et al. [2015] tested E_{pred} using Cluster observations and found a correlation between the E_{pred} and measured rate, which was calculated as the product of the magnetospheric inflow velocities and magnetic field. They noted that the reconnection rate was influenced mostly by magnetosheath fluctuations.

In **Paper III** the local reconnection rate was measured as the out-of-plane electric field E_y at the location of the X-lines. Variations in the reconnection rate are shown in Figure 5.2, where the color coding shows the local reconnection rate. Sometimes the measured reconnection rate changes sign to negative; This corresponds to times when the reconnection between the magnetosheath and magnetospheric field lines ceases and the magnetic islands next to an X-line start to coalesce.

In **Paper III** the measured reconnection rate E_y is compared against the Cassak and Shay [2007] formula E_{pred} (Eq. 2.11). Figure 5.3 shows the scatter plot of a comparison. The correlation coefficient between E_y and E_{pred} is 0.82 and the orthogonal least squares fit is $E_y = E_{pred} - 0.2$ mV. The correlation is very good, especially keeping in mind that the Cassak and Shay [2007] formula is derived for a singe isolated X-line. In Vlasiator, there are multiple X-lines that move along the magnetopause and affect the other X-lines nearby. Nevertheless, there are some scattering in the data, which could be partly caused by the inaccuracy of locating the X-lines and measuring the local reconnection rate E_y. Due to the motion of the X-lines, inaccuracy of measuring the inflow parameters can also affect the result.

Large temporal and spatial variations in the reconnection rate are also detected in the Vlasiator simulation (Fig. 5.2). Therefore the effect of local magnetosheath fluctuations to the reconnection rate was investigated. **Paper III** shows that the fluctuations in the magnetosheath during the studied time period are the dominant cause for the variations in the local reconnection rate, which is consistent with results by Wang et al. [2015]. Especially fluctuations in the inflow velocity and in the inflow magnetic field correlate well with the measured reconnection rate. The magnetic field fluctuations, as well as the density fluctuations, are caused by the mirror mode waves that have been formed in the magnetosheath. The results therefore suggest that the local reconnection

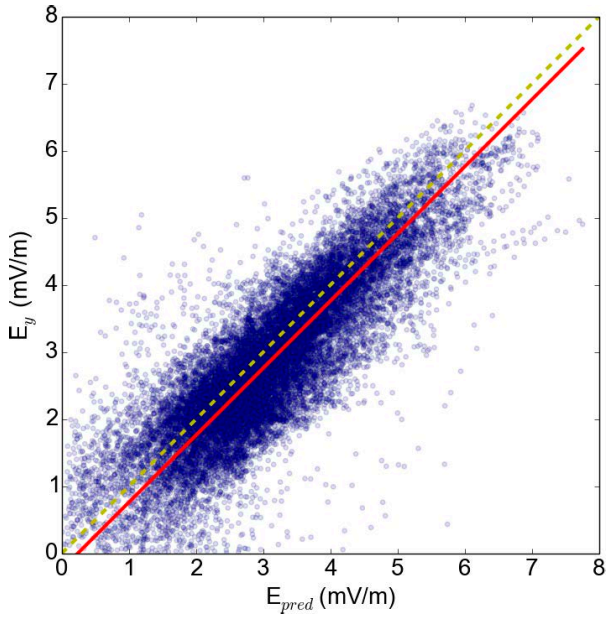

Figure 5.3: Correlation between the measured E_y and predicted reconnection rate E_{pred}. The red line is the orthogonal least squares fit and the yellow line shows where the two parameters would be equal. Figure from **Paper III**.

rate at the dayside magnetopause can be affected by mirror mode waves as has been suggested earlier by Laitinen et al. [2010].

5.4 Energy conversion through the magnetopause

Near the subsolar region, where reconnection takes place, magnetic energy is converted to kinetic energy as the particles are accelerated by reconnection. From the dayside, the field lines convect tailward along the magnetopause and the field lines start to pile up in the lobes. At the magnetopause in the tail lobe the energy is converted from the kinetic back to magnetic energy. This process is also know as the load-generator process [Siscoe and Cummings, 1969]. The dayside subsolar region, where energy is converted from magnetic to kinetic, is the load and the regions tailward of the cusps at the tail lobe magnetopause are generators as shown in Figure 5.1a.

In this thesis the conversion between magnetic and kinetic energies is referred to as energy conversion. In **Paper II** the surface density of energy conversion was calculated as an integral of the divergence of the Poynting vector, $\mathbf{S} = \mathbf{E} \times \mathbf{B}/\mu_0$, through the magnetopause along the local magnetopause normal: $\sigma = -\int \nabla \cdot \mathbf{S} \mathrm{d}l$ [Laitinen et al., 2006]. In a time-independent case the divergence of the Poynting vector is $-\nabla \cdot \mathbf{S} = \mathbf{E} \cdot \mathbf{J}$. In the load region $\mathbf{E} \cdot \mathbf{J} > 0$

and in the generators on the nightside magnetopause $\mathbf{E} \cdot \mathbf{J} < 0$.

In **Paper II** the dependence of energy conversion on the the tilt angle and IMF B_x was studied. The largest amount of energy conversion from kinetic to magnetic energy in the generator region occurs in the summer hemisphere. This is consistent with results by Palmroth et al. [2012] who studied the total energy transfer instead of conversion between kinetic and magnetic energy. The color coding in Figure 5.1 shows energy conversion through the magnetopause. The magnetopause surface is bulged tailward from the cusp of the summer hemisphere and the energy conversion is more intense than in the winter hemisphere. This suggests that there are more magnetic field lines piling up in the tail lobe of the summer hemisphere than in the winter hemisphere. The dipole tilt angle has a larger impact on the energy conversion in the generators whereas the IMF B_x affects more the intensity and distribution of the energy conversion in the load regions.

5.5 Flux transfer events

Reconnection at the dayside magnetopause can lead to formation of magnetic flux ropes known as flux transfer events (FTE). In spacecraft observations, FTEs were first observed Russell and Elphic [1978, 1979] and independently by Haerendel et al. [1978], who named them flux erosion events. FTEs move along the magnetopause away from the subsolar region due to the $\mathbf{J} \times \mathbf{B}$ force and the magnetosheath flow. FTEs are observed as bipolar signatures in the magnetic field component normal to the magnetopause (B_N) as demonstrated in Figure 5.4 that shows a cut through an FTE at the nose of the magnetopause. Even though FTEs are three dimensional structures in nature, formation of the FTEs can also be modeled in 2D simulations. Magnetic islands that have formed between X-lines can be thought of as 2D representations of FTEs (Fig. 5.4).

Statistical studies of the FTEs have shown that they are mostly observed during southward IMF conditions [e.g. Berchem and Russell, 1984, Eastwood et al., 2012, Fear et al., 2009, Rijnbeek et al., 1984, Southwood et al., 1986]. The observed polarity in B_N indicates the direction of the propagation of FTEs. The standard polarity FTEs, for which the magnetic field B_N increases first in the positive direction, propagate northward and they are most often observed in the northern hemisphere. The reverse polarity FTEs with opposite signature in B_N propagate southward [Rijnbeek et al., 1984]. FTEs have been observed to occur quasi-periodically with an average time of 8 min between events [Rijnbeek et al., 1984].

FTEs are formed by spatially and temporally limited (patchy or/and intermittent) reconnection at the magnetopause. The formation was explained by a single X-line model by Southwood et al. [1988] and Scholer [1988]. They suggested that variations in the reconnection rate at a single X-line causes the

magnetopause surface as well as the magnetic field lines to bulge. This bulge then propagates along the magnetopause creating the observed signatures. This single X-line model does not produce a tube of reconnected magnetic flux. Lee and Fu [1985] suggested that simultaneous reconnection at multiple X-lines form the FTEs as helical flux ropes. Spacecraft observations have shown evidence of both types of FTEs. Trenchi et al. [2016] present Cluster observations of multiple consecutive FTEs and reconnection jets that were often observed in the trailing edge of some of the FTEs. They discuss that it is possible that both multiple and single X-line models can produce FTEs at the same time. The largest observed FTE without trailing edge reconnection jet indicated multiple X-line reconnection but the FTEs with the trailing reconnection jets could be produced by singe X-line reconnection.

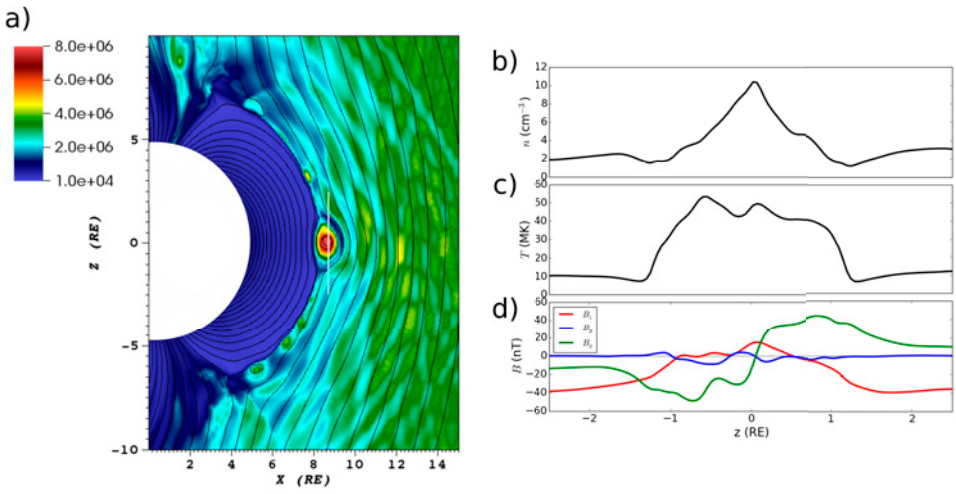

Figure 5.4: a) Global view of an FTE on the subsolar point of the magnetopause. Color shows the number density (unit m^{-3}) and the white line shows the location where the data are taken for panels b)–d) showing the b) number density, c) temperature, d) magnetic field components.

In 2D hybrid-PIC simulations by Omidi and Sibeck [2007] and Sibeck and Omidi [2012] the FTEs formed between multiple X-lines with constant southward IMF. Most of the FTEs propagated tailward but some were also observed to propagate sunward and finally coalesce with other FTEs. This is very similar to Vlasiator results shown in **Paper III**. The FTEs i.e. magnetic islands that form away from the equator and traverse the subsolar region to the opposite hemisphere, spend the longest time near the subsolar region. There they coalesce with multiple smaller magnetic islands growing larger than other FTEs. The FTEs have relatively low velocities in the subsolar region, but they accelerate towards the cusps. The FTEs in the simulation presented in **Paper III**

can accelerate to velocities exceeding 800 km/s.

Reconnection in the GUMICS-4 simulations in **Paper II** occurs along a single steady X-line and therefore there is no formation of FTEs. The lack of FTE production is mainly caused by the too coarse resolution that increases the numerical diffusion [Raeder, 2006]. However, the formation of FTEs has been reported in global MHD simulations that use higher resolution. Raeder [2006] studied FTEs during strong southward IMF using the OpenGGCM model. They found that FTEs formed in multiple X-line reconnection with a large tilt angle, but not in simulations without the dipole tilt. Using the same global simulation model with constant resistivity Dorelli and Bhattacharjee [2009] showed that the FTEs can form in MHD simulations with steady solar wind also without the dipole tilt.

5.5.1 The upstream effect of FTEs

The dayside magnetopause reconnection can have an impact upstream from the magnetopause all the way to the bow shock and solar wind. The motion of the FTEs that propagate along the dayside magnetopause is fast with respect to the magnetosheath flow speed in the simulations of **Paper III** and **IV**. Therefore the FTEs drive bow waves ahead of them in the magnetosheath shown with a black dashed line in Figure 5.5a. The bow waves are fast magnetosonic waves having an increase in plasma density, velocity and magnetic field shown in panels b)–e) in Figure 5.5. Some of the strongest FTEs drive also a stern wave trailing behind the FTE (white dash-dotted line in Fig. 5.5a). These stern waves are fast reverse waves but much weaker than the bow waves. FTE driven magnetosheath waves have been reported previously by Omidi and Sibeck [2007] in a global hybrid-PIC simulation but the waves in their simulation are slow magnetosonic waves.

The bow waves can propagate through the whole magnetosheath all the way to the bow shock. The dynamic, thermal and magnetic pressure are higher downstream of the bow waves. Therefore, when the waves encounter the bow shock, they push the bow shock outward causing a small bulge in the bow shock as shown in Figure 5.6.

In **Paper IV** it is shown that the bulge in the bow shock changes the angle between the IMF and bow shock normal θ_{Bn}. At the foot of the bow shock bulge, θ_{Bn} becomes favorable for some of the protons to reflect ($\theta_{Bn} \lessapprox 50^\circ$) back to the solar wind along the IMF field lines. The bow shock bulge moves along the bows shock as the bow wave propagates in the magnetosheath. Therefore also the location from where the ions reflect moves along the bow shock surface. These reflected proton populations create local and transient foreshock events as can be seen in Figure 5.6. In the simulations of **Paper III** and **IV** local foreshocks are observed both in the southern and northern hemisphere.

Observational evidence of such transient foreshocks is also presented in **Pa-**

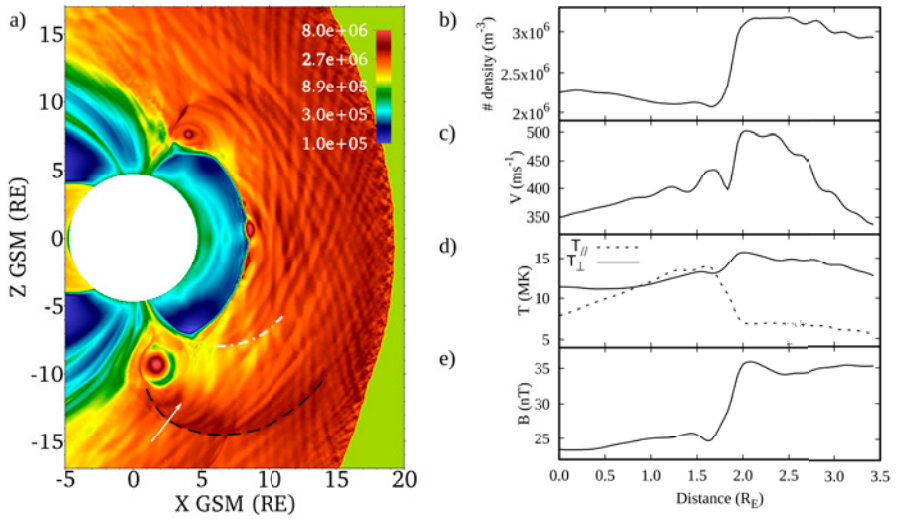

Figure 5.5: a) Global plot showing the bow wave (black dashed line) and the stern wave (white dash-dotted line) driven by the moving FTE. Color coding shows the number density (m^{-3}). Panels b)–e) show the b) number density, c) bulk velocity, d) parallel and perpendicular temperature, e) magnetic field density along the white line in panel a. Figure adapted from **Paper IV**.

per IV. During steady southward IMF and FTE production (shown by SuperDarn and IMAGE magnetometer data), the Geotail spacecraft observes a transient foreshock-like field aligned ion beam. This beam is separate from the bow shock and the regular foreshock and is not related to IMF fluctuations. Such a beam is most likely caused by a local bulge in the bow shock.

Summary

This Chapter summarized results of **Papers II**, **III** and **IV** about the magnetic reconnection at the dayside magnetopause during southward IMF. A set of GUMICS-4 simulations is used in **Paper II** to investigate the effect of IMF B_x and dipole tilt angle on the location of the X-line and energy conversion on the magnetopause. The results show that positive (negative) B_x shifts X-line northward (southward) and positive dipole tilt shits it southward (northward). If the tilt angle and B_x have the same sign their effects to the X-line shift may be partly counteracted. Using the Vlasiator simulation, **Paper III** shows that the X-lines are in constant motion along the dayside magnetopause and local reconnection rates are highly variable even though the solar wind inflow parameters are kept constant. Local reconnection rates correlate well with the 2D analytical formula for asymmetric reconnection by Cassak and Shay [2007]. Variations of the local reconnection rate are shown to be mainly driven by fluctuations

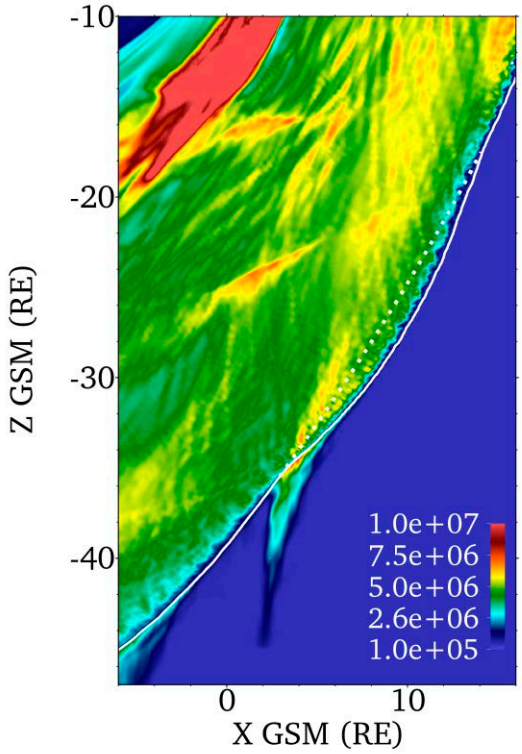

Figure 5.6: Bow shock bulge and transient foreshock phenomenon. Color shows the temperature parallel to the magnetic field $T_{\|}$ (K). Figure adapted from **Paper IV**.

in the magnetosheath parameters near the magnetopause. These fluctuations are partly caused by the magnetosheath mirror mode waves. Vlasiator results show also that the reconnection at the X-lines is affected by reconnection at the nearby X-lines and propagation of the FTEs. **Paper IV** presents results of the bow waves in the magnetosheath, driven by the FTEs propagating along the dayside magnetopause. These bow waves are able to propagate upstream and cause bulges in the bow shock changing the angle between the bow shock and the IMF. This makes the shock locally more quasi-parallel so that some of the protons can be reflected back to the solar wind causing local events called transient foreshocks. These results demonstrate again the importance of describing ions kinetically in a global simulation. The impact of mirror mode waves in the reconnection rate, and the cause of the local transient foreshocks requires the coupling between the local and global scale physics.

Chapter 6

Conclusions and outlook

This thesis investigates solar wind interactions with the Earth's magnetosheath and magnetopause using global magnetospheric simulation models. The emphasis of the thesis is on the dayside magnetopause reconnection, its drivers and global effects. Identification, occurrence and impact of magnetosheath mirror mode waves are also discussed. Two different simulation models are used in this thesis: the global MHD simulation GUMICS-4 and the world's first global magnetospheric hybrid-Vlasov simulation Vlasiator. One important part of this thesis is to verify that the results provided by Vlasiator are consistent with earlier results from both spacecraft observations and simulations.

This thesis shows that magnetic reconnection at the magnetopause is controlled by several factors. First, it is shown using GUMICS-4 simulations that two parameters that have an impact on the location of the X-line, the IMF B_x and the dipole tilt angle, may have partly counteracting effect on the X-line shift if these parameters have the same sign. Using Vlasiator simulations, this thesis demonstrates that the local reconnection rate corresponds well with the analytical formula for asymmetric reconnection by Cassak and Shay [2007]. The local reconnection rate is affected by local variations in the magnetosheath plasma. Fluctuations in the magnetosheath parameters near X-lines are partly generated by mirror mode waves that are observed to grow in the quasi-perpendicular magnetosheath. This thesis also indicates that the local reconnection rate and the motion of the X-lines are not only affected by fluctuations in the inflow parameters but also by reconnection at the neighboring X-lines. Outflow from stronger X-lines pushes against the weaker X-lines and might ultimately suppress reconnection in the weaker X-lines.

Vlasiator results show a strong scale-coupling between ion and global scales, especially via the global effects of the dayside reconnection and FTEs. High resolution MHD models are also able to simulate fast reconnection rates and formation of FTEs. However, they lack an accurate description of the processes upstream of the magnetopause, the formation of the foreshock and quasi-parallel and quasi-perpendicular magnetosheath as well as the growth of the

mirror mode waves in the magnetosheath, which are shown to affect reconnection rates. Dayside reconnection and the formation of FTEs have also unexpected global effects, as the propagation of FTE-driven waves through the magnetosheath is able to accelerate particles and even cause bulging at the bow shock and formation of local foreshocks. Neglecting the global scales in local simulations and vice versa will therefore lead to incomplete conclusions. The overall conclusion of this thesis is that the ion scale kinetic physics is important to accurately model the solar wind–magnetosheath–magnetopause interactions.

The next step in the study of reconnection in Vlasiator is to investigate the proton velocity distribution functions in the reconnection region and compare them with spacecraft observations. Simulations can help to explain the origin of different particle populations near the X-lines and in the accelerated jets. This has already been done using local kinetic simulations, but they lack the coupling between the local and global scales. Further, the interpretation of the fine structures of the velocity distribution functions benefits from Vlasiator's noiseless description of the velocity distribution function. Inclusion of kinetic electrons in Vlasiator simulations is still in the conceptual stage of development; but meanwhile test electrons can be launched and propagated in the fields provided by Vlasiator. It will be interesting to see whether Vlasiator is able to reproduce the crescent-shaped distributions in both electrons and ions that have been reported by MMS observations and local PIC simulations.

Magnetic reconnection and X-line behavior is known to be different in two and three spatial dimensions. In 2D Vlasiator simulations, continuous yet volatile reconnection is observed. In 2D all magnetic flux that arrives at the magnetopause is forced to reconnect but in 3D part of the flux is able to flow around the Earth without reconnecting with the magnetospheric field lines. In 3D, reconnection could become patchy and intermittent but most definitely formation of FTEs that have 3D flux rope structures is observed. Mirror mode structures and other large scale upstream kinetic phenomena that arrive at the magnetopause encounter the X-line draped on the 3D magnetopause, and cause variations in the inflowing plasma. Therefore reconnection rates are expected to vary as a function of distance along the X-line. Consequently, it is possible that mirror modes are able to cause temporal and spatial variations along the X-line.

Transition to global 3D simulations requires improvements to Vlasiator. Vlasiator can be run in 3D local setups but the requirements of global 3D simulations are too demanding for the current computing infrastructures. At the moment, the resolution of both the spatial and velocity space mesh is uniform. This means that computational resources are spent in solving regions of lesser interest, for instance, the solar wind. This issue could be resolved by making the mesh adaptive allowing better resolution in regions of interest.

The benefit of global MHD simulations compared to Vlasiator simulations is that the simulations can be 3D and computationally easy to carry out. In

the GUMICS-4 simulations, dayside reconnection occurs only along a single quasi-steady X-line. MHD models are at the moment the only models that are feasible to use in systematic studies including multiple simulations. They are able to produce the overall structure and global dynamics of the magnetosphere quite well. Global MHD simulations also provide coupling to the ionosphere, which also has global effects on the magnetospheric dynamics.

Supercomputing infrastructure is constantly improving. In order to run large-scale simulations, the code needs to be well parallelized and preferably scale to multiple computational units to benefit from the resources available. Vlasiator has been developed with the newest and future machines in mind. It applies state of the art solvers and scales nearly ideally up to 98000 cores. The novel approaches and divergence-free solvers of Vlasiator could be beneficial for the development of the MHD models. Vlasiator could also be improved with an inner boundary condition representing coupling to the ionosphere, similar to what is typically implemented in MHD models.

In global magnetospheric simulations, one has to compromise between the accuracy of the results and the computational resources required. Space weather prediction models need to provide simulations faster than real-time, meaning that physics cannot be described very accurately. For providing science results there is not much difference if the simulations are completed in a matter of hours, days or weeks. Of course waiting for the results is inconvenient but it can be worth it if the waiting time gains more accurate results.

This thesis shows the importance of the ion kinetic scale phenomena impacting the global scales, like FTE-driven waves in the magnetosheath. These global scale effects potentially have an impact also in the tail dynamics. The current space weather models do not take these phenomena into account, and therefore their accuracy in timing and severity of events may be lacking. Vlasiator simulations show which local phenomena and process are the most important in affecting the global dynamics that are related to severe space weather events. This knowledge can be used in improving the space weather models.

Even though Vlasiator is developed to model the Earth's magnetosphere, which has been its primary application, it can also be applied to other problems in plasma physics. Vlasiator may be used to improve understanding of fundamental evolution of shocks, magnetic reconnection and acceleration of energetic particle in stellar and astrophysical plasmas. Fusion plasma is one of the most interesting possible future application besides space physics. In addition, Vlasiator and other global simulations can be used to educate people about space weather and space physics. Global models are an illustrative way to demonstrate the solar wind-magnetosphere interactions and global dynamics of the magnetosphere. In plasma physics lectures, simulations may be applied to help the students to comprehend basic plasma phenomena. Therefore, global magnetospheric simulations are useful also for educational purposes and public outreach.

Bibliography

Acuña, M. H., Ogilvie, K. W., Baker, D. N., Curtis, S. A., Fairfield, D. H., and Mish, W. H. The Global Geospace Science Program and Its Investigations. *Space Science Reviews*, 71:5–21, February 1995. doi: 10.1007/BF00751323.

Ahmadi, N., Germaschewski, K., and Raeder, J. Effects of electron temperature anisotropy on proton mirror instability evolution. *Journal of Geophysical Research: Space Physics*, 121(6):5350–5365, 2016. ISSN 2169-9402. doi: 10.1002/2016JA022429. 2016JA022429.

Akasofu, S.-I. Energy coupling between the solar wind and the magnetosphere. *Space Sci. Rev.*, 28:121–190, 1981. doi: 10.1007/BF00218810.

Alfvén, H. On Sunspots and the Solar Cycle. *Arkiv for Astronomi*, 29:1–17, 1943.

Angelopoulos, V. The THEMIS Mission. *Space Science Reviews*, 141:5–34, December 2008. doi: 10.1007/s11214-008-9336-1.

Angelopoulos, V. The ARTEMIS Mission. *Space Science Reviews*, 165:3–25, December 2011. doi: 10.1007/s11214-010-9687-2.

Berchem, J. and Russell, C. T. Flux transfer events on the magnetopause - Spatial distribution and controlling factors. *Journal of Geophysical Research*, 89:6689–6703, August 1984. doi: 10.1029/JA089iA08p06689.

Birn, J., Drake, J. F., Shay, M. A., Rogers, B. N., Denton, R. E., Hesse, M., Kuznetsova, M., Ma, Z. W., Bhattacharjee, A., Otto, A., and Pritchett, P. L. Geospace Environmental Modeling (GEM) magnetic reconnection challenge. *Journal of Geophysical Research*, 106:3715–3720, March 2001. doi: 10.1029/1999JA900449.

Boardsen, S. A., Eastman, T. E., Sotirelis, T., and Green, J. L. An empirical model of the high-latitude magnetopause. *Journal of Geophysical Research*, 105:23193–23220, October 2000. doi: 10.1029/1998JA000143.

Borovsky, J. E. Physical improvements to the solar wind reconnection control function for the Earth's magnetosphere. *Journal of Geophysical Research (Space Physics)*, 118:2113–2121, May 2013. doi: 10.1002/jgra.50110.

Borovsky, J. E., Hesse, M., Birn, J., and Kuznetsova, M. M. What determines the reconnection rate at the dayside magnetosphere? *Journal of Geophysical Research (Space Physics)*, 113:A07210, July 2008. doi: 10.1029/2007JA012645.

Borovsky, J. E., Denton, M. H., Denton, R. E., Jordanova, V. K., and Krall, J. Estimating the effects of ionospheric plasma on solar wind/magnetosphere coupling via mass loading of dayside reconnection: Ion-plasma-sheet oxygen, plasmaspheric drainage plumes, and the plasma cloak. *Journal of Geophysical Research: Space Physics*, 118(9):5695–5719, 2013. ISSN 2169-9402. doi: 10.1002/jgra.50527.

Brackbill, J. U. and Barnes, D. C. The effect of nonzero product of magnetic gradient and b on the numerical solution of the magnetohydrodynamic equations. *Journal of Computational Physics*, 35(3):426 – 430, 1980. ISSN 0021-9991. doi: http://dx.doi.org/10.1016/0021-9991(80)90079-0.

Brambles, O. J., Lotko, W., Damiano, P. A., Zhang, B., Wiltberger, M., and Lyon, J. Effects of causally driven cusp o+ outflow on the storm time magnetosphere-ionosphere system using a multifluid global simulation. *Journal of Geophysical Research: Space Physics*, 115(A9):n/a–n/a, 2010. ISSN 2156-2202. doi: 10.1029/2010JA015469. A00J04.

Brecht, S. H., Lyon, J., Fedder, J. A., and Hain, K. A simulation study of east-west IMF effects on the magnetosphere. *Geophysical Research Letters*, 8:397–400, April 1981. doi: 10.1029/GL008i004p00397.

Brecht, S. H., Lyon, J. G., Fedder, J. A., and Hain, K. A time dependent three-dimensional simulation of the earth's magnetosphere - Reconnection events. *Journal of Geophysical Research*, 87:6098–6108, August 1982. doi: 10.1029/JA087iA08p06098.

Burch, J. L. and Phan, T. D. Magnetic reconnection at the dayside magnetopause: Advances with MMS. *Geophysical Research Letters*, 43(16):8327–8338, 2016. ISSN 1944-8007. doi: 10.1002/2016GL069787. 2016GL069787.

Burch, J. L., Moore, T. E., Torbert, R. B., and Giles, B. L. Magnetospheric Multiscale Overview and Science Objectives. *Space Science Reviews*, 199:5–21, March 2016. doi: 10.1007/s11214-015-0164-9.

Burch, J. L., Torbert, R. B., Phan, T. D., Chen, L.-J., Moore, T. E., Ergun, R. E., Eastwood, J. P., Gershman, D. J., Cassak, P. A., Argall, M. R., Wang, S., Hesse, M., Pollock, C. J., Giles, B. L., Nakamura, R., Mauk, B. H., Fuselier, S. A., Russell, C. T., Strangeway, R. J., Drake, J. F., Shay, M. A., Khotyaintsev, Y. V., Lindqvist, P.-A., Marklund, G., Wilder, F. D., Young, D. T., Torkar, K., Goldstein, J., Dorelli, J. C., Avanov, L. A., Oka, M., Baker, D. N., Jaynes, A. N., Goodrich, K. A., Cohen, I. J., Turner, D. L., Fennell, J. F., Blake, J. B., Clemmons, J., Goldman, M., Newman, D., Petrinec, S. M., Trattner, K. J., Lavraud, B., Reiff, P. H., Baumjohann, W., Magnes, W., Steller, M., Lewis, W., Saito, Y., Coffey, V., and Chandler, M. Electron-scale measurements of magnetic reconnection in space. *Science*, 352(6290), 2016. ISSN 0036-8075. doi: 10.1126/science.aaf2939.

Califano, F., Hellinger, P., Kuznetsov, E., Passot, T., Sulem, P. L., and Trávníček, P. M. Nonlinear mirror mode dynamics: Simulations and modeling. *Journal of Geophysical Research (Space Physics)*, 113:A08219, August 2008. doi: 10.1029/2007JA012898.

Case, N. A. and Wild, J. A. The location of the earth's magnetopause: A comparison of modeled position and in situ cluster data. *Journal of Geophysical Research: Space Physics*, 118(10):6127–6135, 2013. ISSN 2169-9402. doi: 10.1002/jgra.50572.

Cassak, P. A. and Shay, M. A. Scaling of asymmetric magnetic reconnection: General theory and collisional simulations. *Physics of Plasmas*, 14(10):102114, October 2007. doi: 10.1063/1.2795630.

Chao, J. K., Wu, D. J., Lin, C.-H., Yang, Y.-H., Wang, X. Y., Kessel, M., Chen, S. H., and Lepping, R. P. Models for the Size and Shape of the Earth's Magnetopause and Bow Shock. In Lyu, L.-H., editor, *Space Weather Study Using Multipoint Techniques*, page 127, 2002.

Chapman, S. and Ferraro, V. C. A. A new theory of magnetic storms. *Terrestrial Magnetism and Atmospheric Electricity*, 36(2):77–97, 1931a. ISSN 0096-8013. doi: 10.1029/TE036i002p00077.

Chapman, S. and Ferraro, V. C. A. A new theory of magnetic storms. *Terrestrial Magnetism and Atmospheric Electricity*, 36(3):171–186, 1931b. ISSN 0096-8013. doi: 10.1029/TE036i003p00171.

Chen, Q., Otto, A., and Lee, L. C. Tearing instability, Kelvin-Helmholtz instability, and magnetic reconnection. *Journal of Geophysical Research*, 102:151–162, January 1997. doi: 10.1029/96JA03144.

Chodura, R. A hybrid fluid-particle model of ion heating in high-mach-number shock waves. *Nuclear Fusion*, 15(1):55, 1975.

Connor, H. K., Raeder, J., Sibeck, D. G., and Trattner, K. J. Relation between cusp ion structures and dayside reconnection for four IMF clock angles: OpenGGCM-LTPT results. *Journal of Geophysical Research (Space Physics)*, 120:4890–4906, June 2015. doi: 10.1002/2015JA021156.

Coppi, B., Laval, G., and Pellat, R. Dynamics of the geomagnetic tail. *Phys. Rev. Lett.*, 16:1207–1210, Jun 1966. doi: 10.1103/PhysRevLett.16.1207.

Courant, R., Friedrichs, K., and Lewy, H. Über die partiellen differenzengleichungen der mathematischen physik. *Mathematische Annalen*, 100(1):32–74, 1928. ISSN 1432-1807. doi: 10.1007/BF01448839.

Cowley, S. and Owen, C. A simple illustrative model of open flux tube motion over the dayside magnetopause. *Planetary and Space Science*, 37(11):1461 – 1475, 1989. ISSN 0032-0633. doi: http://dx.doi.org/10.1016/0032-0633(89)90116-5.

Crooker, N. U. Dayside merging and cusp geometry. *Journal of Geophysical Research*, 84:951–959, March 1979. doi: 10.1029/JA084iA03p00951.

Daldorff, L. K. S., Tóth, G., Gombosi, T. I., Lapenta, G., Amaya, J., Markidis, S., and Brackbill, J. U. Two-way coupling of a global hall magnetohydrodynamics model with a local implicit particle-in-cell model. *Journal of Computational Physics*, 268: 236 – 254, 2014. ISSN 0021-9991. doi: http://dx.doi.org/10.1016/j.jcp.2014.03.009.

Denton, R. E. ULF waves in the magnetosheath. *International Journal of Geomagnetism and Aeronomy*, 2(1):45–55, 2000.

Dimmock, A. P. and Nykyri, K. The statistical mapping of magnetosheath plasma properties based on THEMIS measurements in the magnetosheath interplanetary medium reference frame. *Journal of Geophysical Research (Space Physics)*, 118: 4963–4976, August 2013. doi: 10.1002/jgra.50465.

Dimmock, A. P., Osmane, A., Pulkkinen, T. I., and Nykyri, K. A statistical study of the dawn-dusk asymmetry of ion temperature anisotropy and mirror mode occurrence in the terrestrial dayside magnetosheath using THEMIS data. *Journal of Geophysical Research (Space Physics)*, 120:5489–5503, July 2015. doi: 10.1002/2015JA021192.

Dorelli, J. C. and Bhattacharjee, A. On the generation and topology of flux transfer events. *Journal of Geophysical Research (Space Physics)*, 114:A06213, June 2009. doi: 10.1029/2008JA013410.

Doss, C. E., Komar, C. M., Cassak, P. A., Wilder, F. D., Eriksson, S., and Drake, J. F. Asymmetric magnetic reconnection with a flow shear and applications to the magnetopause. *Journal of Geophysical Research (Space Physics)*, 120:7748–7763, September 2015. doi: 10.1002/2015JA021489.

Dungey, J. W. Interplanetary magnetic field and the auroral zones. *Phys. Rev. Lett.*, 6:47–48, Jan 1961. doi: 10.1103/PhysRevLett.6.47.

Dunlop, M. W., Zhang, Q.-H., Bogdanova, Y. V., Lockwood, M., Pu, Z., Hasegawa, H., Wang, J., Taylor, M. G. G. T., Berchem, J., Lavraud, B., Eastwood, J., Volwerk, M., Shen, C., Shi, J.-K., Constantinescu, D., Frey, H., Fazakerley, A. N., Sibeck, D., Escoubet, P., Wild, J. A., and Liu, Z.-X. Extended magnetic reconnection across the dayside magnetopause. *Phys. Rev. Lett.*, 107:025004, Jul 2011. doi: 10.1103/PhysRevLett.107.025004.

Eastwood, J. P., Lucek, E. A., Mazelle, C., Meziane, K., Narita, Y., Pickett, J., and Treumann, R. A. The Foreshock. *Space Science Reviews*, 118:41–94, June 2005. doi: 10.1007/s11214-005-3824-3.

Eastwood, J. P., Phan, T. D., Fear, R. C., Sibeck, D. G., Angelopoulos, V., Øieroset, M., and Shay, M. A. Survival of flux transfer event (FTE) flux ropes far along the tail magnetopause. *Journal of Geophysical Research (Space Physics)*, 117:A08222, August 2012. doi: 10.1029/2012JA017722.

Eliasson, B. and Shukla, P. K. Simulation study of magnetic holes at the earth's collisionless bow shock. *New Journal of Physics*, 9(6):168, 2007.

Engebretson, M. J., Lin, N., Baumjohann, W., Luehr, H., and Anderson, B. J. A comparison of ULF fluctuations in the solar wind, magnetosheath, and dayside magnetosphere. I - Magnetosheath morphology. II - Field and plasma conditions in the magnetosheath. *Journal of Geophysical Research*, 96:3441–3464, March 1991. doi: 10.1029/90JA02101.

Engebretson, M. J., Beck, J. R., Rairden, R. L., Mende, S. B., Arnoldy, R. L., Cahill, L. J., and Rosenbergs, T. J. *Studies of the Occurrence and Properties of Pc 3-4 Magnetic and Auroral Pulsations at South Pole, Antarctica*, pages 345–353. American Geophysical Union, 1994. ISBN 9781118663943. doi: 10.1029/GM081p0345.

Escoubet, C. P., Schmidt, R., and Goldstein, M. L. Cluster - Science and Mission Overview. *Space Science Reviews*, 79:11–32, January 1997. doi: 10.1023/A:1004923124586.

Fear, R. C., Milan, S. E., Fazakerley, A. N., Fornaçon, K.-H., Carr, C. M., and Dandouras, I. Simultaneous observations of flux transfer events by THEMIS, Cluster, Double Star, and SuperDARN: Acceleration of FTEs. *Journal of Geophysical Research (Space Physics)*, 114:A10213, October 2009. doi: 10.1029/2009JA014310.

Furth, H. P., Killeen, J., and Rosenbluth, M. N. Finite-Resistivity Instabilities of a Sheet Pinch. *Physics of Fluids*, 6:459–484, April 1963. doi: 10.1063/1.1706761.

Fuselier, S. A., Trattner, K. J., and Petrinec, S. M. Antiparallel and component reconnection at the dayside magnetopause. *Journal of Geophysical Research: Space Physics*, 116(A10):n/a–n/a, 2011. ISSN 2156-2202. doi: 10.1029/2011JA016888. A10227.

Ganse, U., Kilian, P., Spanier, F., and Vainio, R. Nonlinear Wave Interactions as Emission Process of Type II Radio Bursts. *The Astrophysical Journal*, 751:145, June 2012. doi: 10.1088/0004-637X/751/2/145.

Garcia, K. S., Merkin, V. G., and Hughes, W. J. Effects of nightside o+ outflow on magnetospheric dynamics: Results of multifluid mhd modeling. *Journal of Geophysical Research: Space Physics*, 115(A12):n/a–n/a, 2010. ISSN 2156-2202. doi: 10.1029/2010JA015730. A00J09.

Gary, S. P. The mirror and ion cyclotron anisotropy instabilities. *Journal of Geophysical Research (Space Physics)*, 97:8519–8529, June 1992. doi: 10.1029/92JA00299.

Gary, S. P., Fuselier, S. A., and Anderson, B. J. Ion anisotropy instabilities in the magnetosheath. *Journal of Geophysical Research (Space Physics)*, 98:1481–1488, February 1993. doi: 10.1029/92JA01844.

Gary, S. P., Montgomery, M. D., Feldman, W. C., and Forslund, D. W. Proton temperature anisotropy instabilities in the solar wind. *Journal of Geophysical Research*, 81(7):1241–1246, 1976. ISSN 2156-2202. doi: 10.1029/JA081i007p01241.

Génot, V., Schwartz, S. J., Mazelle, C., Balikhin, M., Dunlop, M., and Bauer, T. M. Kinetic study of the mirror mode. *Journal of Geophysical Research*, 106:21611–21622, October 2001. doi: 10.1029/2000JA000457.

Génot, V., Budnik, E., Hellinger, P., Passot, T., Belmont, G., Trávníček, P. M., Sulem, P.-L., Lucek, E., and Dandouras, I. Mirror structures above and below the linear instability threshold: Cluster observations, fluid model and hybrid simulations. *Annales Geophysicae*, 27:601–615, February 2009. doi: 10.5194/angeo-27-601-2009.

Génot, V., Broussillou, L., Budnik, E., Hellinger, P., Trávníček, P. M., Lucek, E., and Dandouras, I. Timing mirror structures observed by Cluster with a magnetosheath flow model. *Annales Geophysicae*, 29(10):1849–1860, 2011. doi: 10.5194/angeo-29-1849-2011.

Glocer, A., Tóth, G., Ma, Y., Gombosi, T., Zhang, J.-C., and Kistler, L. M. Multifluid Block-Adaptive-Tree Solar wind Roe-type Upwind Scheme: Magnetospheric composition and dynamics during geomagnetic storms-Initial results. *Journal of Geophysical Research (Space Physics)*, 114:A12203, December 2009. doi: 10.1029/2009JA014418.

Glocer, A., Dorelli, J., Toth, G., Komar, C. M., and Cassak, P. A. Separator reconnection at the magnetopause for predominantly northward and southward IMF: Techniques and results. *Journal of Geophysical Research (Space Physics)*, 121:140–156, January 2016. doi: 10.1002/2015JA021417.

Gonzalez, W. D. and Mozer, F. S. A quantitative model for the potential resulting from reconnection with an arbitrary interplanetary magnetic field. *Journal of Geophysical Research*, 79:4186–4194, October 1974. doi: 10.1029/JA079i028p04186.

Gosling, J. T. and McComas, D. J. Field line draping about fast coronal mass ejecta - A source of strong out-of-the-ecliptic interplanetary magnetic fields. *Geophysical Research Letters*, 14:355–358, April 1987. doi: 10.1029/GL014i004p00355.

Gosling, J. T., Thomsen, M. F., Bame, S. J., Elphic, R. C., and Russell, C. T. Observations of reconnection of interplanetary and lobe magnetic field lines at the high-latitude magnetopause. *Journal of Geophysical Research: Space Physics*, 96 (A8):14097–14106, 1991. ISSN 2156-2202. doi: 10.1029/91JA01139.

Gressl, C., Veronig, A. M., Temmer, M., Odstrčil, D., Linker, J. A., Mikić, Z., and Riley, P. Comparative Study of MHD Modeling of the Background Solar Wind. *Solar Physics*, 289:1783–1801, May 2014. doi: 10.1007/s11207-013-0421-6.

Haerendel, G., Paschmann, G., Sckopke, N., and Rosenbauer, H. The frontside boundary layer of the magnetosphere and the problem of reconnection. *Journal of Geophysical Research*, 83:3195–3216, July 1978. doi: 10.1029/JA083iA07p03195.

Hasegawa, A. Drift mirror instability of the magnetosphere. *Physics of Fluids*, 12: 2642–2650, 1969. doi: 10.1063/1.1692407.

Haynes, A. L. and Parnell, C. E. A method for finding three-dimensional magnetic skeletons. *Physics of Plasmas*, 17(9):092903, September 2010. doi: 10.1063/1.3467499.

Hellinger, P., Kuznetsov, E. A., Passot, T., Sulem, P. L., and Trávníček, P. M. Mirror instability: From quasi-linear diffusion to coherent structures. *Geophysical Research Letters*, 36:L06103, March 2009. doi: 10.1029/2008GL036805.

Herčík, D., Trávníček, P. M., Johnson, J. R., Kim, E.-H., and Hellinger, P. Mirror mode structures in the asymmetric Hermean magnetosheath: Hybrid simulations. *Journal of Geophysical Research (Space Physics)*, 118:405–417, January 2013. doi: 10.1029/2012JA018083.

Hewett, D. W. A global method of solving the electron-field equations in a zero-inertia-electron-hybrid plasma simulation code. *Journal of Computational Physics*, 38:378–395, December 1980. doi: 10.1016/0021-9991(80)90155-2.

Hoilijoki, S., Pomoell, J., Vainio, R., Palmroth, M., and Koskinen, H. E. J. Interpreting solar EUV wave observations from different viewing angles using an MHD model. *Solar Physics*, 286(2):493–507, 2013. ISSN 1573-093X. doi: 10.1007/s11207-013-0276-x.

Hoilijoki, S., Souza, V. M., Walsh, B. M., Janhunen, P., and Palmroth, M. Magnetopause reconnection and energy conversion as influenced by the dipole tilt and the IMF B_x. *Journal of Geophysical Research (Space Physics)*, 119:4484–4494, June 2014. doi: 10.1002/2013JA019693.

Hoilijoki, S., Palmroth, M., Walsh, B. M., Pfau-Kempf, Y., von Alfthan, S., Ganse, U., Hannuksela, O., and Vainio, R. Mirror modes in the Earth's magnetosheath: Results from a global hybrid-Vlasov simulation. *Journal of Geophysical Research (Space Physics)*, 121:4191–4204, May 2016. doi: 10.1002/2015JA022026.

Hoilijoki, S., Ganse, U., Pfau-Kempf, Y., Cassak, P. A., Walsh, B. M., Hietala, H., von Alfthan, S., and Palmroth, M. Reconnection rates and x line motion at the magnetopause: Global 2d-3v hybrid-vlasov simulation results. *Journal of Geophysical Research: Space Physics*, pages n/a–n/a, 2017. ISSN 2169-9402. doi: 10.1002/2016JA023709. 2016JA023709.

Hoppe, M. M., Russell, C. T., Frank, L. A., Eastman, T. E., and Greenstadt, E. W. Upstream hydromagnetic waves and their association with backstreaming ion populations: Isee 1 and 2 observations. *Journal of Geophysical Research: Space Physics*, 86(A6):4471–4492, 1981. ISSN 2156-2202. doi: 10.1029/JA086iA06p04471.

Hubert, D., Lacombe, C., Harvey, C. C., Moncuquet, M., Russell, C. T., and Thomsen, M. F. Nature, properties, and origin of low-frequency waves from an oblique shock to the inner magnetosheath. *Journal of Geophysical Research (Space Physics)*, 103: 26783–26798, November 1998. doi: 10.1029/98JA01011.

Janhunen, P. GUMICS-3 A Global Ionosphere-Magnetosphere Coupling Simulation with High Ionospheric Resolution. In Guyenne, T.-D. and Hilgers, A., editors, *Environment Modeling for Space-Based Applications*, volume 392 of *ESA Special Publication*, page 233, December 1996.

Janhunen, P., Palmroth, M., Laitinen, T., Honkonen, I., Juusola, L., Facskó, G., and Pulkkinen, T. I. The GUMICS-4 global MHD magnetosphere-ionosphere coupling simulation. *Journal of Atmospheric and Solar-Terrestrial Physics*, 80:48–59, May 2012. doi: 10.1016/j.jastp.2012.03.006.

Johnson, J. R. and Cheng, C. Z. Global structure of mirror modes in the magnetosheath. *Journal of Geophysical Research: Space Physics*, 102(A4):7179–7189, 1997. ISSN 2156-2202. doi: 10.1029/96JA03949.

Käpylä, P. On global solar dynamo simulations. *Astronomische Nachrichten*, 332(1): 43–50, 2011. ISSN 1521-3994. doi: 10.1002/asna.201012345.

Karimabadi, H., Roytershteyn, V., Vu, H. X., Omelchenko, Y. A., Scudder, J., Daughton, W., Dimmock, A., Nykyri, K., Wan, M., Sibeck, D., Tatineni, M., Majumdar, A., Loring, B., and Geveci, B. The link between shocks, turbulence, and magnetic reconnection in collisionless plasmas. *Physics of Plasmas (1994-present)*, 21(6):062308, 2014. doi: http://dx.doi.org/10.1063/1.4882875.

Kempf, Y., Pokhotelov, D., Gutynska, O., Wilson, L. B., III, Walsh, B. M., Alfthan, S. v., Hannuksela, O., Sibeck, D. G., and Palmroth, M. Ion distributions in the Earth's foreshock: Hybrid-Vlasov simulation and THEMIS observations. *Journal of Geophysical Research (Space Physics)*, 120:3684–3701, May 2015. doi: 10.1002/2014JA020519.

Kitamura, N., Hasegawa, H., Saito, Y., Shinohara, I., Yokota, S., Nagai, T., Pollock, C. J., Giles, B. L., Moore, T. E., Dorelli, J. C., Gershman, D. J., Avanov, L. A., Paterson, W. R., Coffey, V. N., Chandler, M. O., Sauvaud, J. A., Lavraud, B., Torbert, R. B., Russell, C. T., Strangeway, R. J., and Burch, J. L. Shift of the magnetopause reconnection line to the winter hemisphere under southward imf conditions: Geotail and mms observations. *Geophysical Research Letters*, 43(11):5581–5588, 2016. ISSN 1944-8007. doi: 10.1002/2016GL069095. 2016GL069095.

Kivelson, M. G. and Russell, C. T. *Introduction to Space Physics*. April 1995.

Kivelson, M. G. and Southwood, D. J. Mirror instability II: The mechanism of nonlinear saturation. *Journal of Geophysical Research*, 101:17365–17372, August 1996. doi: 10.1029/96JA01407.

Komar, C. M. and Cassak, P. A. The local dayside reconnection rate for oblique interplanetary magnetic fields. *Journal of Geophysical Research: Space Physics*, pages n/a–n/a, 2016. ISSN 2169-9402. doi: 10.1002/2016JA022530. 2016JA022530.

Komar, C. M., Cassak, P. A., Dorelli, J. C., Glocer, A., and Kuznetsova, M. M. Tracing magnetic separators and their dependence on IMF clock angle in global magnetospheric simulations. *Journal of Geophysical Research (Space Physics)*, 118: 4998–5007, August 2013. doi: 10.1002/jgra.50479.

Komar, C. M., Fermo, R. L., and Cassak, P. A. Comparative analysis of dayside magnetic reconnection models in global magnetosphere simulations. *Journal of Geophysical Research (Space Physics)*, 120:276–294, January 2015. doi: 10.1002/2014JA020587.

Koskinen, H. J. K. *Physics of Space Storms: From the Solar Surface to the Earth*. Springer-Verlag, The address, 1 edition, 2011. ISBN 987-3-642-00310-3. doi: 10.1007/978-3-642-00319-6.

Krauss-Varban, D. *Bow Shock and Magnetosheath Simulations: Wave Transport and Kinetic Properties*, pages 121–134. American Geophysical Union, 1994. ISBN 9781118663943. doi: 10.1029/GM081p0121.

Lacombe, C. and Belmont, G. Waves in the Earth's magnetosheath: Observations and interpretations. *Advances in Space Research*, 15:329–340, March 1995. doi: 10.1016/0273-1177(94)00113-F.

Laitinen, T. V., Janhunen, P., Pulkkinen, T. I., Palmroth, M., and Koskinen, H. E. J. On the characterization of magnetic reconnection in global mhd simulations. *Annales Geophysicae*, 24(11):3059–3069, 2006. doi: 10.5194/angeo-24-3059-2006.

Laitinen, T. V., Palmroth, M., Pulkkinen, T. I., Janhunen, P., and Koskinen, H. E. J. Continuous reconnection line and pressure-dependent energy conversion on the magnetopause in a global MHD model. *Journal of Geophysical Research (Space Physics)*, 112:A11201, November 2007. doi: 10.1029/2007JA012352.

Laitinen, T. V., Khotyaintsev, Y. V., André, M., Vaivads, A., and Rème, H. Local influence of magnetosheath plasma beta fluctuations on magnetopause reconnection. *Annales Geophysicae*, 28(5):1053–1063, 2010. doi: 10.5194/angeo-28-1053-2010.

Lapenta, G., Berchem, J., Zhou, M., Walker, R. J., El-Alaoui, M., Goldstein, M. L., Paterson, W. R., Giles, B. L., Pollock, C. J., Russell, C. T., Strangeway, R. J., Ergun, R. E., Khotyaintsev, Y. V., Torbert, R. B., and Burch, J. L. On the origin of the crescent-shaped distributions observed by mms at the magnetopause. *Journal of Geophysical Research: Space Physics*, pages n/a–n/a, 2017. ISSN 2169-9402. doi: 10.1002/2016JA023290. 2016JA023290.

Leboeuf, J. N., Tajima, T., Kennel, C. F., and Dawson, J. M. Global simulation of the time-dependent magnetosphere. *Geophysical Research Letters*, 5:609–612, July 1978. doi: 10.1029/GL005i007p00609.

Lee, L. C. and Fu, Z. F. A theory of magnetic flux transfer at the Earth's magnetopause. *Geophysical Research Letters*, 12:105–108, February 1985. doi: 10.1029/GL012i002p00105.

Lin, R. L., Zhang, X. X., Liu, S. Q., Wang, Y. L., and Gong, J. C. A three-dimensional asymmetric magnetopause model. *Journal of Geophysical Research: Space Physics*, 115(A4):n/a–n/a, 2010. ISSN 2156-2202. doi: 10.1029/2009JA014235. A04207.

Lin, Y., Wang, X. Y., Lu, S., Perez, J. D., and Lu, Q. Investigation of storm time magnetotail and ion injection using three-dimensional global hybrid simulation. *Journal of Geophysical Research: Space Physics*, 119(9):7413–7432, 2014. ISSN 2169-9402. doi: 10.1002/2014JA020005.

Liu, Y., Richardson, J. D., Belcher, J. W., Kasper, J. C., and Skoug, R. M. Plasma depletion and mirror waves ahead of interplanetary coronal mass ejections. *Journal of Geophysical Research (Space Physics)*, 111:A09108, September 2006. doi: 10.1029/2006JA011723.

Liu, Z. X., Escoubet, C. P., Pu, Z., Laakso, H., Shi, J. K., Shen, C., and Hapgood, M. The Double Star mission. *Annales Geophysicae*, 23:2707–2712, November 2005. doi: 10.5194/angeo-23-2707-2005.

Londrillo, P. and Del Zanna, L. On the divergence-free condition in Godunov-type schemes for ideal magnetohydrodynamics: the upwind constrained transport method. *Journal of Computational Physics*, 195(1):17 – 48, 2004. ISSN 0021-9991. doi: http://dx.doi.org/10.1016/j.jcp.2003.09.016.

Longmore, M., Schwartz, S. J., Geach, J., Cooling, B. M. A., Dandouras, I., Lucek, E. A., and Fazakerley, A. N. Dawn-dusk asymmetries and sub-alfvénic flow in the high and low latitude magnetosheath. *Annales Geophysicae*, 23(10):3351–3364, 2005. doi: 10.5194/angeo-23-3351-2005.

Lopez, R. E., Bruntz, R., Mitchell, E. J., Wiltberger, M., Lyon, J. G., and Merkin, V. G. Role of magnetosheath force balance in regulating the dayside reconnection potential. *Journal of Geophysical Research: Space Physics*, 115(A12):n/a–n/a, 2010. ISSN 2156-2202. doi: 10.1029/2009JA014597. A12216.

Lu, S., Lu, Q., Lin, Y., Wang, X., Ge, Y., Wang, R., Zhou, M., Fu, H., Huang, C., Wu, M., and Wang, S. Dipolarization fronts as earthward propagating flux ropes: A three-dimensional global hybrid simulation. *Journal of Geophysical Research (Space Physics)*, 120:6286–6300, August 2015. doi: 10.1002/2015JA021213.

Lucek, E. A., Dunlop, M. W., Balogh, A., Cargill, P., Baumjohann, W., Georgescu, E., Haerendel, G., and Fornacon, K.-H. Mirror mode structures observed in the dawn-side magnetosheath by Equator-S. *Geophysical Research Letters*, 26:2159–2162, 1999. doi: 10.1029/1999GL900490.

Luhmann, J. G., Walker, R. J., Russell, C. T., Crooker, N. U., Spreiter, J. R., and Stahara, S. S. Patterns of potential magnetic field merging sites on the dayside magnetopause. *Journal of Geophysical Research*, 89:1741–1744, March 1984. doi: 10.1029/0JGREA0000890000A3001741000001.

Lyon, J. G., Brecht, S. H., Huba, J. D., Fedder, J. A., and Palmadesso, P. J. Computer simulation of a geomagnetic substorm. *Physical Review Letters*, 46:1038–1041, April 1981. doi: 10.1103/PhysRevLett.46.1038.

Lyon, J., Fedder, J., and Mobarry, C. The lyon–fedder–mobarry (lfm) global mhd magnetospheric simulation code. *Journal of Atmospheric and Solar-Terrestrial Physics*, 66(15):1333–1350, 2004.

Markidis, S., Lapenta, G., and Rizwan-uddin. Multi-scale simulations of plasma with ipic3d. *Mathematics and Computers in Simulation*, 80(7):1509 – 1519, 2010. ISSN 0378-4754. doi: http://dx.doi.org/10.1016/j.matcom.2009.08.038. Multiscale modeling of moving interfaces in materials.

Nakamura, T. K. M., Fujimoto, M., and Sekiya, H. Interaction of multiple magnetic islands in a long current sheet: Two-fluid simulations. *Geophysical Research Letters*, 37(2):n/a–n/a, 2010. ISSN 1944-8007. doi: 10.1029/2009GL041858. L02103.

Němeček, Z., Šafránková, J., Zastenker, G. N., Pišoft, P., and Paularena, K. I. Spatial distribution of the magnetosheath ion flux. *Advances in Space Research*, 30:2751–2756, 2002. doi: 10.1016/S0273-1177(02)80402-1.

Němeček, Z., Šafránková, J., Koval, A., Merka, J., and Přech, L. MHD analysis of propagation of an interplanetary shock across magnetospheric boundaries. *Journal of Atmospheric and Solar-Terrestrial Physics*, 73:20–29, January 2011. doi: 10.1016/j.jastp.2010.05.017.

Oka, M., Fujimoto, M., Nakamura, T. K. M., Shinohara, I., and Nishikawa, K.-I. Magnetic reconnection by a self-retreating x line. *Phys. Rev. Lett.*, 101:205004, Nov 2008. doi: 10.1103/PhysRevLett.101.205004.

Omidi, N. and Sibeck, D. G. Flux transfer events in the cusp. *Geophysical Research Letterss*, 34:L04106, February 2007. doi: 10.1029/2006GL028698.

Omidi, N. and Winske, D. Structure of the magnetopause inferred from one-dimensional hybrid simulations. *Journal of Geophysical Research*, 100:11935, July 1995. doi: 10.1029/94JA02937.

Omidi, N., Karimabadi, H., and Krauss-Varban, D. Hybrid simulation of the curved dayside magnetopause during southward IMF. *Geophysical Research Letters*, 25: 3273–3276, 1998. doi: 10.1029/98GL02484.

Omidi, N., Karimabadi, H., and Quest, K. B. Global hybrid simulations of solar wind interaction with the magnetosphere. In Büchner, J., Dum, C. T., and Scholer, M., editors, *Space Plasma Simulation*, page 71, 2001.

Omidi, N., Blanco-Cano, X., Russell, C., and Karimabadi, H. Dipolar magnetospheres and their characterization as a function of magnetic moment. *Advances in Space Research*, 33(11):1996 – 2003, 2004. ISSN 0273-1177. doi: http://dx.doi.org/10.1016/j.asr.2003.08.041. Comparative Magnetospheres.

Omidi, N., Sibeck, D., Gutynska, O., and Trattner, K. J. Magnetosheath filamentary structures formed by ion acceleration at the quasi-parallel bow shock. *Journal of Geophysical Research (Space Physics)*, 119:2593–2604, April 2014a. doi: 10.1002/2013JA019587.

Omidi, N., Zhang, H., Chu, C., Sibeck, D., and Turner, D. Parametric dependencies of spontaneous hot flow anomalies. *Journal of Geophysical Research (Space Physics)*, 119:9823–9833, December 2014b. doi: 10.1002/2014JA020382.

Omidi, N., Berchem, J., Sibeck, D., and Zhang, H. Impacts of spontaneous hot flow anomalies on the magnetosheath and magnetopause. *Journal of Geophysical Research (Space Physics)*, 121:3155–3169, April 2016. doi: 10.1002/2015JA022170.

Opher, M., Richardson, J. D., Toth, G., and Gombosi, T. I. Confronting observations and modeling: The role of the interstellar magnetic field in voyager 1 and 2 asymmetries. *Space Science Reviews*, 143(1):43–55, 2009. doi: 10.1007/s11214-008-9453-x.

Ouellette, J. E., Rogers, B. N., Wiltberger, M., and Lyon, J. G. Magnetic reconnection at the dayside magnetopause in global lyon-fedder-mobarry simulations. *Journal of Geophysical Research: Space Physics*, 115(A8):n/a–n/a, 2010. ISSN 2156-2202. doi: 10.1029/2009JA014886. A08222.

Ouellette, J. E., Lyon, J. G., and Rogers, B. N. A study of asymmetric reconnection scaling in the Lyon-Fedder-Mobarry code. *Journal of Geophysical Research (Space Physics)*, 119:1673–1682, March 2014. doi: 10.1002/2013JA019366.

Ouellette, J. E., Lyon, J. G., Brambles, O. J., Zhang, B., and Lotko, W. The effects of plasmaspheric plumes on dayside reconnection. *Journal of Geophysical Research (Space Physics)*, 121:4111–4118, May 2016. doi: 10.1002/2016JA022597.

Palmroth, M., Pulkkinen, T. I., Janhunen, P., and Wu, C.-C. Stormtime energy transfer in global MHD simulation. *Journal of Geophysical Research (Space Physics)*, 108: 1048, January 2003. doi: 10.1029/2002JA009446.

Palmroth, M., Fear, R. C., and Honkonen, I. Magnetopause energy transfer dependence on the interplanetary magnetic field and the earth's magnetic dipole axis orientation. *Annales Geophysicae*, 30(3):515–526, 2012. doi: 10.5194/angeo-30-515-2012.

Palmroth, M., Archer, M., Vainio, R., Hietala, H., Pfau-Kempf, Y., Hoilijoki, S., Hannuksela, O., Ganse, U., Sandroos, A., Alfthan, S. v., and Eastwood, J. P. ULF foreshock under radial IMF: THEMIS observations and global kinetic simulation Vlasiator results compared. *Journal of Geophysical Research (Space Physics)*, 120: 8782–8798, October 2015. doi: 10.1002/2015JA021526.

Park, K. S., Ogino, T., and Walker, R. J. On the importance of antiparallel reconnection when the dipole tilt and imf by are nonzero. *Journal of Geophysical Research: Space Physics*, 111(A5):n/a–n/a, 2006. ISSN 2156-2202. doi: 10.1029/2004JA010972. A05202.

Parker, E. N. Sweet's Mechanism for Merging Magnetic Fields in Conducting Fluids. *Journal of Geophysical Research*, 62:509–520, December 1957. doi: 10.1029/JZ062i004p00509.

Paschmann, G. Recent in-situ observations of magnetic reconnection in near-earth space. *Geophysical Research Letters*, 35(19):n/a–n/a, 2008. ISSN 1944-8007. doi: 10.1029/2008GL035297. L19109.

Paularena, K. I., Richardson, J. D., Kolpak, M. A., Jackson, C. R., and Siscoe, G. L. A dawn-dusk density asymmetry in Earth's magnetosheath. *Journal of Geophysical Research*, 106:25377–25394, November 2001. doi: 10.1029/2000JA000177.

Peng, Z., Wang, C., and Hu, Y. Q. Role of IMF B_x in the solar wind-magnetosphere-ionosphere coupling. *Journal of Geophysical Research (Space Physics)*, 115:A08224, August 2010. doi: 10.1029/2010JA015454.

Petrinec, S. M. and Russell, C. T. Near-Earth magnetotail shape and size as determined from the magnetopause flaring angle. *Journal of Geophysical Research*, 101: 137–152, January 1996. doi: 10.1029/95JA02834.

Petschek, H. E. Magnetic Field Annihilation. *NASA Special Publication*, 50:425, 1964.

Pfau-Kempf, Y., Hietala, H., Milan, S. E., Juusola, L., Hoilijoki, S., Ganse, U., von Alfthan, S., and Palmroth, M. Evidence for transient, local ion foreshocks caused by dayside magnetopause reconnection. *Annales Geophysicae*, 34(11):943–959, 2016. doi: 10.5194/angeo-34-943-2016.

Pfau-Kempf, Y. *Vlasiator – From local to global magnetospheric hybrid-Vlasov simulations*. PhD thesis, University of Helsinki, 2016. URL `http://urn.fi/URN:ISBN:978-952-336-001-3`.

Pokhotelov, O. A., Sagdeev, R. Z., Balikhin, M. A., Onishchenko, O. G., and Fedun, V. N. Nonlinear mirror waves in non-Maxwellian space plasmas. *Journal of Geophysical Research (Space Physics)*, 113:A04225, April 2008. doi: 10.1029/2007JA012642.

Pokhotelov, O. A., Balikhin, M. A., Alleyne, H. S.-C. K., and Onishchenko, O. G. Mirror instability with finite electron temperature effects. *Journal of Geophysical Research: Space Physics*, 105(A2):2393–2401, 2000. ISSN 2156-2202. doi: 10.1029/1999JA900351.

Pomoell, J., Vainio, R., and Kissmann, R. Mhd modeling of coronal large-amplitude waves related to cme lift-off. *Solar Physics*, 253(1):249–261, 2008. ISSN 1573-093X. doi: 10.1007/s11207-008-9186-8.

Powell, K. G., Roe, P. L., Linde, T. J., Gombosi, T. I., and Zeeuw, D. L. D. A solution-adaptive upwind scheme for ideal magnetohydrodynamics. *Journal of Computational Physics*, 154(2):284 – 309, 1999. ISSN 0021-9991. doi: http://dx.doi.org/10.1006/jcph.1999.6299.

Price, C. P., Swift, D. W., and Lee, L.-C. Numerical simulation of nonoscillatory mirror waves at the earth's magnetosheath. *Journal of Geophysical Research: Space Physics*, 91(A1):101–112, 1986. ISSN 2156-2202. doi: 10.1029/JA091iA01p00101.

Pritchett, P. L. Particle-in-Cell Simulation of Plasmas - A Tutorial. In Büchner, J., Dum, C., and Scholer, M., editors, *Space Plasma Simulation*, volume 615 of *Lecture Notes in Physics, Berlin Springer Verlag*, pages 1–24, 2003.

Pulkkinen, T. Space weather: Terrestrial perspective. *Living Reviews in Solar Physics*, 4(1):1, 2007. ISSN 1614-4961. doi: 10.12942/lrsp-2007-1.

Raeder, J. Flux transfer events: 1. generation mechanism for strong southward imf. *Annales Geophysicae*, 24(1):381–392, 2006. doi: 10.5194/angeo-24-381-2006.

Raeder, J., Berchem, J., and Ashour-Abdalla, M. The Geospace Environment Modeling Grand Challenge: Results from a Global Geospace Circulation Model. *Journal of Geophysical Research*, 103:14787–14798, July 1998. doi: 10.1029/98JA00014.

Raeder, J. *Global Magnetohydrodynamics — A Tutorial*, pages 212–246. Springer Berlin Heidelberg, Berlin, Heidelberg, 2003. ISBN 978-3-540-36530-3. doi: 10.1007/3-540-36530-3_11.

Raeder, J., Larson, D., Li, W., Kepko, E. L., and Fuller-Rowell, T. Openggcm simulations for the themis mission. *Space Science Reviews*, 141(1):535–555, 2008. ISSN 1572-9672. doi: 10.1007/s11214-008-9421-5.

Remya, B., Reddy, R. V., Tsurutani, B. T., Lakhina, G. S., and Echer, E. Ion temperature anisotropy instabilities in planetary magnetosheaths. *Journal of Geophysical Research: Space Physics*, 118(2):785–793, 2013. ISSN 2169-9402. doi: 10.1002/jgra.50091.

Rijnbeek, R. P., Cowley, S. W. H., Southwood, D. J., and Russell, C. T. A survey of dayside flux transfer events observed by ISEE 1 and 2 magnetometers. *Journal of Geophysical Research*, 89:786–800, February 1984. doi: 10.1029/JA089iA02p00786.

Roe, P. Approximate riemann solvers, parameter vectors, and difference schemes. *Journal of Computational Physics*, 43(2):357 – 372, 1981. ISSN 0021-9991. doi: http://dx.doi.org/10.1016/0021-9991(81)90128-5.

Russell, C. T. and Elphic, R. C. Initial ISEE magnetometer results - Magnetopause observations. *Space Sci. Rev.*, 22:681–715, December 1978. doi: 10.1007/BF00212619.

Russell, C. T. and Elphic, R. C. ISEE observations of flux transfer events at the dayside magnetopause. *Geophysical Research Letters*, 6:33–36, January 1979. doi: 10.1029/GL006i001p00033.

Russell, C. T., Luhmann, J. G., Elphic, R. C., Southwood, D. J., and Smith, M. F. Upstream waves simultaneously observed by ISEE and UKS. *Journal of Geophysical Research*, 92:7354–7362, July 1987a. doi: 10.1029/JA092iA07p07354.

Russell, C. T., Riedler, W., Schwingenschuh, K., and Yeroshenko, Y. Mirror instability in the magnetosphere of Comet Halley. *Geophysical Research Letters*, 14:644–647, June 1987b. doi: 10.1029/GL014i006p00644.

Russell, C. T., Song, P., and Lepping, R. P. The Uranian magnetopause - Lessons from earth. *Geophysical Research Letters*, 16:1485–1488, December 1989. doi: 10.1029/GL016i012p01485.

Scholer, M. Magnetic flux transfer at the magnetopause based on single X line bursty reconnection. *Geophysical Research Letters*, 15:291–294, April 1988. doi: 10.1029/GL015i004p00291.

Schwartz, S. J., Burgess, D., and Moses, J. J. Low-frequency waves in the Earth's magnetosheath: present status. *Annales Geophysicae*, 14:1134–1150, November 1996. doi: 10.1007/s00585-996-1134-z.

Sgro, A. G. and Nielson, C. W. Hybrid model studies of ion dynamics and magnetic field diffusion during pinch implosions. *Physics of Fluids*, 19(1):126–133, 1976. doi: http://dx.doi.org/10.1063/1.861309.

Shue, J.-H., Chao, J. K., Fu, H. C., Russell, C. T., Song, P., Khurana, K. K., and Singer, H. J. A new functional form to study the solar wind control of the magnetopause size and shape. *Journal of Geophysical Research*, 102:9497–9512, May 1997. doi: 10.1029/97JA00196.

Shue, J.-H., Song, P., Russell, C. T., Steinberg, J. T., Chao, J. K., Zastenker, G., Vaisberg, O. L., Kokubun, S., Singer, H. J., Detman, T. R., and Kawano, H. Magnetopause location under extreme solar wind conditions. *Journal of Geophysical Research*, 103:17691–17700, August 1998. doi: 10.1029/98JA01103.

Sibeck, D. G. and Omidi, N. Flux transfer events: Motion and signatures. *Journal of Atmospheric and Solar-Terrestrial Physics*, 87:20–24, October 2012. doi: 10.1016/j.jastp.2011.07.010.

Siscoe, G. L. and Cummings, W. D. On the cause of geomagnetic bays. *Planet. Space Sci.*, 17:1795–1802, October 1969. doi: 10.1016/0032-0633(69)90055-5.

Sonnerup, B. U. Ö. and Scheible, M. Minimum and Maximum Variance Analysis. *ISSI Scientific Reports Series*, 1:185–220, 1998.

Sonnerup, B. U. O. Magnetic-field re-connexion in a highly conducting incompressible fluid. *Journal of Plasma Physics*, 4:161–174, 2 1970. ISSN 1469-7807. doi: 10.1017/S0022377800004888.

Soucek, J. and Escoubet, C. P. Cluster observations of trapped ions interacting with magnetosheath mirror modes. *Annales Geophysicae*, 29(6):1049–1060, 2011. doi: 10.5194/angeo-29-1049-2011.

Soucek, J., Lucek, E., and Dandouras, I. Properties of magnetosheath mirror modes observed by Cluster and their response to changes in plasma parameters. *Journal of Geophysical Research (Space Physics)*, 113:A04203, April 2008. doi: 10.1029/2007JA012649.

Soucek, J., Escoubet, C. P., and Grison, B. Magnetosheath plasma stability and ULF wave occurrence as a function of location in the magnetosheath and upstream bow shock parameters. *Journal of Geophysical Research (Space Physics)*, 120:2838–2850, April 2015. doi: 10.1002/2015JA021087.

Southwood, D. J. and Kivelson, M. G. Mirror instability. I - Physical mechanism of linear instability. *Journal of Geophysical Research*, 98:9181–9187, June 1993. doi: 10.1029/92JA02837.

Southwood, D. J., Saunders, M. A., Dunlop, M. W., Mier-Jedrzejowicz, W. A. C., and Rijnbeek, R. P. A survey of flux transfer events recorded by the UKS spacecraft magnetometer. *Planetary and Space Science*, 34:1349–1359, December 1986. doi: 10.1016/0032-0633(86)90071-1.

Southwood, D. J., Farrugia, C. J., and Saunders, M. A. What are flux transfer events? *Planetary and Space Science*, 36:503–508, May 1988. doi: 10.1016/0032-0633(88)90109-2.

Stone, E. C., Frandsen, A. M., Mewaldt, R. A., Christian, E. R., Margolies, D., Ormes, J. F., and Snow, F. The Advanced Composition Explorer. *Space Science Reviews*, 86:1–22, July 1998. doi: 10.1023/A:1005082526237.

Stone, R. G. and Tsurutani, B. T. Collisionless shocks in the heliosphere: A tutorial review. *Washington DC American Geophysical Union Geophysical Monograph Series*, 34, 1985. doi: 10.1029/GM034.

Sweet, P. A. The Neutral Point Theory of Solar Flares. In Lehnert, B., editor, *Electromagnetic Phenomena in Cosmical Physics*, volume 6 of *IAU Symposium*, page 123, 1958.

Swift, D. W. Use of a hybrid code to model the Earth's magnetosphere. *Geophysical Research Letters*, 22:311–314, February 1995. doi: 10.1029/94GL03082.

Swisdak, M. and Drake, J. F. Orientation of the reconnection X-line. *Geophysical Research Letters*, 34:L11106, June 2007. doi: 10.1029/2007GL029815.

Swisdak, M., Rogers, B. N., Drake, J. F., and Shay, M. A. Diamagnetic suppression of component magnetic reconnection at the magnetopause. *Journal of Geophysical Research (Space Physics)*, 108:1218, May 2003. doi: 10.1029/2002JA009726.

Tajiri, M. Propagation of hydromagnetic waves in collisionless plasma. ii. kinetic approach. *Journal of the Physical Society of Japan*, 22(6):1482–1494, 1967. doi: 10.1143/JPSJ.22.1482.

Tan, B., Lin, Y., Perez, J. D., and Wang, X. Y. Global-scale hybrid simulation of dayside magnetic reconnection under southward imf: Structure and evolution of reconnection. *Journal of Geophysical Research: Space Physics*, 116(A2):n/a–n/a, 2011. ISSN 2156-2202. doi: 10.1029/2010JA015580. A02206.

Tanaka, T. The state transition model of the substorm onset. *Journal of Geophysical Research: Space Physics*, 105(A9):21081–21096, 2000. ISSN 2156-2202. doi: 10.1029/2000JA900061.

Tátrallyay, M. and Erdős, G. The evolution of mirror mode fluctuations in the terrestrial magnetosheath. *Planetary and Space Science*, 50:593–599, April 2002. doi: 10.1016/S0032-0633(02)00038-7.

Tátrallyay, M. and Erdős, G. Statistical investigation of mirror type magnetic field depressions observed by ISEE-1. *Planetary and Space Science*, 53:33–40, January 2005. doi: 10.1016/j.pss.2004.09.026.

Tátrallyay, M., Erdős, G., Balogh, A., and Dandouras, I. The evolution of mirror type magnetic fluctuations in the magnetosheath based on multipoint observations. *Advances in Space Research*, 41(10):1537 – 1544, 2008. ISSN 0273-1177. doi: http://dx.doi.org/10.1016/j.asr.2007.03.039.

Tátrallyay, M., Erdős, G., Dandouras, I., and Georgescu, E. *On the Growth of Mirror Mode Waves in the Magnetosheath Based on Cluster Observations*, pages 377–385. 2010. doi: 10.1007/978-90-481-3499-1_26.

Temmer, M., Rollett, T., Möstl, C., Veronig, A. M., Vršnak, B., and Odstrčil, D. Influence of the Ambient Solar Wind Flow on the Propagation Behavior of Interplanetary Coronal Mass Ejections. *The Astrophysical Journal*, 743:101, December 2011. doi: 10.1088/0004-637X/743/2/101.

Tóth, G., Jia, X., Markidis, S., Peng, I. B., Chen, Y., Daldorff, L. K. S., Tenishev, V. M., Borovikov, D., Haiducek, J. D., Gombosi, T. I., Glocer, A., and Dorelli, J. C. Extended magnetohydrodynamics with embedded particle-in-cell simulation of Ganymede's magnetosphere. *Journal of Geophysical Research (Space Physics)*, 121:1273–1293, February 2016. doi: 10.1002/2015JA021997.

Trattner, K. J., Mulcock, J. S., Petrinec, S. M., and Fuselier, S. A. Probing the boundary between antiparallel and component reconnection during southward interplanetary magnetic field conditions. *Journal of Geophysical Research (Space Physics)*, 112:A08210, August 2007. doi: 10.1029/2007JA012270.

Trattner, K. J., Petrinec, S. M., Fuselier, S. A., and Phan, T. D. The location of reconnection at the magnetopause: Testing the maximum magnetic shear model with THEMIS observations. *Journal of Geophysical Research (Space Physics)*, 117: A01201, January 2012. doi: 10.1029/2011JA016959.

Trávníček, P., Hellinger, P., Taylor, M. G. G. T., Escoubet, C. P., Dandouras, I., and Lucek, E. Magnetosheath plasma expansion: Hybrid simulations. *Geophysical Research Letters*, 34:L15104, August 2007. doi: 10.1029/2007GL029728.

Trenchi, L., Marcucci, M. F., and Fear, R. C. The effect of diamagnetic drift on motion of the dayside magnetopause reconnection line. *Geophysical Research Letters*, 42: 6129–6136, August 2015. doi: 10.1002/2015GL065213.

Trenchi, L., Fear, R. C., Trattner, K. J., Mihaljcic, B., and Fazakerley, A. N. A sequence of flux transfer events potentially generated by different generation mechanisms. *Journal of Geophysical Research (Space Physics)*, 121:8624–8639, September 2016. doi: 10.1002/2016JA022847.

Tsurutani, B. T., Smith, E. J., Anderson, R. R., Ogilvie, K. W., Scudder, J. D., Baker, D. N., and Bame, S. J. Lion roars and nonoscillatory drift mirror waves in the magnetosheath. *Journal of Geophysical Research*, 87:6060–6072, August 1982. doi: 10.1029/JA087iA08p06060.

Tsurutani, B. T., Smith, E. J., Gonzalez, W. D., Tang, F., and Akasofu, S. I. Origin of interplanetary southward magnetic fields responsible for major magnetic storms near solar maximum (1978-1979). *Journal of Geophysical Research*, 93:8519–8531, August 1988. doi: 10.1029/JA093iA08p08519.

Tóth, G., van der Holst, B., Sokolov, I. V., Zeeuw, D. L. D., Gombosi, T. I., Fang, F., Manchester, W. B., Meng, X., Najib, D., Powell, K. G., Stout, Q. F., Glocer, A., Ma, Y.-J., and Opher, M. Adaptive numerical algorithms in space weather modeling. *Journal of Computational Physics*, 231(3):870 – 903, 2012. ISSN 0021-9991. doi: http://dx.doi.org/10.1016/j.jcp.2011.02.006. Special Issue: Computational Plasma PhysicsSpecial Issue: Computational Plasma Physics.

Vaivads, A., Khotyaintsev, Y., André, M., Retinò, A., Buchert, S. C., Rogers, B. N., Décréau, P., Paschmann, G., and Phan, T. D. Structure of the magnetic reconnection diffusion region from four-spacecraft observations. *Phys. Rev. Lett.*, 93:105001, Aug 2004. doi: 10.1103/PhysRevLett.93.105001.

Valentini, F., Trávníček, P., Califano, F., Hellinger, P., and Mangeney, A. A hybrid-Vlasov model based on the current advance method for the simulation of collisionless magnetized plasma. *Journal of Computational Physics*, 225:753–770, July 2007. doi: 10.1016/j.jcp.2007.01.001.

Volwerk, M., Schmid, D., Tsurutani, B. T., Delva, M., Plaschke, F., Narita, Y., Zhang, T., and Glassmeier, K.-H. Mirror mode waves in Venus's magnetosheath: solar minimum vs. solar maximum. *Annales Geophysicae*, 34:1099–1108, November 2016. doi: 10.5194/angeo-34-1099-2016.

von Alfthan, S., Pokhotelov, D., Kempf, Y., Hoilijoki, S., Honkonen, I., Sandroos, A., and Palmroth, M. Vlasiator: First global hybrid-Vlasov simulations of Earth's foreshock and magnetosheath. *Journal of Atmospheric and Solar-Terrestrial Physics*, 120:24–35, December 2014. doi: 10.1016/j.jastp.2014.08.012.

Walsh, B. M., Sibeck, D. G., Wang, Y., and Fairfield, D. H. Dawn-dusk asymmetries in the Earth's magnetosheath. *Journal of Geophysical Research (Space Physics)*, 117:A12211, December 2012. doi: 10.1029/2012JA018240.

Walsh, B. M., Sibeck, D. G., Nishimura, Y., and Angelopoulos, V. Statistical analysis of the plasmaspheric plume at the magnetopause. *Journal of Geophysical Research (Space Physics)*, 118:4844–4851, August 2013. doi: 10.1002/jgra.50458.

Walsh, B. M., Foster, J. C., Erickson, P. J., and Sibeck, D. G. Simultaneous ground- and space-based observations of the plasmaspheric plume and reconnection. *Science*, 343(6175):1122–1125, 2014. ISSN 0036-8075. doi: 10.1126/science.1247212.

Wang, S., Kistler, L. M., Mouikis, C. G., and Petrinec, S. M. Dependence of the dayside magnetopause reconnection rate on local conditions. *Journal of Geophysical Research (Space Physics)*, 120:6386–6408, August 2015. doi: 10.1002/2015JA021524.

White, L. and Adcroft, A. A high-order finite volume remapping scheme for nonuniform grids: The piecewise quartic method (PQM). *Journal of Computational Physics*, 227(15):7394 – 7422, 2008. ISSN 0021-9991. doi: http://dx.doi.org/10.1016/j.jcp.2008.04.026.

Wiltberger, M., Lotko, W., Lyon, J. G., Damiano, P., and Merkin, V. Influence of cusp o+ outflow on magnetotail dynamics in a multifluid mhd model of the magnetosphere. *Journal of Geophysical Research: Space Physics*, 115(A10):n/a–n/a, 2010. ISSN 2156-2202. doi: 10.1029/2010JA015579. A00J05.

Winske, D., Yin, L., Omidi, N., and et al. Hybrid Simulation Codes: Past, Present and Future - A Tutorial. In Büchner, J., Dum, C., and Scholer, M., editors, *Space Plasma Simulation*, volume 615 of *Lecture Notes in Physics, Berlin Springer Verlag*, pages 136–165, 2003.

Yeates, A. R. and Hornig, G. A generalized flux function for three-dimensional magnetic reconnection. *Physics of Plasmas*, 18(10):102118, 2011. doi: http://dx.doi.org/10.1063/1.3657424.

Zerroukat, M. and Allen, T. A three-dimensional monotone and conservative semi-lagrangian scheme (SLICE-3D) for transport problems. *Quarterly Journal of the Royal Meteorological Society*, 138(667):1640–1651, 2012. ISSN 1477-870X. doi: 10.1002/qj.1902.

Zhang, B., Brambles, O. J., Wiltberger, M., Lotko, W., Ouellette, J. E., and Lyon, J. G. How does mass loading impact local versus global control on dayside reconnection? *Geophysical Research Letters*, 43:1837–1844, March 2016. doi: 10.1002/2016GL068005.

Zhu, C. B., Zhang, H., Ge, Y. S., Pu, Z. Y., Liu, W. L., Wan, W. X., Liu, L. B., Chen, Y. D., Le, H. J., and Wang, Y. F. Dipole tilt angle effect on magnetic reconnection locations on the magnetopause. *Journal of Geophysical Research: Space Physics*, 120 (7):5344–5354, 2015. ISSN 2169-9402. doi: 10.1002/2015JA020989. 2015JA020989.

Paper I

Mirror modes in the Earth's magnetosheath:
Results from a global hybrid-Vlasov simulation

Journal of Geophysical Research: Space Physics
volume 121, 2016
doi:10.1002/2015JA022026

AGU PUBLICATIONS

JGR

Journal of Geophysical Research: Space Physics

RESEARCH ARTICLE
10.1002/2015JA022026

Key Points:
- We observe mirror mode waves in quasi-perpendicular magnetosheath in global hybrid-Vlasov simulation
- Most activities are observed along streamlines entering the sheath near foreshock ULF wave boundary
- The area of the sheath showing mirror mode activity is highly dependent on the selection criteria

Correspondence to:
S. Hoilijoki,
sanni.hoilijoki@fmi.fi

Citation:
Hoilijoki, S., M. Palmroth, B. M. Walsh, Y. Pfau-Kempf, S. von Alfthan, U. Ganse, O. Hannuksela, and R. Vainio (2016), Mirror modes in the Earth's magnetosheath: Results from a global hybrid-Vlasov simulation, *J. Geophys. Res. Space Physics*, *121*, doi:10.1002/2015JA022026.

Received 12 OCT 2015
Accepted 13 MAR 2016
Accepted article online 9 MAY 2016

Mirror modes in the Earth's magnetosheath: Results from a global hybrid-Vlasov simulation

Sanni Hoilijoki[1,2], Minna Palmroth[1], Brian M. Walsh[3], Yann Pfau-Kempf[1,2], Sebastian von Alfthan[4], Urs Ganse[2], Otto Hannuksela[5], and Rami Vainio[6]

[1]Finnish Meteorological Institute, Helsinki, Finland, [2]Department of Physics, University of Helsinki, Helsinki, Finland, [3]Mechanical Engineering and Center for Space Physics, Boston University, Boston, Massachusetts, USA, [4]CSC, Espoo, Finland, [5]Department of Physics, Chinese University of Hong Kong, Shatin, New Territories, Hong Kong, [6]Department of Physics and Astronomy, University of Turku, Turku, Finland

Abstract We investigate mirror mode structures in the Earth's magnetosheath using our global kinetic Vlasiator simulation, which models ion behavior through their distribution function and treats electrons as a charge-neutralizing fluid. We follow the evolution of waves as they advect along velocity streamlines through the magnetosheath. We find that mirror mode waves are observed preferentially in the quasi-perpendicular magnetosheath along velocity streamlines that enter the sheath in the vicinity of the foreshock ULF wave boundary where there are enough initial perturbations in the plasma for the mirror modes to grow, and the plasma properties fulfill the mirror instability condition better than elsewhere in the magnetosheath. We test selection criteria defined by previous studies and show that the spatial extent over which mirror modes occur ranges from much of the magnetosheath on the quasi-perpendicular side of the subsolar point to very small isolated regions depending on the criteria.

1. Introduction

The Earth's magnetosheath is a turbulent region of shocked plasma bounded on the upstream side by the bow shock and the magnetopause on the downstream side. In regions where the interplanetary magnetic field (IMF) is quasi-parallel to the bow shock normal, a foreshock forms upstream of the boundary. On the quasi-parallel bow shock side, the magnetosheath becomes turbulent partly due to the foreshock wave activity [*Denton*, 2000]. The quasi-perpendicular magnetosheath, however, is not as turbulent, and many different low-frequency wave modes have been observed [e.g., *McKean et al.*, 1992; *Schwartz et al.*, 1996]. The passage through the quasi-perpendicular bow shock into the magnetosheath gives rise to a temperature anisotropy in the magnetosheath. This anisotropy is related to the excitation of two low-frequency wave modes, left-handed proton cyclotron waves, and linearly polarized mirror mode waves. Mirror modes are nonpropagating compressional waves with anticorrelation between magnetic field and plasma density [*Hasegawa*, 1969]. According to both observations and simulations [*Gary*, 1992; *Lacombe and Belmont*, 1995; *Samsonov et al.*, 2007; *Tátrallyay et al.*, 2010] the proton cyclotron instability dominates when the ratio between kinetic and thermal pressure (β) is relatively low and when the ratio between the perpendicular and parallel temperature is larger than 1 ($T_\perp/T_\parallel > 1$). On the other hand, the condition where $\beta_\parallel > 1$ and $T_\perp/T_\parallel$ close to 1 is favorable for the growth of mirror modes. The criterion for mirror unstable plasma can be derived assuming cold electrons and bi-Maxwellian ions [*Hasegawa*, 1969]:

$$\frac{T_\perp}{T_\parallel} > 1 + \frac{1}{\beta_\perp} \tag{1}$$

where $\beta_\perp$ is the ratio of thermal and magnetic pressures calculated from the perpendicular ion temperature. In addition to the mirror modes, the density and magnetic field also anticorrelate in connection to the slow mode (ion acoustic) waves. Thus, merely the anticorrelation of the plasma density and the magnetic field is not a sufficient condition for identifying mirror mode waves among all the different low-frequency wave modes.

Nonpropagating mirror modes are observed as waves that are linearly polarized along the background magnetic field [e.g., *Génot et al.*, 2001]. However, the solar wind pushing toward the magnetopause creates strong gradients in density and/or magnetic field that may cause the mirror modes to drift in the plasma frame

[e.g., *Omidi and Winske*, 1995; *Génot et al.*, 2001]. The drift velocity of the mirror modes changes the polarization of the waves. *Génot et al.* [2001] reported that most of the mirror mode events observed were not linearly but elliptically polarized. However, linear polarization has been widely used as a criterion to identify the mirror mode events among other low-frequency waves, especially, slow mode waves [e.g., *Tátrallyay and Erdós*, 2005; *Soucek et al.*, 2008; *Génot et al.*, 2009]. In this current study we vary the identification criteria and show how this impacts the selection.

Mirror modes can be observed as quasi-sinusoidal oscillations, but more often they are observed as trains of either local enhancements or depressions in magnetic field strength (peaks or dips, respectively) [e.g., *Soucek et al.*, 2008; *Génot et al.*, 2009]. Behind the bow shock, where plasma is mirror unstable (i.e., satisfies the mirror instability condition given in equation (1)), the structures appear mostly as peaks. Therefore, the peaks are thought to be the early stage of the mirror modes and they populate mainly the middle magnetosheath [*Soucek et al.*, 2008]. The plasma becomes mirror stable a few Earth radii (R_E) from the magnetopause surface, and this affects the structure of the mirror modes; the peaks evolve to dips. In the mirror stable plasma the mirror modes are observed as dips [*Soucek et al.*, 2008; *Génot et al.*, 2011]. The formation of peaks and dips have been also studied using local simulations [e.g., *Califano et al.*, 2008; *Shoji et al.*, 2012]. *Califano et al.* [2008] performed numerical simulations of Vlasov-Maxwell equations using a hybrid particle-in-cell (PIC) code. Their simulations showed that peaks form as a result of nonlinear saturation of mirror modes. The peaks may evolve to dips when the plasma is far beyond the mirror instability threshold and β is low enough. *Shoji et al.* [2012] also studied the relation between the magnetic structures and the instability by using both 2-D and 3-D open boundary simulations. They found that in high β simulations peaks were formed in both 2-D and 3-D simulations, whereas in low β 2-D simulations mirror structures developed into dips. Using the same plasma parameters in 3-D simulations produced structures which evolved into peaks. *Shoji et al.* [2012] explained this result by noting that in low $\beta_{\parallel}$ plasma, parallel velocities are small and particles tend to have pitch angles close to 90°. The particles with pitch angles near 90° are more easily trapped in magnetic dips than in high β plasma. Additionally, 3-D simulations have nonuniformities in the out-of-plane direction which are not included in 2-D simulations.

Recently, statistical studies of mirror mode events have emerged using many years of spacecraft data [*Soucek et al.*, 2015; *Dimmock et al.*, 2015]. *Dimmock et al.* [2015] found a dawn-dusk asymmetry in the ion temperature anisotropy and therefore also in the observed mirror mode activity by using 6 years of Time History of Events and Macroscale Interactions during Substorms (THEMIS) observations. The level of the asymmetry depends on the solar wind Alfvén Mach number (M_A) and the distance from the magnetopause; the higher M_A and the smaller the distance, the weaker is the asymmetry. Additionally, *Dimmock et al.* [2015] reported that as M_A increases more mirror modes are observed as dips instead of peaks. Using 2 years of Cluster observations, *Soucek et al.* [2015] found that mirror mode waves more likely exist in the quasi-perpendicular magnetosheath and very rarely in the quasi-parallel magnetosheath. They also see the dependence on the M_A; during higher M_A mirror mode activity is higher.

Tátrallyay and Erdós [2002] observed the amplitude of the mirror waves to increase with the increasing distance from the bow shock by using measurements made by ISEE 1 and ISEE 2 spacecraft. They also calculated the growth rate using the observations and a model of *Kobel and Fluckiger* [1994], which estimates the plasma flow lines used to approximate the propagation time of the mirror mode waves frozen in the plasma. The growth rate approximation assumes that the mirror waves grow as $\delta B \sim \exp(\gamma_B t)$, where δB is the magnetic field perturbation amplitude, γ_B is the growth rate, and t is time. Their result for the growth rate was $0.002\ \mathrm{s}^{-1} < \gamma_B < 0.0035\ \mathrm{s}^{-1}$. Similarly, using Cluster measurements, *Tátrallyay et al.* [2010] estimated the growth rate of the mirror modes to about $\gamma_B = 0.001 - 0.008\ \mathrm{s}^{-1}$. The authors point out that the results are almost an order of magnitude smaller than what they get by using the results based on fully kinetic linear Vlasov dispersion theory by *Gary et al.* [1993] and *Hubert et al.* [1998] ($\gamma_{\max} = 0.03\ \mathrm{s}^{-1} - 0.06\ \mathrm{s}^{-1}$), and the analytical solution by *Liu et al.* [2006] ($\gamma_{\max} = 0.001\ \mathrm{s}^{-1} - 0.03\ \mathrm{s}^{-1}$) with the measured plasma parameters.

The theoretical shape and evolution of the ion distribution functions and their kinetic effects on the mirror structures have been widely discussed [e.g., *Southwood and Kivelson*, 1993; *Kivelson and Southwood*, 1996; *Pokhotelov et al.*, 2008, 2010]. They have also been studied using local simulations [e.g., *Califano et al.*, 2008] and spacecraft observations [e.g., *Soucek and Escoubet*, 2011]. *Southwood and Kivelson* [1993] and *Kivelson and Southwood* [1996] discuss the importance of trapped particles in the development and saturation of the mirror mode waves. Using a linear approach, *Southwood and Kivelson* [1993] show that locally trapped particles

with small parallel velocities (i.e., 90° pitch angle), which are resonant with the mirror wave, are important in the evolution of the mirror structure. The magnetic moment of the particles is conserved and as the mirror structures grow, the magnetic field increases in the crests and decreases in the troughs. In the decreasing magnetic field particles with small $v_{\parallel}$ (~0) are decelerated, and in the increasing field they are accelerated due to betatron acceleration. By using quasi-linear theory, *Kivelson and Southwood* [1996] present the role of Fermi acceleration in cooling/heating of trapped ions. In the troughs the particles with $v_{\parallel} \sim 0$ are cooled because their mirror points move farther away from each other as the waves develop and the amplitude increases and/or their magnetic moment is conserved. Similarly, the trapped ions with intermediate pitch angles are accelerated since their mirror points move closer to each other. The role of the trapped particles in the mirror instability saturation is significant [*Kivelson and Southwood*, 1996; *Califano et al.*, 2008; *Pokhotelov et al.*, 2008, 2010]. *Pokhotelov et al.* [2008, 2010] discuss the flattening of the background distribution functions at small parallel velocities due to the motion of the resonant particles in the case of magnetic dips. The width of the flattened region is comparable to the size of the particle trapping zone of the dip.

Previously, mirror modes have been studied in a global simulation by *Herčík et al.* [2013] who used 3-D hybrid particle-in-cell (PIC) simulation. They simulated a down-scaled Hermean magnetosphere during both southward and northward IMF. The work identified the mirror modes by calculating the Pearson correlation coefficient between magnetic field strength and density, β, temperature anisotropy, instability condition, and spatial Fourier transform. They found that in the magnetosheath the mirror modes exist preferably behind the quasi-perpendicular bow shock or close to the magnetopause behind the quasi-parallel bow shock. In addition, *Herčík et al.* [2013] found that a dawn-dusk asymmetry forms in the equatorial plane during southward and northward IMF. β and temperature were larger on the dawnside and thus asymmetry is also seen in the mirror mode activity favoring dawn during southward IMF and dusk during northward. The authors suggested that the asymmetry is caused by local kinetic effect at the bow shock and drifts in the magnetosheath.

The effect of the mirror modes on the global magnetospheric physics is not yet fully known due to difficulties of producing a global view of the mirror mode structures from local observations. However, there are indications that the mirror modes may affect the dayside magnetopause reconnection by making it spatially and temporally varying [*Laitinen et al.*, 2010]. Additionally, depending on the solar wind parameters the mirror mode activity can cover large regions from the quasi-perpendicular magnetosheath [*Soucek et al.*, 2015; *Dimmock et al.*, 2015], indicating that they may have a significant global effect. Here we present the first attempt to investigate the formation and propagation of the mirror modes on the Earth's magnetosheath on the global scale, utilizing the novel hybrid-Vlasov simulation Vlasiator (http://vlasiator.fmi.fi). This paper is organized as follows: First, in section 2 we present Vlasiator and the methods we apply to analyze and identify the mirror mode waves in the magnetosheath. Next, we present the results from our simulations in section 3. Finally, we discuss the results and conclude our study in section 4.

2. Vlasiator

Vlasiator is a global hybrid-Vlasov simulation code [*von Alfthan et al.*, 2014], with a main target to self-consistently model kinetic physics in the near-Earth space. In Vlasiator, protons are described with a 6-D distribution function propagated in time by solving the Vlasov equation using a semi-Lagrangian method [*Zerroukat and Allen*, 2012] with a fifth-order accurate reconstruction [*White and Adcroft*, 2008]. Electrons are described as massless charge-neutralizing fluid using magnetohydrodynamic equations. The Vlasov solver is coupled to the electromagnetic fields self-consistently using the method described in *Londrillo and Del Zanna* [2004] offering divergence-free solutions if the initial and boundary conditions are divergence free. For more technical details, see *von Alfthan et al.* [2014]. In contrast to the runs presented in *von Alfthan et al.* [2014] and *Kempf et al.* [2015] the Hall term has been included in the Ohm's law.

In this paper we present a 5-D run, where the 2-D ordinary space is the equatorial plane, while the velocity space is 3-D. Each cell of the ordinary spatial mesh contains a 3-D velocity mesh. The solar wind flows in from the sunward wall $+x$ in GSE of the simulation box, where all the cells have a static Maxwellian ion velocity distribution. The opposite wall and the y direction have copy boundary conditions, which allow the plasma and fields to flow out of the simulation domain while periodic boundaries are applied out of the plane in the z direction. At a spherical shell of 5 R_E centered around the origin the distribution function is set to a stationary state, and the perturbed component of the magnetic field is set to zero. For the Earth's magnetic field the full

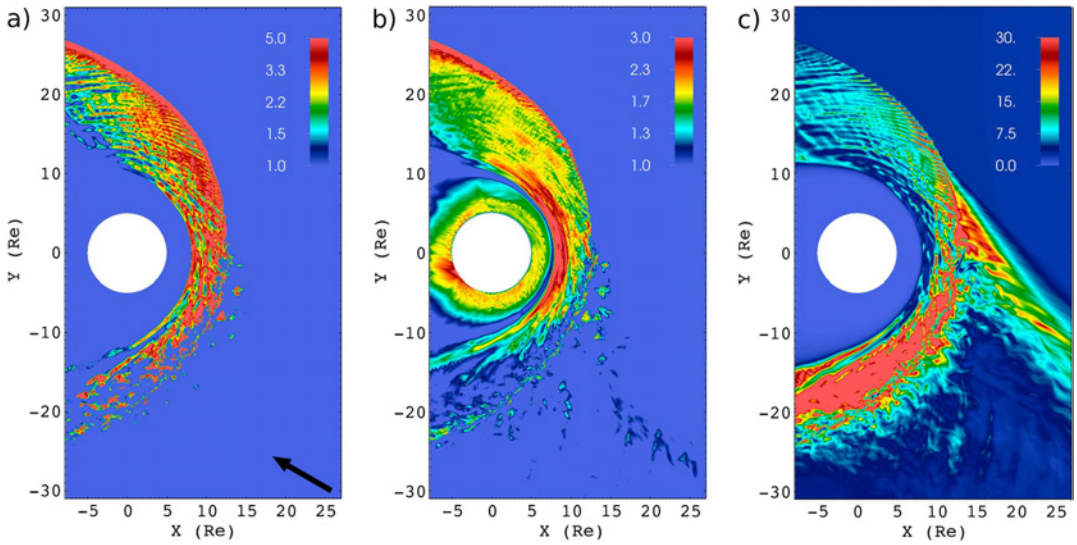

Figure 1. (a) Mirror instability condition in the form $\beta_\perp(T_\perp/T_\parallel - 1)$. The instability condition is fulfilled in the regions with values above 1. The black arrow shows the IMF direction. (b) Ion temperature anisotropy ($T_\perp/T_\parallel$). (c) Plasma β. The snapshots are at $t = 500$ s.

magnetic moment of the Earth's dipole field is used. This is an important distinction to current PIC simulations, where the dipole is typically scaled down preventing direct performance comparisons to Vlasiator.

3. Results

3.1. Description of the Run

The run has a 30° IMF cone angle with IMF components as $B_x = -4.33$ nT and $B_y = 2.5$ nT yielding a total magnetic field strength of 5 nT, and other upstream parameters are chosen to be proton number density $n = 1$ cm^{-3}, plasma velocity $v = 750$ km/s, and the temperature $T = 0.5$ MK corresponding to an Alfvén Mach number of 6.9. The simulation domain extends from $-7.9\ R_E$ to $46.8\ R_E$ in x (GSE) and $\pm 31.3\ R_E$ in y direction. The spatial resolution is $\Delta x = 228$ km, and the resolution of the velocity grid is $\Delta v = 30$ km/s, and the output is saved every 0.5 s.

Figure 1 shows a global view of the run with (a) the mirror instability condition color coded in the form $R = \beta_\perp(T_\perp/T_\parallel - 1)$, (b) the ion temperature anisotropy, and (c) plasma β. The instability condition is fulfilled in the regions where the value exceeds 1. The black arrow shows the direction of the IMF. There is a clear asymmetry between the quasi-parallel and quasi-perpendicular magnetosheath in both parameters. In the quasi-perpendicular side, the instability condition is large behind the bow shock where the temperature anisotropy is formed. There is also a wing of larger instability condition values extending to the sheath starting from the bow shock close to the ULF wave boundary and the boundary of the quasi-perpendicular shock (at $x = 11.5\ R_E$, $y = 7\ R_E$). The temperature anisotropy is also large, close to the magnetopause. This is caused by the magnetic field draping around the magnetosphere, which can also be seen in the observations [e.g., *Dimmock et al.*, 2015]. However, in our simulations the increase of temperature anisotropy toward the magnetopause is much larger than what is seen in the statistical study of spacecraft observations in the magnetosheath by *Dimmock et al.* [2015]. This is possibly due to a numerical effect of the 2-D simulation as the magnetic field cannot flow around the magnetopause, or in the statistical study where averaging has evened out the largest anisotropy values. β is high in the quasi-parallel magnetosheath and close to the ion foreshock edge. It is lower in the quasi-perpendicular magnetosheath, where, however, variations in β are large. Within $1\ R_E$, β can change from 4 to more than 16, indicating anticorrelated fluctuations in magnetic field strength and density.

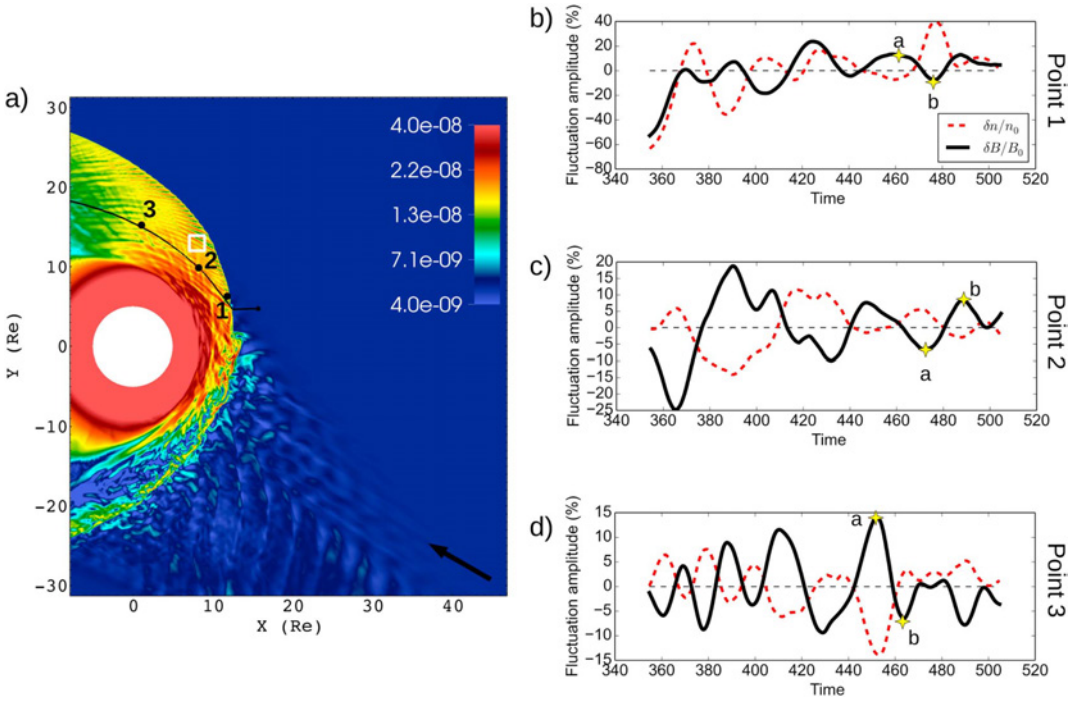

Figure 2. (a) Magnetic field magnitude (T) with a 30° cone angle. The black arrow shows the IMF direction. Numbered dots show the locations of the virtual spacecraft along the velocity streamline (black line). The white square indicates the location where the spatial Fourier transform shown in Figure 5 is performed. (c, d) The amplitude of the number density (red dashed line) and magnetic field strength (black solid line) fluctuations from the virtual spacecraft locations. Yellow stars and labels a and b show the time for the distributions functions shown in Figure 6.

3.2. Wave Properties

Figure 2a shows the global view of the magnetic field strength at time 500 s from the start of the simulation. To evaluate the plasma and wave propagation in the magnetosheath, we investigate the plasma properties along a velocity streamline. The starting point of the velocity streamline in the quasi-perpendicular sheath is chosen such that we measure the wave pattern in the midsheath. The black line in Figure 2a shows the chosen streamline, and the numbered points mark the locations of virtual spacecraft along the streamline. Figures 2b–2d show the fluctuations of the magnetic field strength, proton number density, and velocity measurements from the three points indicated in Figure 2a. The fluctuations are defined as $\delta B/B = (B(t) - \langle B \rangle)/\langle B \rangle$, where $\langle\rangle$ mark the time average over the time period under consideration (from 350 to 510 s = 2.6 min). The period of the anticorrelated structures is 20 s or more in Figures 2b–2d. Thus, to even out fluctuations with shorter periods we have taken a 5 s running average of the raw data.

Virtual spacecraft 1 is located closest to the bow shock and it shows the fluctuations in the magnetic field and plasma density form immediately behind the bow shock. At the location of the virtual spacecraft 2 the magnetic field and the plasma density perturbations are anticorrelated with a Pearson correlation coefficient of −0.8. The maximum amplitude of fluctuations is 20% of the mean averaged background magnetic field and the standard deviation of the fluctuations over the considered time is 9.3%. At virtual spacecraft 3 the amplitude varies between 5% and 15% of the background magnetic field, the standard deviation being 6%. The saturation of the wave amplitude growth takes place after the plasma crosses the virtual spacecraft 2.

Figure 3a shows stacked time series of $|\mathbf{B}|$ along the streamline shown in Figure 2. Time runs in the y axis from bottom toward the top and the x coordinate (in GSE) is given on the x axis. At each time the magnetic field strength is taken along the streamline and color coded. The figure shows that the bow shock edge is at 12 R_E at the beginning of the considered time period, and it extends outward as the simulation time propagates due

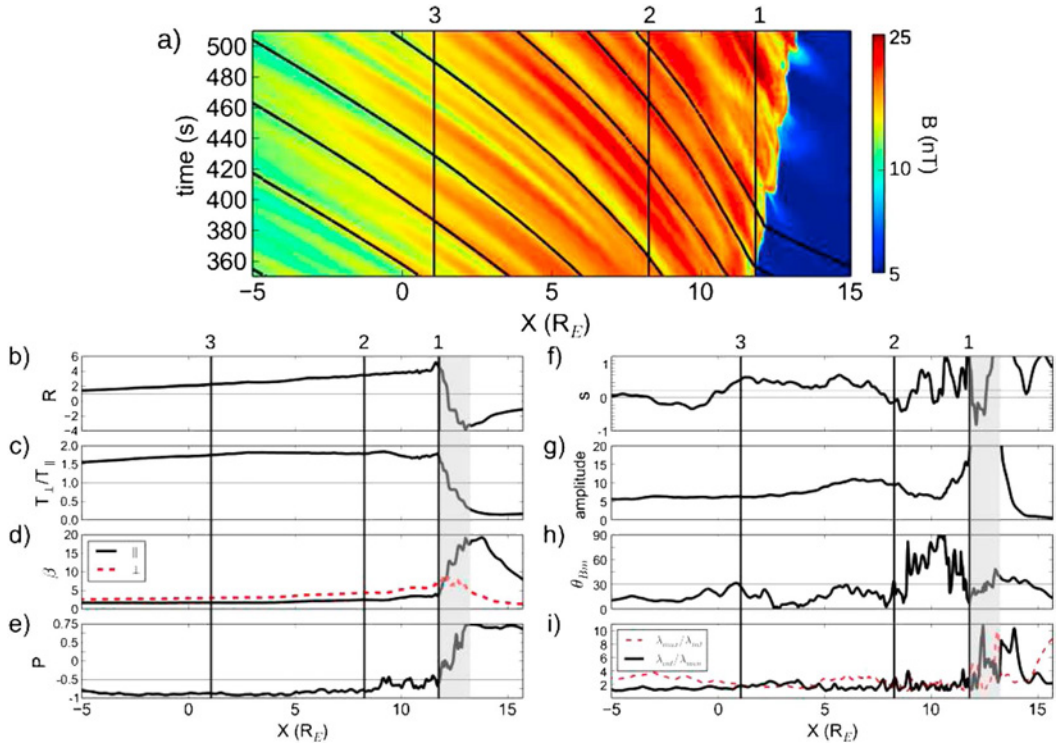

Figure 3. (a) Stacked time series of magnetic field strength along the streamline as shown in Figure 2. The vertical axis shows the time, and the horizontal axis shows the location along the *x* axis (GSE). The color coding indicates the magnetic field strength and the black dots move with the local plasma velocity. (b) The instability condition $R = \beta_\perp(T_\perp/T_\parallel - 1)$; (c) temperature anisotropy $T_\perp/T_\parallel$; (d) parallel and perpendicular components of β; (e) Pearson correlation coefficient (P); (f) skewness (*s*) and the two horizontal lines are at $s = \pm 0.1$, above the higher value the waves can be thought to be peaks, and below the lower value the waves are regarded as dips, (g) amplitude of the fluctuations (standard deviation of magnetic fluctuations); (h) angle between maximum variance direction and the background magnetic field θ_{Bm}; and (i) the ratios of variance matrix eigenvalues along the streamline shown in Figure 2a. Vertical lines show the location of the virtual spacecraft and the gray region shows the distance the bow shock moves during the considered time.

to the magnetic field pileup at the magnetopause. The vertical lines show the location of the virtual spacecraft (discussed above) along the streamline. The black dots show the propagation of the plasma. Initially, dots are located at chosen points along the streamline and then propagated using the local plasma velocity. This is done to compare the magnetic wave propagation and the propagation of plasma. The plasma propagation velocity corresponds well with the wave propagation velocities. This indicates that the waves are advected with the sheath flow and do not propagate relative to the plasma.

Figures 3b–3i show the instability condition, temperature anisotropy, plasma β, Pearson correlation coefficient between magnetic field strength and plasma density, skewness, standard deviation of the magnetic field, angle between maximum variance direction and background magnetic field, and the ratios of the eigenvalues of the variance matrix calculated over time at each point along the streamline. Figures 3b–3d show the instability condition $R = \beta_\perp(T_\perp/T_\parallel - 1)$, $T_\perp/T_\parallel$ and parallel and perpendicular β as an average over the time period 350–510 s at each point. The instability condition is fulfilled at all locations along the plotted streamline in the magnetosheath. The instability condition exhibits higher values at the vicinity of the bow shock, decreasing with distance from the bow shock. The ion temperature anisotropy increases at the bow shock crossing and stays steady along the streamline. The $\beta_\parallel$ increases sharply before the bow shock crossing in the foreshock and then decreases rapidly behind the bow shock, where $\beta_\perp$ is close to 7 and $\beta_\parallel$ is close to 4. Both β components decrease with the distance to the bow shock. Figure 3e shows the Pearson correlation coefficient (P) between magnetic field and plasma density calculated over time at each point separately.

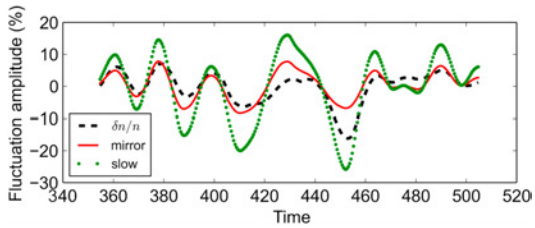

Figure 4. Measured density perturbations (black dashed line) compared to theoretical density perturbation of mirror modes (red solid line) and slow mode waves (green dotted line) from virtual spacecraft 3 marked on Figure 2a.

The correlation coefficients have been calculated using the first-order time derivatives of magnetic field and density in order to remove the effect of the data trend. The correlation coefficient drops below −0.5 at around ~12 R_E meaning that the anticorrelation forms soon after the bow shock crossing in the magnetosheath.

Figure 3f shows the skewness (s) of total magnetic field strength, which is calculated at each point along the streamline over the time period (350–510 s). Skewness indicates whether the mirror mode waves are more like peaks ($s > 0$) or dips ($s < 0$). We use the same limits as *Soucek et al.* [2015]; peaks are those having $s > 0.1$ and dips $s < 0.1$. Peak-like structures populate the midregion of the plotted streamline, and they evolve to dip-like structures close to the end of the streamline. However, the skewness does not grow to either large negative or positive values. This indicates that large isolated peaks or dips do not exist in the simulation. In the quasi-perpendicular flank at few locations close to the back wall, magnetic structures resemble more dip-like structures. However, the majority of the magnetic structures are close to sinusoidal fluctuations.

The two last panels, Figures 3h and 3i, show the results from the minimum variance analysis. When interpreting the results from the minimum variance analysis one has to keep in mind that the method does not work perfectly if multiple wave modes exist simultaneously. Here we use the same minimum variance criteria for the mirror modes as *Soucek et al.* [2008]. Figure 3h is the angle between maximum variance direction and the background magnetic field (θ_{Bm}) and the horizontal line shows the condition for the mirror modes, if $\theta_{Bm} < 30°$ the waves can be mirror modes. Figure 3i shows the results from the minimum variance analysis calculated at each point along the streamline. The red dashed line shows the relation of the maximum and the intermediate variance matrix eigenvalue $\lambda_{max}/\lambda_{int}$ and the black solid line is the relation of the intermediate and the minimum eigenvalue $\lambda_{int}/\lambda_{min}$. The conditions that we chose for the linear polarization ($\lambda_{max}/\lambda_{int} > 1.5$ and $\lambda_{int}/\lambda_{min} < 3.3$, condition 1 from section 3.4) are fulfilled from 9 R_E to the end of the plot. According to other sources the limits of the ratio of the maximum to intermediate eigenvalue should be larger than 5 [e.g., *Génot et al.*, 2001]. Using that as the limit, none of our observed waves fulfills the linear polarization. However, as reported by *Génot et al.* [2001] not all the observed mirror modes in the magnetosheath are linearly polarized. As the mirror modes obtain finite velocity in the plasma frame due to the gradients in the density and/or magnetic field they are no longer observed as linearly polarized waves.

The anticorrelation of the magnetic field strength and plasma density is also present for slow mode waves. Therefore, to verify that our results are mirror modes, we use a second test. We use the method described in *Liu et al.* [2006]. The density fluctuations in the mirror mode waves behave like the following:

$$\frac{\delta n}{n} = -\left(\frac{T_\perp}{T_\parallel} - 1\right)\frac{\delta B}{B} \tag{2}$$

and a similar equation for slow mode waves can be derived assuming highly oblique wave propagation:

$$\frac{\delta n}{n} = -\left(1 + \frac{2}{\beta_\perp}\right)\frac{\delta B}{B}. \tag{3}$$

We apply this calculation for the fluctuations measured by the virtual spacecraft number 3 in Figure 2. We approximate the wave vector direction using the minimum variance analysis, which gives an angle of 84° between the estimated **k** and $\mathbf{B}_0$, which is close to 90°. Therefore, the approximation is valid for our data and the result is shown in Figure 4. The predicted mirror mode fluctuations (red solid line) correspond better to

the measured density fluctuations (black dashed line), while the slow mode estimation (green dotted line) predicts higher amplitude fluctuations.

The growth rate of the mirror instability varies spatially within the magnetosheath as the plasma parameters change, and therefore, one growth rate value cannot be defined to describe the whole magnetosheath. To approximate the rate at which the mirror modes grow at a couple of points along the streamline in the magnetosheath we use the method described in *Tátrallyay et al.* [2010] and compare them to theoretical growth rates. The exception is that they calculate the wave propagation time using a model by *Kobel and Fluckiger* [1994], but with Vlasiator we can get the propagation time directly by following the wave identity from one point to another in time. The growth rate (γ_B) can be approximated with equation:

$$\gamma_B = \frac{\ln\left(\frac{\delta B_2}{\delta B_1}\right)}{t_2 - t_1}. \tag{4}$$

We approximate the rate along the velocity streamline shown in Figure 2a. Some waves grow faster than others, but we use the standard deviation value as an approximation for the fluctuation amplitudes at different points. First, we estimate the growth close to point $x = 10R_E$ on the streamline (Figure 3). Figure 3g shows that the fluctuation amplitude stops decreasing and starts to increase again just before $x = 10R_E$ which could indicate that the mirror instability starts to grow at this point. So for B_1 and t_1 in equation (4) we use values at point $x = 10R_E$ and the B_2 and t_2 are taken from a distance of 1 R_E along the streamline. Times are read by following a wave identity from one point to the other. Mirror modes grow with a rate of 0.002 s^{-1} between these two points. Next, we choose points close to virtual spacecraft 2 (Figure 2), where the mirror modes are close to saturation. Again B_1 and t_1 are taken at spacecraft 2 and B_2 and t_2 from 1 R_E farther along the streamline. At this point the estimated growth rate is 0.005 s^{-1}. From the Cluster observations *Tátrallyay et al.* [2010] calculated rates to be in the range $\gamma_B = 0.001 - 0.008$ s^{-1}. A theoretical growth rate of the mirror instability is then calculated using equation (7) in *Liu et al.* [2006]. At the first point the proton gyrofrequency is $\Omega_p = qB/m_p \approx 1.8$ s^{-1} and the growth rate $\gamma_B \approx 0.1\Omega_p \approx 0.19$ s^{-1} at the second location $\Omega_p = qB/m_p \approx 1.7$ s^{-1} and the growth rate $\gamma_B \approx 0.09\Omega_p \approx 0.16$ s^{-1}.

Figure 5 shows spatial Fourier transforms of (a) total magnetic field, (b) magnetic field on the simulation plane, and (c) B_z from the region marked in Figure 2a. The fluctuations in magnetic field on the simulation plane are the main contributor to the total magnetic field fluctuations. Therefore, their Fourier transforms are almost identical. The wave vector **k** of these fluctuations is highly oblique to the background magnetic field as it is for mirror modes. However, the magnetic fluctuations in B_z seem to propagate in a different direction with **k** almost parallel to the magnetic field. This is a known feature of ion cyclotron waves.

3.3. Velocity Distribution Functions

Vlasiator solves noiseless 3-D ion velocity distribution functions. Distributions have been rotated to coordinates aligned to the magnetic field and shifted to the plasma frame. Figure 6 shows both 2-D slices in the plane ($v_\perp$, $v_\parallel$), where the chosen $v_\perp$ is arbitrary and 1-D cuts of the full distribution. The 1-D cuts are chosen so that they represent pitch angles 90° (red), 60° (blue), and 0° (green) as shown in Figure 6a1. These angles correspond to pitch angles chosen to be plotted by *Soucek and Escoubet* [2011] (in their Figure 7). Cooling of the plasma and the decrease of temperature anisotropy can be recognized from the shape of the distributions when going from the bow shock vicinity (Figures 6a1 and 6b1) farther into the magnetosheath (Figures 6a2, 6b2, 6a3, and 6b3)). The distributions show a dependence on the phase of the waves. Especially at points 2 and 3 at the crest of the wave (Figure 6b2 and 6a3), the population at pitch angle 90° is larger than at pitch angles 60° and 0°. Whereas in the trough of the wave (Figure 6a2 and 6b3), the difference between distributions at perpendicular and at 60° pitch angles is smaller. This is an indication of trapped particles inside the trough and is also seen in the observations [*Soucek and Escoubet*, 2011].

3.4. Spatial Extent

With our global simulation we can investigate the extent of the magnetosheath populated by the mirror modes. The first condition to be checked is the anticorrelation of magnetic field and density. Again, we have taken a 5 s running average of the raw data. We calculate the Pearson correlation coefficient between the first-order time derivatives of the magnetic field strength and number density to remove the effect of the data trend and require the correlation coefficient to be below −0.5. As discussed at the end of section 3.2, the magnetic structures seem to be mirror mode waves even though the standard deviation is less than 10%. Here we

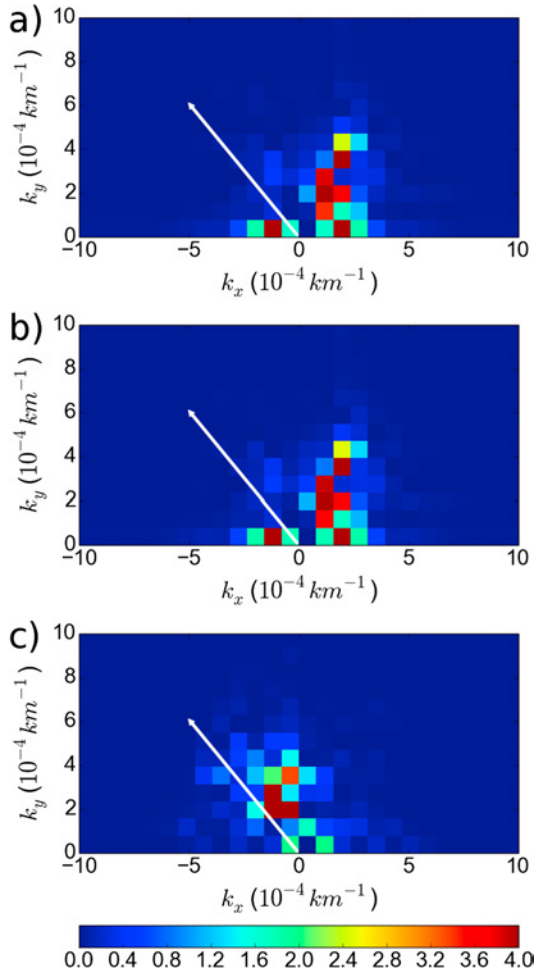

Figure 5. Spatial Fourier transform of (a) $|\mathbf{B}|$, (b) $B_{\text{plane}} = \sqrt{B_x^2 + B_y^2}$ and (b) B_z over the region marked by the white square in Figure 2a. The white arrow shows the direction of $\mathbf{B}_0$. The color scale shows δB^2 in units of 10^{-13} T^2.

require the standard deviation of the magnetic fluctuations to be larger than 5%. For the linear polarization we apply three different conditions from different publications:

1. $\lambda_{\text{max}}/\lambda_{\text{int}} > 1.5$, $\lambda_{\text{min}}/\lambda_{\text{int}} > 0.3$, and angle between maximum variance direction $\theta_{\text{Bm}} < 30°$ [*Soucek et al.*, 2008];
2. $\theta_{\text{Bm}} < 20°$ [*Génot et al.*, 2009, 2011];
3. $\lambda_{\text{max}}/\lambda_{\text{int}} > 5$, and $\theta_{\text{Bm}} < 20°$ [*Tátrallyay et al.*, 2010].

The minimum variance analysis is performed at multiple points at distance of $0.5R_E$ from each other throughout the whole magnetosheath. We exclude points that the bow shock crosses while it expands during the simulation because the crossing affects the results of the minimum variance analysis. Points where the conditions are fulfilled are marked with a black dot. No point fulfills condition 3. Results are shown in Figure 7a showing the results using condition 1 and Figure 7b showing the results using condition 2.

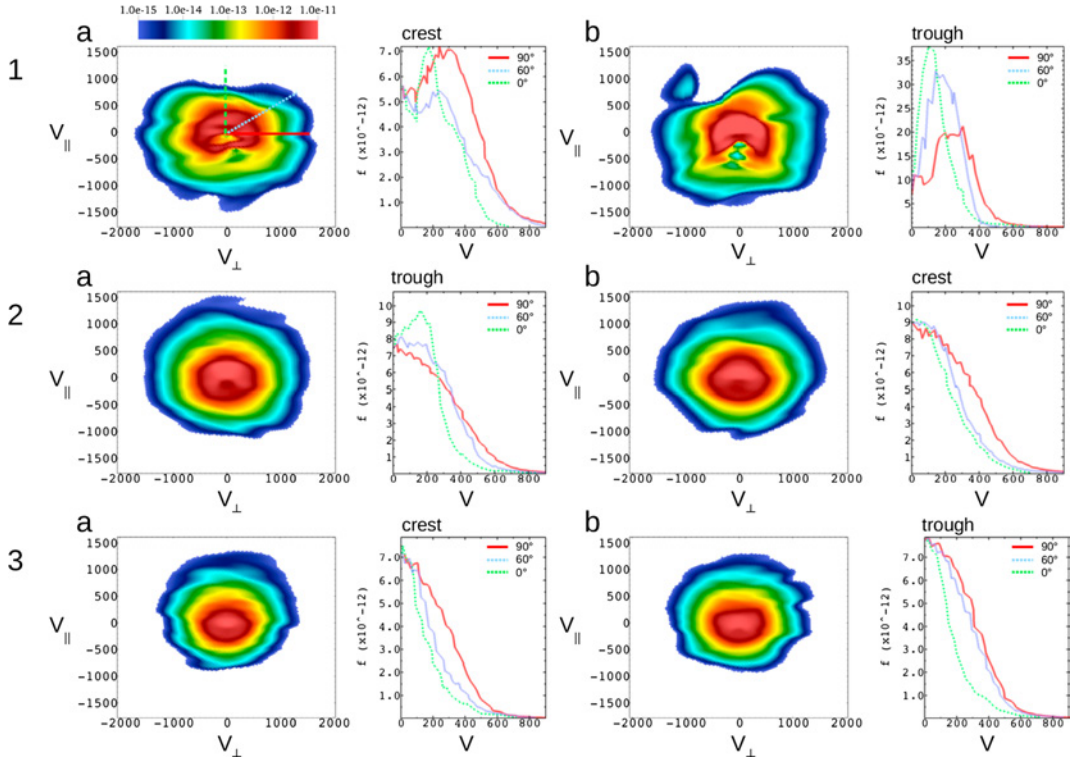

Figure 6. Velocity distribution functions from the virtual spacecraft points marked on Figure 2a at times marked in Figures 2b–2d. On the left-hand side is the 2-D slice of the velocity distribution function on the plane ($V_\perp$, $V_\parallel$), and the plot next to it shows 1-D cuts along the lines shown in Figure 6a1. The lines correspond to pitch angles 0°, 60°, and 90°. Velocities are in km/s and the units of the velocity distributions are $s^3\ m^{-6}$.

The region given by condition 1 (Figure 7a) is larger than the one given by condition 2 (Figure 7b) even though condition 2 does not limit the relations between eigenvalues of the variance matrix in any way whatsoever. However, the criterion for the angle between the maximum variance analysis and the background magnetic field covers a larger range of angles in condition 1. Both conditions show that the mirror mode activity is largest in the midsheath (half the distance between the bow shock and magnetopause). The mirror mode activity closest to the subsolar region is closer to the magnetopause than the bow shock. The largest mirror mode activity seems to be along and close to the streamlines that enter from solar wind to the magnetosheath close to the foreshock ULF wave boundary.

4. Discussion

Even though recent investigations have provided a statistical global view of the magnetosheath [*Soucek et al.*, 2015; *Dimmock et al.*, 2015], they cannot provide a global coverage during a single event. Vlasiator allows us to follow the time evolution of an event. We observe that as the solar wind flows through the bow shock, temperature anisotropy forms and fluctuations appear behind the bow shock and propagate farther into the magnetosheath. The temperature anisotropy peaks at the quasi-perpendicular bow shock and then decreases slowly to the flanks. Along the velocity streamlines that flow toward the magnetopause the anisotropy increases again due to the piling and draping of the magnetic field lines. The plasma that flows into the magnetosheath has a larger anisotropy along the velocity streamlines that emerge into the sheath from the vicinity of the foreshock ULF wave boundary. Additionally, the mirror instability condition is larger along these flow lines. This coincides with the region where we see the mirror mode activity after performing the search for the mirror mode criteria throughout the whole simulated magnetosheath.

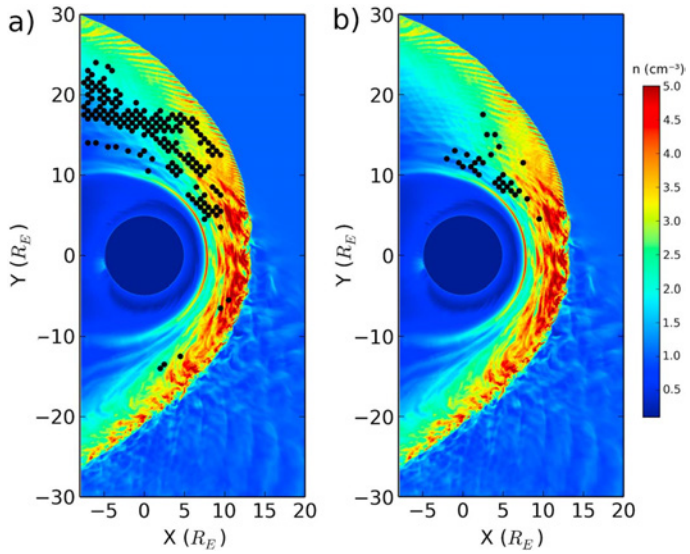

Figure 7. Global extent of the mirror mode activity by using (a) condition 1 and (b) condition 2 described in the text (see section 3.4). The points are chosen every 0.5 R_E throughout the whole magnetosheath, and those fulfilling the criteria are marked with a black dot. The color scale shows the number density in cm^{-3}.

We observe that anticorrelated waves are formed right after the bow shock crossing. However, they do not fulfill the mirror mode criteria until they have propagated approximately 3 R_E from the bow shock. The plasma that enters the quasi-perpendicular magnetosheath toward the flanks is mirror unstable, but the waves do not develop to fulfill the mirror mode criteria. Plasma velocity in the flanks is larger than in the dayside subsolar magnetosheath, and the waves might not have time to develop to mirror modes. Additionally, the initial perturbations in the plasma entering the sheath in the flank are smaller than in the plasma flowing into the sheath close to the ULF wave boundary. The mirror modes also form in the plasma that enters the sheath from the foreshock side of the ULF wave boundary but flows close to the magnetopause into the duskside of the magnetosheath. The plasma that enters the sheath from the foreshock and flows into the quasi-parallel magnetosheath fulfills the mirror mode instability condition, but the waves do not grow there due to the turbulence. Our results indicate that the streamlines close to the foreshock boundary are favorable locations for the mirror mode formation. There are enough initial perturbations in the plasma for the mirror modes to grow and the plasma properties fulfill the mirror instability condition better than elsewhere in the magnetosheath. In the quasi-perpendicular flank and at the quasi-parallel magnetosheath, although the mirror mode condition is in force, the waves cannot grow into mirror modes.

The temperature anisotropy as well as the mirror mode instability condition have a clear dawn-dusk asymmetry in our simulation. Therefore, the mirror mode activity also strongly favors the quasi-perpendicular magnetosheath. Similar behavior has been reported recently by *Dimmock et al.* [2015] which uses 6 years of THEMIS data to map the temperature anisotropy and mirror mode activity during different solar wind conditions. The study observes that with a typical Parker spiral IMF direction and an intermediate Alfvén Mach number, the mirror mode activity is higher in the dusk than during high Mach number solar wind periods. However, the *Dimmock et al.* [2015] statistics also showed mirror mode activity in the quasi-parallel sheath in contrast to our simulation, even though the mirror instability condition is also fulfilled there. A possible explanation is the temperature anisotropy in the simulated event, which is almost 1, thus not enough for the mirror mode formation. Additionally, the quasi-parallel magnetosheath is turbulent and the mirror modes are not able to grow. *Dimmock et al.* [2015] also observe that the anisotropy increases from the bow shock to the magnetopause due to the draping of the field line around the magnetosphere. This is in agreement with our simulation results, although in our simulation the effect is stronger possibly due to the numerical limitation of our 2-D simulation, where the plasma is not able to flow around the Earth and therefore piles

up at the magnetopause. Our results are consistent also with 3-D hybrid-PIC simulations of a down-scaled Hermean magnetosheath by *Herčík et al.* [2013]. They used both southward and northward IMF and identified the mirror modes by looking at the anticorrelation, β, instability condition, and spatial Fourier transform. They find that plasma conditions are good for mirror mode formation in the magnetosheath behind the quasi-perpendicular bow shock and close to the magnetopause behind the quasi-parallel bow shock. We observe magnetic structures that fulfill the mirror mode criteria only at couple of points in the quasi-parallel flank of the magnetosheath. Our results are consistent with a 2 year statistical study of Cluster observations by *Soucek et al.* [2015]. They found that mirror modes more likely exist in the quasi-perpendicular magnetosheath, whereas in the quasi-parallel magnetosheath they are not observed regularly. However, *Herčík et al.* [2013] also show that asymmetry can also form with 0° cone angle. They find that during southward (northward) IMF the temperature and β are higher in the dawn (dusk) and the plasma becomes more favorable for the mirror modes.

The mirror mode waves are described as large-amplitude waves, and the amplitude is often used as a criterion to select mirror mode events [e.g., *Tátrallyay and Erdós*, 2005; *Génot et al.*, 2009; *Dimmock et al.*, 2015]. However, in our simulations the waves have relatively low amplitudes with standard deviation on both sides of 10% of the background magnetic field. All the other aspects of the waves fulfill the criteria set for the mirror mode waves. The approximated rate at which the mirror structures grow at the vicinity of point 2 along the streamline in Figure 2 is 0.005 s^{-1}, which falls in the limits observed by *Tátrallyay et al.* [2010] by using Cluster observations. Similarly, as done by *Tátrallyay et al.* [2010], we compare the calculated growth rate to the analytical maximum growth rate using the equation (7) of *Liu et al.* [2006]. By using the local magnetosheath values from the simulation we get the maximum growth rate $\gamma_{\mathrm{Bmax}} \approx 0.09\Omega_p \approx 0.16\ s^{-1}$, where Ω_p is the ion cyclotron frequency. This obtained value is significantly larger than the rate the structures seem to grow at as they are advected along the streamline. *Tátrallyay et al.* [2010] suggest that the difference between the estimated growth rate and the growth rate given by analytical models can be due to limitations of the method; the two spacecraft might not be measuring mirror modes that originate from the same source. In our model, however, we are able to follow the identity of the waves. This indicates that there are global and local effects in the magnetosheath that are not taken into account in the theoretical models.

Based on our results, possible explanations for the limited amplitude growth are the following: First, in the quasi-perpendicular magnetosheath the magnetic field components in the simulation (*xy*) plane are the ones that are anticorrelated to density fluctuations. Fluctuations in the out-of-the-plane (B_z) magnetic field do not show clear anticorrelation while they propagate in the plasma frame and have wave vector close to $\mathbf{B}_0$. This indicates that those waves might be ion cyclotron waves. However, the amplitude of the fluctuations in B_z is so low that it does not contribute significantly to the total magnetic field strength. As part of the free energy from the temperature anisotropy goes to ion cyclotron waves instead of mirror mode waves, the amplitude cannot grow as fast as it would without the ion cyclotron waves. Second, the wave-particle interactions play a role in the wave growth as the ions are scattered from the waves and the temperature anisotropy decreases affecting also the growth rate [*Gary et al.*, 1993; *Tátrallyay et al.*, 2010]. In addition, the kinetic effects at small velocities play a large role in the physics of the mirror mode waves [e.g., *Southwood and Kivelson*, 1993; *Pokhotelov et al.*, 2008, 2010] as protons at small parallel velocities become resonant with the mirror mode wave and affect the growth rates. It has also been suggested that the trapped particles can be the cause of the mirror mode wave saturation [e.g., *Southwood and Kivelson*, 1993; *Kivelson and Southwood*, 1996, 1993]. However, in our simulation the velocity space resolution is 30 km/s, preventing it from resolving very low velocities. This could prevent the simulation reaching theoretical values of the maximum growth rates.

The velocity distribution functions from the mirror modes provided by Vlasiator show the presence of the trapped particles similarly as seen in the Cluster observations [*Soucek and Escoubet*, 2011]. This can be seen in the troughs of the waves where the trapped particles have almost the same distribution all the way from perpendicular to 60° pitch angles. Closer to the crests of the wave the distribution at 60° pitch angle is decreased compared to the perpendicular direction. Compared to the distribution from the crest of the wave, the population in the perpendicular direction is cooler and the population at 60° pitch angles is hotter in the troughs. *Soucek and Escoubet* [2011] find that in the crests of the waves the enhancement in the particles in the perpendicular directions is mostly seen at low energies below 100 eV corresponding to a velocity of 138 km/s. Our results show that the population to the perpendicular direction is larger all the way up to 800 km/s (3.3 keV).

According to our results the choice of mirror mode criteria affects the extent of observed mirror mode activity. The choice of all considered parameters, the ratios of the maximum to intermediate and minimum to intermediate eigenvalues of the variance matrix and the angle between the background magnetic field and the maximum variance direction, $\lambda_{max}/\lambda_{int}$, $\lambda_{min}/\lambda_{int}$, and θ_{Bm}, respectively, have different effects. The first set of conditions is based on the limits used by *Soucek et al.* [2008]: $\lambda_{max}/\lambda_{int} > 1.5$, $\lambda_{min}/\lambda_{int} > 0.3$, and $\theta_{Bm} < 30°$, and it gives the largest region of mirror mode activity. Condition 1, however, allows a wider range of considered parameters.

The second condition for the linear polarization is the same as that used by *Génot et al.* [2009, 2011] and only limits θ_{Bm} (<20°). This condition yields less than half of the extent of mirror mode activity compared to what is given by using the first set of conditions. In addition to the same limit for θ_{Bm}, the third set of conditions limits the value of the ratio $\lambda_{max}/\lambda_{int}$ to 5, which is higher than in the first set. By using this set of criteria we cannot observe any mirror mode activity. On the contrary, *Génot et al.* [2009], whose only condition regarding the minimum variance analysis for mirror modes was the 20° limit for θ_{Bm}, tested that restraining the mirror modes only to linearly polarized waves $\lambda_{max}/\lambda_{int} > 5$, $\lambda_{min}/\lambda_{int} > 0.3$ did not change their results significantly. In our case the effect of restraining the data to $\lambda_{max}/\lambda_{int} > 5$ is significant. Furthermore, *Génot et al.* [2001] have found that the mirror modes are more often observed as elliptically polarized waves. Therefore, there is no need to restrict the conditions to only well linearly polarized waves.

5. Conclusions and Summary

In this paper we present the first study of the mirror modes in the Earth's magnetosheath using a self-consistent global hybrid-Vlasov model. Under the near Parker spiral IMF conditions (cone angle 30°) the mirror mode instability condition and thus the observed mirror mode activity is largest close to the velocity streamlines entering the magnetosheath close to the foreshock ULF wave boundary, where the initial perturbations in the plasma and magnetic field offer good circumstances for mirror mode growth. Closer to the quasi-perpendicular flank, the plasma crossing the bow shock has less initial perturbations and the plasma closer to the quasi-parallel magnetosheath becomes too turbulent to allow mirror modes to develop.

The mirror modes in our simulation have relatively low amplitudes and they do not grow much larger than 10% of the background magnetic field. The rate at which the mirror mode structures grow in the magnetosheath estimated from the fluctuation amplitudes is 1 order of magnitude smaller than that given by analytical models using local plasma parameters but comparable to the growth rates estimated using spacecraft observations [*Tátrallyay et al.*, 2010]. This indicates that the theoretical models do not apply well in the magnetosheath since they do not take into account the local and global effects, such as local changes in the plasma parameters [*Tátrallyay et al.*, 2010] or other wave modes that can affect the mirror mode wave growth and saturation in the magnetosheath.

The observational papers use varying criteria for selecting the mirror mode events among other low-frequency waves. One of the most used methods is to use the minimum variance analysis, and the numerical values for the eigenvalue ratios and the angle between the maximum variance direction and background magnetic field are chosen differently in different papers [e.g., *Tátrallyay and Erdós*, 2005; *Soucek et al.*, 2008; *Génot et al.*, 2009]. We have shown here that the spatial extent is highly dependent on the selection criteria, but it could be a significant fraction of the magnetosheath downstream of the quasi-perpendicular bow shock.

Acknowledgments
Vlasiator (http://vlasiator.fmi.fi) was developed with the European Research Council starting grant (200141-QuESpace) granted to M.P. in 2007. Academy of Finland grants 38599 and 267144 have supported the work at FMI. Support to B.W. was given by the NASA grant NNX14AK41G. The work of U.G. is supported by the German Research Foundation (DFG) grant GA 1968/1. We acknowledge that the results were achieved using the Sisu supercomputer of CSC-IT Center for Science. Figures of the magnetosphere and the velocity distribution functions are done with VisIt [*Childs et al.*, 2012]. Data shown in this paper can be accessed by following the data policy on our web page http://vlasiator.fmi.fi/rules.php.

References

Califano, F., P. Hellinger, E. Kuznetsov, T. Passot, P. L. Sulem, and P. M. Trávníček (2008), Nonlinear mirror mode dynamics: Simulations and modeling, *J. Geophys. Res.*, *113*, A08219, doi:10.1029/2007JA012898.

Childs, H., et al. (2012), VisIt: An end-user tool for visualizing and analyzing very large data, in *High Performance Visualization: Enabling Extreme-Scale Scientific Insight*, pp. 357–372, Taylor and Francis, Boca Raton, Fla.

Denton, R. (2000), ULF waves in the magnetosheath, *Int. J. Geomagn. Aeron.*, *2*(1), 45–55.

Dimmock, A. P., A. Osmane, T. I. Pulkkinen, and K. Nykyri (2015), A statistical study of the dawn-dusk asymmetry of ion temperature anisotropy and mirror mode occurrence in the terrestrial dayside magnetosheath using THEMIS data, *J. Geophys. Res. Space Physics*, *120*(7), 5489–5503, doi:10.1002/2015JA021192.

Gary, S. P. (1992), The mirror and ion cyclotron anisotropy instabilities, *J. Geophys. Res.*, *97*, 8519–8529, doi:10.1029/92JA00299.

Gary, S. P., S. A. Fuselier, and B. J. Anderson (1993), Ion anisotropy instabilities in the magnetosheath, *J. Geophys. Res.*, *98*, 1481–1488, doi:10.1029/92JA01844.

Génot, V., S. J. Schwartz, C. Mazelle, M. Balikhin, M. Dunlop, and T. M. Bauer (2001), Kinetic study of the mirror mode, *J. Geophys. Res.*, *106*, 21,611–21,622, doi:10.1029/2000JA000457.

Génot, V., E. Budnik, P. Hellinger, T. Passot, G. Belmont, P. M. Trávníček, P.-L. Sulem, E. Lucek, and I. Dandouras (2009), Mirror structures above and below the linear instability threshold: Cluster observations, fluid model and hybrid simulations, *Ann. Geophys.*, *27*, 601–615, doi:10.5194/angeo-27-601-2009.

Génot, V., L. Broussillou, E. Budnik, P. Hellinger, P. M. Trávníček, E. Lucek, and I. Dandouras (2011), Timing mirror structures observed by Cluster with a magnetosheath flow model, *Ann. Geophys.*, *29*(10), 1849–1860, doi:10.5194/angeo-29-1849-2011.

Hasegawa, A. (1969), Drift mirror instability of the magnetosphere, *Phys. Fluids*, *12*, 2642–2650, doi:10.1063/1.1692407.

Herčík, D., P. M. Trávníček, J. R. Johnson, E.-H. Kim, and P. Hellinger (2013), Mirror mode structures in the asymmetric Hermean magnetosheath: Hybrid simulations, *J. Geophys. Res. Space Physics*, *118*, 405–417, doi:10.1029/2012JA018083.

Hubert, D., C. Lacombe, C. C. Harvey, M. Moncuquet, C. T. Russell, and M. F. Thomsen (1998), Nature, properties, and origin of low-frequency waves from an oblique shock to the inner magnetosheath, *J. Geophys. Res.*, *103*, 26,783–26,798, doi:10.1029/98JA01011.

Kempf, Y., D. Pokhotelov, O. Gutynska, L. B. Wilson, B. M. W. III, S. v. Alfthan, O. Hannuksela, D. G. Sibeck, and M. Palmroth (2015), Ion distributions in the Earth's foreshock: Hybrid-Vlasov simulation and THEMIS observations, *J. Geophys. Res. Space Physics*, *120*, 3684–3701, doi:10.1002/2014JA020519.

Kivelson, M. G., and D. J. Southwood (1996), Mirror instability II: The mechanism of nonlinear saturation, *J. Geophys. Res.*, *101*, 17,365–17,372, doi:10.1029/96JA01407.

Kobel, E., and E. O. Fluckiger (1994), A model of the steady state magnetic field in the magnetosheath, *J. Geophys. Res.*, *99*, 23,617–23,622, doi:10.1029/94JA01778.

Lacombe, C., and G. Belmont (1995), Waves in the Earth's magnetosheath: Observations and interpretations, *Adv. Space Res.*, *15*, 329–340, doi:10.1016/0273-1177(94)00113-F.

Laitinen, T. V., Y. V. Khotyaintsev, M. André, A. Vaivads, and H. Rème (2010), Local influence of magnetosheath plasma beta fluctuations on magnetopause reconnection, *Ann. Geophys.*, *28*(5), 1053–1063, doi:10.5194/angeo-28-1053-2010.

Liu, Y., J. D. Richardson, J. W. Belcher, J. C. Kasper, and R. M. Skoug (2006), Plasma depletion and mirror waves ahead of interplanetary coronal mass ejections, *J. Geophys. Res.*, *111*, A09108, doi:10.1029/2006JA011723.

Londrillo, P., and L. Del Zanna (2004), On the divergence-free condition in Godunov-type schemes for ideal magnetohydrodynamics: The upwind constrained transport method, *J. Comput. Phys.*, *195*(1), 17–48, doi:10.1016/j.jcp.2003.09.016.

McKean, M. E., D. Winske, and S. P. Gary (1992), Mirror and ion cyclotron anisotropy instabilities in the magnetosheath, *J. Geophys. Res.*, *97*, 19,421–19,432, doi:10.1029/92JA01842.

Omidi, N., and D. Winske (1995), Structure of the magnetopause inferred from one-dimensional hybrid simulations, *J. Geophys. Res.*, *100*, 11,935–11,955, doi:10.1029/94JA02937.

Pokhotelov, O., S. Walker, R. Sagdeev, and G. Dudnikova (2010), Mirror and Weibel instabilities: Similarities and nonlinear dynamics, in *38th COSPAR Scientific Assembly*, vol. 38, pp. 2108, COSPAR Meeting, Bremen, Germany.

Pokhotelov, O. A., R. Z. Sagdeev, M. A. Balikhin, O. G. Onishchenko, and V. N. Fedun (2008), Nonlinear mirror waves in non-Maxwellian space plasmas, *J. Geophys. Res.*, *113*, A04225, doi:10.1029/2007JA012642.

Samsonov, A. A., O. Alexandrova, C. Lacombe, M. Maksimovic, and S. P. Gary (2007), Proton temperature anisotropy in the magnetosheath: Comparison of 3-D MHD modelling with Cluster data, *Ann. Geophys.*, *25*(5), 1157–1173, doi:10.5194/angeo-25-1157-2007.

Schwartz, S. J., D. Burgess, and J. J. Moses (1996), Low-frequency waves in the Earth's magnetosheath: Present status, *Ann. Geophys.*, *14*, 1134–1150, doi:10.1007/s00585-996-1134-z.

Shoji, M., Y. Omura, and L.-C. Lee (2012), Multidimensional nonlinear mirror-mode structures in the Earth's magnetosheath, *J. Geophys. Res.*, *117*, A08208, doi:10.1029/2011JA017420.

Soucek, J., and C. P. Escoubet (2011), Cluster observations of trapped ions interacting with magnetosheath mirror modes, *Ann. Geophys.*, *29*(6), 1049–1060, doi:10.5194/angeo-29-1049-2011.

Soucek, J., E. Lucek, and I. Dandouras (2008), Properties of magnetosheath mirror modes observed by Cluster and their response to changes in plasma parameters, *J. Geophys. Res.*, *113*, A04203, doi:10.1029/2007JA012649.

Soucek, J., C. P. Escoubet, and B. Grison (2015), Magnetosheath plasma stability and ULF wave occurrence as a function of location in the magnetosheath and upstream bow shock parameters, *J. Geophys. Res. Space Physics*, *120*, 2838–2850, doi:10.1002/2015JA021087.

Southwood, D. J., and M. G. Kivelson (1993), Mirror instability: I. Physical mechanism of linear instability, *J. Geophys. Res.*, *98*, 9181–9187, doi:10.1029/92JA02837.

Tátrallyay, M., and G. Erdós (2002), The evolution of mirror mode fluctuations in the terrestrial magnetosheath, *Planet. Space Sci.*, *50*, 593–599, doi:10.1016/S0032-0633(02)00038-7.

Tátrallyay, M., and G. Erdós (2005), Statistical investigation of mirror type magnetic field depressions observed by ISEE-1, *Planet. Space Sci.*, *53*, 33–40, doi:10.1016/j.pss.2004.09.026.

Tátrallyay, M., G. Erdós, I. Dandouras, and E. Georgescu (2010), On the growth of mirror mode waves in the magnetosheath based on Cluster observations, in *The Cluster Active Archive, Astrophys. and Space Sci. Proc.*, edited by H. Laakso, M. Taylor, and C. P. Escoubet, pp. 377–385, Springer, Berlin, doi:10.1007/978-90-481-3499-1_26.

von Alfthan, S., D. Pokhotelov, Y. Kempf, S. Hoilijoki, I. Honkonen, A. Sandroos, and M. Palmroth (2014), Vlasiator: First global hybrid-Vlasov simulations of Earth's foreshock and magnetosheath, *J. Atmos. Sol. Terr. Phys.*, *120*, 24–35, doi:10.1016/j.jastp.2014.08.012.

White, L., and A. Adcroft (2008), A high-order finite volume remapping scheme for nonuniform grids: The piecewise quartic method (PQM), *J. Comput. Phys.*, *227*(15), 7394–7422, doi:10.1016/j.jcp.2008.04.026.

Zerroukat, M., and T. Allen (2012), A three-dimensional monotone and conservative semi-Lagrangian scheme (SLICE-3D) for transport problems, *Q. J. R. Meteorol. Soc.*, *138*(667), 1640–1651, doi:10.1002/qj.1902.

Paper II

Magnetopause reconnection and energy conversion as influenced by the dipole tilt and the IMF B_x

Journal of Geophysical Research: Space Physics
volume 119, 2014
doi:10.1002/2013JA019693

AGU PUBLICATIONS

JGR

Journal of Geophysical Research: Space Physics

RESEARCH ARTICLE

10.1002/2013JA019693

Key Points:
- Magnetopause shape, reconnection, and energy conversion are coupled together
- IMF Bx affects especially reconnection location and load energy conversion
- Dipole tilt affects more the generator energy conversion and magnetopause shape

Correspondence to:
S. Hoilijoki,
sanni.hoilijoki@fmi.fi

Citation:
Hoilijoki, S., V. M. Souza, B. M. Walsh, P. Janhunen, and M. Palmroth (2014), Magnetopause reconnection and energy conversion as influenced by the dipole tilt and the IMF B_x, *J. Geophys. Res. Space Physics*, *119*, 4484–4494, doi:10.1002/2013JA019693.

Received 05 DEC 2013
Accepted 22 MAY 2014
Accepted article online 27 MAY 2014
Published online 13 JUN 2014

Magnetopause reconnection and energy conversion as influenced by the dipole tilt and the IMF B_x

Sanni Hoilijoki[1,2], Vitor M. Souza[3,4], Brian M. Walsh[4,5], Pekka Janhunen[1], and Minna Palmroth[1]

[1]Finnish Meteorological Institute, Helsinki, Finland, [2]Department of Physics, University of Helsinki, Helsinki, Finland, [3]National Institute for Space Research/INPE, São José dos Campos, Brazil, [4]Heliospheric Division, NASA/Goddard Space Flight Center, Greenbelt, Maryland, USA, [5]Space Sciences Laboratory, University of California, Berkeley, California, USA

Abstract We study the effect of Earth's dipole tilt angle and interplanetary magnetic field (IMF) B_x and B_y components on the location of reconnection and the energy conversion at the magnetopause. We simulate southward IMF satisfying both inward- and outward-type Parker spiral conditions during three different dipole tilt angles using a global magnetohydrodynamic model GUMICS-4. We find that positive (negative) B_x contributes to the magnetopause reconnection line location by moving northward (southward) and positive (negative) dipole tilt angle by moving it southward (northward). The tilt shifts the dayside load region toward the winter hemisphere and the summer cusp toward the equatorial plane. Magnetic flux hence piles effectively in the summer hemisphere leading to increased magnetopause currents that enhance the Poynting flux through the magnetopause. We find that the intensity of the energy conversion in the generators is strongly affected by the dipole tilt angle, whereas intensity in the load region is mainly affected by IMF B_x.

1. Introduction

Space weather is driven by energy transfer from solar wind to the Earth's magnetosphere. Predicting space weather accurately requires knowledge of energy conversion within the solar wind-magnetopause system. *Dungey* [1961] suggested that the dynamics of the magnetosphere are driven by the interplanetary magnetic field (IMF) reconnecting with the Earth's magnetic field at the dayside magnetopause. When the IMF is southward, reconnection leads to advection of open field lines tailward on the magnetopause surface. When the open field lines reach the tail, they are added to the tail lobes until they reconnect again in the tail reconnection region and return back to the dayside. This process also implies energy conversion in a so-called load generator process [*Siscoe and Cummings*, 1969], where the dayside works as a load converting magnetic energy to kinetic energy, whereas in the generator regions located in the tail lobes, the energy is extracted from the magnetosheath flow and is converted from kinetic form into magnetic energy.

Earlier, reconnection at the magnetopause has been explained by antiparallel [*Crooker*, 1979] and component [*Sonnerup*, 1970; *Gonzalez and Mozer*, 1974] reconnection hypotheses, which predict a different reconnection morphology, and therefore different resulting dynamics within the magnetosphere and ionosphere. According to the antiparallel hypothesis, reconnection occurs in regions where the magnetic fields inside and outside the magnetopause are almost antiparallel. During purely southward IMF, for instance, the reconnection line extends continuously through the subsolar point at the equatorial plane, while during finite IMF B_y, it would split at local noon into two regions located in different hemispheres [*Crooker*, 1979; *Luhmann et al.*, 1984]. The component hypothesis states that the optimal region for reconnection is the vicinity of the subsolar point, where the magnetosheath flow first makes contact with the magnetopause. From the first contact point, the reconnection line would stretch along the dayside magnetopause. The shear angle between reconnecting field lines is not as meaningful for component reconnection as it is for antiparallel, as only oppositely directed field components reconnect, whereas the impact of the other components on the process is small. For component reconnection, the relation between the IMF B_y and B_z components determines how much the reconnection line is tilted with respect to the equatorial plane.

More recent magnetopause reconnection theories introduces a maximum magnetic shear model, which can also be used to study the location of the reconnection at the dayside magnetopause [*Trattner et al.*, 2007, 2012]. According to this model, the reconnection on the magnetopause occurs along the ridge of maximum

magnetic shear angle between the draped IMF and the Earth's magnetic field. To predict the reconnection location on the magnetopause, the maximum shear model needs only the IMF and solar wind conditions.

In light of asymmetric 3-D reconnection, we can discuss the dayside reconnection in terms of null points and null-null lines. IMF and Earth's dipole field together compose a magnetic system with two magnetic null points (points where $\mathbf{B} = 0$) and null-null line that connects the two null points. This line is called the separator, a line that intersects four different regions of plasma that are not connected to each other by field lines [*Lau and Finn*, 1990]. This geometric structure enables the reconnection between the field lines in different regions. When the IMF is southward, the null points are close to the equatorial plane and the line connecting the nulls forms a separator line. For northward IMF, the points move closer to the cusps and the null-null line is no longer horizontal. The IMF direction affects the location of the null points and thus the location of the reconnection at the magnetopause [*Komar et al.*, 2013].

Spacecraft observations have been shown to support both component and antiparallel reconnection hypotheses. *Trattner et al.* [2007] estimated the reconnection line location from several ion distributions observations at the northern cusp obtained by the Polar spacecraft. The distance from the spacecraft to the reconnection site is estimated through tracing particle distributions along model magnetic field lines back to the magnetopause. Their results showed that both component and antiparallel reconnection types can occur at the magnetopause depending on IMF conditions. According to *Trattner et al.* [2007, 2012], for B_y-dominated IMF conditions, the reconnection line is of component type extending throughout the dayside magnetopause. On the other hand, during very large positive or negative B_x, as well as dominant southward IMF B_z, the reconnection line does not cross the dayside magnetopause as a single tilted line but splits into two lines instead, which follow the antiparallel reconnection sites tracing to high latitudes. Although spacecraft observations provide a local description of which reconnection scenario is occurring, significant limitations exist in explaining the instantaneous system as a whole since they are point measurements. Therefore, global MHD simulations have also been used to investigate magnetopause reconnection. In the GUMICS-4 global MHD simulation the reconnection line is continuous and compatible with the component hypothesis [*Laitinen et al.*, 2007].

IMF B_x component has been found to have an important role in defining the location of the reconnection line, shape of the magnetopause, and the dayside reconnection rate [e. g., *Trattner et al.*, 2007; *Peng et al.*, 2010]. *Peng et al.* [2010] investigated the impact of the IMF B_x on magnetopause reconnection using global MHD simulations, while neglecting the effect of dipole tilt angle. They found that for low solar wind Alfvén Mach numbers ($MA \lesssim 3$), increasing the magnitude of the B_x changes the shape of the magnetopause in the terminator plane. During southward IMF, the magnetopause shifted southward during positive B_x and northward for negative B_x. They also found that the reconnection line on the dayside magnetopause shifted northward (southward) when $B_x > 0$ ($B_x < 0$), likely due to the relocation of the magnetopause.

Russell et al. [2003] found by using a MHD model that the dipole tilt might affect the reconnection rate and geomagnetic activity by controlling the length and location of the neutral line. *Trattner et al.* [2007] also studied the seasonal effects on the reconnection line location at the magnetopause, concluding that the reconnection line location shifts northward during northern winter (negative tilt angle) and southward during northern summer (positive tilt angle).

The tilt dependence of energy conversion has also been studied using the global MHD simulation code GUMICS-4 [*Palmroth et al.*, 2012], where it was found that during northern winter the energy transfer occurs mainly in the Southern Hemisphere, and vice versa for southern winter. Additionally, *Palmroth et al.* [2012] found that the energy transfer rate is 10% larger during equinox than solstices. Using another global MHD simulation, *Liu et al.* [2012] found that the dipole tilt angle influences the shape of the magnetopause during purely southward IMF. Their results show that when the value of the dipole tilt angle increases (decreases), the nose of the magnetopause moves southward (northward); the northern (southern) cusp moves toward the equatorial plane, and the southern (northern) cusp moves farther away from it.

In this paper we systematically investigate the combined effect of both the dipole tilt angle and IMF B_x component on the location of the dayside reconnection line and the magnetopause energy conversion by using the GUMICS-4 global MHD simulation code. This paper is organized as follows: First, we briefly introduce the GUMICS-4 global MHD simulation and the methods that are used to analyze the simulation results. Then, we describe the in situ observations of a magnetopause reconnection event detected quasi-simultaneously

by Time History of Events and Macroscale Interactions during Substorms (THEMIS) A and Double Star TC1 spacecraft. Next, we validate the simulation results by comparing them to THEMIS A and Double Star TC1 spacecraft observations. Finally, we use the GUMICS-4 to investigate the combined effect of the magnetic dipole tilt angle and southward IMF satisfying both inward- and outward-type Parker spiral conditions. We end the paper with our systematic conclusion on the role of dipole tilt angle and IMF B_x component on the dayside reconnection line morphology and magnetopause energy conversion.

2. Methods

In this paper we use GUMICS-4 [*Janhunen et al.*, 2012], which is a global MHD simulation code including the solar wind and the magnetosphere and solving the conservative MHD equations. The simulation volume extends from $+32\,R_E$ to $-224\,R_E$ in the x direction and $\pm 64\,R_E$ in the y and z directions. The MHD simulation box is coupled to the electrostatic ionosphere. The magnetosphere is coupled to the ionosphere by the field-aligned currents, and electron precipitation is evaluated at the inner edge of the MHD domain at $3.7\,R_E$. The ionospheric electric potential is calculated in the ionospheric simulation domain and passed back to the magnetosphere where it is used as an inner boundary condition at $3.7\,R_E$. Other boundary conditions in the magnetospheric box are the solar wind parameters at the sunward wall and the Earth's dipole field. Solar wind conditions are given as input, and both observational and artificial data can be used. As a result, GUMICS-4 writes the full set of plasma parameters as a function of time and space into an output file. The code uses a cell-by-cell adaptive grid, which allows a better resolution (smallest cell size $0.25\,R_E$) in the areas of large spatial gradients and coarser resolution in areas which are of less interest. The region of interest here is covered fully by $0.25\,R_E$ grid resolution.

GUMICS-4 uses a first-order finite volume method to solve the ideal MHD equations in a discretized grid [*Janhunen et al.*, 2012]. The ideal MHD equations are given in a conservative form. The code uses the Roe's approximate Riemann solver [*Roe*, 1981], but in the rare case where an intermediate state produced by the Roe solver is nonphysical, the Harten-Lax-van Leer solver is used instead. The first-order Godunov-type numerical scheme used in GUMCIS-4 keeps the numerical diffusion small for slowly moving or stagnant structures, such as the magnetopause and bow shock. In order to keep the magnetic divergence at zero, GUMICS-4 uses elliptic cleaning [*Brackbill and Barnes*, 1980] every 20 s.

In order to utilize GUMICS-4 in analysis of dayside magnetopause reconnection, we need to introduce the key methodologies developed earlier. First, the magnetopause in the GUMICS-4 simulations is identified by using a method developed by *Palmroth et al.* [2003]. It is based on following a set of streamlines from $X_{\mathrm{GSE}} = +15\,R_E$ to a distance of $-30\,R_E$ down the magnetotail. The magnetosphere, which is surrounded by the streamlines, forms a cavity in the solar wind. The surface of the magnetopause is the approximate inner edge of this cavity. The magnetopause defined in this method is robust and smooth [e. g., *Janhunen et al.*, 2012].

Magnetic reconnection in GUMICS-4 is caused by numerical diffusion. Earlier studies show that the reconnection location in the GUMICS-4 simulations can be investigated and the results seem meaningful [*Laitinen et al.*, 2006, 2007]. Furthermore, the global dynamics which is largely driven by reconnection is well reproduced (see recent review by *Janhunen et al.* [2012]).

In the region where reconnection takes place, the gradients are strong, and therefore, due to automatic adaptation, the resolution is the smallest ($0.25\,R_E$). The reconnection line location at the magnetopause is found by using a four-field junction method developed by *Laitinen et al.* [2006]. There are four possible types of magnetic topology: (1) both ends of the field line connected to the Earth, (2) one end connected to the Northern Hemisphere with the other embedded in the solar wind flow, (3) same as (2) but connected to the Southern Hemisphere, and (4) both ends are embedded in the solar wind. The method starts by tracing the magnetic field lines from each grid point (with grid spacing $0.25\,R_E$) both forward and backward, and they are labeled according to the magnetic topology (1, 2, 3, or 4). Then the method goes through the grid again and marks a grid point as separator/reconnection point if all four different topologies are found within a distance of $2\,R_E$. The four-field junction method as itself is not enough to prove the existence of reconnection, but when combined with the energy conversion, it is a good indicator of reconnection location at the magnetopause [*Laitinen et al.*, 2007]. *Laitinen et al.* [2007] investigated the effect of the four-field junction region size (here $2\,R_E$) and found that the method itself does not depend on the size of the area. With smaller areas, the point indicating the four-field junction is the same as with $2\,R_E$ area size. However, the $2\,R_E$ area size

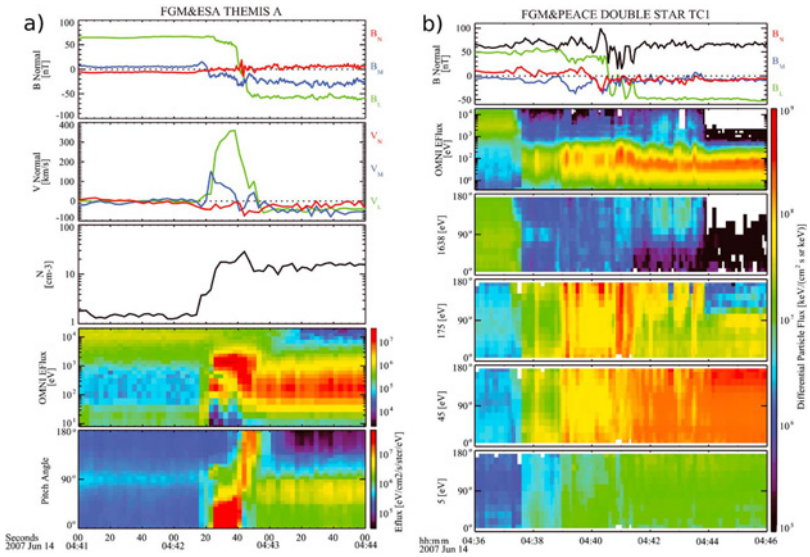

Figure 1. (a) THEMIS A and (b) Double Star TC1 magnetopause crossing on 14 June 2007. For THEMIS A, we have, from top to bottom, magnetic field and ion bulk velocity components in boundary normal coordinates (*LMN*), ion density, ion omnidirectional energy flux, and ion pitch angle distribution. For Double Star TC1 we have, also from top to bottom, magnetic field strength (black line) and components (*LMN* system), electron omnidirectional energy flux, and electron pitch angle distributions for different energy ranges indicated on the left.

ensures that there are enough points forming a continuous separator around the Earth for different solar wind parameters. The method gives a multiple points that form a ribbon around the Earth, now depicted in Figure 2 showing the two events. The separator/reconnection line is the averaged location of this ribbon.

Energy conversion at the magnetopause describes how much energy is converted between magnetic and kinetic forms, calculated as the negative divergence of Poynting flux, $-\nabla \cdot \mathbf{S}$, through the magnetopause [*Laitinen et al.*, 2006]. When the system is independent of time, the divergence can be written as $\nabla \cdot \mathbf{S} = -\mathbf{E} \cdot \mathbf{J}$, where $\mathbf{E}$ is the electric field and $\mathbf{J}$ is the current density. Energy conversion is positive in areas such as subsolar point of the magnetopause where reconnection takes place. This region can be interpreted as the load region [*Siscoe and Cummings*, 1969]. In areas where energy is converted from kinetic to magnetic form, the energy conversion is negative. This usually takes place in tail lobe magnetopause, which can be interpreted as generators [see also *Anekallu et al.*, 2011, 2013]. The general picture of energy conversion and energy transfer, which is defined as total (kinetic + thermal + electromagnetic) energy flux through the magnetopause surface, in GUMICS-4 simulations has been found to agree roughly with observations made by Cluster [*Anekallu et al.*, 2011, 2013; *Palmroth et al.*, 2011a, 2011b]. Even though the magnitudes of the energy conversion and energy transfer do not match, the spatial pattern of the energy conversion in the simulations approximately matches the observations.

3. Instruments and Observations

The observational data shown in this paper were provided by two spacecraft, Double Star TC1 [*Liu et al.*, 2005] and THEMIS A [*Angelopoulos*, 2008]. TC1's 4 s resolution spin-averaged magnetic field data used here were obtained by the Flux Gate Magnetometer instrument (FGM) [*Carr et al.*, 2005] while the electron data were obtained by the Plasma Electron And Current Experiment instrument (PEACE) [*Fazakerley et al.*, 2005] which measures electrons from a few eV to 25 KeV. For THEMIS A, the ion electrostatic analyzer [*McFadden et al.*, 2008] provided the ion plasma data with 3 s time resolution, while the Flux Gate Magnetometer (FGM) [*Auster et al.*, 2008] provided the 0.25 s resolution magnetic field.

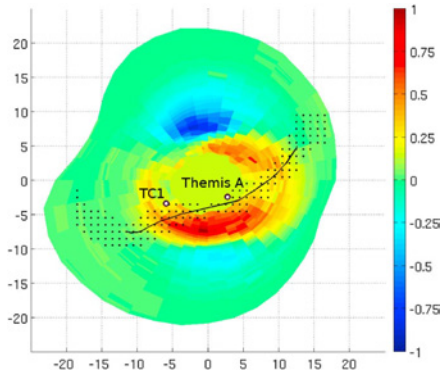

Figure 2. MHD simulation of event on 14 June 2007 at time corresponding approximately UT 4:40. Black rings mark the position of the spacecraft. Color bar shows the energy conversion (defined as a divergence of the Poynting flux) through the magnetopause surface, unit 10^{-4} W/m^2. Black dots extending throughout the dayside magnetopause show the points given by the four-field junction method. An average location of these points is indicated by a black line that represents the location of the reconnection line. Distances are in R_E.

We show in situ observations of two widely separated (~9 R_E) spacecraft, Double Star TC1 and THEMIS A, which crossed a reconnecting magnetopause (quasi-simultaneously) around 04:40 UT on 14 June 2007. Both spacecraft were on the dayside moving outbound near the magnetic equator. This event was previously reported by *Dunlop et al.* [2011], and here we summarize its main features.

THEMIS A observations are presented in Figure 1a for a 3 min window encompassing the magnetopause crossing. The magnetic field and ion bulk velocity components are shown in boundary normal coordinates (*LMN*), where the *N* component is normal to the local magnetopause and points outward, the *M* component, defined as the cross product between *N* and the Z_{GSM} coordinate, points westward, and the *L* component completes the left-handed orthogonal set and is oriented approximately due north. The reversal of the B_L component (~04:42:40 UT), together with the abrupt change in both ion density and energy flux marks the magnetopause crossing. Around the same time, a strong positive enhancement (~350 km/s) in the plasma velocity component V_L occurs, suggesting the presence of a reconnection line southward of THEMIS A location. An FTE-like bipolar B_N signature with a polarity $\pm$ is seen at the time of the magnetopause crossing, which is also consistent with a reconnection line southward of THEMIS A location. Further evidence for reconnection can be probed by looking at the ion pitch angle distribution (Figure 1a, bottom). Just before the B_L reversal (~04:42:30 UT), THEMIS A sampled accelerated ions streaming along magnetospheric magnetic field lines and right after that (~04:42:50 UT) energized back-streaming ions with pitch angles near 180° degrees were detected on magnetosheath magnetic field lines indicating that THEMIS A has crossed the reconnection exhaust northward of the assumed reconnection line [*Dunlop et al.*, 2011].

In Figure 1b TC1 crosses the magnetopause within 2 min of THEMIS A in Figure 1a. TC1's observations are presented in a 10 min window, with magnetic field presented in boundary normal coordinates. Around 04:37 UT, a boundary layer is crossed and electrons with magnetosheath-like energies (~200 eV) are present. After 04:39 UT, on the earthward side of the magnetopause (placed at the B_L reversal at 04:41 UT), there is a clear presence of both bistreaming and beamed populations with magnetosheath energies (45 and 175 eV panels), suggesting that magnetosheath electrons are flowing toward the magnetosphere mirroring in the ionosphere and turning back to the spacecraft detector along magnetic field lines which have been opened by reconnection. At 04:41 UT the magnetic field strength decreases at the same time that electrons are being energized, as evidenced by a small increase in the energy flux, which are consistent with Double Star TC1 passing very close to the ion diffusion region and therefore to the reconnection line location [*Dunlop et al.*, 2011]. After 04:41 UT, both out-flowing magnetospheric (1638 eV panel) and possibly reflected magnetosheath electrons (175 eV panel) are detected. Given the due southward configuration of the magnetosheath magnetic field during this observation ($-B_L$), we conclude that Double Star TC1 is northward of the low-latitude reconnection line right after 04:41 UT. The simultaneous conjunction between the two spacecraft sampling a reconnecting magnetopause suggests the presence of an extended dayside magnetic reconnection line.

4. Results

4.1. Model-Data Comparison

Figure 2 shows the GUMICS-4 simulation result for the reconnection event presented in Figure 1. We run the simulation by using data extracted from NASA/GSFC's OMNI data set through OMNIWeb for a given time. The simulation is initialized by running for 1 h with constant solar wind parameters and then with varying

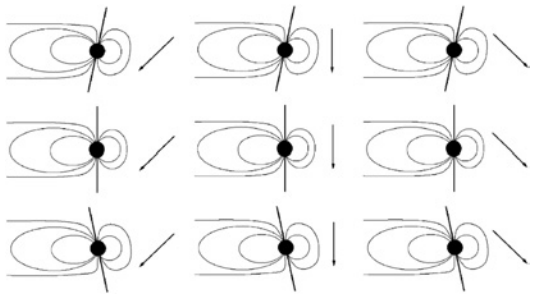

Figure 3. Schematic figure of our studied cases. (top row) The runs with dipole tilt angle 20°, (middle row) runs with zero dipole tilt, and (bottom row) runs with dipole tilt angle −20°. Each panel has the same IMF B_z component (−5 nT). The B_x component has different values in each column: (left) B_x is −5 nT, (middle) zero, and (right) 5 nT. The nonzero IMF B_x components (±5 nT) are incorporated on the middle column.

solar wind for 40 min before the desired event. By this time, the parameters in the vicinity of the Earth and the magnetosphere are properly initialized. At that time of Double Star TC1 magnetopause crossing (~04:40 UT), the OMNI data set revealed a major southward IMF B_z and an outward-type (IMF $B_y > 0$ and IMF $B_x < 0$) Parker spiral configuration. The dipole tilt angle was set to 13°. The colored surface shows the energy conversion through the magnetopause viewed from the front-looking tailward. Black dots extending throughout the dayside magnetopause show the points given by the four-field junction method. An average location of these points is indicated by a black line that represents the location of the reconnection line. Blue colors indicate generators, while red colors represent load regions. Black rings show the location of both spacecraft for each magnetopause crossing. The reconnection line in GUMICS-4 is continuous starting from the Southern Hemisphere at the dawnside and extending through the Northern Hemisphere at the duskside. The line is mainly located south from $z = 0\,R_E$, and a possible explanation is that the event happened during northern summer (positive dipole tilt angle) and negative IMF B_x component. These two combined factors resulted in a southward shifting of the reconnection line. For the same reason, the strongest dayside load is located south from the reconnection line and the strongest generator is in the north. According to the observations shown in Figure 1, the reconnection line is expected to be located southward from both spacecraft. The reconnection line location in our simulated event shown in Figure 2 is also southward from both spacecraft and is therefore in agreement with observations. This gives confidence to the results using synthetic data as input.

4.2. Dayside Reconnection Location

As already indicated in Figure 2, the dipole tilt and the combination of IMF B_x and B_y seem to affect the reconnection line morphology and the intensity of energy conversion. Next, we investigate the effects of both the dipole tilt and the B_x on the dayside reconnection more systematically. Figure 3 shows the setup carried out in this work. We run three sets of runs, each set having a different dipole tilt angle: −20°, 0°, and 20°. Apart from the dipole tilt, the sets are similar including five different runs with inward- and outward-type Parker spiral IMF conditions: $B_x \pm 5$ nT and $B_y = \mp 5$ nT. One of the five runs is purely southward ($B_x = 0$ and $B_y = 0$), and the remaining two runs have zero B_x but $B_y = \pm 5$ nT. We hypothesize that the location of the first contact of the magnetosheath flow on the magnetopause determines the reconnection line location in accordance with the component reconnection theory. This location will be affected by the interplay between the dipole tilt and the IMF B_x. In all of the runs the IMF is southward, having constant $B_z = -5$ nT. Figure 3 shows the initial hypotheses for the influence of the dipole tilt and B_x viewed in *xz* plane. Figure 3 (left and right columns) represents the runs with $B_x = -5$ nT and $B_x = 5$ nT, respectively, and the middle column represents all the runs with $B_x = 0$.

Figure 4 shows results of the parameter study runs. Color shows the energy conversion, and black lines are the location of the reconnection line as determined by the four-field junction method by *Laitinen et al.* [2006]. On the vertical axis is the dipole tilt angle, and on the horizontal axis are the different values of B_x and B_y. These B_x and B_y values span from −5 to 5 nT while the tilt vary from −20° to 20°. All the runs were executed with the same run duration of 1.5 h including the 1 h initialization, during which the solar wind with given parameters passes by the Earth (from the sunward boundary toward the back wall of the

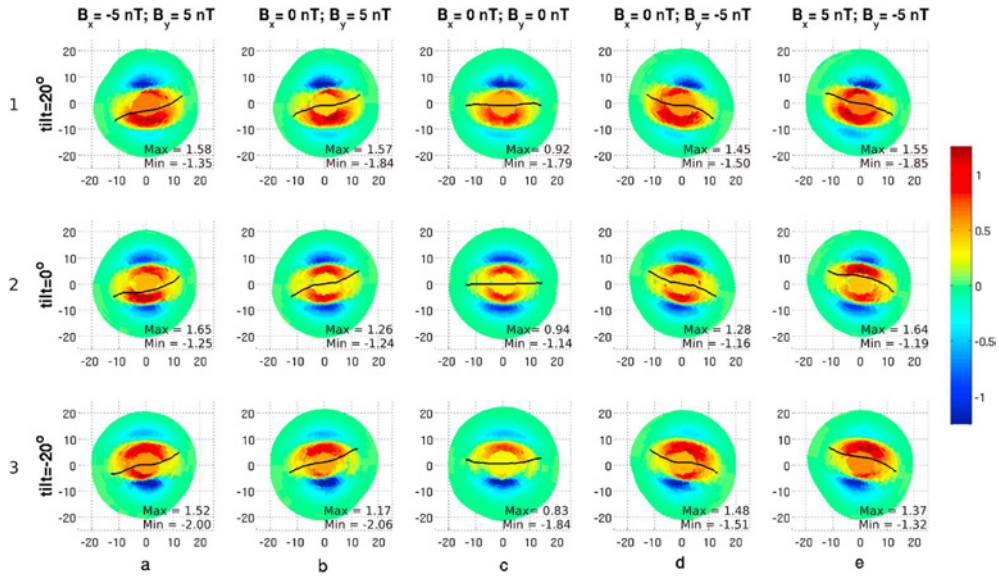

Figure 4. (a–e) Energy conversion through the magnetopause surface for different IMF components and dipole tilt angles from a viewpoint upstream of the magnetosphere. Color bar shows the energy conversion (defined as a divergence of the Poynting flux) through the magnetopause, unit 10^{-4} W/m^2, and black line marks the average position of the reconnection line. On the horizontal axis is the Y_{GSE}, and on the vertical axis the Z_{GSE}. Distances are in R_E. All runs have a southward IMF $B_z = -5$ nT. Min and max show the minimum (generator) and maximum (load) energy conversion value in each run.

simulation box) and forms the magnetosphere. When referring to the reconnection line location, we mean the projection of the line on the GSE *yz* plane from a viewpoint upstream of the magnetosphere.

For purely southward IMF and zero dipole tilt angle (Figure 4c (row 2)) the reconnection line is almost a straight line in a horizontal direction located at $z = 0$, and the energy conversion from magnetic to kinetic energy (red) and from kinetic to magnetic energy (blue) is located symmetrically on both sides of the reconnection line. Figure 4 shows that the results from opposite signs of B_x, B_y, and the dipole tilt angle are mirror images with respect to the *z* axis. For instance, the result from the run with positive B_x, positive dipole tilt angle, and negative B_y (Figure 4e, row 1) is a mirror image of the result of the run with negative B_x, negative dipole tilt angle, and positive B_y (Figure 4a, row 3).

We now concentrate on the different parameters affecting the reconnection line location and shape. In Figure 4 (row 2) we can see how the different values of IMF B_x and B_y affect the reconnection line location when the dipole tilt angle is zero. Figures 4b and 4d demonstrate the effect of the IMF B_y. When the reconnection line is projected to the *yz* plane, both of its ends curve away from the equatorial plane. When B_y is negative (Figure 4d), the duskside end of the reconnection line turns south, whereas the dawnside turns north; the shape is the same but mirrored when B_y is positive (Figure 4b). However, the reconnection line crosses through the subsolar point in both cases. Adding the B_x component keeps the ends of the reconnection line at the same position (B_y remains unchanged) but moves it away from the nose of the magnetopause. The middle parts of the reconnection line moves northward when B_x is positive (Figure 4e, row 2) and southward when B_x is negative (Figure 4a, row 2).

The effect of the dipole tilt angle on the reconnection line in our simulation is not as clear as the effect caused by the IMF components (see Figure 4c). Positive dipole tilt angle moves the reconnection line slightly southward for all IMF cases except B_x positive (Figure 4, row 1). As mentioned above, positive B_x moves the reconnection line northward which counterbalances the southward moving effect caused by the positive dipole tilt angle. Similarly, negative dipole tilt angle moves the reconnection line slightly northward for all IMF cases except B_x negative. In summary, for dipole tilt and IMF B_x sharing the same sign, the reconnection

line remains almost in the same location as when both dipole tilt and B_x are zero (cf. Figures 4e (row 1), 4d (row 2), 4a (row 3), and 4b (row 2)).

On the other hand, when the dipole tilt and B_x have opposite signs, their effects are combined and the reconnection line is pulled more south (north) for positive (negative) dipole tilt and negative (positive) B_x (see Figure 4a, row 1 (Figure 4e, row 3)) when compared to the case without either dipole tilt or B_x. To visualize these features, compare Figure 4a (row 1) (Figure 4e, row 3) with Figure 4b (row 1) (Figure 4d, row 3), tilt $\neq 0°$ and $B_x = 0$, and Figure 4a (row 2) (Figure 4e, row 2), tilt $= 0°$ and $B_x \neq 0$.

We also simulated cases with zero B_y and nonzero B_x with all three dipole tilt angles. The reconnection line location in these runs for different tilt angles behaves similarly as in the cases with nonzero B_y, but the shape of the line is more similar than in the cases with $B_x = B_y = 0$. In the case of zero dipole tilt, the reconnection line shifts northward (southward) from the nose of the magnetopause for positive (negative) B_x so that the line is bent slightly toward the equatorial plane closer to the flanks.

4.3. Energy Conversion

The effect of both dipole tilt angle and IMF B_x on the location and strength of the energy conversion is different from the effect on the reconnection line location. When $B_x = B_y = 0$ (Figure 4c) , the positive dipole tilt (Figure 4c, row 1) makes the load (red) region, where energy is converted from the magnetic to the kinetic form, larger below the reconnection line and also shifts the whole region slightly southward. The generator process on the nightside becomes stronger in the north and weaker in the south. These results are consistent with earlier results by *Palmroth et al.* [2012]. During purely southward IMF, the positive dipole tilt angle does not significantly affect the maximum value of the energy conversion of the load region which remains around $\sim 0.9 \cdot 10^{-4}$ W/m^2, but it does increase the maximum energy conversion value of the generator regions from $\sim 1.1 \cdot 10^{-4}$ W/m^2 to $\sim 1.8 \cdot 10^{-4}$ W/m^2. Negative dipole tilt, on the other hand, shifts the load region slightly northward, and the generator process becomes stronger in the south and weaker in the north, opposite to the effect of positive dipole tilt. The impact of negative dipole tilt is slightly stronger in the generator regions (minimum values in Figure 4 (row 3)) than in the case of positive dipole tilt (minimum values in Figure 4 (row 1)). It also makes the load region slightly weaker than in the cases of zero and positive dipole tilt. The results imply that for purely southward IMF conditions, the impact of the dipole tilt angle is stronger on the intensity of the generator regions than the intensity of the dayside load. For example, the energy conversion maximum absolute value in the generator regions increases 61% (57%) and the maximum value in the load region decreases 11% (2%), when the dipole tilt angle is changed from zero to negative (positive).

The impact of IMF B_y component with no dipole tilt (Figures 4b (row 2) and 4d (row 2)) on the energy conversion is minor. The load area becomes symmetric with respect to the reconnection line instead of plane $z = 0$. The maximum value of the energy conversion in the load region increases on average by a factor of 1.35, but there is no significant change (less than 3%) in minimum values of the generator regions. Adding the nonzero B_x makes the loads asymmetric with respect to the reconnection line. The whole load area has the same shape as in the case without B_x, but for positive (negative) B_x the energy conversion is much stronger above (below) the reconnection line (Figure 4e, row 2 (Figure 4a, row 2)). The maximum value of the energy conversion in the load region increases on average 75% due to the B_x component. The effect of B_x is not as clear on the generator regions as it is for the dayside load (increase in the maximum absolute value is 9% for negative B_x and 4% for positive B_x), although by looking at Figures 4a (row 2) and 4e (row 2) it can be said that the generator region in the Northern (Southern) Hemisphere becomes slightly larger and stronger than the one in the south (north) when B_x is negative (positive). This is a small effect but still noticeable.

When both B_x and dipole tilt angle are nonzero (Figures 4a (row 1), 4e (row 1), 4a (row 3), and 4e row 3) the maximum (minimum) value of the energy conversion in the load (generator) region is increased compared to the case with zero dipole tilt and zero IMF B_x (Figures 4b (row 2), 4c (row 2), and 4d (row 2)). For instance, in the case of positive B_x, the maximum value in the load increases 21% (7%) and the minimum value in the generators decreases 59% (14%) for positive (negative) dipole tilt compared to case with $B_x = 0$, $B_y = -5$ nT (Figure 4d, row 2). With nonzero B_x (Figures 4a and 4e), the maximum absolute value in the generator regions is enhanced and in the load region decreased when the dipole tilt is changed from zero to either positive or negative. For example, when B_x is positive, the maximum value in the load decreases 5% (16%) and the maximum absolute value in the generators increases 55% (11%) for positive (negative) dipole tilt. The negative dipole tilt seems to have a stronger effect on the generator absolute maximum energy

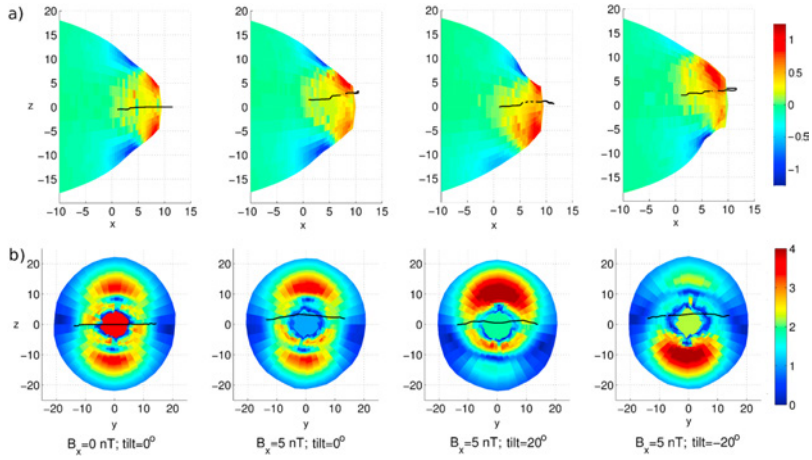

Figure 5. (a) The energy conversion (defined as a divergence of the Poynting flux) through the magnetopause surface for different IMF B_x values and dipole tilt angles viewed in the *xz* plane. Color bar unit is 10^{-4} W/m^2. On the horizontal axis is the X_{GSE}, and on the vertical axis the Z_{GSE}. (b) The magnetic field strength at the magnetopause. Color bar unit is 10 nT. On the horizontal axis is the Y_{GSE}, and on the vertical axis the Z_{GSE}. Black line marks the average position of the reconnection line and distances are in R_E. All runs have a southward IMF $B_y = 0$ and $B_z = -5$ nT.

conversion when the B_x is also negative: the absolute maximum generator value increases then by 60%. As the aforementioned results indicate, the dipole tilt angle affects more the intensity of the generator regions, whereas the effect of B_x on the generators is less significant.

Figure 5a shows the energy conversion through the magnetopause in the *xz* plane in four cases with zero IMF B_y. It shows that the positive dipole tilt moves the dayside load region south from the equatorial plane. The generator region magnetopause tailward of the cusp is bulged outward in the summer hemisphere indicating magnetic flux pileup there. This finding is in line with the results by *Palmroth et al.* [2010], who reported flux accumulation in the tail lobes.

The negative dipole tilt moves the load region northward. Figure 5 shows that IMF B_x does not have a clear impact on the magnetopause shape in our simulation, and the results described above show that neither has the IMF B_y. The energy conversion pattern behaves similarly as in the case of $B_x = B_y = 0$.

To investigate the origin of the stronger generator intensity as influenced by the dipole tilt angle, we show in Figure 5b the magnetic field strength at the magnetopause. This clearly shows how the dipole tilt angle puts stronger magnetic field in the generator region located in the summer hemisphere. The IMF B_x does not have a similar effect. IMF B_y causes asymmetry between the dawnside and duskside, which does not occur when $B_y = 0$. For example, negative B_y shifts the region of strong magnetic field strength (and thus the generator region) in the Northern Hemisphere toward the dawn and in the Southern Hemisphere toward the dusk.

5. Discussion

In this paper, we investigated the effect that the IMF B_x and B_y components and the dipole tilt angle have on the location of the reconnection line and the energy conversion at the magnetopause. The main goal was to study the effect of different combinations of these parameters systematically. We started by simulating the Earth's magnetopause conditions during a reconnection event observed on 14 July 2007, where two widely separated (~9 R_E) spacecraft, THEMIS A and Double Star TC1, cross the dayside magnetopause quasi-simultaneously, on each side of the noon-midnight meridian plane, and both of them observe reconnection signatures [see e. g., *Dunlop et al.*, 2011]. Both in situ observations and global MHD simulation results indicate that reconnection takes place as an extended and tilted line along the dayside magnetopause, supporting the component reconnection hypothesis [*Sonnerup*, 1970; *Gonzalez and Mozer*, 1974]. According to *Trattner et al.* [2007] the continuous reconnection line splits into two antiparallel type lines

when the ratio of IMF B_x and total B is 0.7 or above. At the time of the spacecraft magnetopause crossing, however, the IMF $|B_x|/B$ ratio is approximately 0.58, and no reconnection line splitting is expected. Our MHD simulation also suggests that the reconnection line is not split for this event.

By looking at the schematic Figure 3, it seems logical that reconnection occurs at the location where the IMF first makes contact with the magnetospheric field lines. For purely southward IMF this is clearly the nose of the magnetopause. In case of nonzero B_x the contact point moves either north or south depending on the sign of the B_x component. Positive IMF B_x appears in contact with magnetosphere north from the magnetopause nose and negative B_x south from the magnetopause nose. In the simulations, when the IMF is purely southward, the IMF and Earth's magnetic field are antiparallel at the nose of the magnetopause, which is where the reconnection also takes place. However, when the IMF is not due south, the region where the IMF and the magnetospheric field lines are exactly opposite is no longer at the nose of the magnetopause. During positive IMF B_x this region is north from the nose, and during negative B_x it moves southward. This is in general agreement with the reconnection line location found by the maximum magnetic shear approach developed by *Trattner et al.* [2007, 2012].

The dipole tilt angle clearly affects the magnitude and spatial distribution in the energy conversion of the generator regions as seen earlier by *Palmroth et al.* [2012]. Positive dipole tilt enhances the energy conversion in the Northern Hemisphere and negative dipole tilt in the Southern Hemisphere. The dipole tilt shifts the dayside nose region of the magnetopause away from the equatorial plane. Positive tilt shifts the dayside load region southward, which also brings the cusps and the generator region closer to the equatorial plane. Shifting of the dayside magnetopause and cusp regions have also been seen in other MHD simulation by *Liu et al.* [2012]. The generator region becomes stronger on the summer hemisphere, which is closer to the equatorial plane. This is likely due to the flux pileup, as the open field lines are more easily advected toward the summer hemisphere and therefore are also in better contact with the magnetopause. The piling up of the magnetic flux has also been seen by *Palmroth et al.* [2010]. The increased magnetic field in the generator regions leads to an increasing of the divergence of the Poynting flux, $-\nabla \cdot \mathbf{S} = \mathbf{J} \times \mathbf{B} \cdot \mathbf{V}$ ($\mathbf{E}$ is the electric field, $\mathbf{J}$ is the current density, and $\mathbf{V}$ is the plasma velocity), through the magnetopause. The increased flux and the flux pileup in the generator regions leads also to the bulging of the magnetopause in the summer hemisphere.

The dipole tilt angle shifts the load region toward the winter hemisphere. This explains why the IMF B_x affect the reconnection line location differently during negative and positive dipole tilt angle. For example, when the dipole tilt is positive and the load region is shifted southward, the location where reconnection takes place for positive IMF B_x is also shifted southward compared to the case without the dipole tilt. When the dipole tilt angle is negative, the load region is shifted northward and so is the reconnection line during positive IMF B_x. From this we deduce that the dipole tilt angle affects the shape of the dayside magnetopause, which in turn affects the location of the maximum magnetic shear. In other words, in terms of 3-D reconnection, the dipole tilt and IMF B_x both affect the geometry of the magnetic field and thus move the null points and the location of the null-null line over which the reconnection takes place.

6. Conclusion

Our study shows that magnetopause shape, reconnection, and energy conversion are tightly coupled together. The dipole tilt angle mainly affects the magnetopause shape by shifting the load region away from the equatorial plane toward the winter hemisphere and generator region in the summer hemisphere closer to the equatorial plane. The dipole tilt also enhances the magnitude of the energy conversion in the generator regions especially in the summer hemisphere. This is a result from a magnetic flux piling up in the summer lobe region. IMF B_x, instead, affects the location where the reconnection occurs at the dayside magnetopause. It also has a greater impact on the intensity of the energy conversion in the load region. When IMF B_x is nonzero, the effect of the dipole tilt angle on the reconnection line location is much more prominent compared to the cases without IMF B_x component.

Acknowledgments
The research was supported by project 138599 of the Academy of Finland and ERC Starting grant agreement 200141-QuESpace. We thank Andrew Fazekerley for providing PEACE electron data for Double Star TC1 and Vassilis Angelopoulos for the use of THEMIS data. We also acknowledge use of NASA/GSFC's Space Physics Data Facility's OMNIWeb service, and OMNI data.

Michael Liemohn thanks the reviewers for their assistance in evaluating this paper.

References

Anekallu, C. R., M. Palmroth, T. I. Pulkkinen, S. E. Haaland, E. Lucek, and I. Dandouras (2011), Energy conversion at the Earth's magnetopause using single and multispacecraft methods, *J. Geophys. Res.*, *116*, A11204, doi:10.1029/2011JA016783.

Anekallu, C. R., M. Palmroth, H. E. J. Koskinen, E. Lucek, and I. Dandouras (2013), Spatial variation of energy conversion at the Earth's magnetopause: Statistics from Cluster observations, *J. Geophys. Res. Space Physics*, *118*, 1948–1959, doi:10.1002/jgra.50233.

Angelopoulos, V. (2008), The THEMIS mission, *Space Sci. Rev.*, *141*, 5–34, doi:10.1007/s11214-008-9336-1.
Auster, H. U., et al. (2008), The THEMIS fluxgate magnetometer, *Space Sci. Rev.*, *141*, 235–264, doi:10.1007/s11214-008-9365-9.
Brackbill, J., and D. Barnes (1980), The effect of nonzero product of magnetic gradient and B on the numerical solution of the magnetohydrodynamic equations, *J. Comput. Phys.*, *35*(3), 426–430, doi:10.1016/0021-9991(80)90079-0.
Carr, C., et al. (2005), The Double Star magnetic field investigation: Instrument design, performance and highlights of the first year's observations, *Ann. Geophys.*, *23*, 2713–2732, doi:10.5194/angeo-23-2713-2005.
Crooker, N. U. (1979), Dayside merging and cusp geometry, *J. Geophys. Res.*, *84*, 951–959, doi:10.1029/JA084iA03p00951.
Dungey, J. W. (1961), Interplanetary magnetic field and the auroral zones, *Phys. Rev. Lett.*, *6*, 47–48, doi:10.1103/PhysRevLett.6.47.
Dunlop, M. W., et al. (2011), Extended magnetic reconnection across the dayside magnetopause, *Phys. Rev. Lett.*, *107*, 025004, doi:10.1103/PhysRevLett.107.025004.
Fazakerley, A. N., et al. (2005), The double star plasma electron and current experiment, *Ann. Geophys.*, *23*(8), 2733–2756, doi:10.5194/angeo-23-2733-2005.
Gonzalez, W. D., and F. S. Mozer (1974), A quantitative model for the potential resulting from reconnection with an arbitrary interplanetary magnetic field, *J. Geophys. Res.*, *79*, 4186–4194, doi:10.1029/JA079i028p04186.
Janhunen, P., M. Palmroth, T. Laitinen, I. Honkonen, L. Juusola, G. Facskó, and T. I. Pulkkinen (2012), The GUMICS-4 global MHD magnetosphere-ionosphere coupling simulation, *J. Atmos. Sol. Terr. Phys.*, *80*, 48–59, doi:10.1016/j.jastp.2012.03.006.
Komar, C. M., P. A. Cassak, J. C. Dorelli, A. Glocer, and M. M. Kuznetsova (2013), Tracing magnetic separators and their dependence on IMF clock angle in global magnetospheric simulations, *J. Geophys. Res. Space Physics*, *118*, 4998–5007, doi:10.1002/jgra.50479.
Laitinen, T. V., P. Janhunen, T. I. Pulkkinen, M. Palmroth, and H. E. J. Koskinen (2006), On the characterization of magnetic reconnection in global MHD simulations, *Ann. Geophys.*, *24*(11), 3059–3069, doi:10.5194/angeo-24-3059-2006.
Laitinen, T. V., M. Palmroth, T. I. Pulkkinen, P. Janhunen, and H. E. J. Koskinen (2007), Continuous reconnection line and pressure-dependent energy conversion on the magnetopause in a global MHD model, *J. Geophys. Res.*, *112*, A11201, doi:10.1029/2007JA012352.
Lau, Y. T., and J. M. Finn (1990), Three-dimensional kinematic reconnection in the presence of field nulls and closed field lines, *Astrophys. J.*, *350*, 672–691, doi:10.1086/168419.
Liu, Z.-Q., J. Y. Lu, K. Kabin, Y. F. Yang, M. X. Zhao, and X. Cao (2012), Dipole tilt control of the magnetopause for southward IMF from global magnetohydrodynamic simulations, *J. Geophys. Res.*, *117*, A07207, doi:10.1029/2011JA017441.
Liu, Z. X., C. P. Escoubet, Z. Pu, H. Laakso, J. K. Shi, C. Shen, and M. Hapgood (2005), The Double Star mission, *Ann. Geophys.*, *23*, 2707–2712, doi:10.5194/angeo-23-2707-2005.
Luhmann, J. G., R. J. Walker, C. T. Russell, N. U. Crooker, J. R. Spreiter, and S. S. Stahara (1984), Patterns of potential magnetic field merging sites on the dayside magnetopause, *J. Geophys. Res.*, *89*(A3), 1739–1742, doi:10.1029/JA089iA03p01739.
McFadden, J. P., C. W. Carlson, D. Larson, M. Ludlam, R. Abiad, B. Elliott, P. Turin, M. Marckwordt, and V. Angelopoulos (2008), The THEMIS ESA plasma instrument and in-flight calibration, *Space Sci. Rev.*, *141*, 277–302, doi:10.1007/s11214-008-9440-2.
Palmroth, M., T. I. Pulkkinen, P. Janhunen, and C.-C. Wu (2003), Stormtime energy transfer in global MHD simulation, *J. Geophys. Res.*, *108*(A1), 1048, doi:10.1029/2002JA009446.
Palmroth, M., H. E. J. Koskinen, T. I. Pulkkinen, P. K. Toivanen, P. Janhunen, S. E. Milan, and M. Lester (2010), Magnetospheric feedback in solar wind energy transfer, *J. Geophys. Res.*, *115*, A00I10, doi:10.1029/2010JA015746.
Palmroth, M., H. E. J. Koskinen, T. I. Pulkkinen, C. R. Anekallu, T. V. Laitinen, E. A. Lucek, and I. Dandouras (2011a), Quantifying energy transfer at the magnetopause, in *The Dynamic Magnetosphere*, vol. 3, edited by W. Liu and M. Fujimoto, pp. 29–37, IAGA Special Sopron Book Series, Springer, Houten, Netherlands, doi:10.1007/978-94-007-0501-2_2.
Palmroth, M., T. V. Laitinen, C. R. Anekallu, T. I. Pulkkinen, M. Dunlop, E. A. Lucek, and I. Dandouras (2011b), Spatial dependence of magnetopause energy transfer: Cluster measurements verifying global simulations, *Ann. Geophys.*, *29*(5), 823–838, doi:10.5194/angeo-29-823-2011.
Palmroth, M., R. C. Fear, and I. Honkonen (2012), Magnetopause energy transfer dependence on the interplanetary magnetic field and the Earth's magnetic dipole axis orientation, *Ann. Geophys.*, *30*(3), 515–526, doi:10.5194/angeo-30-515-2012.
Peng, Z., C. Wang, and Y. Q. Hu (2010), Role of IMF B_X in the solar wind-magnetosphere-ionosphere coupling, *J. Geophys. Res.*, *115*, A08224, doi:10.1029/2010JA015454.
Roe, P. (1981), Approximate Riemann solvers, parameter vectors, and difference schemes, *J. Comput. Phys.*, *43*(2), 357–372, doi:10.1016/0021-9991(81)90128-5.
Russell, C. T., Y. L. Wang, and J. Raeder (2003), Possible dipole tilt dependence of dayside magnetopause reconnection, *Geophys. Res. Lett.*, *30*(18), 1937, doi:10.1029/2003GL017725.
Siscoe, G. L., and W. D. Cummings (1969), On the cause of geomagnetic bays, *Planet. Space Sci.*, *17*, 1795–1802, doi:10.1016/0032-0633(69)90055-5.
Sonnerup, B. U. O. (1970), Magnetic-field re-connexion in a highly conducting incompressible fluid, *J. Plasma Phys.*, *4*, 161–174, doi:10.1017/S0022377800004888.
Trattner, K. J., J. S. Mulcock, S. M. Petrinec, and S. A. Fuselier (2007), Probing the boundary between antiparallel and component reconnection during southward interplanetary magnetic field conditions, *J. Geophys. Res.*, *112*, A08210, doi:10.1029/2007JA012270.
Trattner, K. J., S. M. Petrinec, S. A. Fuselier, and T. D. Phan (2012), The location of reconnection at the magnetopause: Testing the maximum magnetic shear model with THEMIS observations, *J. Geophys. Res.*, *117*, A01201, doi:10.1029/2011JA016959.

Paper III

Reconnection rates and X-line motion at the magnetopause: Global 2D-3V hybrid-Vlasov simulation results

Journal of Geophysical Research: Space Physics
volume 122, 2017
doi:10.1002/2016JA023709

AGU PUBLICATIONS

JGR

Journal of Geophysical Research: Space Physics

RESEARCH ARTICLE
10.1002/2016JA023709

Reconnection rates and X line motion at the magnetopause: Global 2D-3V hybrid-Vlasov simulation results

Sanni Hoilijoki[1], Urs Ganse[1], Yann Pfau-Kempf[1], Paul A. Cassak[2], Brian M. Walsh[3], Heli Hietala[4], Sebastian von Alfthan[5], and Minna Palmroth[1,6]

[1]Department of Physics, University of Helsinki, Helsinki, Finland, [2]Department of Physics and Astronomy, West Virginia University, Morgantown, West Virginia, USA, [3]Mechanical Engineering and Center for Space Physics, Boston University, Boston, Massachusetts, USA, [4]Department of Earth, Planetary and Space Sciences, University of California, Los Angeles, California, USA, [5]CSC-IT Center for Science Ltd., Espoo, Finland, [6]Finnish Meteorological Institute, Helsinki, Finland

Abstract We present results from a first study of the local reconnection rate and reconnection site motion in a 2D-3V global magnetospheric self-consistent hybrid-Vlasov simulation with due southward interplanetary magnetic field. We observe magnetic reconnection at multiple locations at the dayside magnetopause and the existence of magnetic islands, which are the 2-D representations of flux transfer events. The reconnection locations (the X lines) propagate over significant distances along the magnetopause, and reconnection does not reach a steady state. We calculate the reconnection rate at the location of the X lines and find a good correlation with an analytical model of local 2-D asymmetric reconnection. We find that despite the solar wind conditions being constant, the reconnection rate and location of the X lines are highly variable. These variations are caused by magnetosheath fluctuations, the effects of neighboring X lines, and the motion of passing magnetic islands.

Key Points:
- We study dayside magnetic reconnection in a global magnetospheric self-consistent hybrid-Vlasov simulation
- Flux transfer events are always present and the dayside X lines are influenced both by magnetosheath properties and other reconnection sites
- The local reconnection rate correlates well with an analytic prediction

Supporting Information:
- Supporting Information S1
- Movie S1

Correspondence to:
S. Hoilijoki,
sanni.hoilijoki@fmi.fi

Citation:
Hoilijoki, S., U. Ganse, Y. Pfau-Kempf, P. A. Cassak, B. M. Walsh, H. Hietala, S. von Alfthan, and M. Palmroth (2017), Reconnection rates and X line motion at the magnetopause: Global 2D-3V hybrid-Vlasov simulation results, *J. Geophys. Res. Space Physics*, *122*, doi:10.1002/2016JA023709.

Received 23 NOV 2016
Accepted 12 FEB 2017
Accepted article online 17 FEB 2017

1. Introduction

Magnetic reconnection takes place when magnetic field with a component that changes direction undergoes a change in topology [*Dungey*, 1953]. At the dayside magnetopause of the Earth's magnetosphere during southward interplanetary magnetic field (IMF), solar wind magnetic field lines reconnect with the terrestrial field. The resulting field lines advect tailward with the solar wind flow allowing mixing between magnetospheric and magnetosheath plasmas [*Dungey*, 1961]. Much has been learned about reconnection at the dayside magnetopause, but there remain a number of open questions. Here we address the following—is reconnection laminar or bursty for steady solar wind conditions, how does structure in the magnetosheath impact dayside reconnection, what controls the reconnection rate at the dayside, and what controls the motion of flux transfer events when reconnection is bursty. A lot of work has been done on these questions using global magnetospheric simulations with magnetohydrodynamic (MHD) models, but as we argue below, these questions require a kinetic approach. We address these questions using global magnetospheric simulations with a hybrid code using the Vlasov description for ions and a fluid model for electrons.

Difficulty in predicting the local reconnection rate at the dayside magnetopause is due to the fact that the reconnecting plasmas on the two sides of the reconnecting current sheet are dissimilar: the process is asymmetric; density is usually higher and magnetic field lower in the magnetosheath than in the magnetosphere. The reconnection rate, a local measure of the efficiency of the reconnection process, can be determined by the amount of magnetic flux reconnected. The reconnection rate in two-dimensional (2-D) asymmetric reconnection has been found to depend on the plasma parameters in both inflow regions [*Cassak and Shay*, 2007], but this study employed a rectangular geometry, so it is not clear whether the theory applies to the magnetosphere. Using a global magnetohydrodynamic (MHD) simulation, both *Borovsky et al.* [2008] and *Ouellette et al.* [2014] have found that the dayside reconnection rate agrees with the analytical equations derived by *Cassak and Shay* [2007] during southward IMF, indicating that the reconnection rate at the magnetopause is driven by local plasma conditions. *Komar and Cassak* [2016] tested the theory against the local reconnection rate in global resistive MHD simulations using oblique IMF directions. They found very good agreement in the scaling sense, with excellent absolute results for southward IMF and an increasing multiplicative offset for decreasing clock angle. However, these tests employed an MHD model. Even in the slab geometry, MHD has limitations

for studying asymmetric reconnection, because the plasma mixing in the exhaust is not described realistically [*Cassak and Shay*, 2009; *Birn et al.*, 2010; *Ouellette et al.*, 2014]. This suggests that a kinetic simulation is better to test the reconnection model.

Reconnection at the magnetopause can lead to the development of flux transfer events (FTEs) that are usually observed as bipolar variations in the magnetic field component normal to the local magnetopause [*Russell and Elphic*, 1978]. The structures are typically observed during southward IMF orientations [e.g., *Kawano and Russell*, 1997; *Wang et al.*, 2005, 2006; *Fear et al.*, 2009, 2010; *Eastwood et al.*, 2012]. In some observational studies, FTEs have also been found to occur as nearly periodic phenomena with average spacing of 8 min [*Rijnbeek et al.*, 1984]. Different theories about the formation mechanisms of FTEs include temporally varying single X line reconnection [*Scholer*, 1988; *Southwood et al.*, 1988] and multiple X line reconnection [*Lee and Fu*, 1985].

Whether the dayside magnetopause reconnection is manifested in single or multiple X line configurations, i.e., whether it is steady or patchy under different solar wind conditions, is not yet well known. Our understanding is limited by the localized nature of individual spacecraft measurements and because most numerical studies used MHD models, which does not describe reconnection physics well in the nearly collisionless magnetosphere. Multiple X line reconnection and/or formation of FTEs has been simulated using global MHD models [e.g., *Fedder et al.*, 2002; *Raeder*, 2006; *Dorelli and Bhattacharjee*, 2009]. *Shi et al.* [1988] found using a 2-D MHD simulation that if the magnetic Reynolds number is high, multiple X lines exist simultaneously, while with a low magnetic Reynolds number, reconnection occurs on a single X line. *Raeder* [2006] reported multiple X lines and formation of FTEs in an MHD simulation during southward IMF with large dipole tilt angle, but without the dipole tilt, the reconnection took place only at one steady X line. However, using a resistive MHD simulation, *Dorelli and Bhattacharjee* [2009] showed that FTEs can also form without a dipole tilt. Yet MHD simulations do not include ion scale physics and therefore are not able to describe, for example, the microphysics of reconnection and foreshock and magnetosheath waves unlike hybrid-PIC and hybrid-Vlasov simulations [e.g., *Blanco-Cano et al.*, 2006, 2009; *Karimabadi et al.*, 2014; *Kempf et al.*, 2015]. Previous studies employing 2-D hybrid-PIC simulations have shown the formation of multiple X lines and FTE with southward IMF and no dipole tilt [*Karimabadi et al.*, 2006; *Omidi and Sibeck*, 2007; *Sibeck and Omidi*, 2012]. Similar results have also been found with 3-D global hybrid-PIC simulations [*Karimabadi et al.*, 2006; *Tan et al.*, 2011]. Variations of the local reconnection rate at the multiple X lines and the plasma parameters that affect the reconnection rate have not been investigated before using a global hybrid simulation.

The motion of X lines has been studied both theoretically and using spacecraft measurements. In a theoretical consideration, *Cowley and Owen* [1989] suggested that the magnetosheath flows affect the motion of newly reconnected flux tubes, which may also be manifested in the motion of the X line itself. *Doss et al.* [2015] found that X lines advect during asymmetric reconnection if there is a velocity shear between the upstream and downstream region. However, the motion of X lines and the parameters that affect it have not been studied in global ion kinetic models. In a global 2-D setup using hybrid-PIC simulations, *Sibeck and Omidi* [2012] studied the formation and propagation of FTEs. In the simulation, FTEs formed between two X lines remaining almost steadily at the subsolar point before they started moving poleward. Some of the structures started moving initially toward the equator before coalescing with other FTEs and escaping poleward.

In this paper we present the first results on the variations of the local reconnection rate and X line motion on the magnetopause as manifested in a global 2D-3V kinetic simulation describing the solar wind-magnetosphere interaction self-consistently. We locate the X lines at the dayside magnetopause and calculate reconnection rates at these points. We find a general agreement with the analytical model derived by *Cassak and Shay* [2007]. We also demonstrate that reconnection takes place continuously at the dayside magnetopause but the location of the dominant X line can move significantly over time even though the solar wind is kept constant and the IMF direction is maintained as due south.

2. Vlasiator Simulation

We use the hybrid-Vlasov code Vlasiator (http://vlasiator.fmi.fi), which is a global simulation code modeling the Earth's magnetosphere using a kinetic physical description [*von Alfthan et al.*, 2014]. Ions are treated as 3-D velocity distribution functions propagated by the Vlasov equation, while electrons are a charge-neutralizing fluid. For a more detailed technical description of Vlasiator, see *von Alfthan et al.* [2014] and *Kempf et al.* [2015].

However, note that those papers did not include the Hall term in the generalized Ohm's law, which was added in the version described in *Palmroth et al.* [2015]; we use the version with the Hall term in this study.

The simulation discussed in this paper is carried out in the Geocentric Solar Ecliptic (GSE) polar *xz* plane in a 2-D setup in ordinary space, while the velocity space in each cell is 3-D. A 2-D line dipole corresponding to the Earth's dipole strength is applied as in *Daldorff et al.* [2014]. While the simulation box extends from $x = -94\ R_E$ to $+48\ R_E$ and in the *z* direction to $\pm 56\ R_E$, we concentrate in this paper only on dayside phenomena. The solar wind with constant magnetic field and Maxwellian velocity distributions flows in from the sunward wall while a copy condition is applied at the other three boundaries; i.e., at the boundary cells the velocity distribution function and magnetic field are copied from the nearest spatial cell that is inside the simulation domain. The resolution is uniform in the entire simulation domain: 300 km in ordinary space and 30 km/s in velocity space. The IMF is purely southward with a magnitude of 5 nT. The number density in the solar wind is $n = 1\ \mathrm{cm}^{-3}$ and the velocity is −750 km/s along the *x* axis. The proton temperature in the solar wind plasma is 0.5 MK. Initially, the whole simulation domain includes constant density and bulk velocity set to the same values as in solar wind and the dipole magnetic field. The magnetosphere, magnetosheath, and the bow shock form self-consistently as the inflowing solar wind interacts with the dipole field. We consider that the dayside magnetosheath and magnetopause are initialized when the inflowing solar wind with southward IMF has crossed the magnetosheath and has reached the subsolar point of the dayside magnetopause. This happens approximately at 800 s simulated time.

3. Results

3.1. Magnetosheath

The results show a number of dynamic kinetic features. Figure 1a shows the ratio of plasma pressure to the magnetic pressure (plasma β) on the dayside magnetosheath and magnetopause (at $t = 1800$ s simulated time) showing large β variations. Waves in the magnetosheath in our simulation have an anticorrelation between magnetic field and density fluctuations as shown in Figure 1c, suggesting that these waves could be mirror mode waves. We test the magnetosheath waves against the mirror mode criteria as has been done previously in the equatorial plane simulation by *Hoilijoki et al.* [2016]. In this study we used the same criteria as those used by *Genot* [2009]. First, mirror mode waves are known to have large amplitude [e.g., *Tatrallyay*, 2005; *Genot*, 2009] and, therefore, we require the standard deviation of the fluctuations of the magnetic field magnitude to be larger than 10%. The linear polarization of waves is checked by calculating the angle between the background magnetic field and the maximum variance direction, which is required to be smaller than 20° [*Genot*, 2009; *Genot*, 2011]. The waves in the magnetosheath, from the central sheath to the vicinity of the magnetopause near the equatorial region fulfill these criteria. The mirror mode waves advect toward the dayside magnetopause where reconnection takes place at many X lines simultaneously.

3.2. Motion of X Lines

Multiple magnetic islands, 2-D representations of FTEs, are forming and evolving at the magnetopause throughout the simulation after the dayside magnetosphere has been initialized. Figure 1b shows the *z* component of the plasma velocity v_z at time 1800 s with magnetic field lines shown in black. At that time, the strongest X line, where the plasma flow along the magnetopause diverts between north and south, is located close to $z = -0.8\ R_E$. Just north of this X line, a large FTE is forming. In addition, multiple other X lines are present simultaneously, but the reconnection at these X lines is not strong enough to divert the plasma flow northward and southward.

We determine the locations of magnetic reconnection points and centers of magnetic islands (X and O points) by finding the local saddle points and maxima, respectively, of the magnetic flux function Ψ that is calculated from $\mathbf{B} = \hat{\mathbf{y}} \times \nabla\Psi$ by integrating $\mathbf{B}$ over the whole simulation domain [e.g., *Yeates and Hornig*, 2011]; magnetic field lines are lines of constant Ψ. The raw flux function is smoothed by convolution with a 5×5 box kernel to decrease the number of points yielded by this sensitive method. Figure 2 indicates the *z* coordinate of the magnetopause X points (black) and O points (yellow) as a function of time. The background is color coded with the *z* component of the bulk velocity V_z measured at the magnetopause and plotted as a function of *z* and time. This plot depicts the location of the strongest X line. This point moves between $z = \pm 3\ R_E$, and occasionally there are two stronger X lines that are able to divert the flow. Figure 2 visualizes how both the X lines and magnetic islands move along the magnetopause. To illustrate the motion of the X lines and magnetic islands, we present a movie of V_z in the dayside magnetosheath (see Movie S1 in the supporting information).

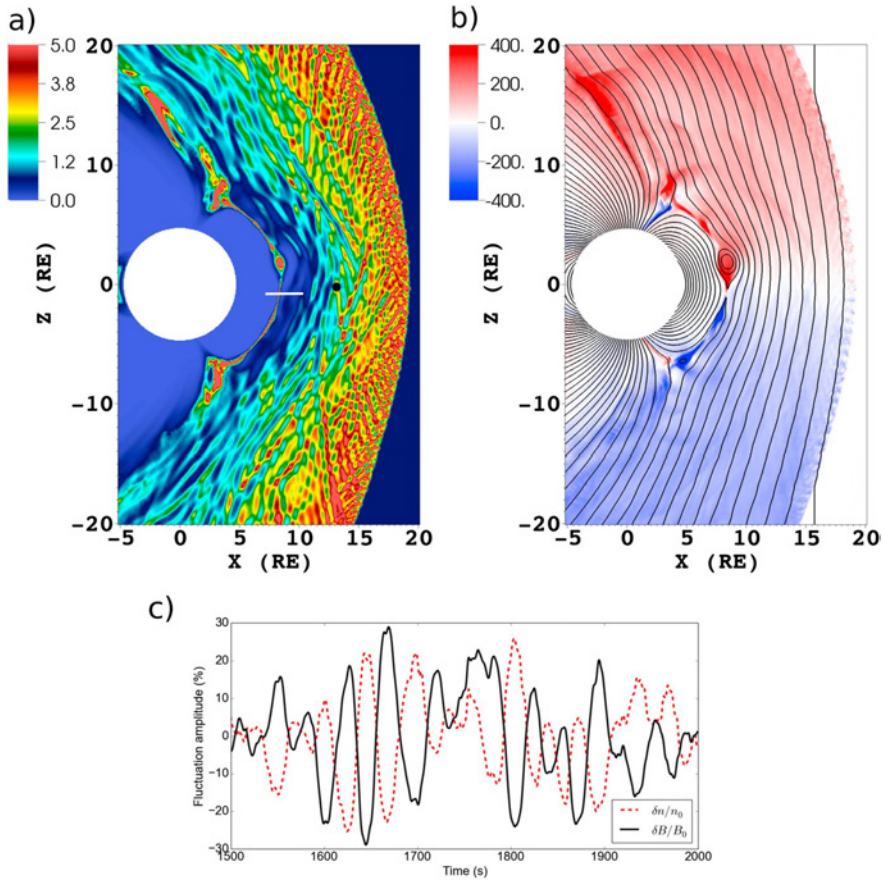

Figure 1. (a) Plasma β and (b) V_z in km/s at time $t = 1800$ s. The black lines show the magnetic field lines. The white line depicts the cut through the magnetopause discussed in Figure 7. Distances are given in R_E. (c) Magnetic field strength (black solid) and density (red dashed) fluctuations from the virtual spacecraft location indicated with the black dot in Figure 1a.

Instead of traveling from the subsolar point toward the poles in the same direction with the magnetosheath plasma flow, some of the X lines and FTEs propagate also toward the subsolar point, change direction, and decelerate or accelerate similar to what was previously reported by *Sibeck and Omidi* [2012]. The motion of the X lines seems to be dependent not only on magnetosheath flow but also on the propagation and the outflow velocities of nearby X lines. The dayside reconnection does not attain a steady state during the simulation even though solar wind parameters are kept constant.

3.3. Reconnection Rate at the X Lines

Figure 3 shows the location of the X lines and O points as in Figure 2, but now the X line markers are color coded with the local reconnection rate, i.e., the out-of-plane electric field E_y at the X line. The reconnection rate is positive when the reconnection takes place between magnetospheric and solar wind magnetic field lines. However, sometimes in Figure 3 the reconnection rate switches from positive to negative. The negative values indicate reconnection between magnetic field lines of newly formed magnetic islands. Coalescing of two magnetic islands is illustrated in Figure 4, which shows a region from the dayside magnetopause at four different time steps. Figure 4a, at $t = 1650$ s, shows the formation of a new magnetic island (labeled as FTE 1 in Figures 3 and 4) near $z = -1\ R_E$ between two X lines (labeled as X1 and X2). At this time the reconnection rate

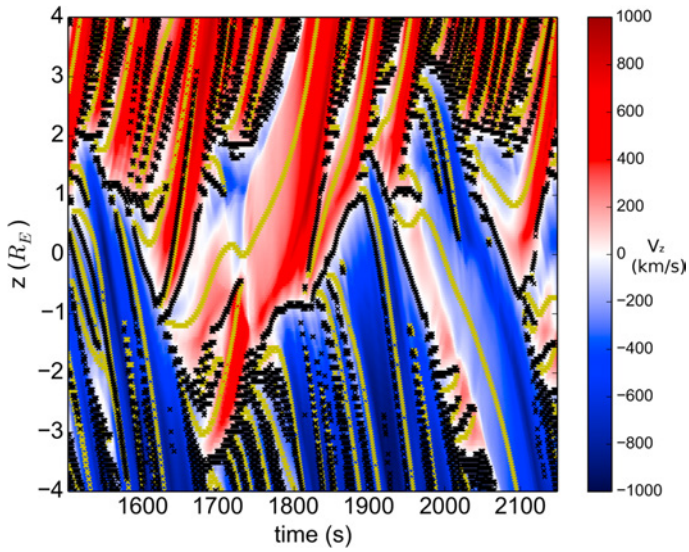

Figure 2. Location of X points (black) and O points (yellow) at the magnetopause and the color coding shows the z component of the ion bulk velocity V_z (km/s) at the magnetopause over time.

at these two X lines is positive. In Figures 4b and 4c two magnetic islands, the one forming in Figure 4a located now at the subsolar point (FTE 1) and another one coming from the south (FTE 2), coalesce. The reconnection rate at the X line between these two islands (X2) turns negative for about 15 s, and finally, the X line disappears as seen also in Figure 3. In Figure 4d at time $t = 1800$ s the large FTE formed by multiple coalesced magnetic islands accelerates toward the northern cusp.

3.4. Comparison With Analytical Prediction

We calculate the reconnection rate analytically using the *Cassak and Shay* [2007] formula for all X lines between $z = \pm 4R_E$. The reconnection rate E_{pred} is given as a function of the upstream magnetic field magnitude B, upstream mass density ρ, and inflow velocity v:

$$E_{\text{pred}} \sim V_{\text{AH}} \left(\frac{B_1 B_2}{B_1 + B_2} \right) \frac{2\delta}{L} = \frac{B_1 B_2 (\rho_1 v_1 + \rho_2 v_2)}{\rho_1 B_2 + \rho_2 B_1}, \tag{1}$$

where δ/L is the aspect ratio of the dissipation region, δ is the half width, and L the half length of the reconnection dissipation region. Subscript 1 stands for the values on the magnetospheric side of the X line and subscript 2 stands for the magnetosheath values. For the reconnecting magnetic field values, B_1 and B_2, we use the tangential components corresponding to the L components in a boundary normal coordinate system (B_{L1} and B_{L2}) of the magnetic field in the inflow plasma regions. Variations in the out-of-plane component of the magnetic field (B_y) close to the magnetopause is less than 1% of the magnetic field on the simulation plane. For inflowing velocities, v_1 and v_2, we use the components normal to the local magnetopause (v_{N1} and v_{N2}). In writing the equality, we have eliminated δ/L using the expression from *Cassak and Shay* [2007] for mass conservation:

$$\delta/L \sim \frac{\rho_1 v_1 + \rho_2 v_2}{2\rho_{\text{out}} V_{\text{AH}}}, \tag{2}$$

where we use the following relations for the outflow density $\rho_{\text{out}} \sim (\rho_1 B_2 + \rho_2 B_1)/(B_1 + B_2)$ and the hybrid Alfvén velocity $V_{\text{AH}} \sim \sqrt{B_1 B_2 (B_1 + B_2)/\mu_0 (\rho_1 B_2 + \rho_2 B_1)}$.

To test whether equation (2) holds in the Vlasiator simulation, we consider the time period when one X line remains roughly at the same location for about 50 s from $t = 1775$ s to 1825 s at $z \approx -0.9\,R_E$ (black square box in Figure 2). Because the outflow is not symmetric, we generalize equation (2) by using

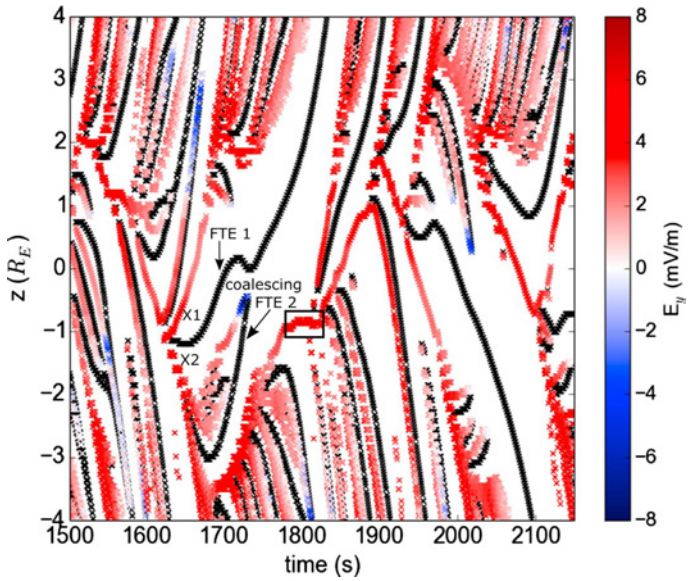

Figure 3. Location of X points (color coding) and O points (black) along the magnetopause z component. The color coding on the X point locations shows the measured local reconnection rate E_y. Labeled X lines and FTEs refer to section 3.2 and the rectangular box refers to sections 3.4 and 3.5.

$\rho_{\text{out},S}v_{\text{out},S} + \rho_{\text{out},N}v_{\text{out},N}$ instead of $2\rho_{\text{out}}V_{\text{out}}$ [*Murphy*, 2010]. Subscripts S and N stand for southward and northward outflow, respectively. Equation (2) becomes

$$\delta/L \sim \frac{\rho_1 v_1 + \rho_2 v_2}{\rho_{\text{out},S}v_{\text{out},S} + \rho_{\text{out},N}v_{\text{out},N}}. \tag{3}$$

As inflow parameters we use the same values that are used to calculate the reconnection rate prediction. The aspect ratio is obtained by calculating the square root of the ratio of the eigenvalues of the Hessian matrix at the X line as was done previously by *Servidio* [2009] and *Servidio*, [2010]: $\delta/L \sim \sqrt{\lambda_{\min}/\lambda_{\max}}$. The mean of the aspect ratio calculated over the considered time period yields 0.225. We estimate 2δ as one half the width of the J_y peak across the magnetopause and use the aspect ratio to calculate L. The outflow density and velocity are taken from a distance L from the X line location. The mean of the ratio of the inflowing and outflowing ρv is 0.234. The good match between these two values shows that equation (3) holds and can be used.

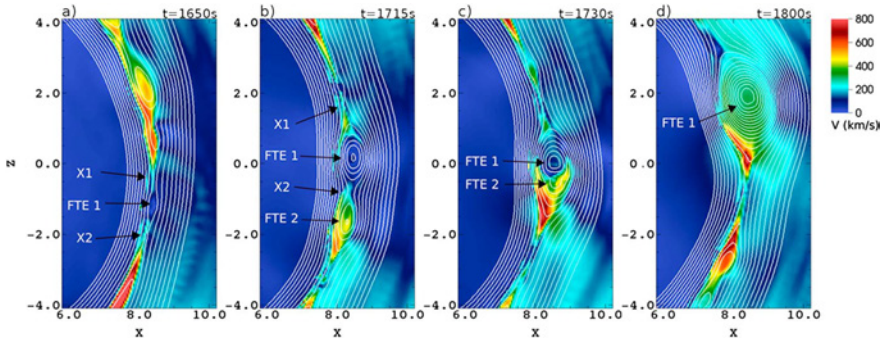

Figure 4. Cut from the dayside magnetopause at four different times (a) $t = 1650$ s, (b) $t = 1715$ s, (c) $t = 1730$ s, and (d) $t = 1800$ s. Color coding shows the magnitude of ion bulk velocity v (km/s), and the white lines depict the magnetic field lines.

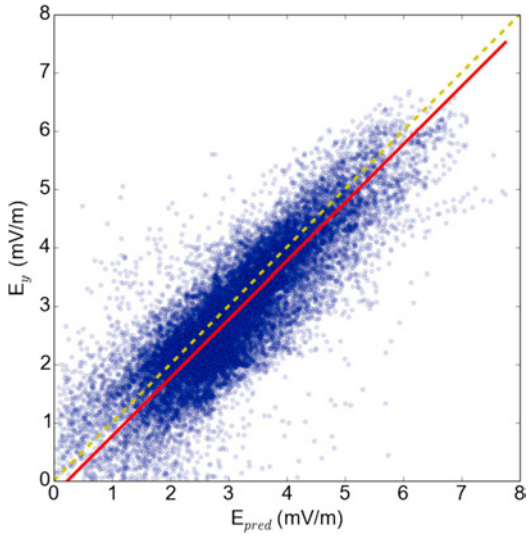

Figure 5. A scatterplot of the analytical prediction of the reconnection rate (*x* axis) and the measured reconnection rate (*y* axis). The yellow dashed line shows where these two would be equal, and the red solid line shows the orthogonal least squares fit $E_y = E_{\text{pred}} - 0.2$ mV/m.

All upstream parameters are taken from a distance of 1200 km ~0.19 R_E from the magnetopause, which corresponds approximately to nine ion inertial lengths of the magnetosheath, from the magnetopause along the magnetopause normal. This distance was chosen by (1) estimating where the current density *J*, *B*, and ρ level off after crossing the magnetopause, as well as, (2) testing which distance gives the best correlation and fit between the measured and predicted reconnection rate. Increasing or decreasing the distance worsen both the correlation coefficient and the least square orthogonal fit. The magnetopause location is determined by finding the B_z reversal, and the normals are calculated by forming a *B* spline fit of the magnetopause points and finding its normal directions.

In Figure 5 blue dots show the scatterplot between E_{pred} from equation (1) and the measured reconnection rate E_y. The yellow dashed line indicates where the two quantities are equal, and the red solid line is an orthogonal least squares fit that yields $E_y = E_{\text{pred}} - 0.2$ mV/m. The Pearson correlation coefficient between the measured and analytical prediction is 0.85. The results suggest that there is an overall good agreement with the predicted reconnection rate. However, there is some scatter in the data, so it is useful to investigate reasons why the match is not ideal.

One effect that could alter the reconnection rate is the presence of the magnetosheath flow, which was not included in the original model. It has been suggested that this flow can slow and even stop reconnection [e.g., *Mitchell Jr. and Kan*, 1978; *La BelleHamer et al.*, 1994; *Chen et al.*, 1997; *Li and Ma*, 2010; *Cassak and Otto*, 2011]. *Doss et al.* [2015] derived an analytical formula for the reconnection rate similarly as *Cassak and Shay* [2007] but for the case when there is an in-plane velocity shear between the inflowing regions. The correction term to the reconnection rate due to the shear is $1 - (v_{\text{shear}}/V_{\text{AH}})^2(4\rho_1 B_{L2}\rho_2 B_{L1})/(\rho_1 B_{L2} + \rho_2 B_{L1})^2$, where $v_{\text{shear}} = (v_{L1} - v_{L2})/2$ and the v_L components are in the outflow direction tangential to the magnetopause. For the present simulation, the effect of the correction term in the reconnection rate results is insignificant, yielding the same least squares fit and correlation coefficient when it is compared to the measured reconnection rate. This is very reasonable since we are only looking at X lines within 4 R_E of the subsolar point, so the flow shear is expected to be small. In addition, *Doss et al.* [2015] derived a formula for the drift speed of an isolated X line when there is a velocity shear: $v_{\text{drift}} \sim (\rho_1 B_{L2} v_{L1} + \rho_1 B_{L2} v_{L1})/(\rho_1 B_{L2} + \rho_2 B_{L1})$. In our simulation, the predicted v_{drift} for the X lines near the subsolar region often points in the opposite direction than the X lines are moving. This indicates that the other effects, such as outflow jets from nearby X lines, are more

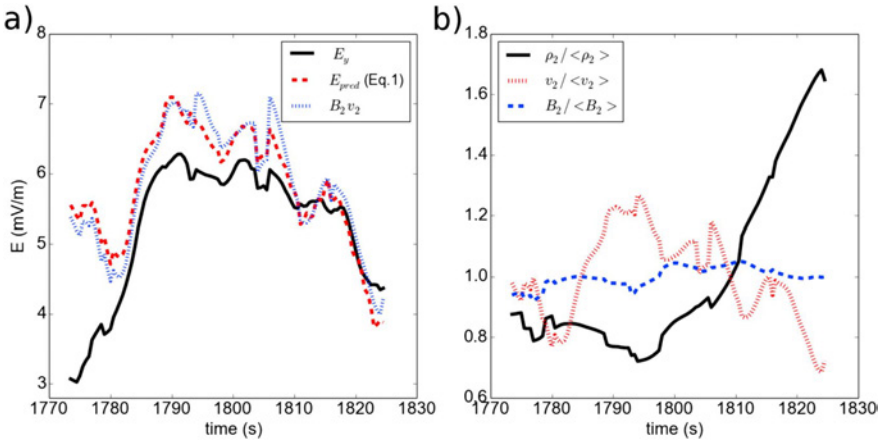

Figure 6. (a) Reconnection rate at the steady X line location (black line), corresponding rate given by equation (1) (red dashed line) and B_2v_2 (blue dotted line), where the subscript 2 stands for magnetosheath inflow values. (b) Inflow density ρ_2 (black solid line), ion velocity v_2 (red dotted line), and tangential magnetic field component B_2 (blue dashed line) scaled by their time averages from the point where the magnetosheath values are read for equation (1).

important in defining the absolute X line motion near the subsolar region, consistent with the discussion in *Doss et al.* [2015].

Another reason for the differences between the measured and analytical reconnection rate is the possible inaccuracy of measuring the inflowing parameters as well as locating the X lines where the E_y is measured. The variance between the E_y values at the X line and its neighboring cells could be of the same order of magnitude than the difference between the measured and predicted rate. The fraction of points having a large difference between the measured and analytical reconnection rates increases slightly with latitude. At higher latitudes the X lines move faster, as does the magnetosheath plasma. The motion might cause inaccuracy in measuring the inflow values. Similarly, the choice of the distance, where the inflow values are taken, affects the correlation as mentioned above.

We do not assume that the aspect ratio δ/L is constant as has been done previously [e.g., *Borovsky et al.*, 2008], but we eliminated δ/L from equation (1) using the relation given by equation (2). Interestingly, when we test equation (1) with an assumed value of $\delta/L = 0.1$, we find that the Pearson correlation coefficient becomes significantly worse and is only 0.3. This implies that δ/L is not constant for our simulations. We suspect that the cause of the aspect ratio not being fixed at 0.1 is because we are not resolving the ion inertial scale with our computational grid, so the reconnection is likely more Sweet-Parker-like governed by grid scale diffusion, consistent with a varying aspect ratio.

3.5. Effect of Magnetosheath Parameters

To check whether magnetosheath waves have an effect on the reconnection rate, we consider again the X line that remains roughly at the same location for about 50 s from $t = 1775$ s to 1825 s at $z \approx -0.9\,R_E$ (black box in Figure 2). We plot the measured reconnection rate at the steady X line in Figure 6a (black), and in the same panel we plot the corresponding theoretical rate given by equation (1) (red dashed line). During this time period the Pearson correlation coefficient between these two is 0.73. The reconnection rate variations are dominated by the magnetosheath plasma parameters. Setting B_1, ρ_1, and v_1 (subscript 1 stands for magnetospheric values) to a constant value (mean over the considered time period), the reconnection rate prediction is almost identical than with varying magnetospheric inflow parameters. We also plot $B_{L2}v_2$ (subscript 2 = magnetosheath) in the same panel as the measured and predicted reconnection rate (Figure 6). The behavior of $B_{L2}v_2$ is almost the same as the reconnection rate calculated using all inflow values in equation (1). This is very reasonable, since $\mathbf{E} \sim -\mathbf{v} \times \mathbf{B}$ upstream of the reconnection site.

Next, we take a closer look at the terms in the numerator and denominator of equation (1). In the numerator, the term $\rho_2 v_2$ is larger than the magnetospheric $\rho_1 v_1$ due to the much higher density in the magnetosheath.

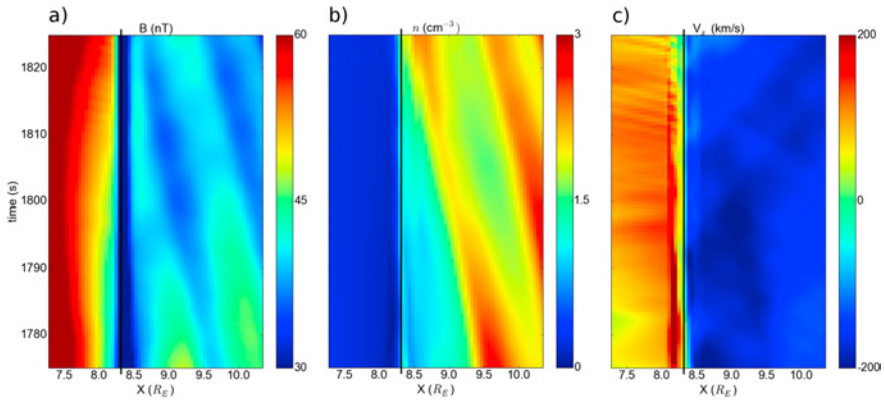

Figure 7. Stacked time series of (a) magnetic field magnitude, (b) number density, and (c) *x* component of the bulk velocity along the white line marked in Figure 1a. Time is on the vertical axis and *x* coordinate on the horizontal axis. The black line in each panel shows the location of the X line.

In the denominator the term with the magnetosheath density $\rho_2 B_{L1}$ is at least 10 times larger than $\rho_1 B_{L2}$ during the considered time period. Since $\rho_2 B_{L1}$ is in the denominator we calculate the Pearson correlation coefficient between the measured rate E_y and $(\rho_2 B_{L1})^{-1}$ and the result is 0.09. The correlation coefficient between $\rho_2 v_2$ and the E_y is 0.25 showing no correlation. In Figure 6b we show the density ρ_2, inflow velocity v_2, and the inflowing magnetic field B_{L2} normalized with the average value over the considered time period. The correlation between the measured reconnection rate and the magnetosheath inflow velocity is 0.69, that is, consistent with $B_{L2} v_2$ having very similar behavior as E_{pred} as expected from Ohms law, since the X line being studied is in a quasi-steady state. Correlation coefficient between E_y and B_{L2} is 0.58 showing weak correlation. The measured rate correlates well with v_2, but even better with $B_{L2} v_2$ with correlation coefficient 0.8 showing that B_{L2} affects the reconnection rate.

Figure 7 shows stacked time series of *B*, *n*, and the *x* component of the bulk velocity v_x, which can be used as an approximation of the inflow velocity, along the cut through the magnetopause at the X line location that is marked with a white line in Figure 1. Fluctuations in the magnetosheath ρ and *B* near the X line are caused by the mirror mode waves. Anticorrelation between these two parameters can still be observed near the magnetopause. Because B_{L2} had an effect on the reconnection rate and mirror modes cause the fluctuations in *B*, mirror mode waves have an effect on the measured reconnection rate. These waves propagate to the magnetopause affecting the inflow parameters. Fluctuations in the v_x seem to be independent of the mirror mode waves and are probably caused by other wave activity. Further, waves in the magnetosheath are the FTE-driven bow and stern waves that propagate in the magnetosheath from the magnetopause toward the bow shock that are discussed in the recent paper by *Pfau-Kempf* [2016]. There is also another wave activity in the magnetosheath, the study of which is outside of the scope of this work.

4. Discussion

In this paper we present the first study of the reconnection rate from a 2D-3V hybrid-Vlasov simulation of Earth's magnetosphere capable of describing ion kinetic physics globally and self-consistently. In a Vlasiator polar plane run under steady southward IMF, we observe that the reconnection is not steady; there is copious production of FTEs. Therefore, the locations of reconnection X lines vary significantly over time. Multiple X lines simultaneously exist along the magnetopause throughout the simulation, while at any given time there are only one or a few dominant X lines that are able to divert plasma flow on the magnetopause. In most cases they move away from the subsolar point toward the poles, but we also observe X lines that return back to the subsolar point after moving away from it, as has been reported before by *Sibeck and Omidi* [2012].

Observations have indicated that reconnection can occur continuously in time for several hours [*Frey et al.*, 2003; *Phan et al.*, 2004]. Our simulations show that although reconnection can occur continuously, it occurs in a dynamic nature even with steady solar wind conditions. In the subsolar region (*z* between $\pm 3\, R_E$) the

dominant X line moves significantly. Although the signatures are monitored along the magnetopause, many R_E from the X line or in the ionosphere [*Frey et al.*, 2003] may present a picture of continuous reconnection, the X line itself may be quite dynamic, even for steady IMF.

We have studied the motion of X lines at the dayside magnetopause. Previously, global magnetopause reconnection had been simulated mostly with MHD simulations. In ideal-MHD simulations with a coarse enough grid, the X line is located close to the subsolar point and reconnection attains a quasi-steady state during steady southward solar wind conditions [e.g., *Raeder*, 2006; *Hoilijoki et al.*, 2014]. We note that the X lines move more in the Vlasiator simulation under purely southward IMF than when *Hoilijoki et al.* [2014] added Parker spiral or tilted the Earth dipole in a global MHD simulation, or tilting the Earth dipole field at 20° shifted the average location of the reconnection line as much as the X lines move in the Vlasiator simulation under purely southward IMF. Using resistive-MHD simulations, *Dorelli and Bhattacharjee* [2009] showed that multiple X lines and FTEs can form in MHD simulations with a fine enough grid during steady southward IMF as well. However, MHD simulations cannot describe magnetosheath waves such as mirror mode waves. We have shown here that they can have an effect on the local reconnection rate. Therefore, adding kinetic physics in global magnetospheric modeling is important to fully describe the global effects on the local reconnection rate. Previous studies using global hybrid simulations show also that during steady southward IMF, multiple X lines exist and FTEs form [*Omidi and Sibeck*, 2007; *Sibeck and Omidi*, 2012; *Karimabadi et al.*, 2006; *Tan et al.*, 2011].

Isolated X lines drift if there is a velocity shear between the upstream regions [*Doss et al.*, 2015]. We find that the shear between the magnetospheric and magnetosheath velocities within 4 R_E of the subsolar point is small making this effect negligible. Instead, the effect of neighboring X lines dominates the X line motion. However, at higher latitudes the shear increases, along with the velocities of the X lines as they propagate toward the cusps. In general, multiple reconnection and the effect of neighboring X lines dominate near the subsolar region, while nearer the cusps the magnetosheath velocities start to play a role, as suggested by *Cowley and Owen* [1989] and *Doss et al.* [2015].

We have also studied the local reconnection rate at dayside reconnection sites. The *Cassak and Shay* [2007] formula, which has received attention as possibly describing dayside reconnection, was derived for a single nonpropagating X line assuming steady state antiparallel reconnection in a 2-D planar geometry. In our simulation there are multiple X lines reconnecting simultaneously, and reconnection at X-lines sometimes turns off as magnetic islands coalesce. In spite of this, our simulation results reveal a good correlation with the reconnection rate calculated using the analytical formula for the well-developed reconnection sites, suggesting that the local model for a single X line is still a good approximation for reconnection at the dayside magnetopause even if multiple X lines exist simultaneously. The good correlation between the measured and analytical prediction of the reconnection rate implies that the local reconnection depends on the local plasma conditions and not so much on the solar wind parameters as suggested also by *Borovsky et al.* [2008] using MHD simulations. We find that during the chosen time period the fluctuations in magnetosheath parameters are more dominant in defining the variations in the local reconnection rate being consistent with spacecraft observations by *Wang* [2015]. It is important to note, however, that here we find that the agreement with the *Cassak and Shay* [2007] analytical formula holds only if we do not assume a constant aspect ratio and use equation (2) instead (likely because of the grid resolution).

The local plasma conditions are modified by the processes upstream of the X line and by the neighboring reconnection sites at the magnetopause. Here, we find that mirror mode waves modify the local plasma parameters near the X-line, which in turn have an effect on the reconnection rates as suggested by *Laitinen et al.* [2010]. We note that the formation and propagation of magnetic islands disturb the local plasma conditions at the vicinity of the magnetopause, which influences the inflow parameters and, therefore, also reconnection rates. Propagating magnetic islands push plasma causing the X lines ahead of the islands to move; it can sometimes eventually cause them to stop reconnecting. Some X lines remain topologically as saddle points of the flux function, while the reconnection between the magnetic field lines of the Earth and magnetosheath stops and the newly reconnected field lines of the magnetic islands start to reconnect with each other. However, as the X lines are in constant motion, investigating the effect of individual factors on the reconnection rate separately is complicated.

5. Conclusions

In this paper we present the first study of the reconnection rate from a global magnetospheric 2D-3V hybrid-Vlasov simulation in the polar plane with due southward interplanetary magnetic field. We observe that even with steady southward IMF the reconnection is not steady; there are multiple X lines reconnecting simultaneously and there is copious production of FTEs. Our simulation results reveal a good correlation with the reconnection rate calculated using the *Cassak and Shay* [2007] analytical formula. The local reconnection rate depends on the local plasma conditions, which are modified by the processes upstream of the X line such as magnetosheath waves, the motion of passing magnetic islands, and the activity of the neighboring reconnection sites at the magnetopause.

Acknowledgments
The work of S.H., U.G., Y.P-K., S.V.A., and M.P. is supported by the Academy of Finland (SA-Vlasov grant 267144) and ERC consolidator grant ERC-CoG-682068-PRESTISSIMO. The work of P.A.C. is supported by NSF grant AGS-0953463, and NASA grants NNX16AF75G and NNX16AG76G. B.M.W. is supported by NASA grants NNX16AD91G and NNX16AJ73G. H.H. is supported by NASA contract NAS5-02099. The run was carried out using HLRS/Stuttgart Hazel Hen through PRACE Tier-0 resource grant (2014112573) from the 12th call. Data shown in this paper can be accessed by following the data policy on our web page http://vlasiator.fmi.fi/rules.php.

References

Birn, J., J. E. Borovsky, M. Hesse, and K. Schindler (2010), Scaling of asymmetric reconnection in compressible plasmas, *Phys. Plasmas*, *17*(5), 052108, doi:10.1063/1.3429676.

Blanco-Cano, X., N. Omidi, and C. Russell (2006), ULF waves and their influence on bow shock and magnetosheath structures, *Adv. Space Res.*, *37*(8), 1522–1531, doi:10.1016/j.asr.2005.10.043.

Blanco-Cano, X., N. Omidi, and C. T. Russell (2009), Global hybrid simulations: Foreshock waves and cavitons under radial interplanetary magnetic field geometry, *J. Geophys. Res.*, *114*, A01216, doi:10.1029/2008JA013406.

Borovsky, J. E., M. Hesse, J. Birn, and M. M. Kuznetsova (2008), What determines the reconnection rate at the dayside magnetosphere?, *J. Geophys. Res.*, *113*, A07210, doi:10.1029/2007JA012645.

Cassak, P. A., and A. Otto (2011), Scaling of the magnetic reconnection rate with symmetric shear flow, *Phys. Plasmas*, *18*(7), 074501, doi:10.1063/1.3609771.

Cassak, P. A., and M. A. Shay (2007), Scaling of asymmetric magnetic reconnection: General theory and collisional simulations, *Phys. Plasmas*, *14*(10), 102114, doi:10.1063/1.2795630.

Cassak, P. A., and M. A. Shay (2009), Response to comment on scaling of asymmetric magnetic reconnection: General theory and collisional simulations, *Phys. Plasmas*, *16*(3), 034702, doi:10.1063/1.3083264.

Chen, Q., A. Otto, and L. C. Lee (1997), Tearing instability, Kelvin-Helmholtz instability, and magnetic reconnection, *J. Geophys. Res.*, *102*, 151–162, doi:10.1029/96JA03144.

Cowley, S. W. H., and C. J. Owen (1989), A simple illustrative model of open flux tube motion over the dayside magnetopause, *Planet. Space Sci.*, *37*, 1461–1475, doi:10.1016/0032-0633(89)90116-5.

Daldorff, L. K., G. Tóth, T. I. Gombosi, G. Lapenta, J. Amaya, S. Markidis, and J. U. Brackbill (2014), Two-way coupling of a global hall magnetohydrodynamics model with a local implicit particle-in-cell model, *J. Comput. Phys.*, *268*, 236–254, doi:10.1016/j.jcp.2014.03.009.

Dorelli, J. C., and A. Bhattacharjee (2009), On the generation and topology of flux transfer events, *J. Geophys. Res.*, *114*, A06213, doi:10.1029/2008JA013410.

Doss, C. E., C. M. Komar, P. A. Cassak, F. D. Wilder, S. Eriksson, and J. F. Drake (2015), Asymmetric magnetic reconnection with a flow shear and applications to the magnetopause, *J. Geophys. Res. Space Physics*, *120*, 7748–7763, doi:10.1002/2015JA021489.

Dungey, J. W. (1953), The motion of magnetic fields, *Mon. Not. R. Astron. Soc.*, *113*, 679–682, doi:10.1093/mnras/113.6.679.

Dungey, J. W. (1961), Interplanetary magnetic field and the auroral zones, *Phys. Rev. Lett.*, *6*, 47–48, doi:10.1103/PhysRevLett.6.47.

Eastwood, J. P., T. D. Phan, R. C. Fear, D. G. Sibeck, V. Angelopoulos, M. Øieroset, and M. A. Shay (2012), Survival of flux transfer event (FTE) flux ropes far along the tail magnetopause, *J. Geophys. Res.*, *117*, A08222, doi:10.1029/2012JA017722.

Fear, R. C., S. E. Milan, A. N. Fazakerley, K.-H. Fornaçon, C. M. Carr, and I. Dandouras (2009), Simultaneous observations of flux transfer events by THEMIS, Cluster, Double Star, and SuperDARN: Acceleration of FTEs, *J. Geophys. Res.*, *114*, A10213, doi:10.1029/2009JA014310.

Fear, R. C., S. E. Milan, J. Raeder, and D. G. Sibeck (2010), Asymmetry in the bipolar signatures of flux transfer events, *J. Geophys. Res.*, *115*, A11217, doi:10.1029/2010JA015363.

Fedder, J. A., S. P. Slinker, J. G. Lyon, and C. T. Russell (2002), Flux transfer events in global numerical simulations of the magnetosphere, *J. Geophys. Res.*, *107*, 1048, doi:10.1029/2001JA000025.

Frey, H. U., T. D. Phan, S. A. Fuselier, and S. B. Mende (2003), Continuous magnetic reconnection at Earth's magnetopause, *Nature*, *426*, 533–537.

Génot, V., E. Budnik, P. Hellinger, T. Passot, G. Belmont, P. M. Trávníček, P.-L. Sulem, E. Lucek, and I. Dandouras (2009), Mirror structures above and below the linear instability threshold: Cluster observations, fluid model and hybrid simulations, *Ann. Geophys.*, *27*, 601–615, doi:10.5194/angeo-27-601-2009.

Génot, V., L. Broussillou, E. Budnik, P. Hellinger, P. M. Trávníček, E. Lucek, and I. Dandouras (2011), Timing mirror structures observed by Cluster with a magnetosheath flow model, *Ann. Geophys.*, *29*(10), 1849–1860, doi:10.5194/angeo-29-1849-2011.

Hoilijoki, S., V. M. Souza, B. M. Walsh, P. Janhunen, and M. Palmroth (2014), Magnetopause reconnection and energy conversion as influenced by the dipole tilt and the IMF B_X, *J. Geophys. Res. Space Physics*, *119*, 4484–4494, doi:10.1002/2013JA019693.

Hoilijoki, S., M. Palmroth, B. M. Walsh, Y. Pfau-Kempf, S. V. Alfthan, U. Ganse, O. Hannuksela, and R. Vainio (2016), Mirror modes in the Earth's magnetosheath: Results from a global hybrid-Vlasov simulations, *J. Geophys. Res. Space Physics*, *121*, 4191–4204, doi:10.1002/2015JA022026.

Karimabadi, H., H. X. Vu, D. Krauss-Varban, and Y. Omelchenko (2006), Global hybrid simulations of the Earth's magnetosphere, in *Numerical Modeling of Space Plasma Flows*, vol. 359, edited by G. P. Zank, pp. 257, Astronomical Society of the Pacific Conference Series, Palm Springs, Calif.

Karimabadi, H., et al. (2014), The link between shocks, turbulence, and magnetic reconnection in collisionless plasmas, *Phys. Plasmas*, *21*(6), 062308, doi:10.1063/1.4882875.

Kawano, H., and C. T. Russell (1997), Survey of flux transfer events observed with the ISEE 1 spacecraft: Dependence on the interplanetary magnetic field, *J. Geophys. Res.*, *102*, 11,307–11,314, doi:10.1029/97JA00481.

Kempf, Y., D. Pokhotelov, O. Gutynska, L. B. Wilson III, B. M. Walsh, S. V. Alfthan, O. Hannuksela, D. G. Sibeck, and M. Palmroth (2015), Ion distributions in the Earth's foreshock: Hybrid-Vlasov simulation and THEMIS observations, *J. Geophys. Res. Space Physics*, *120*, 3684–3701, doi:10.1002/2014JA020519.

Komar, C. M., and P. A. Cassak (2016), The local dayside reconnection rate for oblique interplanetary magnetic fields, *J. Geophys. Res. Space Physics*, *121*(6), 5105–5120, doi:10.1002/2016JA022530.

La BelleHamer, A. L., A. Otto, and L. C. Lee (1994), Magnetic reconnection in the presence of sheared plasma flow: Intermediate shock formation, *Phys. Plasmas*, *1*(3), 706–713, doi:10.1063/1.870816.

Laitinen, T. V., Y. V. Khotyaintsev, M. André, A. Vaivads, and H. Rème (2010), Local influence of magnetosheath plasma beta fluctuations on magnetopause reconnection, *Ann. Geophys.*, *28*(5), 1053–1063, doi:10.5194/angeo-28-1053-2010.

Lee, L. C., and Z. F. Fu (1985), A theory of magnetic flux transfer at the Earth's magnetopause, *Geophys. Res. Lett.*, *12*, 105–108, doi:10.1029/GL012i002p00105.

Li, J. H., and Z. W. Ma (2010), Nonlinear evolution of resistive tearing mode with sub-Alfvenic shear flow, *J. Geophys. Res.*, *115*, A09216, doi:10.1029/2010JA015315.

Mitchell Jr., H. G., and J. R. Kan (1978), Merging of magnetic fields with field-aligned plasma flow components, *J. Plasma Phys.*, *20*, 31–45, doi:10.1017/S0022377800021346.

Murphy, N. A., C. R. Sovinec, and P. A. Cassak (2010), Magnetic reconnection with asymmetry in the outflow direction, *J. Geophys. Res. Space Physics*, *115*, A09206, doi:10.1029/2009JA015183.

Omidi, N., and D. G. Sibeck (2007), Flux transfer events in the cusp, *Geophys. Res. Lett.*, *34*, L04106, doi:10.1029/2006GL028698.

Ouellette, J. E., J. G. Lyon, and B. N. Rogers (2014), A study of asymmetric reconnection scaling in the Lyon-Fedder-Mobarry code, *J. Geophys. Res. Space Physics*, *119*, 1673–1682, doi:10.1002/2013JA019366.

Palmroth, M., et al. (2015), ULF foreshock under radial IMF: THEMIS observations and global kinetic simulation Vlasiator results compared, *J. Geophys. Res. Space Physics*, *120*, 8782–8798, doi:10.1002/2015JA021526.

Pfau-Kempf, Y., H. Hietala, S. E. Milan, L. Juusola, S. Hoilijoki, U. Ganse, S. von Alfthan, and M. Palmroth (2016), Evidence for transient, local ion foreshocks caused by dayside magnetopause reconnection, *Ann. Geophys.*, *34*(11), 943–959, doi:10.5194/angeo34-943-2016.

Phan, T., et al. (2004), Cluster observations of continuous reconnection at the magnetopause under steady interplanetary magnetic field conditions, *Ann. Geophys.*, *22*, 2355–2367, doi:10.5194/angeo-22-2355-2004.

Raeder, J. (2006), Flux transfer events: 1. Generation mechanism for strong southward IMF, *Ann. Geophys.*, *24*(1), 381–392, doi:10.5194/angeo-24-381-2006.

Rijnbeek, R. P., Cowley, S. W. H., Southwood, D. J., and C. T. Russell (1984), A survey of dayside flux transfer events observed by ISEE 1 and 2 magnetometers, *J. Geophys. Res.*, *89*, 786–800, doi:10.1029/JA089iA02p00786.

Russell, C., G. Le, and H. Kuo (1996), The occurrence rate of flux transfer events, *Adv. Space Res.*, *18*(8), 197–205, doi:10.1016/0273-1177(95)00965-5.

Russell, C. T., and R. C. Elphic (1978), Initial ISEE magnetometer results—Magnetopause observations, *Space Sci. Rev.*, *22*, 681–715, doi:10.1007/BF00212619.

Scholer, M. (1988), Magnetic flux transfer at the magnetopause based on single X line bursty reconnection, *Geophys. Res. Lett.*, *15*, 291–294, doi:10.1029/GL015i004p00291.

Servidio, S., W. H. Matthaeus, M. A. Shay, P. A. Cassak, and P. Dmitruk (2009), Magnetic reconnection in two-dimensional magnetohydrodynamic turbulence, *Phys. Rev. Lett.*, *102*, 115,003, doi:10.1103/PhysRevLett.102.115003.

Servidio, S., W. H. Matthaeus, M. A. Shay, P. Dmitruk, P. A. Cassak, and M. Wan (2010), Statistics of magnetic reconnection in two-dimensional magnetohydrodynamic turbulence, *Phys. Plasmas*, *17*(3), 032,315, doi:10.1063/1.3368798.

Shi, Y., C. C. Wu, and L. C. Lee (1988), A study of multiple X line reconnection at the dayside magnetopause, *Geophys. Res. Lett.*, *15*, 295–298, doi:10.1029/GL015i004p00295.

Sibeck, D. G., and N. Omidi (2012), Flux transfer events: Motion and signatures, *J. Atmos. Sol. Terr. Phys.*, *87*, 20–24, doi:10.1016/j.jastp.2011.07.010.

Southwood, D., C. Farrugia, and M. Saunders (1988), What are flux transfer events?, *Planet. Space Sci.*, *36*(5), 503–508, doi:10.1016/0032-0633(88)90109-2.

Tan, B., Y. Lin, J. D. Perez, and X. Y. Wang (2011), Global-scale hybrid simulation of dayside magnetic reconnection under southward IMF: Structure and evolution of reconnection, *J. Geophys. Res.*, *116*(A2), A02206, doi:10.1029/2010JA015580.

Tátrallyay, M., and G. Erdős (2005), Statistical investigation of mirror type magneticfield depressions observed by ISEE-1, *Planet. Space Sci.*, *53*, 33–40, doi:10.1016/j.pss.2004.09.026.

von Alfthan, S., D. Pokhotelov, Y. Kempf, S. Hoilijoki, I. Honkonen, A. Sandroos, and M. Palmroth (2014), Vlasiator: First global hybrid-Vlasov simulations of Earth's foreshock and magnetosheath, *J. Atmos. Sol. Terr. Phys.*, *120*, 24–35, doi:10.1016/j.jastp.2014.08.012.

Wang, Y. L., et al. (2005), Initial results of high-latitude magnetopause and low-latitude flank flux transfer events from 3 years of Cluster observations, *J. Geophys. Res.*, *110*, A11221, doi:10.1029/2005JA011150.

Wang, S., L. M. Kistler, C. G. Mouikis, and S. M. Petrinec (2015), Dependence of the dayside magnetopause reconnection rate on local conditions, *J. Geophys. Res. Space Physics*, *120*, 6386–6408, doi:10.1002/2015JA021524.

Wang, Y. L., R. C. Elphic, B. Lavraud, M. G. G. T. Taylor, J. Birn, C. T. Russell, J. Raeder, H. Kawano, and X. X. Zhang (2006), Dependence of flux transfer events on solar wind conditions from 3 years of Cluster observations, *J. Geophys. Res.*, *111*, A04224, doi:10.1029/2005JA011342.

Yeates, A. R., and G. Hornig (2011), A generalized flux function for three-dimensional magnetic reconnection, *Phys. Plasmas*, *18*(10), 102118, doi:10.1063/1.3657424.

Paper IV

Evidence for transient, local ion foreshocks caused by dayside magnetopause reconnection

Annales Geophysicae
volume 34, 2016
doi:10.5194/angeo-34-943-2016

Ann. Geophys., 34, 943–959, 2016
www.ann-geophys.net/34/943/2016/
doi:10.5194/angeo-34-943-2016

Annales Geophysicae
Open Access
EGU

Evidence for transient, local ion foreshocks caused by dayside magnetopause reconnection

Yann Pfau-Kempf[1,2], Heli Hietala[3], Steve E. Milan[4], Liisa Juusola[1], Sanni Hoilijoki[1,2], Urs Ganse[5,1], Sebastian von Alfthan[6], and Minna Palmroth[1]

[1]Earth Observation, Finnish Meteorological Institute, Helsinki, Finland
[2]Department of Physics, University of Helsinki, Helsinki, Finland
[3]Department of Earth, Planetary, and Space Sciences, University of California, Los Angeles, USA
[4]Department of Physics and Astronomy, University of Leicester, Leicester, UK
[5]Department of Physics and Astronomy, University of Turku, Turku, Finland
[6]CSC, IT Center for Science, Espoo, Finland

Correspondence to: Yann Pfau-Kempf (yann.kempf@helsinki.fi)

Received: 20 May 2016 – Revised: 31 August 2016 – Accepted: 17 October 2016 – Published: 4 November 2016

Abstract. We present a scenario resulting in time-dependent behaviour of the bow shock and transient, local ion reflection under unchanging solar wind conditions. Dayside magnetopause reconnection produces flux transfer events driving fast-mode wave fronts in the magnetosheath. These fronts push out the bow shock surface due to their increased downstream pressure. The resulting bow shock deformations lead to a configuration favourable to localized ion reflection and thus the formation of transient, travelling foreshock-like field-aligned ion beams. This is identified in two-dimensional global magnetospheric hybrid-Vlasov simulations of the Earth's magnetosphere performed using the Vlasiator model (http://vlasiator.fmi.fi). We also present observational data showing the occurrence of dayside reconnection and flux transfer events at the same time as Geotail observations of transient foreshock-like field-aligned ion beams. The spacecraft is located well upstream of the foreshock edge and the bow shock, during a steady southward interplanetary magnetic field and in the absence of any solar wind or interplanetary magnetic field perturbations. This indicates the formation of such localized ion foreshocks.

Keywords. Interplanetary physics (planetary bow shocks) – magnetospheric physics (magnetosheath; solar wind–magnetosphere interactions)

1 Introduction

The super-Alfvénic solar wind impinging upon the geomagnetic field is slowed down and diverted around the Earth by the bow shock which forms upstream of our planet. Most of the plasma is abruptly compressed and heated by the shock while being transported downstream into the magnetosheath. There, it flows along the magnetopause surface, which delimits the magnetosphere, that is, the magnetic cavity in which the Earth is situated.

Fluid theories such as ideal magnetohydrodynamics imply that no wave or matter can travel upstream from a shock. However, it is well-known observationally and explained by kinetic plasma theory that, given a high enough Mach number and a small enough angle $\theta_{\boldsymbol{B}-\boldsymbol{n}}$ between the upstream magnetic field ($\boldsymbol{B}$) and the shock normal direction ($\boldsymbol{n}$) ($\theta_{\boldsymbol{B}-\boldsymbol{n}} \lessapprox 40$–$60°$, e.g. Greenstadt et al., 1980; Schwartz et al., 1983), a fraction of the incoming ions is reflected by the shock surface and streams back along the magnetic field direction. The region where such a backstreaming ion population exists is called the ion foreshock. It is the stage for a variety of plasma beam instabilities generating waves and has been studied observationally as well as in simulations for several decades (e.g. Bavassano-Cattaneo et al., 1983; Sanderson et al., 1983; Thomsen et al., 1983; Fuselier et al., 1987; Le and Russell, 1992; Eastwood et al., 2005b; Burgess et al., 2012; Wilson et al., 2013). The value of $\theta_{\boldsymbol{B}-\boldsymbol{n}}$ allowing the reflection of particles is dependent on several factors,

among which most notably is the assumed reflection mechanism, as the results of Greenstadt et al. (1980), for example, show.

The bow shock under steady solar wind conditions is generally assumed to be a simple surface such as a paraboloid with a dawn–dusk asymmetry primarily due to the Earth's orbital motion. This follows from fluid dynamical considerations, numerical simulations as well as statistical studies of spacecraft observations. The inherently local nature of spacecraft measurements compared to the spatial scale of the bow shock, even in the case of spacecraft constellations such as Cluster (Escoubet et al., 1997), Time History of Events and Macroscale Interactions during Substorms (THEMIS; Angelopoulos, 2008) or the Magnetospheric Multi-Scale (MMS; Burch et al., 2016a) missions, does not allow us to determine the global shape of the bow shock surface at a given instant in time. Statistical studies are the method of choice (e.g. Merka et al., 2005; Meziane et al., 2014). Thus it is also usually assumed that under steady conditions, the ion foreshock is located in the solar wind volume magnetically connected to the bow shock surface region where $\theta_{\boldsymbol{B}-\boldsymbol{n}} \lessapprox 50^\circ$. Depending on the orientation of the interplanetary magnetic field (IMF), this can be one or two compact regions in space.

Another tenet of ideal magnetohydrodynamics is the conservation of magnetic field line topology, which is a good assumption on large scales or in collisional plasma but breaks down on smaller scales when strong magnetic field gradients are present. Through the kinetic process of magnetic reconnection, antiparallel magnetic field lines rearrange their topology while strongly accelerating inflowing plasma out of the reconnection region (see, e.g., reviews by Zweibel and Yamada, 2009, and Treumann and Baumjohann, 2013, and references therein). A prime example of magnetic reconnection in near-Earth space occurs at the magnetopause in the subsolar region, when inflowing southward IMF reconnects with the northward-oriented geomagnetic field lines (e.g. Phan et al., 2000; Paschmann, 2008; Dunlop et al., 2011). This phenomenon drives global magnetospheric dynamics as first proposed by Dungey (1961), and therefore it is key to space weather studies (e.g. Cassak, 2016; Burch et al., 2016b).

The topological reconfiguration of magnetic field lines at the magnetopause can lead to the formation of well-delimited structures called flux transfer events (FTEs). The classic picture of an FTE is that of a magnetic flux tube connected both to the magnetosheath and the magnetosphere, but its topology can be more complex. FTEs were first observed by Russell and Elphic (1978, 1979) and Haerendel et al. (1978) (who termed the process magnetic flux erosion) and subsequently much studied in space and ground observations as well as simulations (e.g. Kawano and Russell, 1997; Wild et al., 2001, 2003; McWilliams et al., 2004; Fear et al., 2009; Eastwood et al., 2016; Hasegawa et al., 2016; Milan et al., 2016). FTEs travel downstream along the magnetopause with the magnetosheath plasma and are recognized by their signature in magnetic field measurements, such as the bipolar deflection of the component normal to their axis in the case of a flux rope or magnetic island (e.g. Omidi and Sibeck, 2007; Dorelli and Bhattacharjee, 2009; Sibeck and Omidi, 2012; Eastwood et al., 2012). Their signatures also include poleward moving auroral forms (PMAFs) and their equivalent in radar observations named poleward moving radar auroral forms (PMRAFs), which result from poleward ionospheric flows. Oscillations can also be observed by ground magnetometers (e.g. Øieroset et al., 1996; Milan et al., 2000; Pang et al., 2009). Although their role is crucial in the solar wind–magnetosphere interaction, allowing plasma exchange along the reconnected magnetic field lines, FTEs have not so far been thought to be the direct cause of significant upstream effects.

In this work, we propose a scenario by which dayside magnetopause reconnection generates FTEs, which in turn cause steepening fast magnetosonic bow and stern waves to propagate throughout the magnetosheath. The increased pressure behind the steepened wave fronts causes the bow shock to bulge outward in an area travelling along the bow shock surface. The geometry at the edge of such a bulge can lead $\theta_{\boldsymbol{B}-\boldsymbol{n}}$ to become smaller than $\sim 50^\circ$ in a well-delimited region, detached from the "regular" foreshock, upstream of which a beam of reflected ions generates a local, transient and travelling foreshock. This chain of processes has first been identified in a two-dimensional polar-plane hybrid-Vlasov simulation of steady southward IMF interacting with an Earth-like dipolar magnetic field. The simulation was performed using the Vlasiator model (http://vlasiator.fmi.fi). We also present observational data supporting the scenario. Geotail spacecraft observations show the existence of short foreshock-like ion beams during steady southward IMF, in a region well-detached from both the bow shock and the regular ion foreshock region and in the absence of any IMF fluctuations, thus excluding a momentary transit of the spacecraft through the regular foreshock due to a change in IMF orientation. Simultaneously, the signatures of FTEs moving poleward are found in ground magnetometer and SuperDARN (Super Dual Auroral Radar Network) radar data.

Section 2 describes the simulation and the observational methods. The scenario of magnetopause–bow-shock–foreshock interaction is detailed in Sect. 3, while the ground and spacecraft observations are presented in Sect. 4. The results are then discussed in Sect. 5 before the conclusions are given in Sect. 6.

2 Methods

2.1 Hybrid-Vlasov simulation

The hybrid-Vlasov model Vlasiator has been developed with the aim of producing global magnetospheric simulations

of the Earth's magnetosphere including kinetic physics beyond magnetohydrodynamics while avoiding the limitations due to the statistical sampling inherent to particle-in-cell approaches (von Alfthan et al., 2014). Vlasiator has been used to study amongst other things the magnetosheath and the foreshock in equatorial plane simulations of the terrestrial magnetosphere (Pokhotelov et al., 2013; Kempf et al., 2015; Palmroth et al., 2015; Hoilijoki et al., 2016). It solves Vlasov's equation to propagate the ion (proton) velocity distribution function in up to three spatial and three velocity dimensions. The equation system is closed via Ampère's and Faraday's laws as well as a generalized Ohm's law including the Hall term (see von Alfthan et al., 2014, and Palmroth et al., 2015, for more details).

The simulation used in this study is two-dimensional in the polar x–z plane and three-dimensional in velocity space. It covers both the dayside and the nightside magnetosphere. The spatial coordinates are similar to the Geocentric Solar Magnetospheric (GSM) coordinate system with the x axis pointing from the Earth towards the Sun and the z axis orthogonal to the x axis and parallel to the geomagnetic dipole field axis (no dipole tilt). We use a two-dimensional line dipole centred at the origin and scaled to match the geomagnetic dipole strength in the same way as is done by Daldorff et al. (2014). The steady solar wind has a proton density of $1 \times 10^6\,\mathrm{m}^{-3}$, an inflow temperature of 0.5 MK and a velocity of $-750\,\mathrm{km\,s}^{-1}$ purely along the x axis. The constant and purely southward IMF has an intensity of 5 nT. The upstream boundary maintains a constant field and a Maxwellian velocity distribution; the three other outer boundaries have copy conditions ensuring proper outflow. The inner boundary, which is set at a distance of 30 000 km ($\sim$ 5 Earth radii, R_E) around the origin, enforces a static Maxwellian velocity distribution and perfect conductor field boundary conditions. The out-of-plane direction is treated periodically. The boundaries are located at 47 R_E from the origin in each direction. Since this study concentrates on dayside phenomena, the nightside is not shown in this work. The spatial resolution is 300 km or 0.047 R_E or 1.3 solar wind ion inertial lengths and the velocity space extends from -4000 to $+4000\,\mathrm{km\,s}^{-1}$ in all three dimensions with a resolution of $30\,\mathrm{km\,s}^{-1}$ or 0.33 solar wind ion thermal speeds. The phase space density sparsity threshold is $10^{-15}\,\mathrm{m}^{-6}\,\mathrm{s}^3$ (see von Alfthan et al., 2014, and Kempf et al., 2015, for details on the sparse phase space strategy used in Vlasiator).

The simulation has been run for over 1850 s or 140 solar wind proton gyroperiods, and it reaches a steady state on the dayside after less than 900 s or 70 gyroperiods. The bow shock and the magnetopause form as expected and there is a foreshock at high latitudes both in the Northern and Southern hemispheres. The magnetosheath is pervaded by anisotropy-driven waves, most notably mirror-mode waves as has been demonstrated by Hoilijoki et al. (2016). Figure 1 shows an overview of the simulation setup after 1150 s of simulated time. The magnetopause–magnetosheath–bow-shock structure is clear, and a large magnetic island can be recognized due to its high density at the position $(+6, -7)$ R_E. A smaller magnetic island is in the southern polar cusp region, while a series of even smaller islands is also visible along the dayside magnetopause boundary northward of the equator. The animation provided in the Supplement to this work shows the time evolution of the ion number density and the parallel temperature for the same spatial extents as Fig. 1 and with the same colour scales as Figs. 1 and 5a.

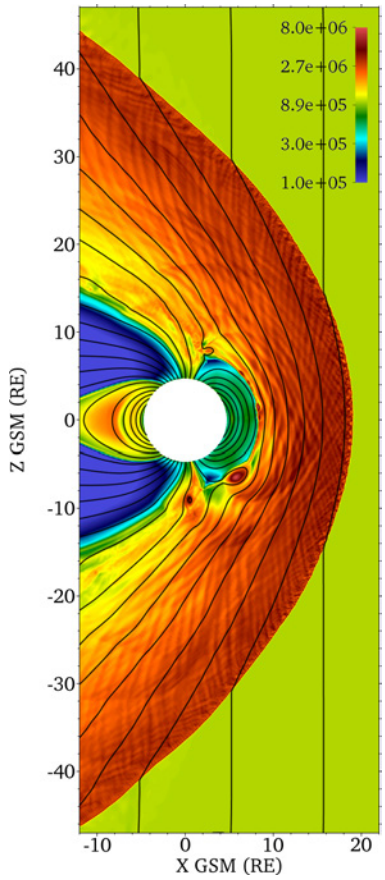

Figure 1. Colour code: plasma number density (protons m^{-3}) after 1150 s of simulation time. Contour lines: magnetic field lines. A large magnetic island is prominent at $(+6, -7)$ R_E; another one is in the southern cusp region and a series of smaller magnetic islands is visible at the dayside magnetopause northward of the equator.

2.2 Spacecraft and ground measurements

We first use solar wind densities, velocities and the IMF one-minute averaged data from NASA/GSFC's OMNI data

set accessed through CDAweb (Coordinated Data Analysis Web) to identify suitable intervals of stable solar wind and steady southward IMF conditions.

We also use in situ spacecraft measurements from Geotail in this study. The ion velocity distribution measurements are taken from the Low Energy Particle instrument (LEP; Mukai et al., 1994). During the event presented in Sect. 4.3, LEP was in the EA (energy-per-charge analyser) mode, which is not well-suited to properly measure the cold core solar wind ion population but does not impact the quality of suprathermal ion measurements. Editor-B data are available for that event, meaning that only two-dimensional velocity distributions are available. These projected distributions are produced using data from all three-dimensional channels (LEP instrument team, personal communication, 26 August 2016). They are provided in Geocentric Solar Ecliptic (GSE) coordinates (x_{GSE}-axis pointing from the Earth towards the Sun, y_{GSE}-axis in the ecliptic plane pointing towards dusk and z_{GSE}-axis perpendicular to the ecliptic plane). Magnetic field measurements are from the Magnetic Field Measurement fluxgate magnetometers (MGF; Kokubun et al., 1994).

The following measurements from the Wind spacecraft are used: solar wind data from its Solar Wind Experiment (SWE; Ogilvie et al., 1995), IMF data from its Magnetic Fields Investigation (MFI; Lepping et al., 1995), moments from its 3-D Plasma and Energetic Particle Analyzer (3-DP; Lin et al., 1995) as well as densities retrieved from the electron plasma frequency measured by the radio and plasma wave instrument (WAVES; Bougeret et al., 1995). The following datasets from the Advanced Composition Explorer (ACE) spacecraft are used: IMF measurements from the Magnetic Fields Experiment (MAG; Smith et al., 1998) and ion moments from the Solar Wind Electron Proton Alpha Monitor (SWEPAM; McComas et al., 1998).

Ground-based ionospheric backscatter data from SuperDARN (Greenwald et al., 1995) as well as ground magnetometer data from the International Monitor for Auroral Geomagnetic Effects (IMAGE, http://space.fmi.fi/image, Tanskanen, 2009) are used. Additionally, we use the electrojet activity auroral electrojet (AE) indices provided by the University of Kyoto through the World Data Center for Geomagnetism (Davis and Sugiura, 1966).

3 Magnetopause–bow-shock–foreshock interaction scenario

The scenario proposed in this work has been identified in the simulation presented in Sect. 2.1. We describe the scenario here in Sect. 3 in a narrative fashion and present the corresponding observations in Sect. 4. Limitations are discussed in Sect. 5.

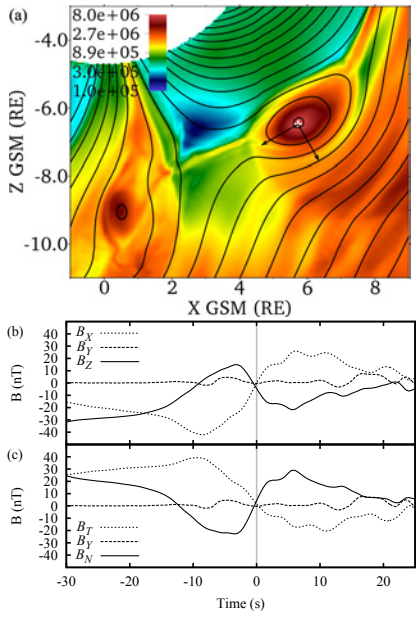

Figure 2. (a) Close-up view of the large magnetic island from Fig. 1 travelling tailward along the magnetopause. Colour code: plasma number density, protons m^{-3}. Contour lines: magnetic field lines. Arrows: rotated coordinate system (N, Y, T) with N normal to the magnetopause and T parallel to it. **(b)** Magnetic field evolution at a virtual spacecraft located at the white cross in panel **(a)**, in simulation (GSM) and **(c)** rotated coordinates. The grey vertical bar indicates the time of panel **(a)** and Fig. 1. The characteristic bipolar signature of the passing magnetic island is obvious in the $\boldsymbol{B}_N$ component.

3.1 Magnetopause reconnection

Under steady southward IMF, magnetic reconnection occurs typically along a line at the equator on the magnetopause (e.g. Trattner et al., 2007; Dunlop et al., 2011; Hoilijoki et al., 2014). In the present simulation, the position of the X-line is not stable in time and multiple reconnection sites can coexist at any given time on the magnetopause. Reconnected field lines form magnetic islands in the exhaust regions of reconnection sites, which grow and travel downstream (poleward) along the magnetopause. This continuously ongoing process is prominent in the animation provided in the Supplement. The magnetic islands can be seen as the two-dimensional equivalents of FTEs, that is, cuts through an out-of-plane flux rope. A more detailed analysis of the propagation of the magnetic islands and the location and intensity of magnetic reconnection is the subject of a separate study.

Figure 2 shows such a magnetic island and time series of the magnetic field components seen at a virtual spacecraft over which the magnetic island flows. The magnetic

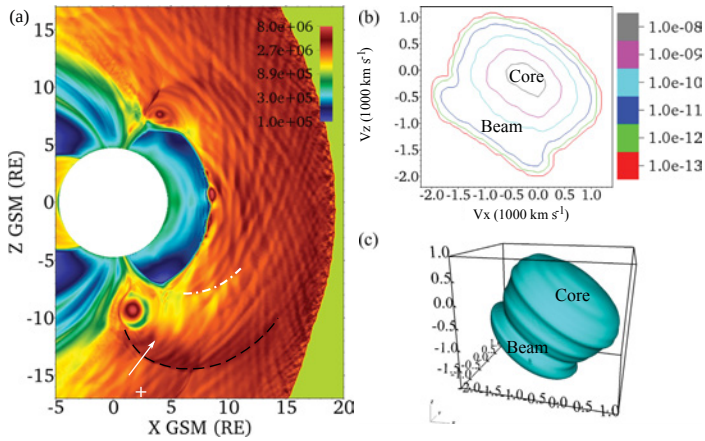

Figure 3. (a) Example of bow (black dashed) and stern (white dash–dotted) fast wave fronts driven by a magnetic island (density peak at $(2, -9)$ R_E; colour code: plasma number density; protons m^{-3}; simulation time 1340 s). The bow wave accelerates particles ahead of it, as can be seen in the **(b)** two-dimensional projected isocontour and **(c)** three-dimensional isocontour plots of the ion velocity distribution (phase space density in $s^3\,m^{-6}$; 3-D isocontour at $1 \times 10^{-15}\,s^3\,m^{-6}$) taken at the location of the white cross. The core population with very low drift velocity (blue, pink and grey isocontours, centre and top right part of the 3-D isocontour) is preceded by an accelerated population in the $-V_x$ and $-V_z$ direction. The white arrow shows the location of the profiles shown in Fig. 4.

field components are shown both in the simulation coordinates and in a coordinate system (N, Y, T) rotated by 150° in the plane of the simulation so that N points in the direction normal to the magnetopause and T points along the magnetopause. The strong bipolar fluctuation in the $\boldsymbol{B}_N$ component is characteristic of the passage of a magnetic island.

3.2 Magnetosheath waves and bow shock perturbations

Figure 3a shows a magnetic island in the southern cusp region. The increased dynamic pressure of the magnetic islands with respect to the surrounding magnetosheath plasma drives bow waves ahead of the islands. These fast magnetosonic waves propagate throughout the magnetosheath and steepen to almost form fast forward shocks. In some cases, strong magnetic islands can also be followed by a fast reverse wave front, but these stern waves are less steep than the bow wave fronts. Both the bow and stern fast mode waves are visible in Fig. 3a. The profiles of plasma density, velocity and temperature perpendicular to the magnetic field as well as the magnetic field intensity show clearly the steep correlated increase corresponding to the fast forward wave front in Fig. 4a–d. The forward wave fronts are steep enough to reflect ions much in the way a shock can accelerate ions to generate upstream foreshock populations. Figure 3b and c shows the two- and three-dimensional velocity distribution function isocontours at the location of the white cross in Fig. 3a. The accelerated ions are clearly visible ahead of the core population in the $-V_x$ and $-V_z$ direction. The structure is also readily visible in the profile of the temperature parallel to the

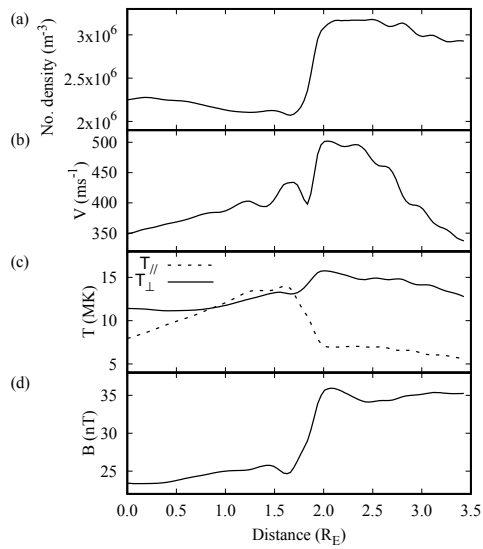

Figure 4. Cut across the bow wave front along the white arrow in Fig. 3 showing **(a)** the plasma density and **(b)** velocity, **(c)** the temperature parallel and perpendicular to the magnetic field, and **(d)** the magnetic field intensity. The correlated jump in all these parameters at the abscissa 2 R_E characterizes the steep fast forward wave front. Note the fast wave signature in the perpendicular temperature while the parallel temperature is much more sensitive to the particle beam accelerated ahead of the wave front.

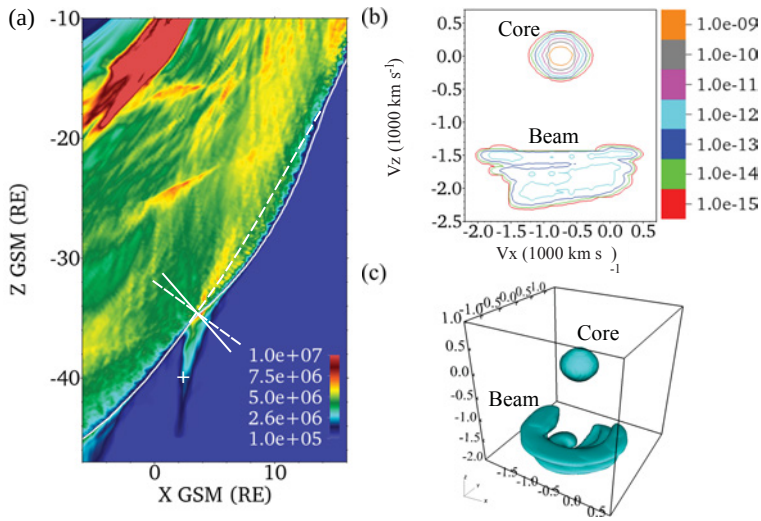

Figure 5. **(a)** Colour code: temperature (K) parallel to the magnetic field in a region presenting a local foreshock at 1548.5 s simulation time. This variable is sensitive to the presence of an ion beam, hence the choice to bring out the local foreshock. The continuous white isocontour curve shows where the ion density is $2 \times 10^6\,\mathrm{m}^{-3}$ (twice the solar wind density), thus indicating the bow shock location. The dashed white curve would show the approximate position of the bow shock were it not for the increased pressure due to a fast wave front in the magnetosheath. The continuous and dashed segments indicate the normal direction for each of these curves. $\theta_{\boldsymbol{B}-\boldsymbol{n}}$: 41° and 54°; thus the angle between both is 13°. **(b)** Two-dimensional projected isocontour and **(c)** three-dimensional isocontour plots of the ion velocity distribution (phase space density in $\mathrm{s}^3\,\mathrm{m}^{-6}$; 3-D isocontour at $1 \times 10^{-15}\,\mathrm{s}^3\,\mathrm{m}^{-6}$) at the location of the white cross. The field-aligned beam is prominent and directly comparable to Figs. 2 and 6 in the work by Kempf et al. (2015).

magnetic field in Fig. 4c; the steep increase in the parallel temperature from 7 to 14 MK is the direct signature of the presence of an accelerated ion population upstream of the wave front in addition to the background magnetosheath ion population. The increased parallel temperature ahead of the wave fronts is visible too in the right panel of the animation provided in the Supplement.

Downstream of the fast magnetosonic waves, the magnetosheath plasma has higher thermal, dynamic and magnetic pressure. The straightforward consequence of this phenomenon is – considering the pressure balance when the wave fronts reach the bow shock – that the bow shock is pushed outwards against the solar wind, forming a localized bulge corresponding to the region of enhanced magnetosheath pressure.

3.3 Local foreshocks

Figure 5a shows the detailed view of a small region of the bow shock south of the subsolar point. When the angle between the shock normal and the upstream magnetic field $\theta_{\boldsymbol{B}-\boldsymbol{n}}$ is lower than $\sim 50°$, incoming particles with sufficient energy can be accelerated back upstream and form a foreshock. Consequently, when the bow shock bulge caused by the fast-wave-mediated pressure increase is pronounced enough, the region of the bulge with $\theta_{\boldsymbol{B}-\boldsymbol{n}} \lessapprox 50°$ is the source of a separate ion beam propagating upstream along the IMF direction. This is of course only the case when the bulge has not yet travelled into the region where the mean $\theta_{\boldsymbol{B}-\boldsymbol{n}}$ is allowing ion reflection anyway. The spatial extent in the direction parallel to the bow shock surface is limited to the corresponding patch of favourable $\theta_{\boldsymbol{B}-\boldsymbol{n}}$, and this localized foreshock travels along with the driving magnetosheath wave front until it merges with the regular foreshock further downstream. Due to its being a travelling and transient ion beam, the expected beam instabilities do not have time to grow to form ultra low-frequency (ULF) waves as in the regular foreshock (see, e.g., von Alfthan et al., 2014; Palmroth et al., 2015). This means that the typical ULF wave signature characteristic of the regular foreshock is absent from this structure.

Figure 5a shows an example of a localized foreshock driven by a magnetosheath wave. The colour code in the figure shows the temperature parallel to the magnetic field, which is sensitive to the presence of a field-aligned ion beam. The white contour curve is set at a plasma density of $2 \times 10^6\,\mathrm{m}^{-3}$ (twice the solar wind density), which highlights the position and shape of the bow shock. The dashed curve would indicate the approximate location of the bow shock were it not for the pressure increase in the magnetosheath

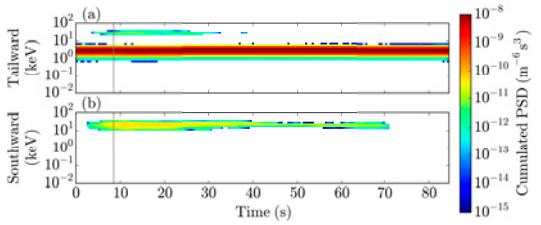

Figure 6. Energy–time spectrogram of the simulated local foreshock crossing event at the location marked in Fig. 5. The grey vertical bar indicates the time of Fig. 5. The velocity distribution has been split into four sectors (sunward, southward, tailward and northward in the simulation/polar plane, ±45° from the $+x$, $-z$, $-x$ and $+z$ direction respectively), two of which are plotted here. **(a)** The dense tailward population at an energy of a few kiloelectronvolt is the solar wind core. **(b)** The local foreshock beam forms the population at a few tens of kiloelectronvolt in the southward sector and lasts almost 70 s. Thus the expected observational signature is that of a field-aligned beam with a duration of the order of 1 min.

after the passage of a fast forward wave front. The continuous and dashed segments indicate the local direction normal to the respective curve. Their $\theta_{\boldsymbol{B}-\boldsymbol{n}}$ is respectively 41° and 54°. The ion beam is generated by solar wind ions reflected at the foot of the bow shock bulge where $\theta_{\boldsymbol{B}-\boldsymbol{n}}$ is favourable. Beyond $-3\,R_{\mathrm{E}}(x_{\mathrm{GSM}})$, the regular foreshock is also visible upstream of the bow shock as a region of increased parallel temperature. The fact that the density and parallel temperature increases due to the bow shock do not coincide, illustrates that the shock primarily heats plasma in the perpendicular direction. Isotropization of the velocity distribution happens further downstream in the magnetosheath.

The animation provided in the Supplement to this work shows that such local foreshocks occur both north and south of the ecliptic whenever favourable $\theta_{\boldsymbol{B}-\boldsymbol{n}}$ conditions are met at the foot of a bow shock perturbation.

Figure 5b–c shows the ion velocity distribution function corresponding to a field-aligned beam population, which is similar to the distribution expected at the edge of the regular foreshock upstream of the ULF foreshock boundary (Kempf et al., 2015). The density of the beam is of the order of 1 % of the inflowing density as in the regular foreshock (not shown). Figure 6 shows an energy–time spectrogram for the tailward and southward sectors of the velocity distribution. The tailward part contains the cold solar wind core population, while the southward sector, in the direction of the field-aligned beam, indicates the typical signature expected when a local foreshock crosses an upstream spacecraft. The timescale of a local foreshock crossing is on the order of 1 min in the simulation (almost 70 s in Fig. 6), but this value can vary depending on the geometry of the event. Other factors affecting the observational signatures are discussed in Sect. 5.

4 Spacecraft and ground observations

In Sect. 3 we present a scenario based on a global hybrid-Vlasov simulation, in which dayside reconnection eventually leads to the formation of local, transient foreshock-like structures upstream of the terrestrial bow shock and outside of the region where the angle between the shock normal and the IMF ($\theta_{\boldsymbol{B}-\boldsymbol{n}}$) would normally be favourable for ion reflection. In this section, we present observational data from an event on 30 August 2004 which supports the interpretation of the simulation. While Geotail observed transient field-aligned ion beams in the solar wind upstream of the bow shock and the foreshock between 08:09 and 08:24 UT, ground-based SuperDARN radar data and IMAGE magnetometer data indicate that dayside reconnection was active and producing FTEs.

4.1 Upstream pristine solar wind conditions

The OMNI data set (from ACE) containing the upstream magnetic field, ion velocity, ion density and ion temperature on 30 August 2004 is plotted in Fig. 7. It shows that the IMF turned south at about 05:00 UT and $\boldsymbol{B}_z$ remained strongly negative around −10 nT for most of the day until about 22:00 UT. The velocity and temperature of the solar wind remained stable around 480–490 km s^{-1} and 10^4 K respectively between 08:00 and 19:00 UT, while $\boldsymbol{B}_z$ slowly decreased from −8 to −11 nT and the density slowly increased from about 5 to 10 cm^{-3}.

4.2 Ground observations

The strong southward $\boldsymbol{B}_z$ component of the IMF is the cause of strong magnetic reconnection at the dayside magnetopause, which in turn is known to produce numerous FTEs (e.g. Kawano and Russell, 1997). Global activity indices clearly indicate ongoing magnetic reconnection during the event. The prolonged period of southward IMF triggered a geomagnetic storm and the increased levels of magnetic reconnection both on the dayside and the nightside are reflected in the AE indices, which started picking up between 05:00 and 06:00 UT and reached levels above AE = 500 nT after 08:00 UT.

Evidence for continuous FTE activity during the period 06:00 to 10:00 UT is observed by two SuperDARN radars in the Southern Hemisphere, presented in Fig. 8. The Kerguelen and Syowa East radars were observing backscatter from the pre-noon and noon region during this period. Figure 8a–c show the Kerguelen line-of-sight velocity data at 07:08, 07:32 and 08:22 UT. Three regions of backscatter are labelled A to C. In the polar cap (A), 1 km s^{-1} flows away from the radar (antisunwards) are observed, 700 m s^{-1} flows away from the radar (polewards) are seen entering the polar cap near noon (B), and 700 m s^{-1} flows towards the radar (sunwards) are seen in the return flow region (C). As the

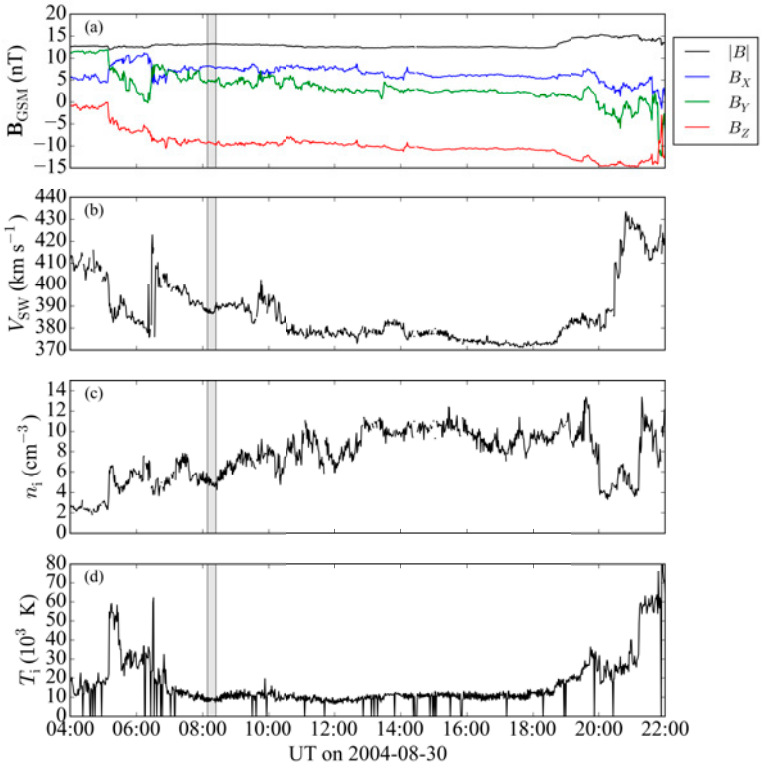

Figure 7. Upstream solar wind observations between 04:00 and 22:00 UT on 30 August 2004, from the OMNI dataset with 1 min time resolution. **(a)** Magnetic field. **(b)** Velocity. **(c)** Ion number density. **(d)** Ion temperature. The grey box shows the interval of the event presented in Fig. 11 and Sect. 4.3.

Earth rotates the look direction of the radar changes, but these backscatter regions continue to be observed. Range–time plots show that these backscatter regions are quasi-periodically pulsed with periods near 10–15 min, the expected signature of pulsed reconnection (e.g. Provan et al., 1998; Milan et al., 1999a, 2000; Wild et al., 2001). This is seen as poleward-moving enhancements in the backscatter power in the polar cap flows of region A in Fig. 8f. It is also observed as pulses of backscatter and flow in the return flow region, as first discussed by Milan et al. (1999b), that is, pulsed flows observed moving towards the Kerguelen radar (i.e. sunwards) in the return flow backscatter region C (Fig. 8e) and pulsing moving away from the Syowa East radar (also sunwards), in backscatter collocated with region C (Fig. 8i).

IMAGE magnetometers also observed signatures that could be interpreted as FTE activity. Figure 9a shows the ionospheric equivalent current density at 110 km altitude in the Northern Hemisphere at 08:15 UT. The equivalent current density was derived from 10 s IMAGE magnetometer data using spherical elementary current systems (SECS; Amm, 1997; Amm and Viljanen, 1999). Before applying the SECS method, a baseline was subtracted from the variometer data following van de Kamp (2013). The J_{eq} data are presented as a function of Altitude Adjusted Corrected Geogmagnetic Coordinates (AACGM; Shepherd, 2014) latitude and longitude, which at the given UT correspond to 09:05–11:09 magnetic local time (MLT). The plot has been rotated such that local noon is at the top. The plot shows eastward and equatorward equivalent current density vectors in the poleward part of the IMAGE field of view. If gradients of the ionospheric conductances are vanishingly small or aligned with the electric field in a large enough area, the equivalent current equals the Hall current, which flows antiparallel to the ionospheric $\boldsymbol{E} \times \boldsymbol{B}$ drift. According to Weygand et al. (2012), this is often a good approximation. Thus, the equatorward equivalent current in Fig. 9a may indicate poleward plasma flow entering the polar cap.

Figure 9b shows a $|J_{eq}|$ keogram, that is, latitude profiles of $|J_{eq}|$ along 105° longitude presented as a function of time

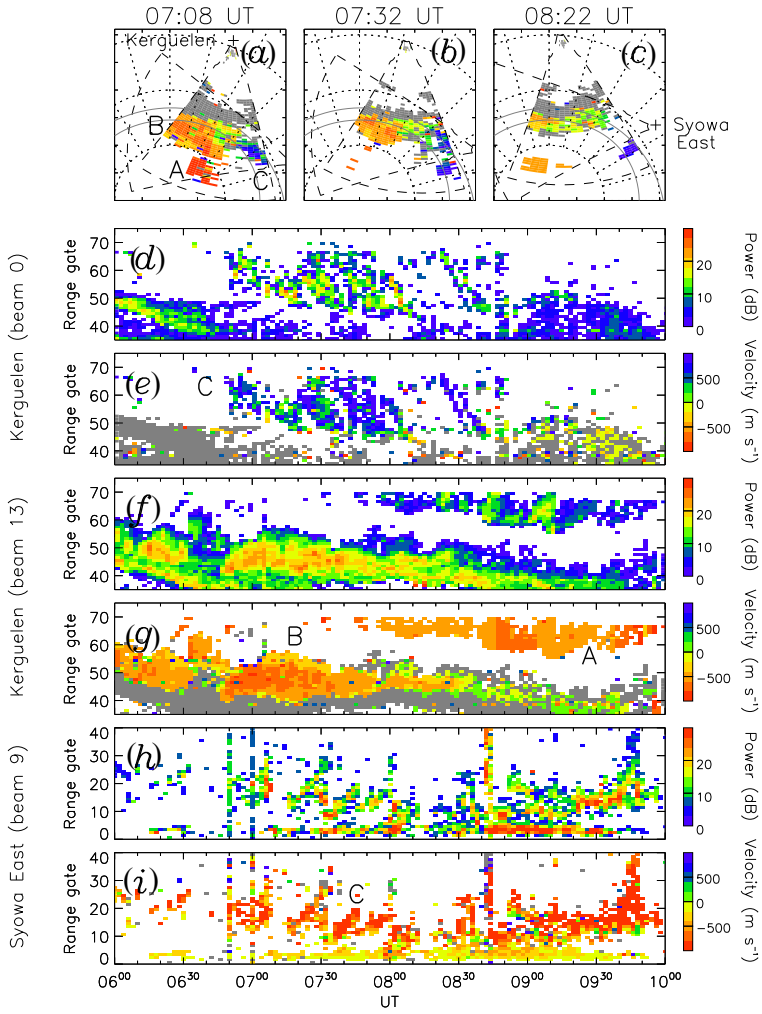

Figure 8. (a–c) Line-of-sight velocities (blue towards the radar, red away from the radar) from the Kerguelen SuperDARN radar in the Southern Hemisphere, at 07:08, 07:32 and 08:22 UT. Grey regions are ground scatter. The data are presented in geomagnetic latitude and magnetic local time coordinates, with dotted circles indicating geomagnetic latitudes of 60, 70 and 80° and dotted lines showing local time meridians with local noon at the top. The outline of the radar field of view is shown by dashed lines, as is the field of view of the Syowa East radar. Grey circles indicated the expected locations of the poleward and equatorward edges of the auroral oval. Three regions of backscatter are indicated by the letters A, B and C. **(d–i)** Backscatter power and line-of-sight velocity from beams 0 and 13 of the Kerguelen radar and beam 9 of the Syowa East radar. Regions of backscatter are also labelled A to C.

between 06:00 and 10:00 UT. The vertical lines indicate the interval 08:09–08:24 UT during which Geotail observed the ion beam signature. The occurrence of the $|J_{eq}|$ intensifications observed by IMAGE between 70 and 75° latitude before about 09:00 UT roughly agrees in time with the Southern Hemisphere FTE signatures observed by SuperDARN. One of the intensifications occurred during the interval when Geotail observed the ion beam signature.

4.3 Geotail observations

On 30 August 2004, Geotail was located on the dayside of the Earth and upstream of the bow shock in the solar wind. Between about 08:00 and 08:30 UT, Geotail was

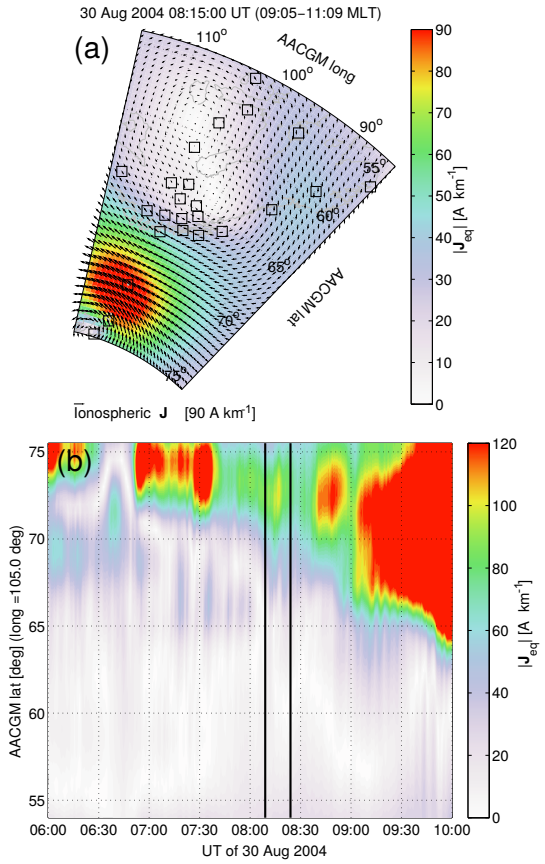

Figure 9. (a) Ionospheric equivalent current density at 110 km altitude (J_{eq}, arrows; $|J_{eq}|$, colour) in the Northern Hemisphere on 30 August 2004 at 08:15 UT, derived from 10 s IMAGE magnetometer (squares) data. The data are presented as a function of geomagnetic (AACGM) latitude and longitude, which at the given time correspond to 09:05–11:09 MLT. The plot has been rotated such that local noon is at the top. **(b)** $|J_{eq}|$ keogram (latitude profiles along 105° longitude presented as a function of time between 06:00 and 10:00 UT). The vertical lines indicate the interval (08:09–08:24 UT) during which Geotail observed the ion beam signature.

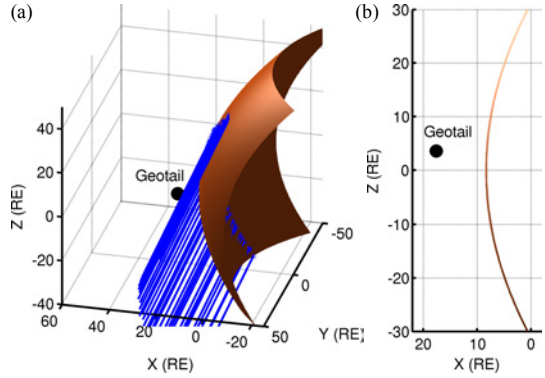

Figure 10. (a) Plot showing the location of Geotail at 08:16:10 UT on 30 August 2004 with respect to the bow shock following the model by Merka et al. (2005) and the foreshock edge assuming that the maximum $\theta_{\boldsymbol{B}-\boldsymbol{n}}$ for ion reflection is 60° and the reflected ions have twice the solar wind speed (in the solar wind frame). **(b)** x–z slice at the y coordinate of Geotail showing the spacecraft and the bow shock location. (Plots in GSE coordinates.)

located at $(17.6, 23.0, -9.2)\,R_E$ in GSM coordinates and $(17.6, 24.5, 3.6)\,R_E$ in GSE coordinates. The location of Geotail with respect to a model bow shock and ion foreshock edge is shown in Fig. 10 (details of the bow shock and foreshock models are given in Sect. 5.1). Geotail/MGF observed stable IMF with $\boldsymbol{B}_{GSM} = (7, 5, -9)$ nT, as shown in Fig. 11c. No perturbations of the magnetic field are seen which would modify its orientation, thus altering the magnetic connection to the bow shock and the location of the foreshock. Small-amplitude regular fluctuations are visible throughout, which coincide with Geotail's nominal spin rate of 20 rpm. They are therefore likely a residual from the data calibration process.

The energy–time spectrograms from the Geotail/LEP instrument for the ions flying in the tailward and duskward directions are shown in Fig. 11a and b. Only two-dimensional projected ion velocity distributions in the ecliptic plane are available from LEP for this event, hence the choice of sectors. The tailward sector is dominated by the steady cold and dense solar wind core population just below 1 keV. Between about 08:09 and 08:24 UT (time delimited by the black dotted lines in Fig. 11) the duskward sector exhibits several occurrences of an ion population at energies of a few kiloelectronvolt reminiscent of the signature of foreshock field-aligned beam ions. The presence of a beam in this sector is consistent with the significant $\boldsymbol{B}_y$ component of the IMF.

In contrast to regular foreshock field-aligned beams, this beam is transient and appears several times after 08:10 UT for one to a few minutes without correlation with changes in the magnetic field direction, as can be seen by comparing panels a–c in Fig. 11. Panel d shows the velocity and number density of the ions from the OMNI data set with a 1 min time resolution. The velocity is stable and varies only by about 1 %, while the density fluctuates between 4.5 and 5.5 cm^{-3} but without correlating with the transient beam event. We choose the OMNI density and velocity data because the densities reported by Geotail/LEP do not seem to be consistent. This is likely due to the fact that LEP is in EA mode and not in SW (solar wind analyser) mode, which would have ensured a better measurement of the solar wind core population. To ensure that the choice of the OMNI data is sensible, we compare shifted ACE and Wind magnetic field mea-

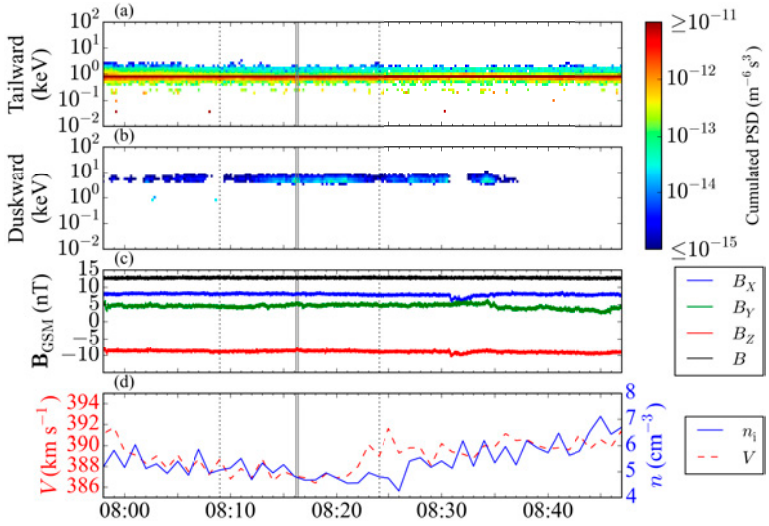

Figure 11. Geotail/LEP energy–time spectrogram on 30 August 2004 between 07:48 and 08:47 UT, for the **(a)** tailward and **(b)** duskward sectors (±45° from the $+x$ and $+y$ direction respectively), extracted from the two-dimensional reduced velocity distribution in the GSE ecliptic plane. The tailward sector shows the cold and dense solar wind core population just below 1 keV. The duskward sector shows the signature of a transient beam whose density peaks several times between 08:09 and 08:24 UT (time delimited by the black dotted lines). **(c)** Geotail/MGF magnetic field in GSM coordinates. The magnetic field components and thus its orientation are stable during the event. The short-period oscillations coincide with Geotail's nominal spin rate of 20 rpm. **(d)** OMNI plasma number density and velocity. The grey continuous bars indicate the time at which the velocity distribution shown in Fig. 12 is measured.

surements to the Geotail/MGF data to check that the OMNI propagation algorithm is successful. We then check that the densities and velocities from ACE and Wind are similar to each other and to the OMNI dataset. Since this is the case and the OMNI values are similarly stable to the ACE (which was used to produce the OMNI dataset) and Wind data at a higher time resolution, we conclude that the OMNI dataset is reliable and sufficient here. LEP being in EA mode instead of SW affects the quality of the measurement for the core population but not for the beam, which is of prime interest here.

Figure 12 shows the projected two-dimensional velocity distribution in the V_x–V_y GSE plane measured by the Geotail/LEP between 08:16:10 and 08:16:22 UT (time delimited by the grey continuous bars in Fig. 11). The solar wind core population is prominent in the lower left at $V_x \sim -400\,\mathrm{km\,s^{-1}}$, while a typical field-aligned beam flows back upstream along the magnetic field with positive V_x and V_y components. The black arrow points in the average direction of the magnetic field in the x–y GSE plane during the time interval, and the grey dots indicate all measurements taken at an 8 Hz cadence by the MGF instrument during the same time. Their close grouping once more indicates the stability of the magnetic field direction.

It is worth noting that while exactly similar magnetic field and solar wind conditions prevail in the 10 min preceding the event, no such field-aligned beam is seen before 08:10 UT. Additional ion beams are visible between 08:24 and 08:40 UT, but in their case the influence of magnetic field perturbations observed simultaneously cannot be conclusively ruled out.

5 Discussion

In Sect. 4 we present Geotail observations of transient field-aligned ion beams upstream of the Earth's bow shock, while ground-based SuperDARN radar data and IMAGE magnetometer data show that pulsed dayside reconnection producing FTEs was occurring at the same time. This matches the observational signatures expected from the scenario drawn in Sect. 3 based on a global magnetospheric simulation. In this Sect. 5 we first investigate the position of Geotail with respect to the regular foreshock, and we then discuss the more general factors which might affect the interpretation of the simulation and the measurements.

5.1 Position of Geotail relative to the regular foreshock

It is important to ascertain that Geotail is not too close to the bow shock or to the foreshock. Indeed if it were in the vicinity of either, it could observe for example shock foot ion populations or the edge of field-aligned beam populations

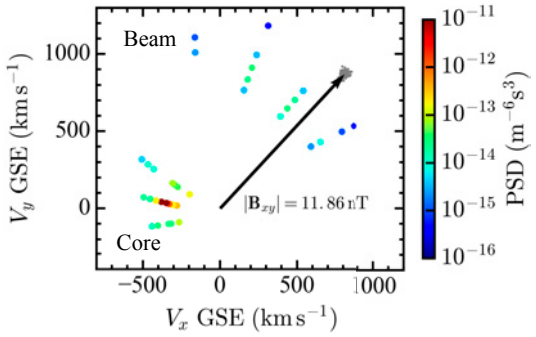

Figure 12. Coloured dots: Two-dimensional reduced ion velocity distribution in GSE coordinates measured by Geotail/LEP between 08:16:10 and 08:16:22 UT. The cold solar wind core flows with $V_x \sim -400\,\mathrm{km\,s^{-1}}$, and the hotter field-aligned beam propagates in the opposite direction. Black arrow: averaged magnetic field direction in the x–y GSE plane measured by Geotail/MGF during the interval. Grey dots: all individual Geotail/MGF measurements taken at 8 Hz cadence. The stability of the orientation of the magnetic field is remarkable.

from the foreshock, which would look very similar to the signature expected from a local foreshock.

We use the bow shock model from Merka et al. (2005) with the OMNI solar wind parameters and the Geotail/MGF observed magnetic field as inputs to determine the expected bow shock shape and position. As a first approach we determine the position of the expected ion foreshock edge. We trace the observed magnetic field to find the locus on the bow shock surface where $\theta_{\boldsymbol{B}-\boldsymbol{n}} = 60°$, and then we trace the trajectories of ions reflected from there with twice the solar wind inflow speed in the solar wind rest frame. This is typical of field-aligned beams in the foreshock (e.g. Greenstadt et al., 1980; Eastwood et al., 2005a; Kis et al., 2007). From this modelling we determine that Geotail is 3–5 R_E away from the foreshock edge and 9–10 R_E clear of the bow shock during the event between 08:09 and 08:24 UT, whence we could conclude that the spacecraft is well beyond reach of bow shock foot or foreshock edge ions. The result of this analysis is what is presented in Fig. 10.

However, as can readily be estimated from the observed velocity distribution shown in Fig. 12, the beam is significantly faster in the solar wind rest frame than twice the solar wind inflow velocity in the spacecraft frame. To get a better estimate of whether Geotail is within reach of the regular foreshock, we consider the trajectory of foreshock ions assuming adiabatic reflection at the bow shock (Schwartz et al., 1983; Liu et al., 2016). Adiabatic reflection and not specular reflection is assumed because it yields higher beam speeds and would thus be more likely to reach the spacecraft. Incoming ions at velocity $\boldsymbol{V}$ impinge on the bow shock, which has a local normal vector $\boldsymbol{n}$, and are reflected with a velocity

$$\boldsymbol{V}_\mathrm{r} = -\boldsymbol{V} + 2\boldsymbol{V}_\mathrm{HT}, \tag{1}$$

where

$$\boldsymbol{V}_\mathrm{HT} = \frac{\boldsymbol{n} \times (\boldsymbol{V} \times \boldsymbol{B})}{\boldsymbol{n} \cdot \boldsymbol{B}} \tag{2}$$

is the de Hoffmann–Teller velocity of the bow shock (De Hoffmann and Teller, 1950) and $\boldsymbol{B}$ is the IMF.

The validity of the assumption that ions are reflected adiabatically can be checked against the simulation. In Fig. 5a we have $\theta_{\boldsymbol{B}-\boldsymbol{n}} = 41°$ at the foot of the local foreshock, the solar wind velocity is $-750\,\mathrm{km\,s^{-1}}$ purely along the x axis, and the IMF is constant and purely southward at 5 nT. With those parameters, Eqs. (1) and (2) yield $\boldsymbol{V}_\mathrm{r}^\mathrm{sim} = (-750, 0, 1725.6)\,\mathrm{km\,s^{-1}}$. This does indeed correspond to the beam velocity as shown by the projected velocity distribution function in Fig. 5b, confirming the assumed adiabatic reflection process.

To check whether Geotail observed adiabatically reflected ions from the regular foreshock, we trace the observed beam from Geotail back to the bow shock along the IMF direction and invert Eq. (1) to reconstruct the solar wind velocity vector $\boldsymbol{V}'$ that would yield the measured beam velocity with the assumed model bow shock. For the observed beam (Fig. 12), the resulting solar wind velocity vector would have the components $\boldsymbol{V}' = (-557, -602, 317)\,\mathrm{km\,s^{-1}}$ in GSE coordinates, which is obviously not in accordance with the observed solar wind (Figs. 7b and 11d). Having thus ascertained that in these solar wind and IMF conditions the observed beam cannot have been reflected adiabatically from the modelled bow shock, we perturb the model bow shock until the adiabatically reflected ion trajectory matches the observed beam. When $\boldsymbol{n}$ is rotated towards $\boldsymbol{B}$ by an angle of 15°, the adiabatically reflected ion beam does indeed hit Geotail. This value is remarkably close to the angle of 13° between the unperturbed and perturbed bow shock normals at the foot of the local foreshock in the global simulation (Fig. 5a). It has to be noted though that the beam velocities obtained with this approach do not agree well with the observed ones (reconstructed velocity $688\,\mathrm{km\,s^{-1}}$, observed velocity $885\,\mathrm{km\,s^{-1}}$ in the spacecraft frame), which means that the reflection and acceleration process and their geometry are probably more complex than the simple adiabatic reflection we assume here.

In summary this analysis demonstrates that Geotail is out of reach for adiabatically reflected field-aligned beam ions originating from the unperturbed foreshock under the prevailing solar wind and IMF conditions. By introducing an ad hoc local perturbation of the bow shock normal of 15°, we recover a beam direction consistent with the Geotail observations, which is similar to the bow shock perturbation seen in the global simulation.

5.2 Estimating the propagation direction of the perturbation

Assuming that three-dimensional velocity distribution measurements were available with a high cadence, it would be possible to estimate the direction and speed of propagation of the field-aligned ion beam. Indeed at the edge of an ion beam, non-gyrotropic partial ring or beam distributions are observed in a region of one gyrodiameter width (e.g. Schwartz et al., 2000; Kempf et al., 2015). Timing the transition from a partial to a full gyrotropic beam and back on each side of the beam passage across the spacecraft yields an approximate beam propagation speed since the gyrodiameter of the ions is known. Furthermore, the gyrophase of the ions at the very edge of the beam indicates on which side of the spacecraft the beam is located, so that the incoming and outgoing edges yield an estimate of the beam edge orientation. However the lack of knowledge of the shape of the beam complicates the matter to some extent. For the event presented in Sect. 4, such estimates are not feasible with the Geotail data available and the comparison of the event timings in the absence of a more detailed knowledge of the shape of the bow shock perturbation and beam is of no use.

5.3 Simulation model limitations

The main limitation of the simulation presented is its two-dimensionality. Due to this configuration, all inflowing magnetic flux is forced to reconnect at the magnetopause and cannot flow past without reconnecting, unlike in three dimensions. This forces magnetic reconnection to be strong and occur all the time at the magnetopause. Further, this likely means that the magnetic islands carry more momentum and thus drive stronger bow and stern waves into the magnetosheath than they would in three dimensions.

Additionally, the steady solar wind conditions in the simulation preclude any upstream turbulence, yielding a smooth bow shock and no more downstream turbulence than the anisotropy-driven wave activity in the magnetosheath. Therefore the magnetic-island-driven fast waves can propagate relatively unhindered in the magnetosheath and the localized field-aligned beam is also very prominent in the solar wind. More realistic turbulent conditions would certainly yield less conspicuous signatures.

Nevertheless, none of these limitations mean that the fully three-dimensional and turbulent case could not exhibit transient local foreshocks, they might only be more difficult to detect and distinguish from other sources of bow shock and foreshock perturbations or ion beams.

5.4 Observational limitations

The long chain of phenomena from the magnetopause through the magnetosheath and bow shock to the foreshock, constituting the scenario presented in this work, makes it daunting to observe the whole cascade of a single event in space and time. This would require the fortuitous availability of adequate measurement data firstly at the magnetopause to identify FTEs, secondly in the magnetosheath to single out steepened fast wave fronts, and thirdly upstream in a narrow region close to but definitively more than one ion gyroradius away form both the bow shock foot and the regular foreshock edge, all of this during a stable southward IMF stretch and in the absence of any magnetic field fluctuations which could either drive an ion beam or produce a regular foreshock crossing at the upstream spacecraft instead. No suitable spacecraft were located in the magnetosheath or at the magnetopause during the Geotail event presented above so that a direct observation of fast-mode magnetosheath wave fronts is not possible in this case.

As shown in Sect. 4, transient foreshock-like ion beams upstream but well-separated from both the bow shock and the foreshock are observed. At the same time, ground-based measurements confirm that dayside reconnection was occurring and producing FTEs propagating towards the poles. Without adequate magnetosheath observations, it is not possible to claim with certainty that the complete scenario mapped in Sect. 3 holds. Yet the observations are consistent with the first and the last part of the story, namely that while dayside reconnection is active and pulsed, a localized change in the bow shock shape causes localized ion reflection and the formation of a transient, local foreshock. It cannot be excluded that sources other than FTE-driven fast waves exist, but it is unlikely there would be distinctive features helping to tell them apart purely based on the observation of the ion beam without other measurements, from within the magnetosheath for example. Such putative sources could include unpredicted magnetosheath waves interacting with the bow shock or very localized solar wind transients not observed by the upstream spacecraft. Finally, we note that the presented scenario offers an alternative mechanism to explain transient foreshock encounters that may have been interpreted previously as foreshock skimmings due to a change in the magnetic connection of the spacecraft to the bow shock.

6 Conclusions

Global hybrid-Vlasov simulations of the terrestrial magnetosphere in the polar plane under constant southward IMF show that the two-dimensional equivalents of flux transfer events, formed by dayside magnetopause reconnection, drive steepening bow and stern fast-mode waves in the magnetosheath. The increased pressure behind the wave fronts causes the bow shock to bulge out, inducing favourable ion reflection conditions which can result in the generation of local, transient foreshock-like field-aligned ion beams upstream of the bow shock. The two-dimensionality of the simulation exacerbates the phenomena, but the scenario would be entirely similar in three dimensions.

Ground-based and spacecraft observations support this scenario. During an extended period of stable southward IMF, we observe ionospheric signatures of dayside reconnection and flux transfer events in SuperDARN radar data and IMAGE magnetometer data. Simultaneously, using Geotail magnetic field and ion velocity distribution measurements we observe the expected signature of an ion beam detached both from the bow shock and the regular foreshock and not linked to any upstream magnetic field fluctuation. Further observations especially in the magnetosheath are needed though to confirm that indeed fast-mode waves lead to bow shock deformations generating localized, transient field-aligned ion beams.

7 Data availability

The simulation dataset is available on request from the Vlasiator team (http://vlasiator.fmi.fi, von Alfthan et al., 2014). IMAGE magnetometer data are available from http://www.space.fmi.fi/image (Tanskanen, 2009). The AACGM software is available from http://engineering.dartmouth.edu/superdarn/aacgm.html (Shepherd, 2014). The SuperDARN data can be accessed from the SuperDARN data portal hosted by Virginia Tech at http://vt.superdarn.org (Greenwald et al., 1995).

The Supplement related to this article is available online at doi:10.5194/angeo-34-943-2016-supplement.

Author contributions. Sebastian von Alfthan and Yann Pfau-Kempf designed and ran the simulation presented in this work. Heli Hietala helped in the analysis of the Geotail observations. Steve E. Milan provided the analysis and figure of the SuperDARN observations. Liisa Juusola provided the analysis and figure of the IMAGE observations. Yann Pfau-Kempf, Heli Hietala, Sanni Hoilijoki, Urs Ganse and Sebastian von Alfthan developed analysis tools used in this study. Minna Palmroth is the Principal Investigator of the Vlasiator team at the Finnish Meteorological Institute. Yann Pfau-Kempf led the analysis and prepared the manuscript and figures with the help of all co-authors.

Acknowledgements. The simulation was run on the Sisu supercomputer at the CSC – IT Center for Science, Espoo, Finland.

We thank T. Mukai at ISAS, JAXA in Japan for providing Geotail/LEP data; S. Kokubun at STELAB, Nagoya University, Japan for providing Geotail/MGF data; A. Szabo at NASA/GSFC for providing Wind/MFI data; K. Ogilvie at NASA/GSFC for providing Wind/SWE data; R. Lin and S. Bale at UC Berkeley for providing Wind/3DP data; M. L. Kaiser at GSFC for providing Wind/WAVES data; N. Ness at Bartol Research Institute for providing ACE/MAG data; D. J. McComas at SWRI for providing ACE/SWEPAM data; and J. H. King and N. Papatashvili at AdnetSystems and GSFC for providing OMNI data, all through CDAweb. We also thank T. Nagai and Y. Saito for providing Geotail/MGF and Geotail/LEP data through DARTS at ISAS, JAXA in Japan. We thank the University of Kyoto for providing the AE electrojet indices through the World Data Center for Geomagnetism.

We acknowledge the use of SuperDARN data. SuperDARN is a collection of radars funded by national scientific funding agencies of Australia, Canada, China, France, Japan, South Africa, United Kingdom and United States of America.

We thank the institutes who maintain the IMAGE magnetometer array.

Yann Pfau-Kempf, Sanni Hoilijoki, Sebastian von Alfthan and Minna Palmroth acknowledge financial support from the Academy of Finland under the project 267144/Vlasov. Part of this study was done by Yann Pfau-Kempf, Liisa Juusola, Urs Ganse, Sanni Hoilijoki and Minna Palmroth under the ERC CoG-682068-PRESTISSIMO project, a Consolidator grant to Minna Palmroth from the European Research Council. The work of Heli Hietala is funded by NASA contract NAS5-02099. Steve E. Milan was supported by the Science and Technology Facilities Council (STFC), UK, grant no. ST/N000749/1. Urs Ganse acknowledges funding from the German Research Foundation Grant GA1968/1 and the Academy of Finland project 267186.

The topical editor, C. Owen, thanks two anonymous referees for help in evaluating this paper.

References

Amm, O.: Ionospheric elementary current systems in spherical coordinates and their application, J. Geomagn. Geoelectr., 49, 947–955, doi:10.5636/jgg.49.947, 1997.

Amm, O. and Viljanen, A.: Ionospheric disturbance magnetic field continuation from the ground to ionosphere using spherical elementary current systems, Earth Planets Space, 51, 431–440, doi:10.1186/BF03352247, 1999.

Angelopoulos, V.: The THEMIS Mission, Space Sci. Rev., 141, 5–43, doi:10.1007/s11214-008-9336-1, 2008.

Bavassano-Cattaneo, M. B., Bonifazi, C., Dobrowolny, M., Moreno, G., and Russell, C. T.: Distribution of MHD wave activity in the foreshock region and properties of backstreaming protons, J. Geophys. Res.-Space, 88, 9280–9286, doi:10.1029/JA088iA11p09280, 1983.

Bougeret, J. L., Kaiser, M. L., Kellogg, P. J., Manning, R., Goetz, K., Monson, S. J., Monge, N., Friel, L., Meetre, C. A., Perche, C., Sitruk, L., and Hoang, S.: WAVES: The radio and plasma wave investigation on the WIND spacecraft, Space Sci. Rev., 71, 231–263, doi:10.1007/BF00751331, 1995.

Burch, J. L., Moore, T. E., Torbert, R. B., and Giles, B. L.: Magnetospheric Multiscale Overview and Science Objectives, Space Sci. Rev., 199, 5–21, doi:10.1007/s11214-015-0164-9, 2016a.

Burch, J. L., Torbert, R. B., Phan, T. D., Chen, L.-J., Moore, T. E., Ergun, R. E., Eastwood, J. P., Gershman, D. J., Cassak, P. A., Argall, M. R., Wang, S., Hesse, M., Pollock, C. J., Giles, B. L., Nakamura, R., Mauk, B. H., Fuselier, S. A., Russell, C. T., Strangeway, R. J., Drake, J. F., Shay, M. A., Khotyaintsev, Y. V., Lindqvist, P.-A., Marklund, G., Wilder, F. D., Young, D. T., Torkar, K., Goldstein, J., Dorelli, J. C., Avanov, L. A., Oka, M.,

Baker, D. N., Jaynes, A. N., Goodrich, K. A., Cohen, I. J., Turner, D. L., Fennell, J. F., Blake, J. B., Clemmons, J., Goldman, M., Newman, D., Petrinec, S. M., Trattner, K. J., Lavraud, B., Reiff, P. H., Baumjohann, W., Magnes, W., Steller, M., Lewis, W., Saito, Y., Coffey, V., and Chandler, M.: Electron-scale measurements of magnetic reconnection in space, Science, 352, 6290, doi:10.1126/science.aaf2939, 2016b.

Burgess, D., Möbius, E., and Scholer, M.: Ion Acceleration at the Earth's Bow Shock, Space Sci. Rev., 173, 5–47, doi:10.1007/s11214-012-9901-5, 2012.

Cassak, P. A.: Inside the Black Box: Magnetic Reconnection and the Magnetospheric Multiscale Mission, Space Weather, 14, 186–197, doi:10.1002/2015SW001313, 2016.

Daldorff, L. K. S., Tóth, G., Gombosi, T. I., Lapenta, G., Amaya, J., Markidis, S., and Brackbill, J. U.: Two-way coupling of a global Hall magnetohydrodynamics model with a local implicit particle-in-cell model, J. Comput. Phys., 268, 236–254, doi:10.1016/j.jcp.2014.03.009, 2014.

Davis, T. N. and Sugiura M.: Auroral electrojet activity index AE and its universal time variations, J. Geophys. Res., 71, 785–801, doi:10.1029/JZ071i003p00785, 1966.

De Hoffmann, F. and Teller, E.: Magneto-Hydrodynamic Shocks, Phys. Rev., 80, 692–703, doi:10.1103/PhysRev.80.692, 1950.

Dorelli, J. C. and Bhattacharjee, A.: On the generation and topology of flux transfer events, J. Geophys. Res.-Space, 114, A06213, doi:10.1029/2008JA013410, 2009.

Dungey, J. W.: Interplanetary Magnetic Field and the Auroral Zones, Phys. Rev. Lett., 6, 47–48, doi:10.1103/PhysRevLett.6.47, 1961.

Dunlop, M. W., Zhang, Q.-H., Bogdanova, Y. V., Lockwood, M., Pu, Z., Hasegawa, H., Wang, J., Taylor, M. G. G. T., Berchem, J., Lavraud, B., Eastwood, J., Volwerk, M., Shen, C., Shi, J.-K., Constantinescu, D., Frey, H., Fazakerley, A. N., Sibeck, D., Escoubet, P., Wild, J. A., and Liu, Z.-X.: Extended Magnetic Reconnection across the Dayside Magnetopause, Phys. Rev. Lett., 107, 025004, doi:10.1103/PhysRevLett.107.025004, 2011.

Eastwood, J. P., Balogh, A., Lucek, E. A., Mazelle, C., and Dandouras, I.: Quasi-monochromatic ULF foreshock waves as observed by the four-spacecraft Cluster mission: 1. Statistical properties, J. Geophys. Res.-Space, 110, A11219, doi:10.1029/2004JA010617, 2005a.

Eastwood, J. P., Lucek, E. A., Mazelle, C., Meziane, K., Narita, Y., Pickett, J., and Treumann, R. A.: The Foreshock, Space Sci. Rev., 118, 41–94, doi:10.1007/s11214-005-3824-3, 2005b.

Eastwood, J. P., Phan, T. D., Fear, R. C., Sibeck, D. G., Angelopoulos, V., Øieroset, M., and Shay, M. A.: Survival of flux transfer event (FTE) flux ropes far along the tail magnetopause, J. Geophys. Res.-Space, 117, A08222, doi:10.1029/2012JA017722, 2012.

Eastwood, J. P., Phan, T. D., Cassak, P. A., Gershman, D. J., Haggerty, C., Malakit, K., Shay, M. A., Mistry, R., Øieroset, M., Russell, C. T., Slavin, J. A., Argall, M. R., Avanov, L. A., Burch, J. L., Chen, L. J., Dorelli, J. C., Ergun, R. E., Giles, B. L., Khotyaintsev, Y., Lavraud, B., Lindqvist, P. A., Moore, T. E., Nakamura, R., Paterson, W., Pollock, C., Strangeway, R. J., Torbert, R. B., and Wang, S.: Ion-scale secondary flux-ropes generated by magnetopause reconnection as resolved by MMS, Geophys. Res. Lett., 43, 4716–4724, doi:10.1002/2016GL068747, 2016.

Escoubet, C., Schmidt, R., and Goldstein, M.: Cluster – Science And Mission Overview, Space Sci. Rev., 79, 11–32, doi:10.1023/A:1004923124586, 1997.

Fear, R. C., Milan, S. E., Fazakerley, A. N., Fornaçon, K.-H., Carr, C. M., and Dandouras, I.: Simultaneous observations of flux transfer events by THEMIS, Cluster, Double Star, and SuperDARN: Acceleration of FTEs, J. Geophys. Res.-Space, 114, A10213, doi:10.1029/2009JA014310, 2009.

Fuselier, S. A., Gary, S. P., Thomsen, M. F., Bame, S. J., and Gurnett, D. A.: Ion beams and the ion/ion acoustic instability upstream from the Earth's bow shock, J. Geophys. Res.-Space, 92, 4740–4744, doi:10.1029/JA092iA05p04740, 1987.

Greenstadt, E., Russell, C., and Hoppe, M.: Magnetic field orientation and suprathermal ion streams in the Earth's foreshock, J. Geophys. Res.-Space, 85, 3473–3479, doi:10.1029/JA085iA07p03473, 1980.

Greenwald, R. A., Baker, K. B., Dudeney, J. R., Pinnock, M., Jones, T. B., Thomas, E. C., Villain, J. P., Cerisier, J. C., Senior, C., Hanuise, C., Hunsucker, R. D., Sofko, G., Koehler, J., Nielsen, E., Pellinen, R., Walker, A. D. M., Sato, N., and Yamagishi, H.: DARN/SuperDARN, Space Sci. Rev., 71, 761–796, doi:10.1007/BF00751350, 1995.

Haerendel, G., Paschmann, G., Sckopke, N., Rosenbauer, H., and Hedgecock, P. C.: The frontside boundary layer of the magnetosphere and the problem of reconnection, J. Geophys. Res.-Space, 83, 3195–3216, doi:10.1029/JA083iA07p03195, 1978.

Hasegawa, H., Kitamura, N., Saito, Y., Nagai, T., Shinohara, I., Yokota, S., Pollock, C. J., Giles, B. L., Dorelli, J. C., Gershman, D. J., Avanov, L. A., Kreisler, S., Paterson, W. R., Chandler, M. O., Coffey, V., Burch, J. L., Torbert, R. B., Moore, T. E., Russell, C. T., Strangeway, R. J., Le, G., Oka, M., Phan, T. D., Lavraud, B., Zenitani, S., and Hesse, M.: Decay of mesoscale flux transfer events during quasi-continuous spatially-extended reconnection at the magnetopause, Geophys. Res. Lett., 43, 4755–4762, doi:10.1002/2016GL069225, 2016.

Hoilijoki, S., Souza, V. M., Walsh, B. M., Janhunen, P., and Palmroth, M.: Magnetopause reconnection and energy conversion as influenced by the dipole tilt and the IMF Bx, J. Geophys. Res.-Space, 119, 4484–4494, doi:10.1002/2013JA019693, 2014.

Hoilijoki, S., Palmroth, M., Walsh, B. M., Pfau-Kempf, Y., von Alfthan, S., Ganse, U., Hannuksela, O., and Vainio, R.: Mirror modes in the Earth's magnetosheath: Results from a global hybrid-Vlasov simulation, J. Geophys. Res.-Space, 121, 4191–4204, doi:10.1002/2015JA022026, 2016.

Kawano, H. and Russell, C. T.: Survey of flux transfer events observed with the ISEE 1 spacecraft: Dependence on the interplanetary magnetic field, J. Geophys. Res.-Space, 102, 11307–11313, doi:10.1029/97JA00481, 1997.

Kempf, Y., Pokhotelov, D., Gutynska, O., Wilson III, L. B., Walsh, B. M., von Alfthan, S., Hannuksela, O., Sibeck, D. G., and Palmroth, M.: Ion distributions in the Earth's foreshock: Hybrid-Vlasov simulation and THEMIS observations, J. Geophys. Res.-Space, 120, 3684–3701, doi:doi:10.1002/2014JA020519, 2015.

Kis, A., Scholer, M., Klecker, B., Kucharek, H., Lucek, E. A., and Rème, H.: Scattering of field-aligned beam ions upstream of Earth's bow shock, Ann. Geophys., 25, 785–799, doi:10.5194/angeo-25-785-2007, 2007.

Kokubun, S., Yamamoto, T., Acuña, M. H., Hayashi, K., Shiokawa, K., and Kawano, H.: The GEOTAIL Magnetic Field Experiment, J. Geomagn. Geoelectr., 46, 7–21, doi:10.5636/jgg.46.7, 1994.

Le, G. and Russell, C.: A study of ULF wave foreshock morphology – I: ULF foreshock boundary, Planet. Space Sci., 40, 1203–1213, doi:10.1016/0032-0633(92)90077-2, 1992.

Lepping, R. P., Acuña, M. H., Burlaga, L. F., Farrell, W. M., Slavin, J. A., Schatten, K. H., Mariani, F., Ness, N. F., Neubauer, F. M., Whang, Y. C., Byrnes, J. B., Kennon, R. S., Panetta, P. V., Scheifele, J., and Worley, E. M.: The WIND magnetic field investigation, Space Sci. Rev., 71, 207–229, doi:10.1007/BF00751330, 1995.

Lin, R. P., Anderson, K. A., Ashford, S., Carlson, C., Curtis, D., Ergun, R., Larson, D., McFadden, J., McCarthy, M., Parks, G. K., Rème, H., Bosqued, J. M., Coutelier, J., Cotin, F., D'Uston, C., Wenzel, K. P., Sanderson, T. R., Henrion, J., Ronnet, J. C., and Paschmann, G.: A three-dimensional plasma and energetic particle investigation for the WIND spacecraft, Space Sci. Rev., 71, 125–153, doi:10.1007/BF00751328, 1995.

Liu, T. Z., Hietala, H., Angelopoulos, V., and Turner, D. L.: Observations of a new foreshock region upstream of a foreshock bubble's shock, Geophys. Res. Lett., doi:10.1002/2016GL068984, 2016.

McComas, D., Bame, S., Barker, P., Feldman, W., Phillips, J., Riley, P., and Griffee, J.: Solar Wind Electron Proton Alpha Monitor (SWEPAM) for the Advanced Composition Explorer, Space Sci. Rev., 86, 563–612, doi:10.1023/A:1005040232597, 1998.

McWilliams, K. A., Sofko, G. J., Yeoman, T. K., Milan, S. E., Sibeck, D. G., Nagai, T., Mukai, T., Coleman, I. J., Hori, T., and Rich, F. J.: Simultaneous observations of magnetopause flux transfer events and of their associated signatures at ionospheric altitudes, Ann. Geophys., 22, 2181–2199, doi:10.5194/angeo-22-2181-2004, 2004.

Merka, J., Szabo, A., Slavin, J. A., and Peredo, M.: Three-dimensional position and shape of the bow shock and their variation with upstream Mach numbers and interplanetary magnetic field orientation, J. Geophys. Res.-Space, 110, A04202, doi:10.1029/2004JA010944, 2005.

Meziane, K., Alrefay, T. Y., and Hamza, A. M.: On the shape and motion of the Earth's bow shock, Planet. Space Sci., 93–94, 1–9, doi:10.1016/j.pss.2014.01.006, 2014.

Milan, S. E., Lester, M., Cowley, S. W. H., Moen, J., Sandholt, P. E., and Owen, C. J.: Meridian-scanning photometer, coherent HF radar, and magnetometer observations of the cusp: a case study, Ann. Geophys., 17, 159–172, doi:10.1007/s00585-999-0159-5, 1999a.

Milan, S. E., Lester, M., Greenwald, R. A., and Sofko, G.: The ionospheric signature of transient dayside reconnection and the associated pulsed convection return flow, Ann. Geophys., 17, 1166–1171, doi:10.1007/s00585-999-1166-2, 1999b.

Milan, S. E., Lester, M., Cowley, S. W. H., and Brittnacher, M.: Convection and auroral response to a southward turning of the IMF: Polar UVI, CUTLASS, and IMAGE signatures of transient magnetic flux transfer at the magnetopause, J. Geophys. Res.-Space, 105, 15741–15755, doi:10.1029/2000JA900022, 2000.

Milan, S. E., Imber, S. M., Carter, J. A., Walach, M.-T., and Hubert, B.: What controls the local time extent of flux transfer events?, J. Geophys. Res.-Space, 121, 1391–1401, doi:10.1002/2015JA022012, 2016.

Mukai, T., Machida, S., Saito, Y., Hirahara, M., Terasawa, T., Kaya, N., Obara, T., Ejiri, M., and Nishida, A.: The Low Energy Particle (LEP) Experiment onboard the GEOTAIL Satellite, J. Geomagn. Geoelectr., 46, 669–692, doi:10.5636/jgg.46.669, 1994.

Ogilvie, K. W., Chornay, D. J., Fritzenreiter, R. J., Hunsaker, F., Keller, J., Lobell, J., Miller, G., Scudder, J. D., Sittler, E. C., Torbert, R. B., Bodet, D., Needell, G., Lazarus, A. J., Steinberg, J. T., Tappan, J. H., Mavretic, A., and Gergin, E.: SWE, a comprehensive plasma instrument for the WIND spacecraft, Space Sci. Rev., 71, 55–77, doi:10.1007/BF00751326, 1995.

Øieroset, M., Lühr, H., Moen, J., Moretto, T., and Sandholt, P. E.: Dynamical auroral morphology in relation to ionospheric plasma convection and geomagnetic activity: Signatures of magnetopause X line dynamics and flux transfer events, J. Geophys. Res.-Space, 101, 13275–13292, doi:10.1029/96JA00613, 1996.

Omidi, N. and Sibeck, D. G.: Flux transfer events in the cusp, Geophys. Res. Lett., 34, L04106, doi:10.1029/2006GL028698, 2007.

Palmroth, M., Archer, M., Vainio, R., Hietala, H., Pfau-Kempf, Y., Hoilijoki, S., Hannuksela, O., Ganse, U., Sandroos, A., von Alfthan, S., and Eastwood, J. P.: ULF foreshock under radial IMF: THEMIS observations and global kinetic simulation Vlasiator results compared, J. Geophys. Res.-Space, 120, 8782–8798, doi:10.1002/2015JA021526, 2015.

Pang, Y., Deng, X., Yuan, Z., Zhou, M., Lin, M., Shu, Z., Li, S., Wang, J., and Balogh, A.: Polar ionosphere and geomagnetic response for the flux transfer events: A case study, Adv. Space Res., 43, 957–963, doi:10.1016/j.asr.2008.08.008, 2009.

Paschmann, G.: Recent in-situ observations of magnetic reconnection in near-Earth space, Geophys. Res. Lett., 35, L19109, doi:10.1029/2008GL035297, 2008.

Phan, T. D., Kistler, L. M., Klecker, B., Haerendel, G., Paschmann, G., Sonnerup, B. U. Ö., Baumjohann, W., Bavassano-Cattaneo, M. B., Carlson, C. W., DiLellis, A. M., Fornacon, K.-H., Frank, L. A., Fujimoto, M., Georgescu, E., Kokubun, S., Moebius, E., Mukai, T., Øieroset, M., Paterson, W. R., and Reme, H.: Extended magnetic reconnection at the Earth's magnetopause from detection of bi-directional jets, Nature, 404, 848–850, doi:10.1038/35009050, 2000.

Pokhotelov, D., von Alfthan, S., Kempf, Y., Vainio, R., Koskinen, H. E. J., and Palmroth, M.: Ion distributions upstream and downstream of the Earth's bow shock: first results from Vlasiator, Ann. Geophys., 31, 2207–2212, doi:10.5194/angeo-31-2207-2013, 2013.

Provan, G., Yeoman, T. K., and Milan, S. E.: CUTLASS Finland radar observations of the ionospheric signatures of flux transfer events and the resulting plasma flows, Ann. Geophys., 16, 1411–1422, doi:10.1007/s00585-998-1411-0, 1998.

Russell, C. T. and Elphic, R. C.: Initial ISEE magnetometer results: magnetopause observations, Space Sci. Rev., 22, 681–715, doi:10.1007/BF00212619, 1978.

Russell, C. T. and Elphic, R. C.: ISEE observations of flux transfer events at the dayside magnetopause, Geophys. Res. Lett., 6, 33–36, doi:10.1029/GL006i001p00033, 1979.

Sanderson, T. R., Reinhard, R., Wenzel, K.-P., Roelof, E. C., and Smith, E. J.: Observations of upstream ions and low-frequency waves on ISEE 3, J. Geophys. Res.-Space, 88, 85–95, doi:10.1029/JA088iA01p00085, 1983.

Schwartz, S. J., Thomsen, M. F., and Gosling, J. T.: Ions upstream of the Earth's bow shock: A theoretical comparison of alterna-

tive source populations, J. Geophys. Res.-Space, 88, 2039–2047, doi:10.1029/JA088iA03p02039, 1983.

Schwartz, S. J., Daly, P. W., and Fazakerley, A. N.: Multi-spacecraft analysis of plasma kinetics, in: Analysis methods for multi-spacecraft data, edited by: Paschmann, G. and Daly, P. W., ISSI Scientific Reports, International Space Science Institute, 1, 159–183, 2000.

Shepherd, S. G.: Altitude-adjusted corrected geomagnetic coordinates: Definition and functional approximations, J. Geophys. Res.-Space, 119, 7501–7521, doi:10.1002/2014JA020264, 2014.

Sibeck, D. and Omidi, N.: Flux transfer events: Motion and signatures, J. Atmos. Sol.-Terr. Phy., 87–88, 20–24, doi:10.1016/j.jastp.2011.07.010, 2012.

Smith, C., L'Heureux, J., Ness, N., Acuña, M., Burlaga, L., and Scheifele, J.: The ACE Magnetic Fields Experiment, Space Sci. Rev., 86, 613–632, doi:10.1023/A:1005092216668, 1998.

Tanskanen, E. I.: A comprehensive high-throughput analysis of substorms observed by IMAGE magnetometer network: Years 1993–2003 examined, J. Geophys. Res., 114, A05204, doi:10.1029/2008JA013682, 2009.

Thomsen, M. F., Schwartz, S. J., and Gosling, J. T.: Observational evidence on the origin of ions upstream of the Earth's bow shock, J. Geophys. Res.-Space, 88, 7843–7852, doi:10.1029/JA088iA10p07843, 1983.

Trattner, K. J., Mulcock, J. S., Petrinec, S. M., and Fuselier, S. A.: Probing the boundary between antiparallel and component reconnection during southward interplanetary magnetic field conditions, J. Geophys. Res.-Space, 112, A08210, doi:10.1029/2007JA012270, 2007.

Treumann, R. A. and Baumjohann, W.: Collisionless Magnetic Reconnection in Space Plasmas, Frontier. Phys., 1, 31, doi:10.3389/fphy.2013.00031, 2013.

van de Kamp, M.: Harmonic quiet-day curves as magnetometer baselines for ionospheric current analyses, Geosci. Instrum. Method. Data Syst., 2, 289–304, doi:10.5194/gi-2-289-2013, 2013.

von Alfthan, S., Pokhotelov, D., Kempf, Y., Hoilijoki, S., Honkonen, I., Sandroos, A., and Palmroth, M.: Vlasiator: First global hybrid-Vlasov simulations of Earth's foreshock and magnetosheath, J. Atmos. Sol.-Terr. Phy., 120, 24–35, doi:10.1016/j.jastp.2014.08.012, 2014.

Weygand, J. M., Amm, O., Angelopoulos, V., Milan, S. E., Grocott, A., Gleisner, H., and Stolle, C.: Comparison between SuperDARN flow vectors and equivalent ionospheric currents from ground magnetometer arrays, J. Geophys. Res., 117, A05325, doi:10.1029/2011JA017407, 2012.

Wild, J. A., Cowley, S. W. H., Davies, J. A., Khan, H., Lester, M., Milan, S. E., Provan, G., Yeoman, T. K., Balogh, A., Dunlop, M. W., Fornaçon, K.-H., and Georgescu, E.: First simultaneous observations of flux transfer events at the high-latitude magnetopause by the Cluster spacecraft and pulsed radar signatures in the conjugate ionosphere by the CUTLASS and EISCAT radars, Ann. Geophys., 19, 1491–1508, doi:10.5194/angeo-19-1491-2001, 2001.

Wild, J. A., Milan, S. E., Cowley, S. W. H., Dunlop, M. W., Owen, C. J., Bosqued, J. M., Taylor, M. G. G. T., Davies, J. A., Lester, M., Sato, N., Yukimatu, A. S., Fazakerley, A. N., Balogh, A., and Rème, H.: Coordinated interhemispheric SuperDARN radar observations of the ionospheric response to flux transfer events observed by the Cluster spacecraft at the high-latitude magnetopause, Ann. Geophys., 21, 1807–1826, doi:10.5194/angeo-21-1807-2003, 2003.

Wilson, L. B., Koval, A., Sibeck, D. G., Szabo, A., Cattell, C. A., Kasper, J. C., Maruca, B. A., Pulupa, M., Salem, C. S., and Wilber, M.: Shocklets, SLAMS, and field-aligned ion beams in the terrestrial foreshock, J. Geophys. Res.-Space, 118, 957–966, doi:10.1029/2012JA018186, 2013.

Zweibel, E. G. and Yamada, M.: Magnetic Reconnection in Astrophysical and Laboratory Plasmas, Annu. Rev. Astron. Astr., 47, 291–332, doi:10.1146/annurev-astro-082708-101726, 2009.

FINNISH METEOROLOGICAL INSTITUTE
Erik Palménin aukio 1
P.O. Box 503
FI-00101 HELSINKI
tel. +358 29 539 1000
WWW.FMI.FI

FINNISH METEOROLOGICAL INSTITUTE
CONTRIBUTIONS No. 132
ISBN 978-952-336-018-1 (paperback)
ISSN 0782-6117
Erweko
Helsinki 2017

ISBN 978-952-336-019-8 (pdf)
Helsinki 2017